Gurney Flaps and Micro-Tabs for Load Control on Wind Turbines

vorgelegt von
Dipl.-Ing.
Alena Berit Bach
geb. in Bremen

von der Fakulät V - Verkehrs- und Maschinensysteme
der Technischen Universität Berlin
zur Erlangung des akademischen Grades

Doktor der Ingenieurwissenschaften
-Dr.-Ing.-

genehmigte Dissertation

Promotionsausschuss:

Vorsitzender:	Prof. Dr.-Ing. V. Popov
Gutachter:	Prof. Dr.-Ing. C. O. Paschereit
Gutachter:	Prof. Dr.-Ing. D. Greenblatt
Gutachter:	Dr.-Ing. G. Pechlivanoglou

Tag der wissenschaftlichen Aussprache: 9. Februar 2016

Berlin 2016

Abstract

In the last decades, wind turbine innovation has led to significant growth in capacity and size per turbine. Consequently, the blade experiences additional local fluctuations due to local gusts, horizontal or vertical wind shear, blade-tower interference, turbulence, or yaw and tilt misalignment. Reducing these fatigue loads is directly connected to an enhanced overall turbine lifetime as well as a reduction of the levelised cost of energy [74].
A well known fast and effective technique to address these challenges is the usage of local active elements. Possible active load control solutions are flaps or tabs at the trailing edge, leading edge spoilers or flaps as well as solutions dealing with blowing, suction, synthetic jets or plasma actuators [54, 14, 110, 53].
The control with small devices which are placed close to the trailing edge such as Gurney flaps or micro-tabs are generally regarded as an effective solution. Gurney flaps are small flaps placed at the trailing edge of an airfoil with a flap height in the range of the local boundary layer. Micro-tabs are closely related: They deploy perpendicular to the airfoil surface close to the trailing edge and are of the same magnitude of height. If either device is deployed towards the pressure side, a positive lift change is generated. If the devices are deployed to the suction side lift, reduction is achieved.

In the past, extensive research has been conducted with passive Gurney flaps as well as micro-tabs on airfoils under steady inflow. However, little is understood of the unsteady aerodynamic effects of active micro-tabs under unsteady inflow. In the following work, steady as well as unsteady aerodynamics of micro-tabs and Gurney flaps are presented and compared:
First, the effects of the passive devices under steady inflow were recapitulated. Special attention is paid to the surrounding flow field to understand the driving mechanisms of the devices. Results of Particle Image Velocimetry (PIV) as well as hot-wire measurements are shown to display the wake system and its influence on the loads.
Second, the unsteady aerodynamics of active micro-tabs and Gurney flaps were investigated. Effects of the deployment time, function or height were studied. The main differences between the flaps and the tabs were found in the immediate response after the device deployment: While the loads change immediately using an active Gurney flap, micro-tabs first cause an adverse lift response.
Third, after examining the active control devices, an unsteady pitching airfoil was studied with passive, non-moving flaps and tabs. The effects of the reduced frequency and angle of attack motion of the pitching airfoil as well as the tab placement and height are presented.
Finally, the two unsteady systems consisting of the pitching airfoil and active flaps or tabs were analyzed together. Experiments as well as analytical models are presented to understand the rather complex system.

Contents

List of Figures

List of Tables

Nomenclature

Latin Symbols

Symbol	Unit	Designation
A	$[m^2]$	Area
A_1, A_2, A_3	[/]	Constants of indicial response function
A_{tv}	[/]	Model constant
AR	[/]	Aspect ratio
C	[/]	Coefficient
$C(k)$	[/]	Theodorsen's function
D	$[N]$	Aerodynamic drag
D_n	[/]	Deficiency function
H_v	[/]	Hankel function
J_v	[/]	Bessel function
P	$[N]$	Rotor power
L	$[N]$	Aerodynamic lift
L_{arm}	$[m]$	Moment arm
M	$[Nm]$	Aerodynamic moment
Ma	[/]	Mach number
Re	[/]	Reynolds number
St	[/]	Strouhal number
Tr	$[N]$	Rotor thrust
T	$[s]$	Time period
Tu	[%]	Turbulence intensity
T_v	[/]	Model constant
T_{TE}	[/]	Model constant
U	$[m/s]$	Mean Velocity in x-direction
V	$[m/s]$	Mean Velocity in y-direction
W	$[m/s]$	Mean Velocity in w-direction
X_n,Y_n	[/]	Indicial function
Y_v	[/]	Bessel function
Z	$[m]$	Spacing of vortex generators
a	[/]	Wind turbine induction factor
b	$[m]$	Airfoil span

b_1, b_2, b_3	[/]	Constants of indicial response function
b^1	$[m]$	Half chord for aerodynamic model
c	$[m]$	Airfoil chord length
$\bar{c}$	$[m/s]$	Local overall velocity
f	$[Hz]$	Frequency
h	$[m]$	Height
$h_{TE,0}$	[/]	Model constant
h^+	[/]	Non-dimensional rate of tab motion
k	[/]	Reduced frequency
l	$[m]$	Length
n	[/]	Time step
$n_{T\nu}$	[/]	Model constant
t	$[s]$	Time
s	[/]	Dimensionless time (refers to half chord)
u	$[m/s]$	Velocity in x-direction
v	$[m/s]$	Velocity in y-direction
w	$[m/s]$	Velocity in w-direction
x	$[m]$	Cartesian coordinates
y	$[m]$	Cartesian coordinates
y^+	[/]	Dimensionless wall distance
z	$[m]$	Cartesian coordinates

Greek Symbols

Symbol	**Unit**	**Designation**
Γ	$[m^2/s]$	Circulation
Δ	[/]	Difference
Ξ	[/]	Aerodynamic damping
$\Phi(s)$	[/]	Wagner function
$\Psi(s)$	[/]	Küssner function
α	[°]	Angle of attack
β	[/]	Compressibility factor
γ	$[m/s]$	2D circulation at a section
δ^*	$[m]$	Boundary layer height
$\delta(t)$	[/]	Dirac-delta function
ζ	[°]	Angle of pressure ports
θ	[°]	Flap deflection angle
ρ	$[kg/m^3]$	Density
σ	[/]	Solidity ratio

ϕ	[°]	Phase angle
ω	$[1/s]$	Vorticity of flow field

Subscripts

Index	Designation
BV	Bound vortex
D	Drag (full span)
L	Lift (full span)
M	Moment
MT	Micro-tab
P	Rotor power
SV	Spanwise vortex
T	Rotor thrust
act	Actuation
b	Bound
$base$	Baseline
$circ$	Circulatory
$crit$	Critical
d	Sectional drag
$delay$	Time delay
dep	Deployment
eff	Effective
$flap$	Gurney flap
gap	Gap between tab/flaps
ini	Initial
l	Sectional lift
m	Sectional moment
max	Maximum
min	Minimum
$norm$	Normalised
ov	Overshoot
p	Pressure
qs	Quasi-steady
rel	Relative
ret	Retraction
tab	Micro-tab
$trans$	Transition
$trip$	Tripped flow
vtx	Vortex
w	Wake
∞	Inflow

Supscripts

Index	Designation
$()^*$	Dimensionless

Abbreviations

Abbreviation	Designation
BL	**B**oundary **L**ayer
BV	**B**ound **V**ortex
DFG	**D**eutsche **F**orschungs **G**emeinschaft (German Science Foundation)
HFI	**H**ermann **F**öttinger **I**nstitute
HS	**H**igh **S**peed
ISTA	**I**nstitut für **S**trömungsmechanik und **T**echnische **A**kustik
LiDAR	**Li**ght **D**etection **A**nd **R**anging
MEM	**M**icro-**E**lectro-**M**echanical
MiTE	**M**icro-**T**railing Edge **E**ffectors
PIV	**P**article **I**mage **V**elocimetry
POD	**P**roper **O**rthogonal **D**ecomposition
PS	**P**ressure **S**ide
PSD	**P**ower **S**pectra **D**ensity
PSU	**P**ennsylvania **S**tate **U**niversity
SODAR	**SO**ound **D**etection **A**nd **R**anging
SS	**S**ustion **S**ide
SV	**S**panwise **V**ortex
TU	**T**echnische **U**niversität
VG	**V**ortex **G**enerator

1 Introduction

In the last decades, wind turbine innovation has led to significant growth in capacity and size per turbine. This is due to the 'square-cube law', which states that as the diameter of a turbine increases, the theoretical energy output increases by the square of the rotor diameter. Typical state of the art wind turbines feature rotor diameters of more than 80m. In order to increase the efficiency, the size of the rotors and the installed capacity has been increased from 17m in diameter and 50kW rated power to 126m and 7.55MW (see Figure 1.1). This represents a growth of factor 7 in diameter and 150 in rated power within the past 25 years. Prototypes of up to 10MW in power and rotor diameters of more than 150m are under development and will be introduced onto the market in the next years.

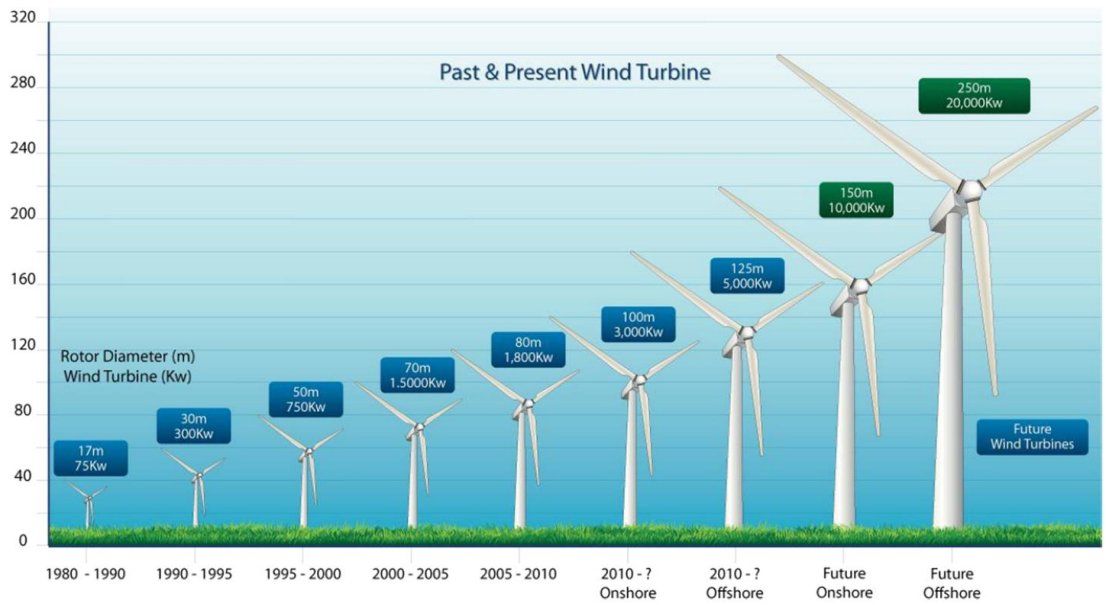

Figure 1.1: Growth of wind turbines in the past and the future [39]

However, the growth of the rotor diameter is associated with larger blade masses and a higher strain of the used materials. Furthermore, the higher blade masses lead to stronger gear boxes which need in turn more overall maintenance. All these facts sum up to increasing turbine costs. So far this trend has been countered by e.g. advanced aerodynamic rotor design concepts, the availability of modern, lighter and yet stronger materials (such as carbon fiber composites) or advanced manufacturing methods or control strategies for the reduction of mechanical loads [39]. These advances in material technology have led to a blade mass scaling factor of 2.4

instead of 3 for an increase in rotor diameter [55]. However, these methods are slowly reaching their limits and new concepts must be found for the future.

So far, the up-scaling of the whole turbine concept has been the most efficient way to produce more energy. The rather young wind energy industry has abandoned the experimental methods employed in the early years of wind turbine development. Before learning from the results and experience of the first generation, the second and third generations were tested and produced. A general approach to increase the rotor diameter while limiting the increase of the material requirement is to reduce the blade loading. Therefore, for the purposes of maximizing energy capture below rated wind speeds and limiting the loads above these speeds, load control is employed, which is achieved for most of the large wind turbines through the use of variable speed and adjustable collective pitch mechanisms. However, collective pitch mechanisms only operate effectively for relatively slow wind speed changes and affect the entire rotor area, even though individual blades of rotors with large diameters experience wind changes locally. An initial improvement, motivated by the helicopter industry, was to apply an individual pitch control mechanism for each blade.

Due to the increasing rotor size, modern wind turbines also operate in large layers of the atmosphere, from 50m up to 200m. Consequently, the blades experience additional local fluctuations due to local gusts, horizontal or vertical wind shear, blade-tower interference, turbulence, or yaw and tilt misalignment. Thus, a much more complicated mechanism is necessary to alleviate and control blade loads and their fluctuations. Control could be achieved by additional active or passive flow control devices on the rotor. For active control, open-loop or closed-loop predictive control strategies using remote sensing technologies can be applied. Hence, fatigue loads can be reduced and the mechanical stability can be increased significantly. This results in increased lifetime and a reduced levelised cost of energy.

2 Theory of Wind Turbines

2.1 Wind Turbine Aerodynamics

The most simplified model of a wind turbine is the 1D actuator disc model. Basic Equations for the shaft power and the rotor thrust of the rotor can be derived using the Bernoulli equation as well as the axial momentum equation. The rotor disc is modelled using a pressure drop Δp over the rotor. The incoming wind speed U_∞ is reduced to U_1 in the process of passing through the streamtube (see Figure 2.1).

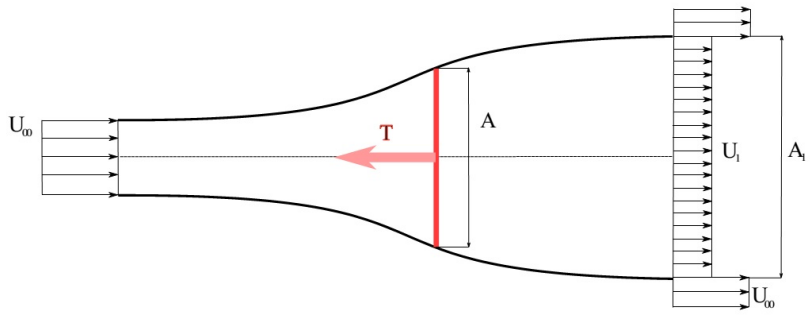

Figure 2.1: Actuator disc model for wind turbines

Therefore, the axial induction factor of the velocities is defined as

$$U_1 = (1-2a)U_\infty. \tag{2.1}$$

Using the above mentioned means one can derive the equations for power and thrust as follows [57]:

$$P = 1/2 * \rho(U_\infty)^3 a(1-a)^2 A, \tag{2.2}$$

and

$$Tr = 2 * \rho(U_\infty)^2 a(1-a)^2 A. \tag{2.3}$$

Meanwhile, the available power in the wind can be calculated from the formulation of the kinetic energy as

$$P = 1/2 * \rho A(U_\infty)^3. \tag{2.4}$$

Finally, a power and thrust coefficient can be defined as

$$C_P = 4a(1-a)^2, \tag{2.5}$$

and

$$C_T = 4a(1-a). \tag{2.6}$$

Differentiating the power coefficient shows that a theoretical limit exists with a maximum of $C_P = 16/17$ for $a = 1/3$. Hence, not all the available kinetic energy in the flow can be used to generate power and a certain rest kinetic energy must remain in the flow behind the turbine. This limit is known as the Betz limit.

2.2 Aerodynamics of Wind Turbine Airfoils

Today's wind turbine rotors are generally three bladed rotors with a highly efficient aerodynamic design. Unlike the aerodynamics of a typical aviation airfoil, the wind turbine profile experiences two inflow velocities: The incoming wind and the velocity due to the rotational motion of the blade. Both velocities add up to the apparent wind, which generate the lift and drag (see Figure 2.2, left). The inflow angle is a result of the two velocity components and is generally chosen in a way that the airfoil operates at the best lift-to-drag ratio.
The resultant force of lift and drag can also be divided into the thrust component and the tangential component. The component tangential to the plane of rotor rotation is responsible for the turbine's power (see Figure 2.2, right). The power is generally controlled through the blade's pitch. Thereby, conventional turbines have a collective pitch mechanism which controls all three blades at the same time. Modern turbines generally have an individual pitch mechanism so that the pitch of every single blade can be controlled separately. The pitch angle β is defined as the angle between the plane of rotor rotation and the airfoil's chord. Relatively small changes in the pitch angle can have a big effect on the power output. This way, the blade can adjusted depending on the current wind conditions.

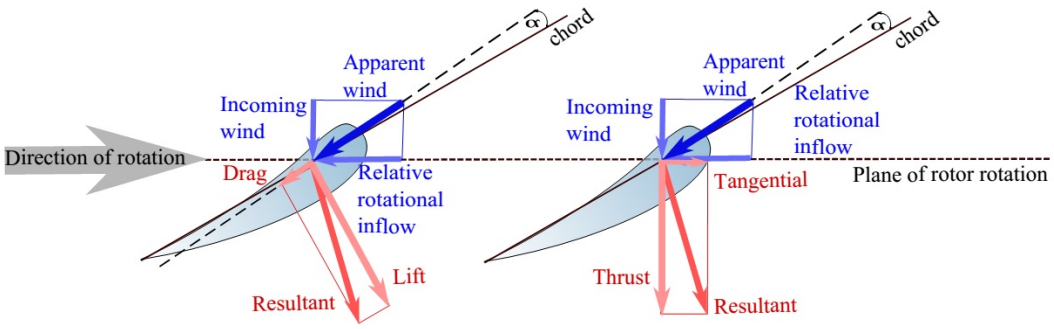

Figure 2.2: Typical forces and inflow conditions of a wind turbine airfoil

In Figure 2.3 three airfoils are depicted at different radial positions. The airfoil to the left is close to the hub, the airfoil in the centre is at mid-span, and the airfoil at the right is positioned

at the outer blade. Since the blade pitch must be the same over one blade's span, the angle of attack of the incoming flow is clearly changing as a result of the increasing rotational inflow component. Hence, in this constellation the airfoils in the inner rotor parts experience a much higher angle of attack than the outer rotor parts.

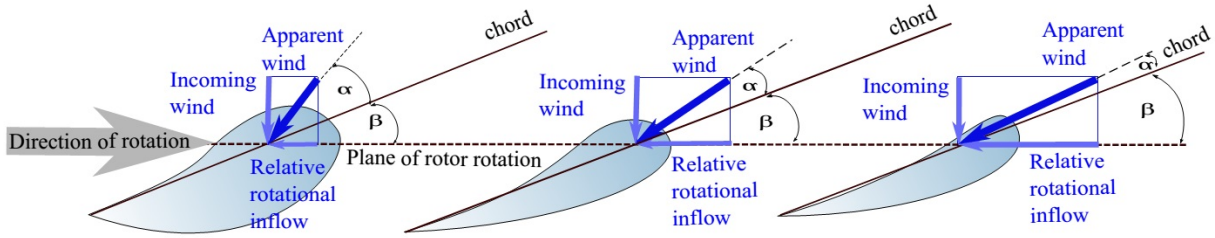

Figure 2.3: Typical inflow condition for wind turbine airfoils along the blade span

However, in reality the blade is usually pre-twisted by an angle θ to prohibit stall and to operate close to the best lift-to-drag ratio (shown in Figure 2.4). Hence, each section has a specific airfoil shape, a chord length and a twist angle. Thereby, the twist angle is a property of the blade meanwhile the pitch angle is part of the control system of the turbine. However, due to manufacturing reasons it is not cost effective to create highly twisted blades. Therefore, most of the blades have a maximum root twist of about 18°, which is less than the optimal value [109]. Consequently, the inner rotor sections operate at angles higher as the angle corresponding to best lift-to-drag ratio or often even at angles within the post stall regime.

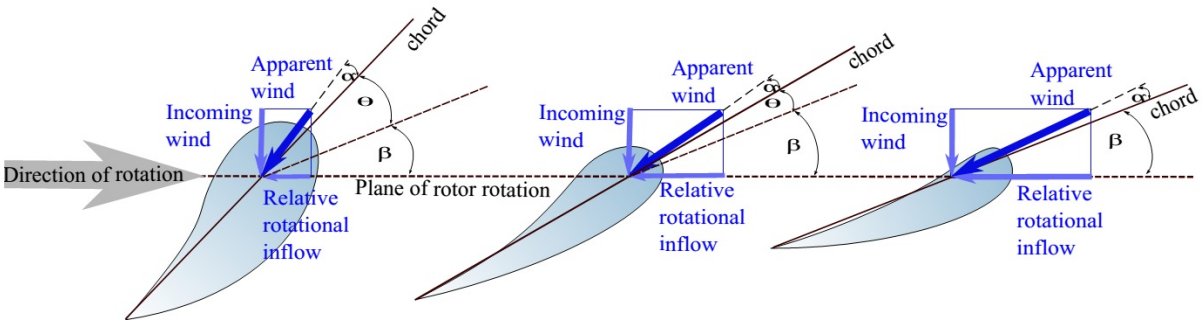

Figure 2.4: Optimal twist distribution along the blade span

2.3 The Effects of Unsteady Inflow

Various different wind speeds due to the local weather, the turbine side or the time of the year are generally represented by the Weibull distribution. However, wind conditions vary even within one single rotor revolution. This is mainly due to gusts, horizontal or vertical wind shear,

blade-tower inference, turbulence or yaw and tilt misalignment.
A fluctuating incoming wind, will not only result in a change in apparent wind velocity but also in a change in angle of attack. Hence, a gust results in higher inflow coupled with a higher angle of attack at the same time. This yields a more drastic change in lift than a change in velocity on its own. Figure 2.5 illustrates the unsteady inflow over the turbine height, causing unsteady lift over time. Hereby, a steady state lift curve is used for reasons of simplification; in reality the unsteady lift as well as aeroelastic effects multiply the resulting lift variations.

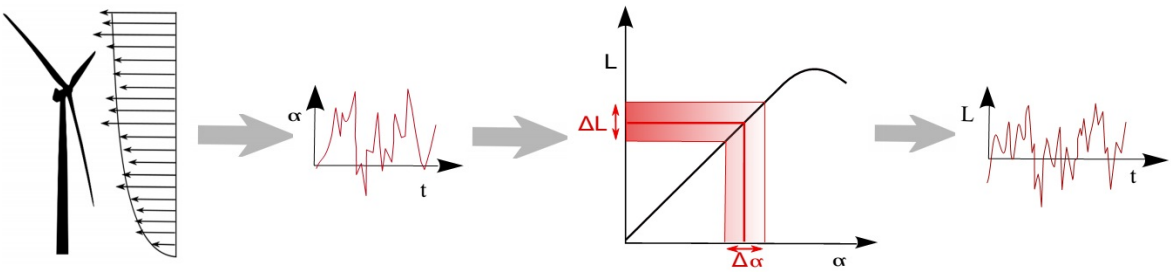

Figure 2.5: Unsteady inflow and loads on a wind turbine section

Generally, the inner rotor parts are more affected than the outer rotor part, since the incoming wind is in the same range as the rotational velocity component (see again Figure 2.4). Therefore, the inner rotor sections experience large angle of attack variations up to high angles of attack; the consequence of which is often dynamic stall [23]. Dynamic stall is a well known occurrence for most wind turbines operating in yawed, stalled or turbulent conditions. As a consequence, a spanwise vortex forms near the leading edge which grows quickly and convects rapidly downstream. During this process, the dynamic stall vortex generates a region of low pressure on the lifting surface, causing the lift to even exceed the maximum static values. When the vortex finally sheds from the trailing edge an abrupt deep stall follows. It has been shown that dynamic stall occurs on horizontal axis wind turbine blades [99], and contributes significantly to wind turbine rotor load fluctuation [117] [4].
These anomalous load fluctuations along the blade affect the whole conversion of wind energy, starting with the lift forces at the profiles [116], transferring to structural and mechanical loads [93] and finally leading to fluctuations in the power production [50]. However, the structural and mechanical loads connected to these fluctuations are the most severe. A strong gust results in a shock through the whole system: From the blade structure, through the gearbox, the generator to the tower and the foundation. All together, these fatigue loads therefore reduce the overall lifetime of the turbine and hence affect the cost of energy.

3 Load Control Techniques

Most of the large wind turbines work under variable speed and collective pitch mechanisms for the rotor power regulation. Pitch control is primarily used to maximise energy capture below the rated wind speed and to limit the loads above [120]. However, the pitch system is not constructed for a fast and continuous operation as it would be needed for the control of unsteady loads. Furthermore, with increasing rotor size, a more localised, spanwise control is necessary to alleviate and control blade loads and thus to increase mechanical stability.
The collective pitch mechanism only operates effectively for relatively slow wind speed changes and affects the whole rotor area even though rotors with a large diameter experience local wind changes. A first improvement motivated by the helicopter industry was to apply an individual pitch control for each blade. However, in the case of sudden load changes the pitch control mechanism is often too slow to react appropriately. A well-known, fast and efficient technique to meet these challenges is spanwise distributed flow control. The basic idea is keeping a certain target lift constant across a blade section. This can be achieved e.g. by externally varying the angle of attack relative to the wind inflow if the inflow wind speed is diverging (as it is done for the whole blade during pitch). However, this is mostly hard to achieve section-wise since the section is integrated in the 3D blade structure. Therefore, most concepts are based on the modification of the airfoil's circulation and hence the lift according to the inflow state. In that way the dynamic lift variations can be held minimal and the fatigue loads are reduced.
When such a system is simulated by analytical methods this is mostly done through the use of multiple steady-state curves which are each assigned to a certain state of the control device. E.g. for trailing edge flaps multiple curves for an airfoil section would exist; thereby each curve is associated to a different flap angle. The simulation algorithm then changes the aerodynamic characteristics of the airfoil by using for each change in inflow the optimal available lift polar. This results in a much more constant lift value close to the target lift and reduced fatigue loads. Figure 3.1 illustrates this basic simulation principle of the control concept which deviates from the initial situation as described in Figure 2.5.

Several active flow control (AFC) solutions are well-known from the aviation industry and have been tested for wind turbine applications. General overviews about the possible implementation of AFC on wind turbines are outlined in [54] and [14]. In the past, reports of research programmes on the flow control of whole wind turbines have been conducted, e.g. in the work packages on 'Smart-Rotor-Blades' and 'Rotor Control' by the European UPWIND project [42] or further work by *TEMBRA GmbH Co. KG* funded by the *German Federal Ministry for the Environment, Nature Conservation, Building and Nuclear Safety* [67, 44]. At the *HFI* research on active flow control on wind turbines is conducted in the frame of the collaborative research project (DFG PAK780) which includes the work of five German universities and is funded by the *DFG*. Within

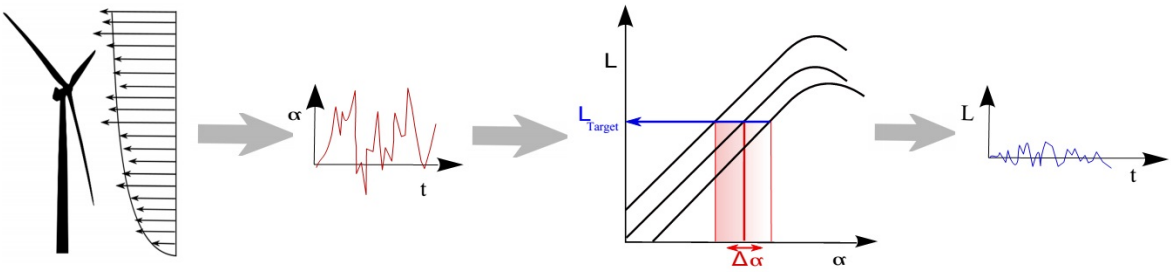

Figure 3.1: Simulation concept using multiple lift curves for fatigue load reduction

this work the *HFI* has build-up a small research wind turbine for experimental work on active trailing edge flaps for the investigation on future load control concepts [42, 141, 146].
Generally, flow control solutions can be divided into passive and active methods. In the following section a general overview on the conducted research of these devices for the application on wind turbines is given.

3.1 Passive Methods

Passive control methods are defined as devices that are not driven by a control set-up. Most of the passive control devices are fixed elements which change the airfoil aerodynamics without reacting to a change of the inflow. However, there are a few self controlling methods, where the flow itself changes e.g. the geometry of element and therefore the aerodynamic properties without the need of an external control set-up.
Some of the passive methods are particularly interesting for the inner rotor parts, where stall and dynamic stall play an important role: If stall occurs at the inner blade sections the separated region is transported from the root towards the middle region of the blade due to the rotational effects. This mechanism results in a reduction of the performance and efficiency of the whole wind turbine. Hence, to minimise the stall and the incidence of dynamic stall passive stall control mechanism are advantageous.

3.1.1 Vortex Generators

One well-known approach to change an airfoil's stall characteristic is the use of vortex generators (VGs), which are commonly used in the aviation industry [122, 121, 83]. They are usually applied upstream of flight control surfaces where the boundary layer attachment is critical. The VGs create strong vortices which mix high momentum free stream air into the bottom of the boundary layer and thus reducing the effects of adverse pressure gradients and delaying separation [82]. An illustration of their general effect can be found in Figure 3.2. To have an effect over a whole blade section the vortex generators need to be mounted in arrays. Depending on their orientation they either produce co- or counter-rotating vortices. However, an effective

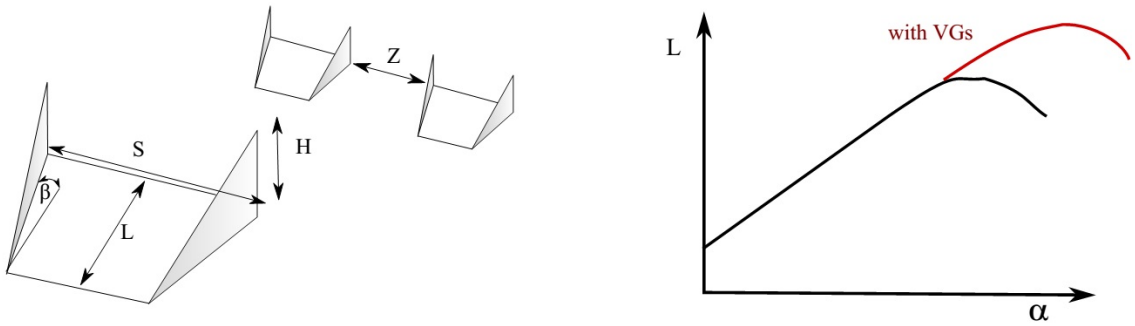

Figure 3.2: Geometry and effect of vortex generators

application depends strongly on the chosen parameters like the size, aspect ratio, spacing, angle of incidence to the flow, chordwise position in relation to the separation line, configuration of the co- or counter-rotating vortices etc. A parameter optimisation study which gives a good guideline has been carried out by Godard and Stanislas [49].
Velte and Hanson [137] [138] experimentally investigated the flow structure downstream of vortex generators with Particle Image Velocimetry (PIV) in order to gain insight into the physical processes of the flow. The VGs as illustrated in Figure 3.2 create counter-rotating stream-wise vortices transporting momentum from the outer flow into the near-wall region in the down-wash region. The effect of these vortices in combination with a dynamic stall vortex (DSV) has been further studied by Mai et al. in 2006 [89]. The streamwise vortices of the VGs disturb the crosswise DSV and the dynamic separation could be partly prevented. Furthermore, the VGs inhibit the negative pitching moment peak and the overall drag is being reduced at dynamic-stall conditions.
The strong effect on flow separation and the DSV make VGs especially interesting for the application on wind turbines. The devices can be used for controlling the aerodynamic and aeroelastic behaviour of wind turbine blades, adjust the power or loads of the turbine and prevent undesired vibrations. In the early 1980s the application of VGs on wind turbines was first tested by the NASA [96] [131]. Performance tests, showed an increase in annual energy production of 20% for the Boeing MOD-2 wind turbine (2.5MW) with the addition of vortex generators. Later Corrigan and Savino [36] were able to show similar performance improvements on the smaller MOD-0 wind turbine.
Similar results were obtained by Oye in 1995 [106], who measured a power curve on a ELKRAFT 1000kW experimental wind turbine with and without vortex generators on the inner part of the blades. The maximum power was increased from approximately 850 kW of the clean configuration to 1050kW when using vortex generators.
In a more recent investigation performed by Johansen et al. [63] for Risø, 3D CFD computations on VGs on wind turbines were carried out. Several test cases were investigated: The non-rotating airfoil section with VGs, the rotating airfoil section with VGs and the non-rotating wind turbine blade with VGs. Both, VGs causing either contra-rotating or co-rotating vortices were investigated at several chord-wise positions. The contra-rotating VGs showed to have the largest effect on cross-flow leading to a delayed stall and therefore to a higher lift coefficient in the

post stall region.

3.1.2 Blowing and Suction

Blowing and suction techniques generally delay stall by adding high momentum air in the boundary layer (blowing) or by removing low momentum air (suction). Hence the boundary layer is reenergised and can sustain a higher adverse pressure gradient and therefore postpone separation. The blowing or suction is generally done through a slot in the airfoil surface (see e.g. for blowing in Figure 3.3). The optimal position for the actuation is closely upstream of the separation. However, since the separation is traveling upstream with increasing angle of attack, the optimal actuation position is changing. Therefore, a combined actuation at the leading and at the trailing edge is often chosen.

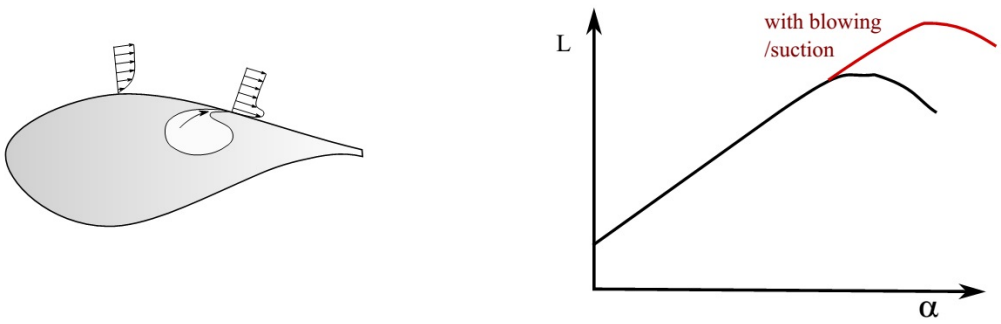

Figure 3.3: Effect of a blowing mechanism

In recent years, research on fluidic actuators was reactivated. The small actuators produce a sweeping air-jet at the outlet and are driven by an external pressure differential which are connected to the system with so called feeding channels (see Figure 3.4). The frequency as well as the amplitude of this sweep can be influenced by the actuator geometry or the connected external pressure [104, 150, 114]. The small actuators can be used similar to the constant blowing slots, as described above. A major advantage is, however, that less air is needed for a comparable effect.
Other researchers have proposed to use the inner airfoil structure as a large fluidic actuator [101]. Thereby, one of the control ports is connected to the suction side while the other one opens to the pressure side. With varying angle of attack, this pressure differential also varies and is hence a good control feedback channel for a pasive, self-regulating system. Depending on the pressure difference the actuation air is directed through different outlet channels which then aim at different chordwise positions. In that way, an optimal blowing position is always maintained for separation control.

Suction and blowing techniques have been successfully implemented on airplane wings in the past. However, the application on wind turbines is more difficult. Pressurised air is needed within the blades and hence in the rotating system. Even through a compressor could be stored within

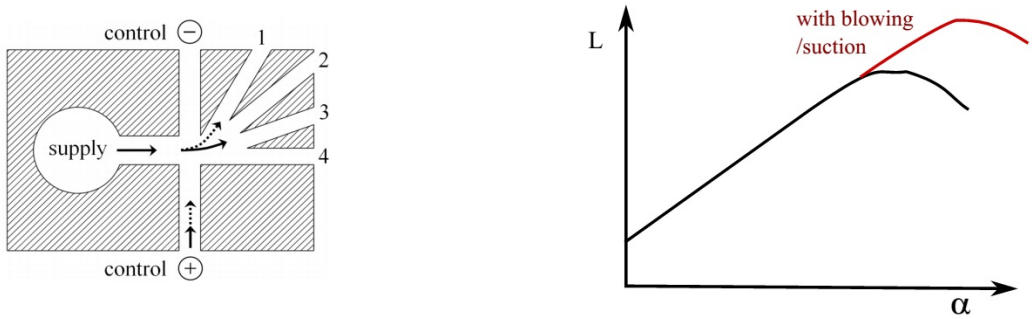

Figure 3.4: Geometry [101] and effect of fluidic actuators

the hub, air tubes must be installed though the joint of the blade and the hub. Furthermore, the blade structure would be seriously affected by the presence of multiple slots the blade. As a consequence smart rotor concepts often prefer other devices, such as VGs or leading edge slats which do not have such a drawback.

3.1.3 Back-Flow Flaps

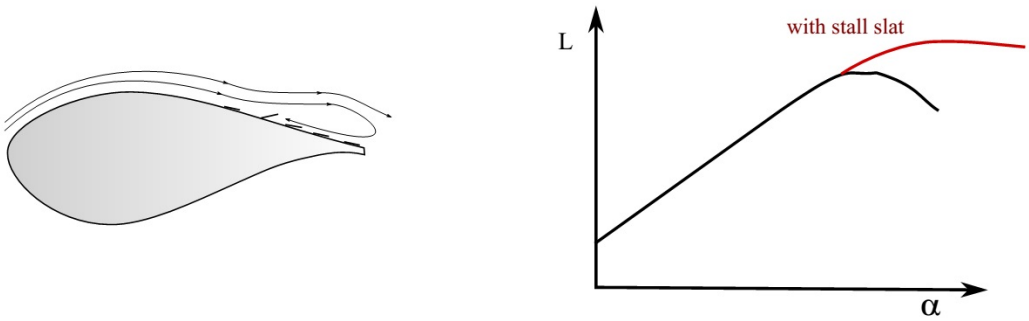

Figure 3.5: Principle and effect of multiple stall flaps

Back-flow flaps are motivated in their design by the aerodynamic features of a bird's wing [95]. If stall takes place, certain feathers raise (see Figure 3.5). This prohibits the back-flow of the stalled region and hence reattaches the flow. If the stall grows in strength and moves in upwind direction, a second row of feathers is used simultaneously. If no stall is apparent, the flaps are attached to the airfoil and do not further change the aerodynamics. Hence, the back-flow flaps are a passive control method, however, they can react to a change in inflow without needing a complicated control setup.
Different wind turbine airfoils were tested in combination with the flaps in the wind tunnel. The light flaps were chosen to be around 2% of the cord length and located on the suction side. As a result, the lift remains constant at post-stall and hence provides independent load alleviation with no special needs for active control [1].

3.1.4 Passive Leading Edge Slat

A leading edge slat in front of a profile generally shifts the onset of stall to higher angles of attack. Therefore, it can be used for stall control in the inner and mid rotor sections of a wind turbine which generally work under high angles of attack.

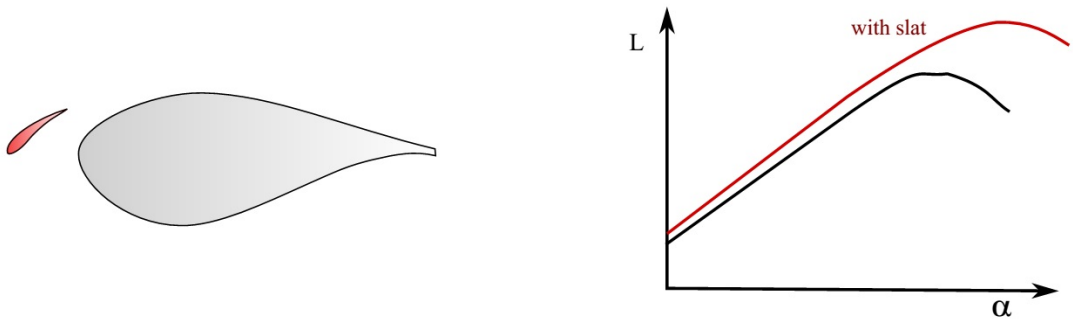

Figure 3.6: Effect of a leading edge slat

The leading edge slat was first developed by Lachmann in 1918 [73]. Until now, the concept has been investigated to a great extent and further developed by numerous researchers. Today, the slat is a standard tool as a high lift device and stall control mechanism and is commonly used during the starting and landing procedure of airplanes. The slat is usually formed through an additional airfoil which is mounted in front of the main airfoil section. A slat is introduced between the two parts in a way that flow is transported from the pressure to the suction side (see Figure 3.6). The effect of the slat can by divided into five major principles [126]:
First, the circulation of a separate element in front of the main airfoil induces a reduction of pressure peaks on the main airfoil. Second, the presence of the downstream element causes the trailing edge of the first element to be inclined in a region of high velocities; that in turn results is a substantial higher circulation of the first element. The orientation of the trailing edge of the first element in the region of high velocities further leads to a dumping effect on the boundary layer and hence acts as an alleviation of separation. The forth principle is called the off-surface pressure recovery. As the name suggest, the boundary layer of the first element is dumped in the wake at velocities much higher that the freestream velocity and the subsequent deceleration tales place effective without wall contact. The last principle is the fact, that multiple elements each start with a fresh boundary layer and hence each layer can withstand higher adverse pressure gradients.
As a result of these points, the angle of attack of the stall onset is shifted to higher values, and the slope of the lift is slightly increased. Moreover, the auxiliary leading edge airfoil has shown to reduce dynamic stall effects [25].
Because of these benefits, the leading edge slat is favourable for the application at the inner rotor parts. An additional advantage is that the element can be easily mounted on the blade without changing the blade manufacturing procedure. Furthermore, the higher lift and prevention of stall allow airfoils with smaller chord which results in an overall smaller blade mass and hence

lower material costs [109].

3.1.5 Passively Morphing Structures

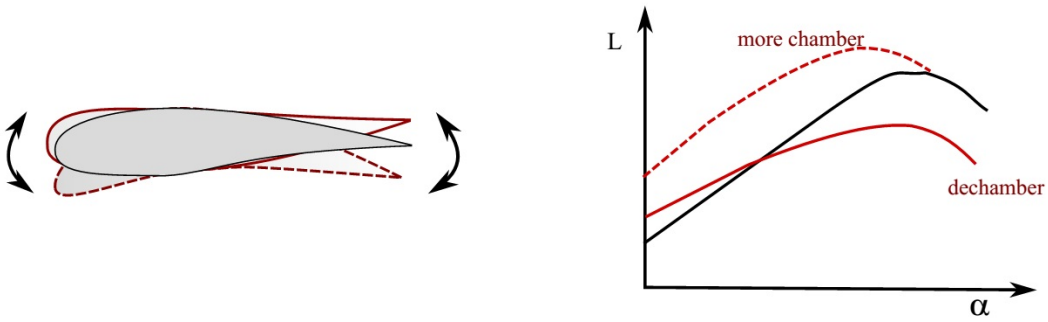

Figure 3.7: Principle of a morphing airfoil and its effect on lift

Next to the above mentioned conventional passive flow control mechanisms, more innovative systems have been developed in the last years. One of these concepts is the passive camber change due to a morphing self-aligning structure. This concept uses the pressure changes arising from the varying angle of attack to adjust the airfoil camber through kinematically coupled leading and trailing-edge flaps. Thereby, the change in angle of attack induces increased pressure forces on the airfoil which then actuates the leading-edge flap. The trailing-edge flap is kinematically coupled to the motion of the leading-edge flap. Hence, the two flaps together increase or decrease the airfoil camber without any further control algorithm which therefore represents a passive load control system (see Figure 3.7). Extensive work on a morphing airfoil structure had been previously done by Lambie [76] and is currently extended as a part of the DFG funded collaborative research on wind turbine load control under realistic turbulent inflow conditions (DFG PAK780).

3.2 Active Methods

Active flow control devices have been known from research activities in the aviation industry for decades. Often the purpose is to improve the aerodynamic performance and enhance the lift over an airfoil. However, for the load control of wind turbines, load reduction is also often needed in order to minimise excessive loads.

3.2.1 Active Trailing Edge Flaps

In the past, trailing edge flaps have been extensively investigated and have proven to be efficient in changing the aerodynamic loads in numerous studies. The flap deflected to the suction side offers load reduction, meanwhile the flap deflected to the pressure side yields a load enhancement

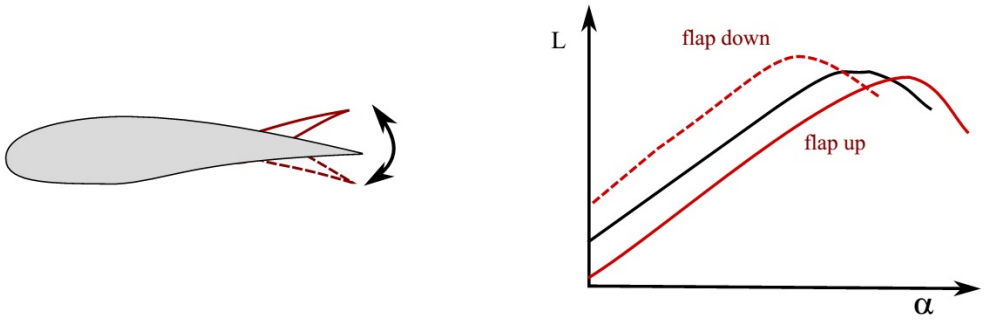

Figure 3.8: Active trailing edge flaps for load control

(see Figure 3.8). Generally, one can say that the larger the flap, the higher the effect on the lift. However, the airfoil's drag is increased along with the lift. If the flaps are applied to the suction side of the airfoil, the flaps need a sufficient height to not submerge in the thicker boundary layer and separation region; otherwise, the flaps lose their effectiveness at high angles of attack at the onset of stall.
Recently, initial measurements of an active trailing edge system were conducted on a full scale turbine [28]. Further ongoing work is conducted at the *HFI* concentrated on a research wind turbine with multiple active flaps [43, 141, 139]. Multiple flaps along the blade shave proven to be advantageous instead of a single large flap. A single flap could not encounter local gusts or load variations and, in addition, can not influence the flap modes. As a rule, a flap placed further outboard has a larger effect on the blade root bending moment. However, flaps which are placed too close to the blade tip region do not work optimally due to the blade tip loss effects. Next to plain flaps, further investigations were made on flexible and morphing trailing edge structures [70] [112].

3.2.2 Active Spoilers

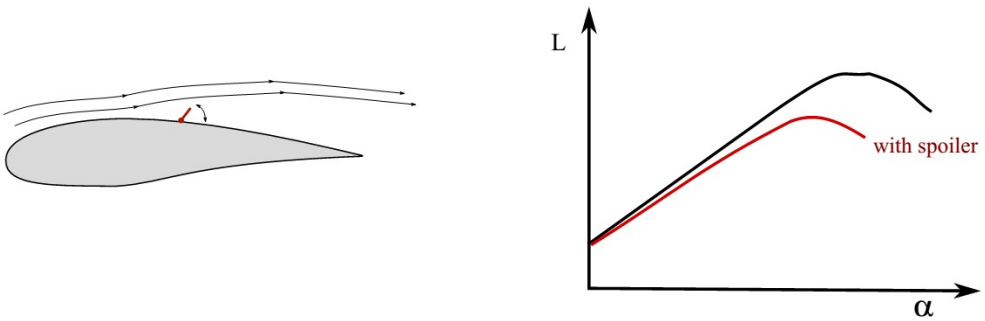

Figure 3.9: Active spoiler and its effect on lift

Trailing edge flaps are only effective at pre-stall angles due to the onset of separation at the trailing edge. Therefore, the flaps are not effective at high angles of attack or very unsteady

flow such as gusts. Hence, spoilers are often used for load reduction. Spoilers are small flap-like plates placed on the suction side surface at around 50% to 70% chord and can be extended upward in the flow (see Figure 3.9). The upward directed spoiler then generates a controlled stall region behind the device. Thus the lift is reduced meanwhile the drag is increased. Studies have been conducted for both passive and active control.
For the control of fast gusts, the active spoilers need high deployment times. However, this implies that the device works under aerodynamically unsteady effects. In 1984 Consigny et al. experimentally studied the effect of a rapid deploying spoiler on the lift [34]. It was confirmed that during the deployment process a strong vortex forms behind the spoiler which locally induces a large negative pressure. This pressure results in a temporary adverse lift response which is only abolished when the vortex is subsequently convected in the wake. Afterwards, the deployed spoiler induces a fluctuating region with a reduced total pressure and hence the overall lift is reduced.
However, these adverse effects can be minimized by optimizing the design or utilizing advances control strategies [68, 118, 105]. E.g. the adverse lift response can be reduced by variations of the angular speed, the deflection of the spoiler or, most effectively, by the introduction of a gap between the airfoil and the spoiler. The flow through the gap reduces the effect of the starting vortex on the surface pressure and hence the magnitudes of the adverse lift and moment response are reduced [154].
For the application of spoilers on wind turbines is noted, that the spoiler deployment may induce large pitching moments which in turn can increase the torsional load on the blade significantly [119]. Hence, the spoilers on wind turbines are best placed close to the main spar to reduce the aerodynamic torque arm [107].

3.2.3 Micro-Tabs and Gurney-Flaps

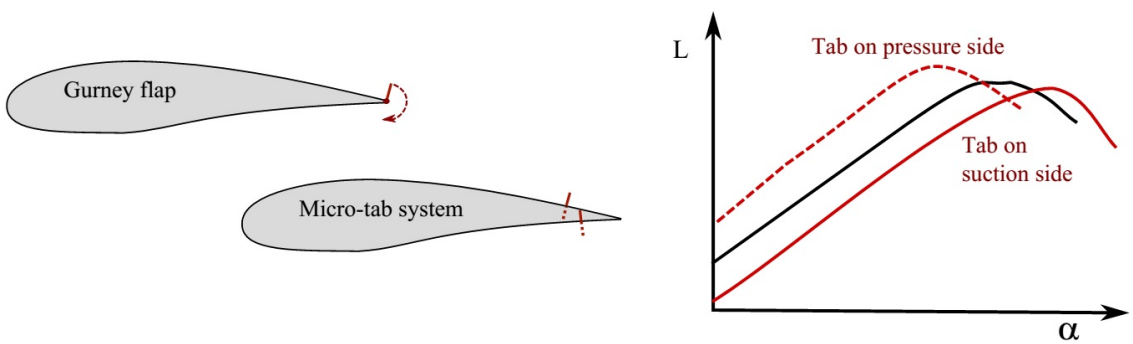

Figure 3.10: Active micro-tab system for load control

Micro-tabs are closely related to the well-known Gurney flaps and are often also referred to as interceptors, Micro-Trailing Edge Effectors (MiTE's) or Micro-Electro-Mechanical (MEM) translational tabs. The underlying principle of a deflected Gurney flap is thereby the formation of two counter-rotating vortices which form behind the flap [81]. The presence of the flap produces

a stagnation point downstream of the trailing-edge and change the overall airfoil circulation and thus the lift [84]. The device height is in the order of the local boundary layer thickness (approx.1% - 4% c), causing only minimal additional drag while maintaining reasonable lift differences for load alleviation.
While Gurney flaps are placed at the trailing edge [145, 52, 51, 17], the micro-tabs are placed slightly upstream of the trailing edge featuring the same height as the Gurney flap (compare Figure 3.10). The micro-tabs deploy perpendicular to the airfoil's surface and are able to retract completely inside the airfoil. If the tab is placed on the pressure side, this recirculation zone captures the streamline leaving the airfoil from the suction side and leads it through the bubble to the end-point of the micro-tab where the streamlines from the suction- and pressure side meet and leave in the wake [135]. This process changes the airfoil circulation and hence the lift (see Figure 3.11).

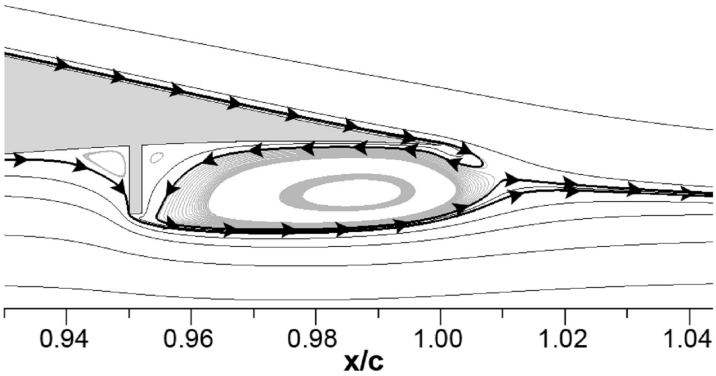

Figure 3.11: Streamlines around micro-tabs [135]

Both devices can achieve load reduction or load enhancement: The flap can either deflect upwards or downwards. However, the micro-tab system then consists of two tabs placed on the suction and the pressure side. Local lift changes from around $\Delta C_l = 0.2 - 0.5$ may be obtained for moderate angles where no flow separation occurs [13]. The advantage is that the short flaps or tabs require only a very low energy input and are generally cost effective, while still providing a significant control authority. Furthermore, the aerodynamic drag is significantly smaller than for e.g. a larger conventional flap. An additional advantage of the micro-tabs in comparison to Gurney flaps is that they are slightly more efficient for load reduction at high angles of attack. This is due to the onset of stall: The trailing edge separation reduces the effective height of the Gurney flap at the trailing edge. Hence, the micro-tab, which is placed further upstream, is not affected as strongly. A further aerodynamic advantage is that the non-deployed micro-tabs retract completely inside the blade without any further disturbance of the flow. However, regarding the structure, the Gurney flap does not need a change in the blade manufacturing but can even be mounted as a retro-fit device externally. Both devices have been used successfully in the past for numerous applications:
For wind turbine airfoils Yen et al. [152] first numerically and experimentally investigated the

feasibility of active micro-tabs on the pressure side of the blade section for active load control on wind turbines in 2001. Different tab positions on the pressure side for load enhancement were examined. The GU25-5(11)8 [47] was selected as a test airfoil because of its larger trailing edge thickness and nearly flat bottom surface to integrate the tabs. Results showed an increase of 50% in the linear range of the lift. It could be shown that the tabs still work effectively when positioned at locations up to 10% chord upstream of the trailing edge. A tab placed at 95% chord length turned out to be the best position for this geometry by offering the best lift to drag ratio. In a follow-up study Yen et al. [153] remotely investigated controllable active micro-tabs for span-wise array actuation.
The work of Yen was further extended by Standish [129], who did a comprehensive two-dimensional study on passive micro-tabs to investigate the influence of tab height and locations on the upper and lower surface of the S809 [127] and the GU25-5(11)8. It could be shown that the aerodynamic performance characteristics strongly depend on the chordwise location of the tab and its deployment height in relation to the boundary layer thickness.
In 2005 Mayda et al. [92] conducted three-dimensional Reynolds-Averaged Navier-Stokes (RANS) calculations on airfoils with different configurations of passive finite width micro-tabs. Mayda was able to show that the gap physically employs a corridor for the flow to pass by the load control devices. The larger the gap, the more flow can pass by. It could be shown that the introduction of gaps causes a global change in the pressure distribution. The gap weakens the suction peak of the airfoil and hence the lift increment is reduced while the drag is also reduced. This drastically improves the lift-to-drag ratio L/D. However, the normal force coefficient was determined to remain almost constant along the span.
In 2007 van Dam et al. [135] [30] numerically investigated the time dependent effect of the aerodynamic coefficients of deployed active micro-tabs and their effectiveness on mitigating high frequency loads on wind turbines. The focus of this study was the transient response of the lift when the micro-tab is deployed as an active load control device. As the tab deploys, the lift and pitching moment show a slightly delayed and adverse response. This transient response of the micro-tab differs massively form the response of a Gurney flap on the trailing edge. This is due to the fast streamwise vortex built up at the tab which then convects over the airfoil's remaining surface behind the tab, causing an effect on lift and moment. In more detail, the vortex formed by the deployment of the micro-tab causes a temporary low pressure region which results in a temporary adverse lift. When the vortex reaches the trailing edge, the adverse lift reaches its maximum. If the vortex further convects in the wake, the lift converts asymptotically to its steady state value. However, the speed of these transient lift and drag responses clearly depend on the deployment times. Van Dam could generally show, that shorter deployment times generate a larger adverse lift overshoot in both lift and drag. However,the aerodynamic loads reach their final values faster.
Gurney flaps under more arbitrary inflow conditions typically experienced by wind turbine sections were examined by the group by Pechlivanoglou et al. [41]. The aim was to measure the load reduction potential of Gurney flaps on a wind turbine blade section under more realistic inflow conditions. Therefore, the inflow was simulated by varying the angle of attack of the airfoil model. The time-dependent inflow angle was generated by assuming a varying inflow of $\alpha = 7^\circ +/- 6^\circ$. Additional turbulence was simulated by adding white noise to the signal of the angle of attack.

Thereby, it was estimated that with the active Gurney flaps the dynamic lift could be reduced by 70% using a manually tuned PID-Controller.

For the implementation on wind turbines, fully three-dimensional rotor simulations have been made by several researchers since experimental methods are often too expensive on whole wind turbine models. Simulations for the effect of micro trailing edge devices on the UPWIND reference wind turbine were recently undertaken by Gaunaa et al. [20] [12]. The aim was to evaluate the effect of the adverse loads of the structure caused by rapidity deploying micro-tabs in comparison to the usage of Gurney flaps without such effects. It could be shown that the response of the micro-tabs did not matter for the structural response of the turbine blade, because the time in which the adverse lift response occurred was much smaller than the response time of the blade structure. Furthermore, the delayed micro-tab response only showed a small impact on the load reduction potential.
Furthermore, Plumley et al. analytically investigated the differences of individual pitch control and distributed trailing edge flaps on a wind turbine model [113]. Collective pitch generally controls the turbine speed and consequently the power output. However, for modern very large wind turbines individual pitch is further used to reduce fatigue loads; especially the predictable periodic load induced by wind shear. The work of Plumley et al. aims to replace the individual pitch for load reduction with trailing edge flaps. It could be shown that the small flaps achieve the same load reductions as the individual pitch. However, using a local active solution is advantageous because of overall lower power requirements and increased actuator duty.
Eisele et al. [41] and Weinzierl et al. [147] conducted analytical simulations based on the Blade Element Method (BEM) on a wind turbine with Gurney flaps. Gurney flaps are closely related to micro-tabs in their response functions and overall achievable lift difference. However, the Gurney flaps do not have an adverse overshoot in their response function and lose their effectiveness earlier at high angles of attack when placed on the suction side. For the simulations, the active flaps were placed at the outer 30% of the blade and were controlled with a simple PID controller. The controller modified the flap movement aiming at a given target value of a certain control variable. Possible control variables are: The blade deflection rate, the blade flap angle or the out-of-plane root bending moment [147]. For the best configuration a maximum load reduction of 35.8% with a simple PID controller was achieved. In comparison with other active elements the Gurney flap was advantageous because of the low force actuation requirements as well as the lower production and replacement costs.
Macquart and Maheri integrated aeroelastic control analysis of wind turbine blades equipped with micro-tabs [88] [87]. An unsteady BEM theory was used with an incorporated aerodynamic model for the micro-tab response. However, the response of the micro-tab was simplified by three major assumptions: First, the model did not incorporate the effect of the adverse overshoot since the time during which the effect occurs is too short to significantly impact the time dependent loads on the blade structure. Second, the lift response is insensitive to variation of high Reynolds numbers and third, the responses of the tab on the upper and lower surface are the same. Based on these assumptions an aerodynamic response model was derived and a reduced order aeroelastic model as well as a controller simulator was applied. It could be shown that the applied micro-tabs could effectively alleviate the unsteady loads over a wide range of

frequencies. However, the applied controller type is of importance for the overall load reduction potential.

3.2.4 Active Blowing

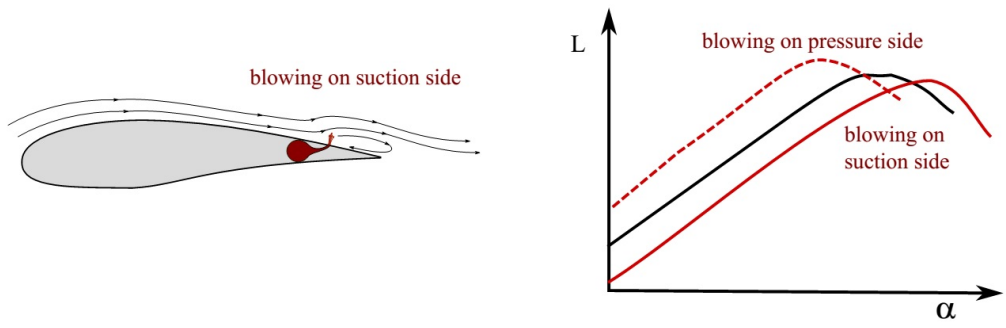

Figure 3.12: Active blowing mechanism for load control

In recent studies the solid mechanical tabs were replaced with micro-jets [21]. The jets work with pressurised air emerging through a slot in the surface. The air is blown out perpendicular to the airfoil's surface at the same place as a micro-tab (see Figure 3.12). The aerodynamic principle is very close to the principle of the solid tab. It was shown that micro-jets achieve similar values for the change in lift and moment. Furthermore, the micro-jets produced slightly less drag and showed a smaller transient adverse lift effect than the micro-tabs.
An advantage of the blowing mechanism is that no cost intensive maintenance of moving mechanical parts along the blade is needed. Furthermore, the actuator speed is faster and more flexible than for a mechanical system. However, the supply of pressurised air in the blade is a major drawback as stated above.

4 Research Objective

So far, most of the experimental investigations on load control for wind turbines conducted were stationary and concentrated on two-dimensional geometries with mostly passive control devices neglecting unsteady effects. Therefore, to advance the realisation of these devices on wind turbines, research on active control of unsteady effects to reduce dynamic load fluctuations is now strongly needed [14].

The objective of this PhD thesis is the experimental investigation of an active micro-tab and Gurney flap control system for load reduction on future large wind turbines under dynamic effects. Both devices are studied and their advantages and disadvantages evaluated considering steady and unsteady effects. The initial work packages of this study thereby cover the following topics:

1. Understanding the effect of passive micro-tabs and Gurney flaps on lift, drag and pitching moment under steady inflow conditions.
2. Investigation of the unsteady flow structure during the transient deployment and retraction process of the active micro-tabs and flaps under steady inflow conditions and fixed angle of attack.
3. Experiments on airfoils undergoing pitching movements with passive, fixed flaps or tabs.
4. Evaluation of the combinations of an actively pitching airfoil with active elements to counter the dynamic load changes through experiments as well as with the help of analytical models.

5 Static Airfoil with Passive Micro-Tabs and Gurney Flaps

In this chapter the aerodynamic behaviour of static non-moving Gurney flaps and micro-tabs are evaluated. First of all, force measurements of various tab heights as well as positions have been carried out, followed by a study of multiple tabs with different solidity ratios over the blade span. A deeper understanding of the flow structure around these multiple tabs was gained with the help of oil paint flow visualisation as well as flow measurements in the wake behind the tabs. Finally, the flow field around a single finite tab was analysed with surface pressure measurements.

5.1 Single Passive Gurney flap or Micro-Tab

Subsequently, the forces on a wind turbine airfoil with passive micro-tabs and Gurney flaps were studied. For thick airfoils, the possibility arises for micro-tabs at the trailing edge, where they are placed on the flat back and deploy perpendicular to the surface with the height of the flat back height or less. Even though no thick airfoil is investigated here, in this thesis it is only referred to a flap in case it can deflect upwards or downwards having different an angles in respect to the chord line. Passive, glued on devices with a L-shape will be always addressed as tabs, even when they are placed at the trailing edge. However in the case of a placement at the trailing edge, they may also represent then the case of a Gurney flap deployed with $\pm 90°$, since the part of the L-Shaped tab profile with in glued on the surface in submerged in the recirculation bubble in front of the tab and has a negligible effect on the aerodynamics.
In the following, the lift and drag coefficients were calculated for various configurations. Furthermore, the Karman vortex street in the wake was analysed.[1]

5.1.1 Experimental Set-up

Experimental investigation in the wind tunnel has been conducted on an Althaus AH93W174 [5] wind turbine profile with passive micro-tabs or flaps. The measurement section of the wind tunnel has a size of 1.5m x 2m with a turbulence level of $Tu < 0.5\%$. For a better

[1] Results for the tripped measurement presented in Section 5.1.4 and 5.1.6 were previously published by Bach et al. in [9]. Co-author, M. Lennie performed analytical simulations with QBlade and FAST for this publication; however, these analytical results were not used for this thesis. S. Vey helped with the measurements and analysis leading to the LIC flow visualisation (Figure 5.27) and O. Krüger and T. Boehm performed the CFD simulations leading to Section 5.1.7. All other tasks were carried out by the author.

two-dimensionality, additional splitter plates were installed between the model and the wind tunnel wall (see Figure 5.1). The chord length of the profile was $c = 0.6m$ and the span was $b = 1.554m$. Measurements were performed at a Reynolds number of $Re = 1 \cdot 10^6$. Wind tunnel correction methods for solid blockage, wake blockage and the effect of streamline curvatures were used. For a few measurements the flow was tripped on the upper surface. This was done to see the impact of the elements with an increased boundary layer height. This is because environmental effects cause a much larger roughness on exposed wind turbines and hence the boundary layer height is generally much larger than for the clean airfoil.
For the study various tab configurations were installed and tested. The devices were placed close to the trailing edge between $90\% \leq x/c \leq 100\%$ and varied in height from $1\% \leq h/c \leq 4\%$. The four elements of different heights were attached according to Figure 5.2, however at different chordwise positions.

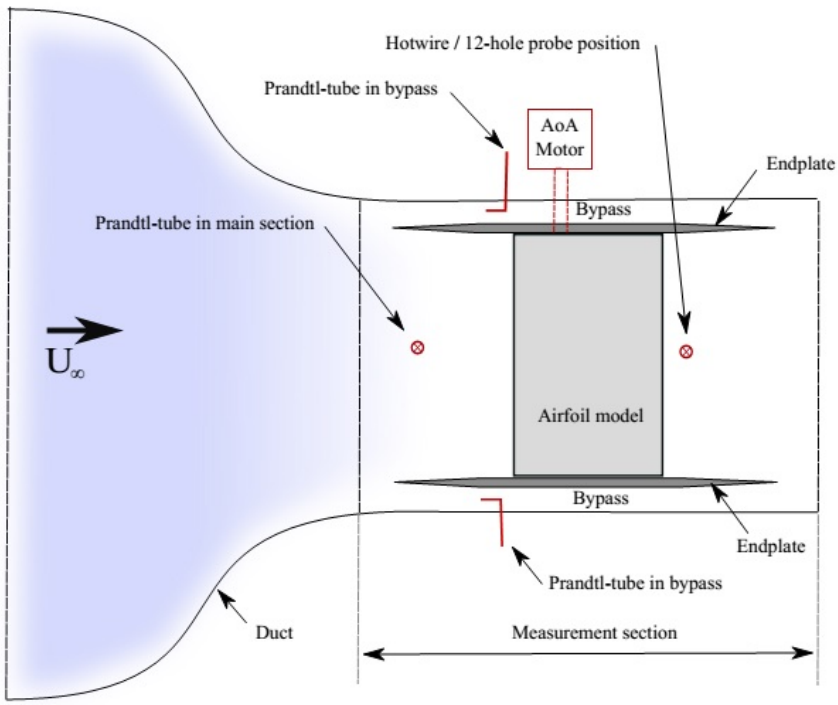

Figure 5.1: Experimental set-up of the AH93W174 airfoil

Furthermore, the difference of a full-span tab and multiple smaller tabs was investigated. The solidity ratio was introduced in the following way: $\sigma = \Sigma(l_{tab})/b$. A full-span tab has the solidity ratio of $\sigma = 1$. For the experimental investigation of the micro-tab concept, different measurement approaches were chosen. First of all, a 6-component force balance underneath the wind tunnel measured the aerodynamic forces. Second, a hotwire was used to evaluate underlying frequencies in the wake. The single-wire had a measurement sampling rate of $f = 2000Hz$ and was placed $\Delta x = 20mm$ behind the trailing edge. Third, measurements with a 12-hole probe were carried out in the same plane in the wake in order to analyse the extent and interaction of the tab's streamwise vortices. Finally, oil paint as well as a quantitative digital flow analysis technique

based on flow tufts (SMARTviz) visualised the flow around various finite tab configurations [140].

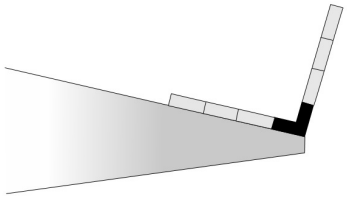

Figure 5.2: Tab attachment on the AH93W174 airfoil

5.1.2 Effect of the Tab Height

Lift and drag curves were measured for the tab placed on the pressure side and on the suction side directly at the trailing edge with $x/c = 100\%$ and the curves were compared to the baseline case. In doing so, the tab height was varied between $1\% \leq h_{tab}/c \leq 4\%$.
Figure 5.3 shows the lift curves for tabs placed on the pressure side as well as the baseline. The main observation is that the tab shifts the curve to higher lift values and changes the angle of attack where stall occurs to smaller inflow angles. The lift difference does not scale linearly with the tab height but slowly converges. This non-linearity was observed by several researchers in the past [33, 152].

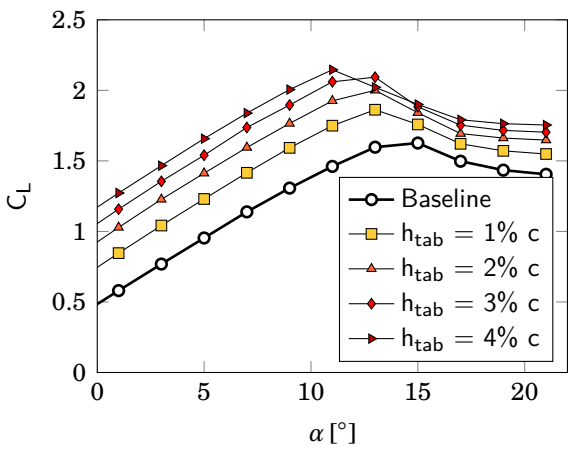

Figure 5.3: Lift curve for tabs placed on the pressure side at the trailing edge with various heights ($Re = 1 \cdot 10^6$)

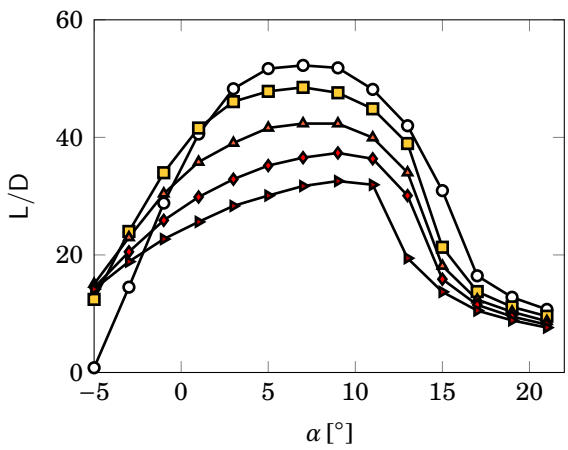

Figure 5.4: Lift-to-drag for tab placed on the pressure side at the trailing edge with various heights ($Re = 1 \cdot 10^6$)

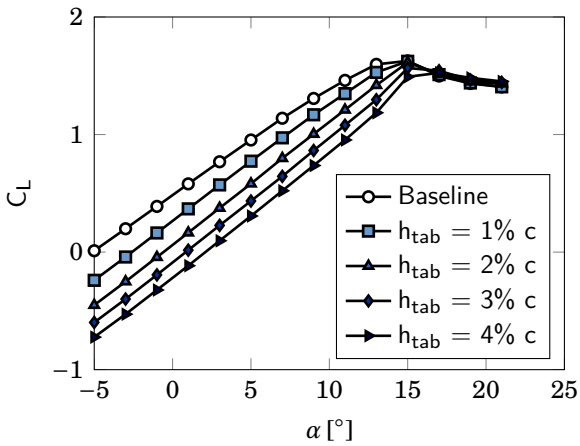

Figure 5.5: Lift curve for tab placed on the suction side at the trailing edge with various heights ($Re = 1 \cdot 10^6$)

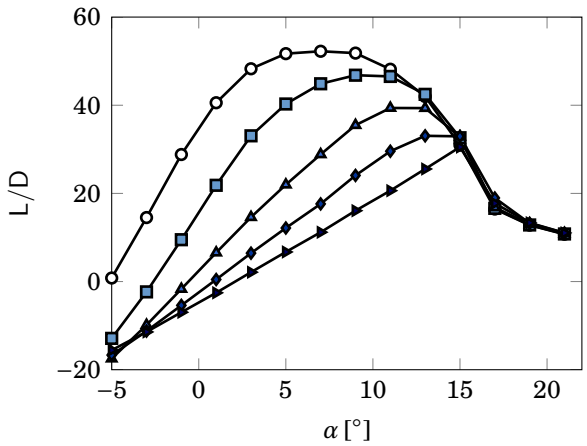

Figure 5.6: Lift-to-drag for tab placed on the suction side at the trailing edge with various heights ($Re = 1 \cdot 10^6$)

For the tab on the suction side, the lift decrease is less pronounced if the angle of attack is increased (see Figure 5.5). If the profile stalls, the tab is submerged in the recirculation zone and loses its effectiveness. This is starting with the tab of the lowest tab height but eventually for angles of attack higher than $\alpha = 15°$ all curves finally coincidence with the baseline case.
The tab influence on the airfoil's drag is visible in Figure 5.4 and 5.6. It can be seen that for the pressure side an interesting effect occurs: For small angles of attack and the lift-to-drag ratio is better than for the baseline case. This status can be maintained longer by the smaller tab when the angle of attack is increased. As explained above, this effect has been observed in the earliest investigations of Gurney tabs and is one reason why the application of these devices is so popular.
For the suction side tab, the consequence for the lift-to-drag ratio is more drastic. No positive effect was found for any angle of attack. The reduction of the ratio was only observed to disappear when the tab was ineffective and enclosed by the trailing edge stall. This can be observed by the merging of the curves for high angles of attack. Consequently, the curves of the lift-to-drag ratio of the airfoil with and without tab merge at a lower angle of attack if the tab is smaller.

5.1.3 Effect of the Tab Position

The effect of the envelopment of the tab first in a thicker boundary layer height and later in the separation bubble at high angles of attack can be partly circumvented by either choosing a higher tab or by moving the tab position further upstream. The best tab position depends on the inner space of each profile as well as the aerodynamic gain which can be achieved. However, if the tab is not placed at the trailing edge but further upstream, a minimal tab height is needed for the recirculation bubble behind the tab to reach the trailing edge. Only then a lift change in the desired direction is achieved: E.g. if the tab is placed on the pressure side and the

recirculation bubble does not reach the trailing edge, the Kutta condition is not shifted and the tab produces instead an unintended reduction in lift [13, 130]. However, this minimal necessary tab height strongly depends on the airfoil's geometry and is usually around or below the height of $h_{tab}/c = 1\%$, which can be seen in the comparison of airfoil geometries performed by Cole et al. [33].

Figures 5.7 and 5.8 show the lift increase for all four tab heights placed between 90% and 98% of the chord length close to the trailing edge for the tab on the pressure and the suction side and compared with the trailing edge tabs. The angle of attack was $\alpha = 12°$. It can be seen that for the tab on the pressure side, a placement further upstream of the trailing edge is disadvantageous for the lift gain. For all tab positions was found consistently that a higher tab again yields a higher lift difference. The maximum lift gain with $\Delta C_L = 0.28$ is achieved at the trailing edge with a $h_{tab} = 4\%$. For the smallest tab of $h_{tab} = 1\%$, it can be seen that the tab height is sufficient to generate a recirculation zone which extended to the trailing edge for the positions of $x/c = 98\%$. However, for the two more upstream positions, this was not the case and therefore negative lift differences were produced.

For a placement on the suction side (Figure 5.8) a placement further upstream yielded the best lift reduction. However, the overall effect of the location is not as pronounced as on the suction side. Here, a maximal negative lift difference of around $\Delta C_L = 0.23$ was achieved for the tab height of $h_{tab} = 4\%$ at 90% chord.

Figures 5.9 and 5.10 show the ratio $(L/D)/(L/D)_{base}$ as coloured surface lines for the various heights and positions. Generally, all configurations on the suction side show a much smaller L/D ratio than for the tab on the pressure side. The lift-to-drag ratio for a tab with a height of 3% chord on the pressure side only reaches around 70% of the baseline case, meanwhile the same tab on the suction side has a lift-to-drag ratio of only around 35% of the baseline case. However, one can summarise that the impact of the tab height is still more severe than the effect of the position.

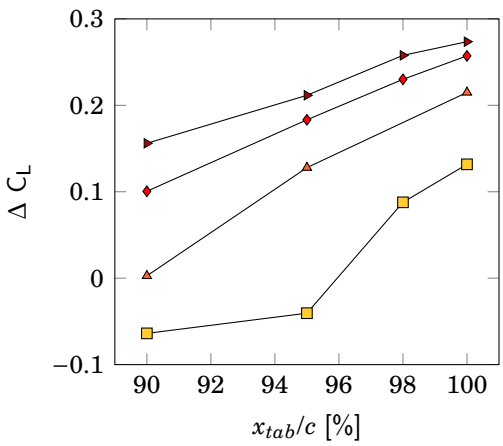

Figure 5.7: Lift difference depending on tab height and placement for the pressure side ($Re = 1 \cdot 10^6$,$\alpha = 12°$)

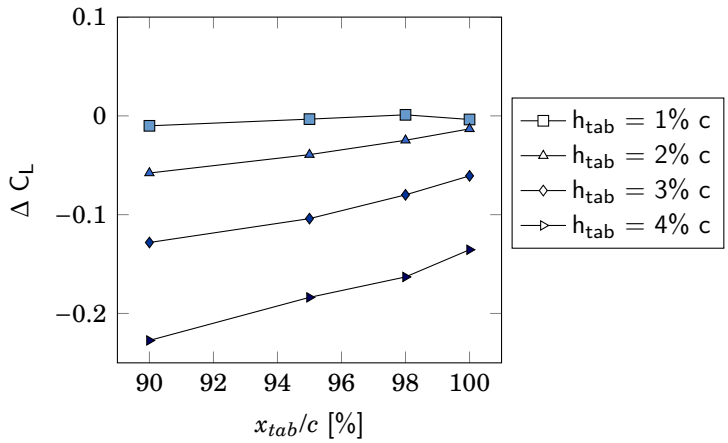

Figure 5.8: Lift difference depending on tab height and placement for the suction side ($Re = 1 \cdot 10^6$, $\alpha = 12°$)

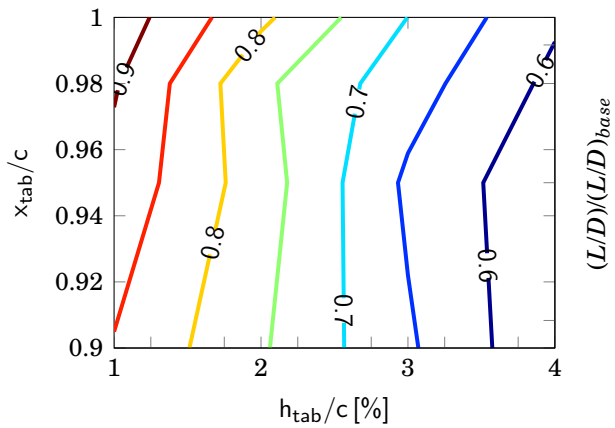

Figure 5.9: Lift-to-drag (coloured lines) depended on tab height and placement (PS, $Re = 1 \cdot 10^6$, $\alpha = 12°$)

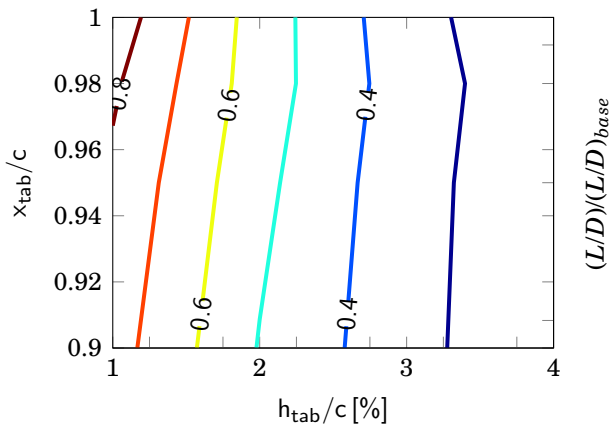

Figure 5.10: Lift-to-drag (coloured lines) depended on tab height and placement (SS, $Re = 1 \cdot 10^6$, $\alpha = 12°$)

5.1.4 Effect of Transition

For the application on wind turbines, the sensitivity of the load control devices due to transition or roughness are crucial. Modern wind turbines suffer greatly from environmental effects such as rain erosion, sand, ice or other residuals changing the airfoil shape and local roughness [108]. The tab effectiveness on the suction side is strongly connected to the boundary layer development over the suction side of the surface which is in turn affected by the boundary layer transition. The measurements conducted earlier with a free transition (presented in Figures 5.5 and 5.6) were repeated with a fixed transition location at $x/c_{trans} = 15\%c$ on the suction side. Therefore

a zick-zack tape was used with a thickness of 0.8mm. Figures 5.11 and 5.12 illustrate the resulting lift and lift-to-drag curves for the AH93W174 airfoil.

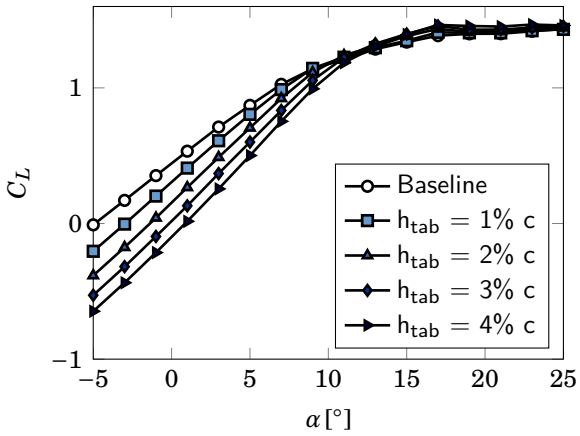

Figure 5.11: Lift curve for tabs placed on the suction side with fixed transition ($x/c_{trans} = 15\%c$, $Re = 1 \cdot 10^6$)

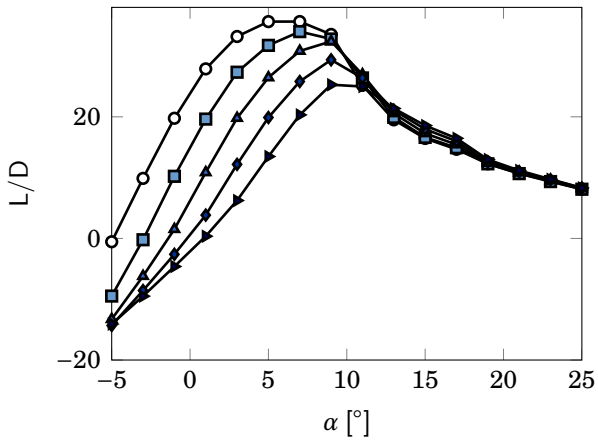

Figure 5.12: Lift-to-drag for tabs placed on the suction side with fixed transition ($x/c_{trans} = 15\%c$, $Re = 1 \cdot 10^6$)

One can see that due to the fixed transition the lift curves generally have a lower slope, lower overall maximum lift values and an earlier, but smoother separation. The curves of the baseline and for the different tab heights cross at an angle of around $\alpha = 10°$, which is 5 degree lower than for the case of the free transition depicted in Figure 5.5. Furthermore, the curves in the post stall region behave differently. They do not merge after trailing edge separation is reached but the configurations with flpas yield a slightly higher lift than the baseline case. This effect can also be observed in the measurements on micro-tabs, e.g. by Nakafuji [100] or on the closely related spoilers by Pechlivanoglou [111]. Flow visualisation suggests that the tabs or tabs placed on the suction side both reduce the three-dimensional effect of the necklace vortices in the wind tunnel. At the same time, one can assume, that the presence of the tabs or flaps in the stall region interact with the shear layer and the post stall vortex shedding of the airfoil under high angles of attack. This effect is critical for the load control reduction mechanism and it is a subject of ongoing research. Section 5.1.7. is designated to investigate this effect more closely with computational fluid dynamics (CFD).

For a deeper understanding, the transition location was fixed at various positions and the lift curves were compared. Figure 5.13 shows the behaviour of the lift curve with flap (filled markers) and without flaps (white markers) for the three different locations of the transition. It can be seen that the curve with the flap reaches the baseline at a certain angle of attack during the onset of stall. This angle at which the flap loses its effectiveness shifts to lower angles as the transition location is closer to the leading edge. With the boundary layer being turbulent from that early stage on, the flap is more immersed in the thicker boundary layer and hence less effective.

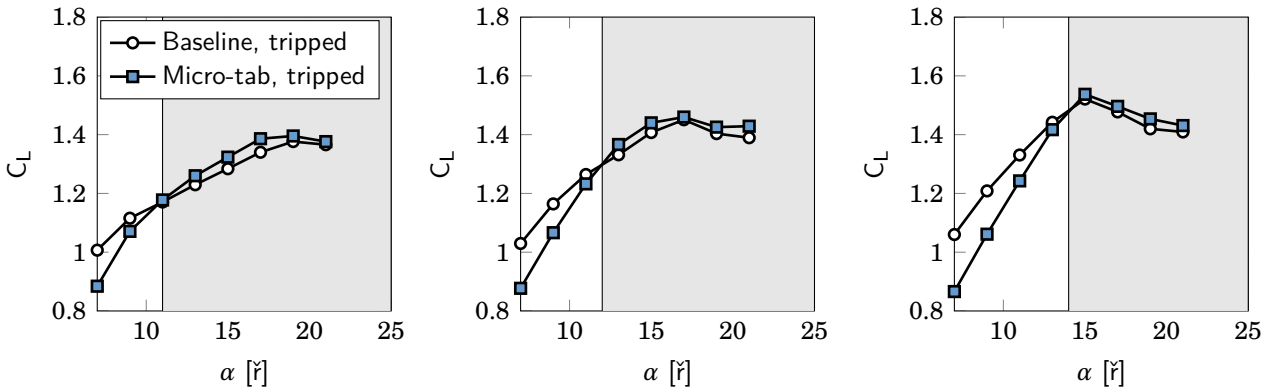

(a) $x_{trip}/c = 10\%$ **(b)** $x_{trip}/c = 15\%$ **(c)** $x_{trip}/c = 20\%$

Figure 5.13: Lift overshoot for various tripped locations

This finding is interesting for the application on wind turbine blades, because the environmental effect on the blade shape and flow structure are much more severe than for example on airplane wings [108]. Therefore, the surface roughness changes on a turbines side may greatly influence the effectiveness of a load control system based on this concept.

5.1.5 Effect of Additional VGs

Applying additional vortex generators may circumvent the small load control range for high angles of attack for the suction side tab or flap. The VGs cause the flow to remain attached longer and hence prevent a thickening boundary layer. The VGs dimension were chose according to studies performed by in the same wind tunnel and under the aspect of an application for wind turbines [97]. A parametric study has been carried out investigating the chordwise position, spanwise spacing and VG size. The VG dimension optimal VG dimensions in this case were found to be with a spacing of $Z = 3H$ for a best stall suppression, a chordwise position between 15% and 20% and a height of $H = 1.7\%c$ which produced a higher lift increase in the static stall angle and a larger maximum lift coefficient.
This geometric design was applied on the Althaus model and several chordwise positions were tested. The best overall performance was found for the case of a chordwise position of the VGs of 15%. In Figure 5.14 the lift curves for three cases with and without VGs are shown: The baseline of the clean airfoil, the airfoil with a tab placed at 90% chord on the pressure and on the suction side. When comparing the curves with and without VGs, one can see that in case of VGs the effectiveness of both tabs remains up to very high angles of attack.
In Figure 5.15 the lift-to-drag curves for the same cases are shown. As stated before, the tab on the pressure side has generally a better lift-to-drag ratio than the suction side tab. The behaviour is also found for the case of added VGs even though the drag values with VGs are higher due to the skin friction drag component of VGs.

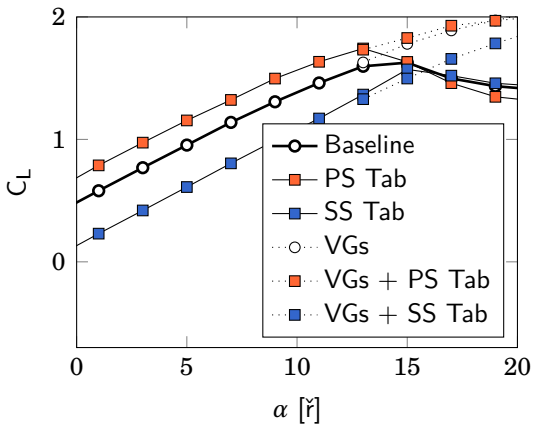

Figure 5.14: Lift for VGs in combination with micro-tabs (x_{tab}/c = 90% placed at 15%c, $Re = 1 \cdot 10^6$)

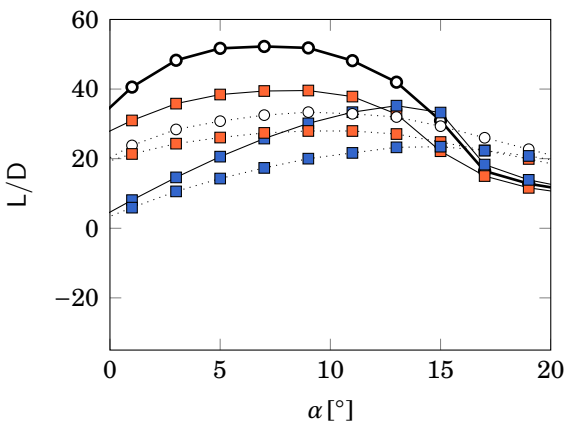

Figure 5.15: Lift-to-drag for VGs and micro-tabs ($x_{tab}/c = 90\%$ placed at 15%c, $Re = 1 \cdot 10^6$)

5.1.6 The Karman Vortex Street

The formation of a vortex street behind the Gurney flap is one major reason for the drag of the flap and furthermore causes a time-dependent variation of the lift [135]. The basic principle of the shedding mechanism is based on the interaction of the two separating shear layers from the upper and the lower side of the airfoil. The shear layer eventually rolls up and forms a vortex which in turn draws the shear layer from the other side of the airfoil [62]. When this shear layer of opposite sign crosses the center-line of the wake it is eventually cutting off the supply of the vorticity of the first vortex. This mechanism replicates periodically and forms the vortex street in the wake. The Strouhal number based on the tab height and the incoming velocity is found to be around $St_{1st} = 0.13 - 0.17$ for a 2% high Gurney tab on the pressure side [134]. However, the frequency associated with the vortex shedding is not a fixed value but depends on further parameters. The frequency is known to decrease if the distance between the shear layers is increased. This is due to the increased time it takes for the vortices to travel to the center-line and hence to cut of the opposing vortex. Furthermore, the theory of bluff bodies states, that the shedding frequency is connected to the thickness of the shear layer.
Hot-wire measurements have been carried on the tripped airfoil out to analyse the dominant frequency of the vortices at a distance of $\Delta x = 20mm$ behind the trailing edge. Different tab heights on the suction side and the pressure side were investigated as well as the dependency of the Strouhal number of the current angle of attack. The tab was positioned at the trailing edge. The Strouhal number was based on the tab height and the velocity of the incoming flow: $St = f \cdot h_{tab}/U_\infty$. It was found that the higher the tab, the smaller the frequency becomes and hence the larger the Strouhal number (Figure 5.16). Furthermore, the Strouhal numbers for the suction side tab were found to be around $\Delta St = 0.05$ higher than for the pressure side tab. This can be explained with the difference in the boundary layer at the suction side and at the pressure side. The boundary layer is thicker at the suction side and hence the tab is within a region with smaller velocities which cause a larger Strouhal number.

The boundary layer thickness is not only dependent on the chordwise position and the side of the profile but also on the angle of attack. Hence, the Strouhal number must also change according to the current inflow angle. Figure 5.17 shows how the Strouhal number is influenced by the angle of attack for a tab height of $h_{tab}/c = 4\%$. Additionally, the displacement thickness of the boundary layer is plotted as calculated by QBlade based on the XFOIL code [91]. Again, the Strouhal number for the tab on the suction side is found to be larger than for the pressure side for all angles of attack. The boundary layer thickness on the suction side is rising with angle of attack, which is accompanied by a rising Strouhal number for the suction side tab. However, the amplitude of the power density signal of the vortex street became less pronounced for the higher angles of attack. Finally, at the onset of stall at $\alpha = 10°$, the signal was weak and the Strouhal number dropped. For an angle of $\alpha = 12°$ no dominant frequency was found in the wake for the suction side tab, whereas the Strouhal number for the pressure side tab was found to have an opposite effect. The boundary layer gets thinner the higher the angle is and hence the Strouhal number gets smaller.
The vortex street is not only responsible for additional drag but as well a possible source of noise on the blade section. A good indicator for the noise is the amplitude of the peak in the power density spectrum. For the tab on the pressure and suction side it was observed that the amplitude of the signal increased together with the tab height. This indicates a higher noise for the higher tab. Furthermore, the amplitude decreased with rising angle of attack. On a real turbine with static, non-moving tabs, placed at the outer section, one can estimate a wake frequency of $f_{SS} \approx 160Hz$ for the tab on the suction side and $f_{PS} \approx 120Hz$ for the pressure side (assuming $U_{rel} = 80m/s$, $c = 2.5m$ and $h_{tab}/c = 4\%$). However, since the tabs are not going to be fixed in its position but will be actively deploying during each rotor revolution, an exact answer is hard to estimate.

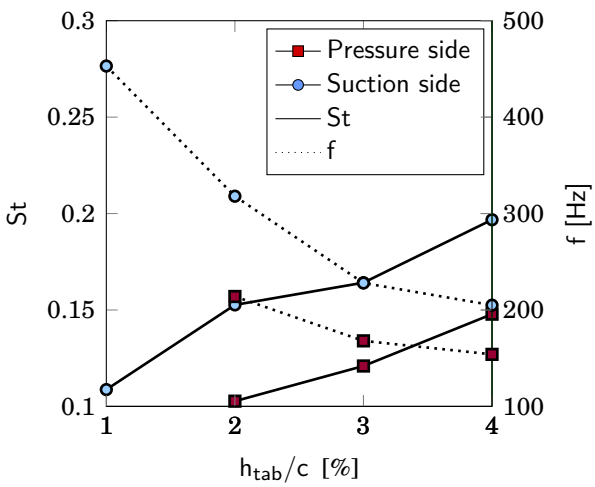

Figure 5.16: Dependency of Strouhal number on tab height
($\alpha = 5°$, $Re = 1 \cdot 10^6$)

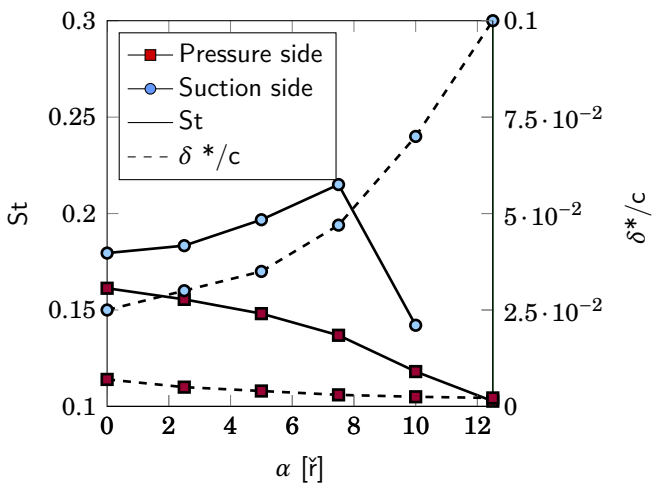

Figure 5.17: Dependency of Strouhal number on angle of attack
($h_{tab}/c = 4\%$, $Re = 1 \cdot 10^6$)

5.1.7 The Micro-Tab in Post Stall

As noted above, the micro-tabs on the suction side show an unexpected behaviour: At high angles of attack, the micro-tabs on the suction side can cause a higher lift than the baseline case. This was noted especially in the case of the tripped flow (compare again Figures 5.11 and 5.13). Similar results have been found e.g. by [64] or [153]. However, most of the researchers only did experimental work that was not able to deliver more insights about the reasons for this phenomenon. Therefore, the flow around the Althaus $AH93W174$ airfoil was simulated with CFD with for three high angles of attack: $\alpha = 15°$, $\alpha = 18°$ and $\alpha = 20°$ for a Reynolds number of Re=800000. Next to the clean airfoil, the flow around an airfoil with a micro-tab placed at a position of $x/c = 90\%$ and a height of $h_{tab}/c = 2\%$ was analysed.

CFD Set-up

The simulations are performed employing the open source framework [148] and a solver based on the PISO procedure [61]. Furthermore, the $kk_L\omega$-turbulence model was used, which is based on conventional $k\omega$ models [144]. The grid was block-structured with dimensions of 32m in x-direction and 24m in y-direction. A grid refinement study has been performed. The tab was modeled as a surface contour, with a fine grid resolution surrounding the same. Thereby, the chord length was c=1m and the leading edge was placed 11.75m behind the grid border. Further information about the simulation parameters can be found in Table 5.1. It is understood, that a study based on RANS is suboptimal for highly separated flow as it is present for the airfoil at high angles of attack. However, for the objective of getting a basic idea of what might happen to cause the above mentioned effects the simulations were sufficient within the scope of this thesis.

cells (hexahedral)	465,472	546,084
mesh-points	535,936	629,088
y^+_{min}	$1.395 \cdot 10^{-3}$	$8.601 \cdot 10^{-9}$
y^+_{max}	0.949	$0.115 \cdot 10^{-3}$
$y^+_{average}$	0.144	$4.493 \cdot 10^{-6}$

Table 5.1: CFD parameters of mesh

CFD Results

From the average flow field, the lift coefficients as well as pressure distributions were extracted. However, only for the angle of attack of $\alpha = 18°$ the lift for the airfoil with tab was found higher than for the clean airfoil. For the angle of $\alpha = 15°$ and $\alpha = 20°$ the lift of the clean airfoil was slightly higher as for the airfoil with micro-tab. Figure 5.18 illustrates the average pressure distribution for the case of $\alpha = 18°$ and Figure 5.19 for the case of an angle of attack of $\alpha = 20°$. For the case of an angle of attack of $\alpha = 18°$, the pressure is generally much lower on the suction

side, if a tab is present. Furthermore, at a position of around $x/c = 60\%$ a slight rise in negative pressure can be seen. This rise seems to be the major reason for the higher lift of the airfoil with tab present. For the case of the $\alpha = 20°$ the airfoil is in full stall and the pressure distribution on the suction side is not lower with a micro-tab present. Only the pressure before the tab is slightly lower than behind the tab, but the overall lift of the airfoil with tab is lower than for the clean airfoil.

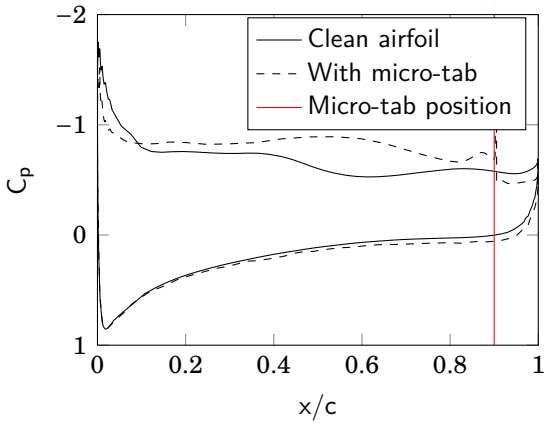

Figure 5.18: Average pressure distribution with and without tab (α = 18°, Re=800000)

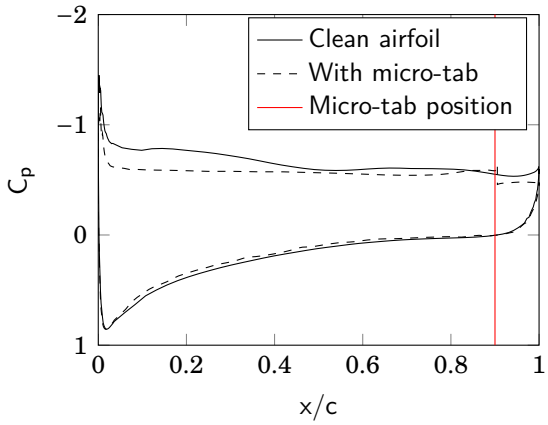

Figure 5.19: Average pressure distribution with and without tab (α = 20°, Re=800000)

The unsteady vortex shedding of all three angles of attack were observed in short animations (not shown here). Here, it could be seen that the presence of the tab as well as the actual angle of attack influenced the shedding of the stalled airfoil. For the case of the micro-tab configuration that yielded a higher lift than the baseline case, the vortex shedding was stabilized through the presence of the tab leading to a stronger vortex which remained longer and closer on the upper surface of the airfoil and hence inducing the negative pressure leading to the higher lift.
This effect can be seen in the average vorticity field shown in Figures 5.20 and 5.21. Comparing both Figures, it can be seen that for the case of the airfoil with a micro-tab the massive recirculation of the wake is drawn closer upstream: For the case of the clean airfoil, the streamlines circulate around a centre placed around $x/c = 90\%$ meanwhile with a tab this centre is moved up to $x/c = 75\%$. Hence, even though the point of flow separation is moved upstream the closer proximity of the vortex introduces additional negative pressure on the suction side and in turn increases the overall lift of the airfoil.

Hence, if the tab is placed right and has a sufficient height, a stabilisation of the wake recirculation can be achieved through the presence of the tab. In this case the recirculation zone dominates the near flow field of the airfoil and influences the pressure and hence the overall lift. This process is highly dependent on the transition location since this in turn influence the shear layer

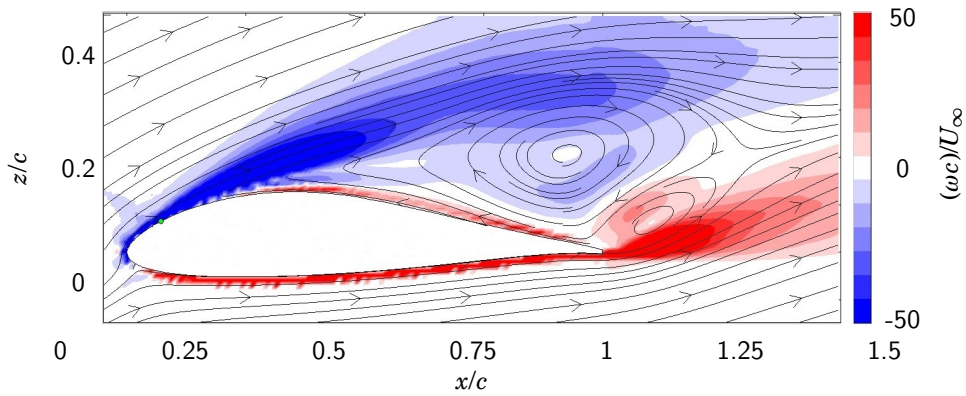

Figure 5.20: Average vorticity field without tab ($\alpha = 18°$, Re=800000)

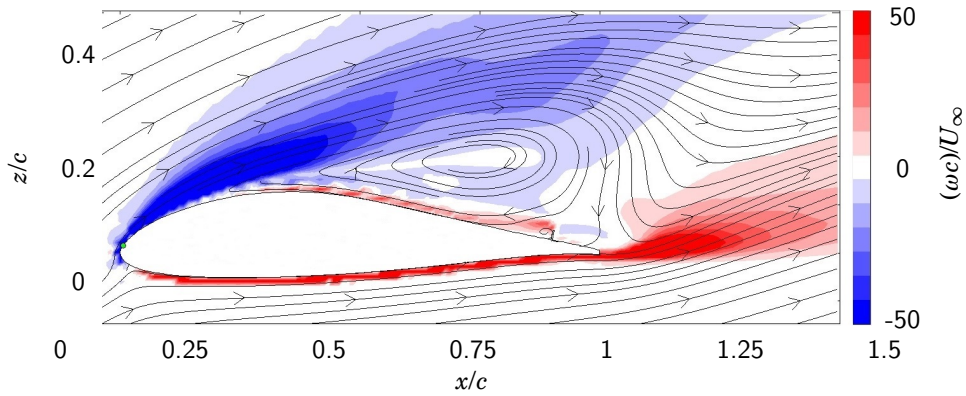

Figure 5.21: Average vorticity field with tab ($\alpha = 18°$, Re=800000

thickness and the formation of the recirculating vortex.

Back-Flow flaps

This concept of how micro-tabs enhance the lift in this case differs from other concepts. For reasons of a comprehensive overview, another possible concept should be mentioned here: Back-flow flaps (see again Figure 3.5) are an aerodynamic concept originated and motivated from the aerodynamics of birds to enhance the lift in post stall regions. This concept has among others been studied in the past at the *HFI* [15, 16, 95]. The back-flow flaps are flaps placed on the suction side of an airfoil. Under high angles of attack, when separation starts at the trailing edge the flaps rise due to the pressure difference on and below the flap. The presence of the back-flow flap works as a barrier for the separation zone which cannot move further upstream unhindered. As a result the separation zone is smaller in size and the point of separation is further downstream than in comparison to the clean airfoil [95]. However, the flaps are only effective if the flap is large enough to reach the shear layer of the separation. If this requirement is not complied with, an adverse effect is the case: The separation zone will extend to regions even upstream of the flap resulting in a much lower lift.

In comparison to back flaps, micro-tabs are generally smaller and might be placed even further upstream. As a result, the micro-tabs might only delay the start of the separation, when the separation zone is still small and the height of the tab is sufficient. However, the conducted CFD simulations were done considering a deep stall region within a fully established recalculating stall region. Therefore, both mechanisms might occur depending on the nature of the shear layer, the angle of attack, the airfoil geometry and the micro-tab height.

5.2 Multiple Passive Elements

In an attempt to reduce the drag and improve the lift-to-drag ratio, serrated, perforated as well as multiple finite micro-tabs have been studied in the past [92]. In the following section, the effects of multiple finite micro-tabs or tabs are presented as an alternative aerodynamic control concept. For a tab height of $h_{tab}/c = 2\%$ various measurement have been carried out with different solidity ratios applied. In doing so, the tab length l_{tab} was varied as well as the length of the gap l_{gap} between the tabs.

5.2.1 Effect of the Solidity Ratio

For the study of the effect on the aerodynamic properties of multiple finite tabs, the airfoil was equipped with a row of single tabs or tabs. Each tab had a total length of $l_{tab} = 1/3c$ and had a minimal gap of 10% of the tab length between each other. In total seven of such tabs could be attached on the airfoil model (see Figure 5.22). Results labeled with the single T specify the airfoil with all seven deployed tabs. The curve labeled as TG indicates a repeating deployed tab followed by gap (a not deployed tab) and so on. All tested configurations are visualised in Figure 5.22 for tabs on the pressure side, however, they were also tested on the suction side.

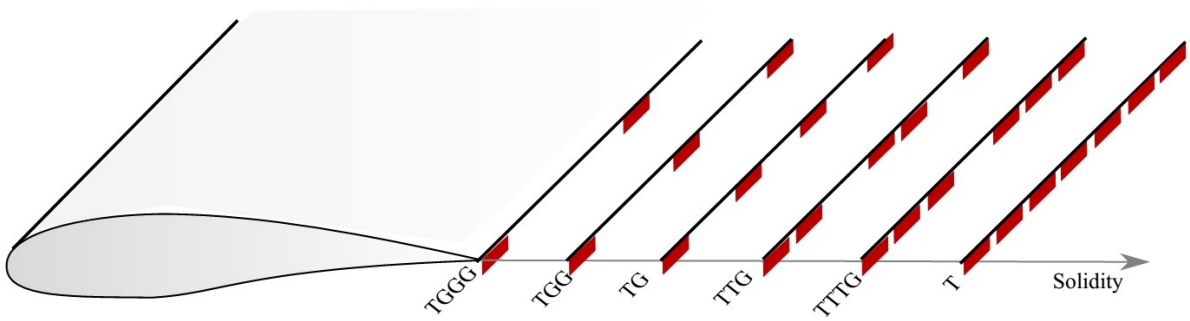

Figure 5.22: Overview of finite tab configurations

In Figures 5.23 and 5.25 the lift curves for various tab configurations on the pressure and suction side are shown. It was found that the solidity ratio of multiple tabs depend more or less linearly

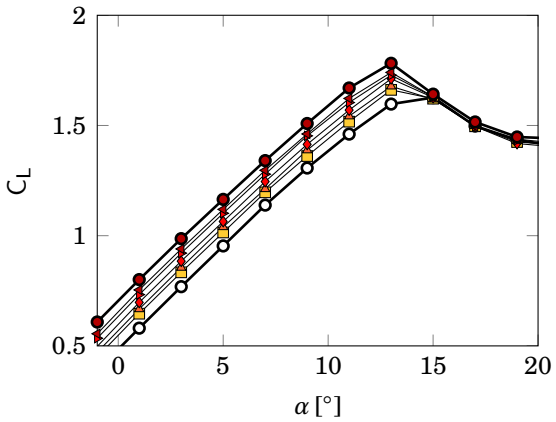

Figure 5.23: Lift curve for tabs placed at the trailing edge with various heights (PS)

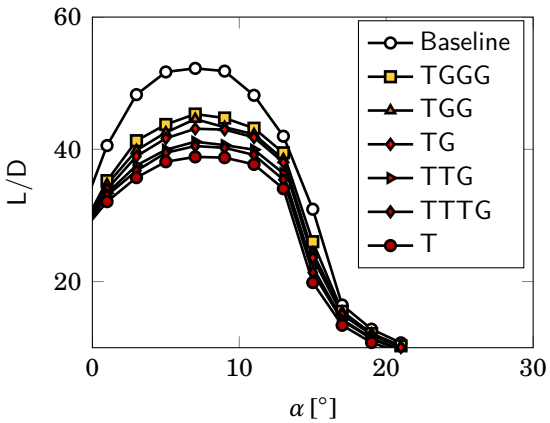

Figure 5.24: Lift-to-drag for tabs placed at the trailing edge with various heights (PS)

on the lift gain or loss. Hence, by selecting the right ratio between deployed tab (T) and gaps (G) a specific lift value can be employed. This connection can be seen e.g. in Figure 5.23, where the placement of one tab next to one gap (TG) on the pressure side gave more lift than leaving two tabs out (TGG) and so forth. The matching lift-to-drag curves are plotted in Figures 5.24 and 5.26. Generally, one can say that the more gaps are left, the closer the curves become to the baseline case.

It can be concluded, that if the lift curves for various solidity rations of a multiple tab systems are known a method is found to alleviate the airfoil's lift without changing the tab height but instead the amount of deployed devices. This is an advantageous, since the positioning of the correct element height is more difficult to accomplish since highly accurate motor control systems are needed. Whereas a system built out of multiple tabs or tabs based on a simple on/off system would be more stable, cost efficient and accurate in its positioning and would therefore requires less maintenance [107].

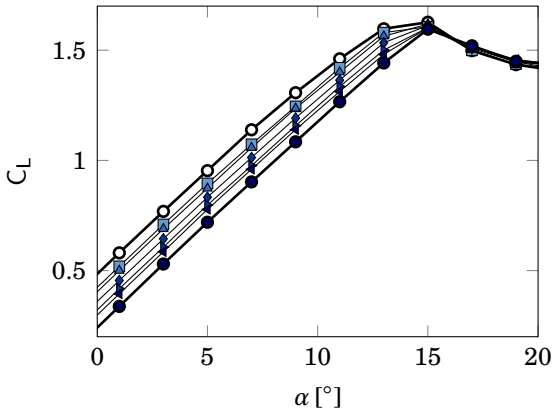

Figure 5.25: Lift curve for tabs placed at the trailing edge with various heights (SS)

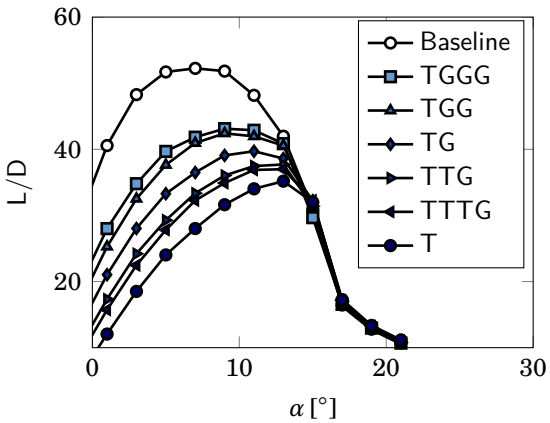

Figure 5.26: Lift-to-drag for tabs placed at the trailing edge with various heights (SS)

5.2.2 Flow Visualisation around Multiple Tabs

The flow field around the finite micro-tab is characterised by the flow through the gaps between the finite tabs. This bypass stream reduces the overall drag. The flow field around the tab has been analysed with oil paint as well as a quantitative tuft flow visualisation technique that was developed at TU Berlin in cooperation with SmartBlade GmbH [140]. For this technique the wing is equipped with flow indicators and image registration markers. Using a high-resolution digital camera, the individual tuft-orientations are tracked using 500 images. Using this data, the mean tuft-orientations and their respective standard deviations were calculated. In order to visualise the surface flow patterns, the data was interpolated and a line integral convolution (LIC) was performed. Additionally, the contours of the tufts' standard deviations were plotted. The red shading indicates regions of large flow angle variations. The LIC pattern has a visual appearance that is comparable to the oil flow visualisation technique.

Figure 5.27 shows the flow around micro-tabs placed on the suction side at $x_{tab}/c = 90\%$ with a height of $h_{tab}/c = 2\%$ for an angle of attack of $\alpha = 5°$. The two pictures at the left hand side are the results of the oil paint flow visualisation on the suction side which are compared to the results from the flow tufts found on the right hand side. Both measurements were performed without boundary layer tripping present. In the first row the flow field around a tab with the length of $l_{tab} = 400mm$ is depicted. The second row shows both measurement techniques used for multiple tabs with the tab length of each $l_{tab} = 200mm$ and an overall solidity ratio of $\sigma = 0.5$. The oil paint visualisation on the left hand side shows a laminar separation bubble at around 45% of the chordlength. The absence of the laminar separation bubble in the tuft flow visualisation can be explained by the early boundary layer tripping caused by the intrusive flow tufts. However, both measurement techniques show the flow evasion around the tab as well as the separation right before and behind the tab where the recirculation zones are present. For the visualisation with multiple tabs, it has to be noted that more fluid passed through the

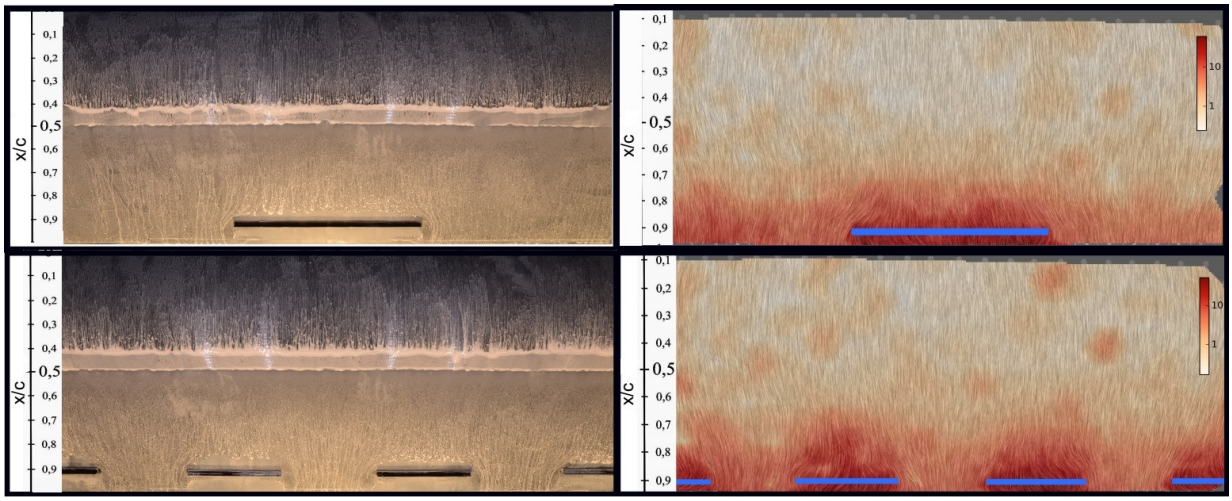

Figure 5.27: Flow visualisation from oil paint (left) and LIC calculation (right)

gaps between the tabs than surpassing over the tabs. As a consequence, one can see a strong upstream effect of the tabs on the standard variation of the flow direction.

5.2.3 Velocity Field

12-hole probe measurements were conducted for the same angle of attack of $\alpha = 5°$ in the wake $\Delta x = 20mm$ behind the trailing edge to evaluate the tip vortices. Figures 5.28 and 5.29 show the velocity field behind the finite tab at the trailing edge ($h_{tab} = 2\%c$). It can be seen that the wake position shifts depending on the airfoil side on which the tab is placed. If the tab is placed on the pressure side for lift enhancement, the lower wake position indicates a higher circulation associated with the higher lift. The opposite case is found for the tab on the suction side, where the wake is orientated at a higher z-position. Furthermore, at the tab tips the formation of a vortex can be seen. According to the stream-lines this vortex is more pronounced for the pressure side tabs and hence affects the adjacent area more strongly.

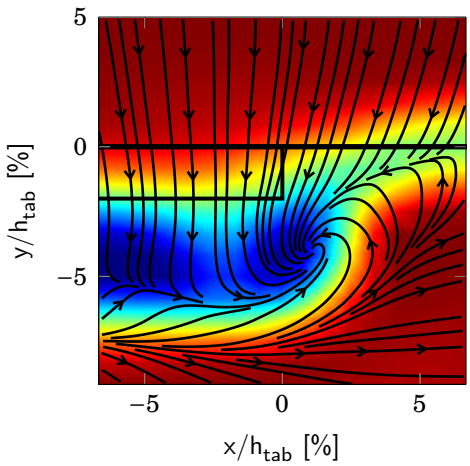

Figure 5.28: Velocity field for finite tab on pressure side ($l_{tab} = 1/3c$, $h_{tab} = 2\%c$, $\alpha = 5°$)

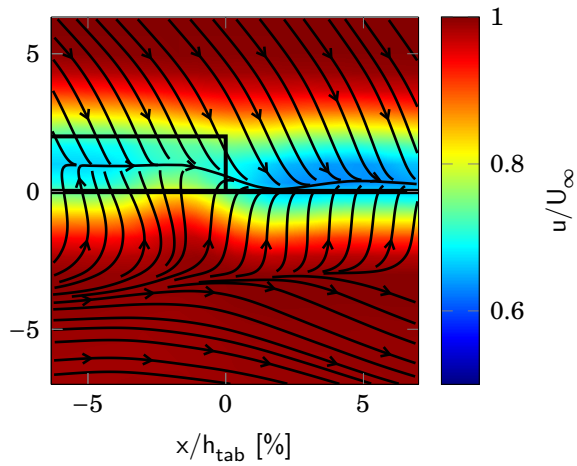

Figure 5.29: Velocity field for finite tab on suction side ($l_{tab} = 1/3c$, $h_{tab} = 2\%c$, $\alpha = 5°$)

5.2.4 Tab Tip Vortices

Figures 5.30 and 5.31 show the corresponding vortices for the tab placed at the trailing edge on the pressure and suction side. While the vorticity is positive for the tab on the pressure side, the vorticity for the suction side tab is negative and less pronounced. The circulation for various finite tab configurations has been calculated and is summarised in Table 5.2 below. For the pressure side, a higher tab yielded in a stronger vortex formation (Figure 5.33). Meanwhile, a tab with the same height but greater length over the span had no effect (Figure 5.32).
Furthermore, the vortex interaction of two adjacent tab tip vortices was investigated. Therefore, two tabs with the same height and length were placed at the trailing edge on the pressure side with varying gap sizes with a solidity ratio of $\sigma = 0.75$ and $\sigma = 0.9$ (Figures 5.34 and 5.35). The vortex pairs for both configurations are less pronounced and displaced by the presence of the counter-rotating vortex in comparison to the tip vortex of the single tab. Hence the larger the solidity ratio, the smaller the vortex pair becomes in its size and strength.

Airfoil side	h_{tab}	l_{tab}	$\Gamma/(U_\infty \cdot c)$
Suction side	2% c	1/3 c	-3.3258 $\cdot 10^{-4}$
Pressure side	2% c	1/3 c	11.8305 $\cdot 10^{-4}$
Pressure side	2% c	c	15.2631 $\cdot 10^{-4}$
Pressure side	3% c	1/3 c	15.4991 $\cdot 10^{-4}$

Table 5.2: Circulation of tab tip vorticies of various configurations

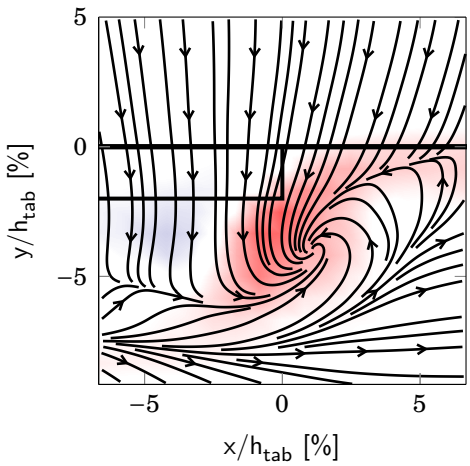

Figure 5.30: Vorticity field of finite pressure side tab ($l_{tab} = 1/3c$, $h_{tab} = 2\%c$)

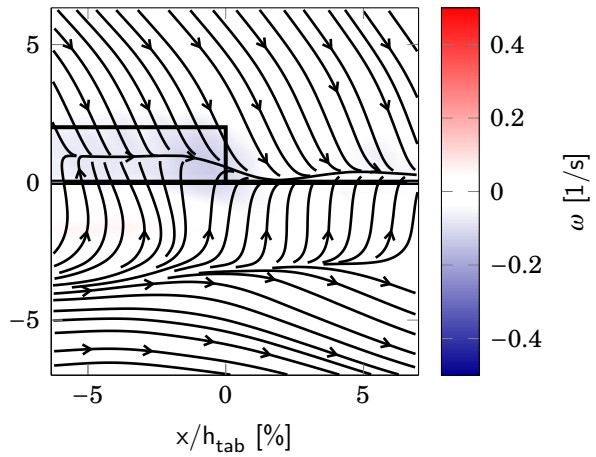

Figure 5.31: Vorticity field of finite suction side tab ($l_{tab} = 1/3c$, $h_{tab} = 2\%c$)

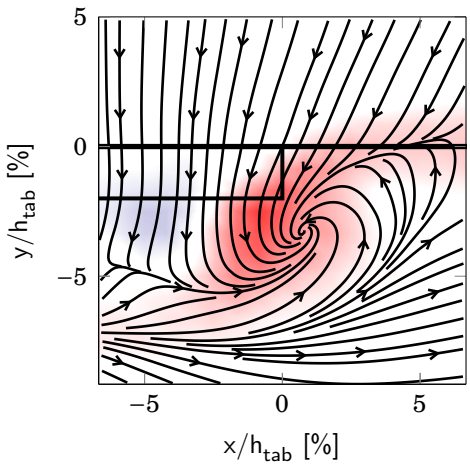

Figure 5.32: Vorticity field of finite pressure side tab ($l_{tab} = c$ and $h_{tab} = 2\%c$)

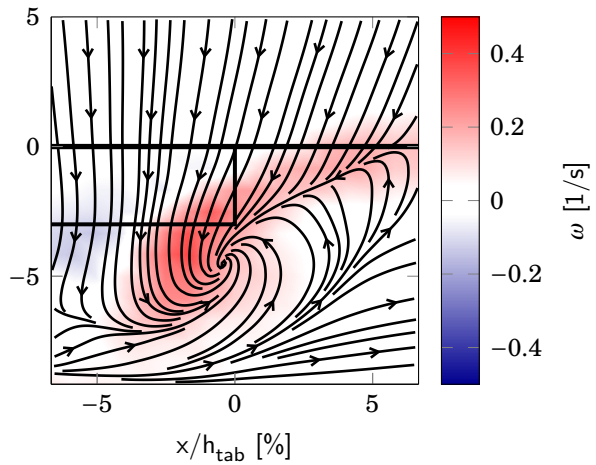

Figure 5.33: Vorticity field of finite pressure side tab ($l_{tab} = 1/3c$ and $h_{tab} = 3\%c$)

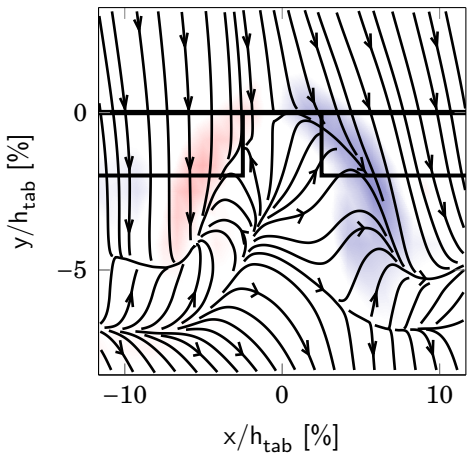

Figure 5.34: Vorticity field between tabs on pressure side ($\sigma = 75\%$)

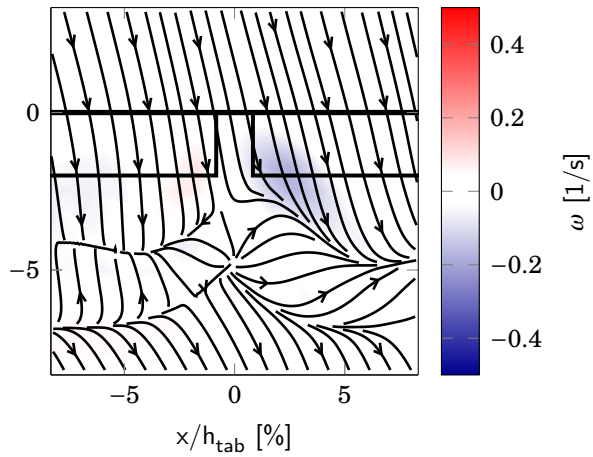

Figure 5.35: Vorticity field between tabs on pressure side ($\sigma = 90\%$)

5.3 Single Finite Flap

In this section the aerodynamic behaviour of the flaps on low-Reynolds-airfoils were investigated. Low-Reynolds-airfoils as they might be used for smaller vertical axis wind turbines have a smaller chord and therefore nearly no installation space within the airfoil to install or retract micro-tabs. Hence the use of a Gurney flap is advantageous. Measurements with full span flaps as well as a single finite flap were performed and the surface pressure measurements around the flap investigated. Additional PIV measurements in the wake were done. [2]

5.3.1 Experimental Set-up

Local, spanwise distributed as well time resolved pressure measurements are needed for the investigation of the local effects of a single active flap. Therefore, these measurements were conducted in the smaller Eiffel wind tunnel of the *HFI* with a test section size of 0.28m x 0.4m, a maximum Reynolds number of $Re = 180000$ as well as a turbulence level of $Tu < 0.5\%$ (see Figure 5.36). The size and built-up of the wind tunnel permitted the cost reduced manufacturing of a small wing, which a large amount of pressure tubes with a short tube length to ensure a direct and unaltered measurement of the dynamic pressure response. Previous studies on the FX63-137 airfoil [6, 128] were conduced at the *HFI* [11, 59] where the airfoil was chosen due to the good low-Reynolds characteristics. The two-dimensional airfoil with a chord of $c = 0.14m$ and a span of $b = 0.28m$ was equipped with a flap at the trailing edge with a height of $h_{flap} = 3.57\%c$. If the flap was not deflected with a flap angle of $\theta = 0°$, the flap was orientated tangential to the surface at the trailing edge. This resulted in an angle of $\theta_0 = 20°$ between the flap and the chord. Furthermore, the flap could be deflected $\theta_{min} = -110°$ to the suction side and $\theta_{max} = 70°$ to the pressure side (see Figure 5.37). Experiments were conducted with a full-span flap as well as a finite flap which was centred at the wings trailing edge and a spanwise length of $l_{flap} = c/2$.

The wing was laminated and equipped with seven spanwise rows of pressure taps to measure the surface pressure distribution on the surface. Each row consisted of 45 pressure taps along the chord, which results in 405 total measurement locations. However, due to the thin trailing edge and due to the manufacturing process of the airfoil no pressure measurement could be made downstream of $x/c = 0.85$ on the suction side and $x/c = 0.8$ on the pressure side.

For the data collection time-resolved differential pressure sensors were used, which measured each row of pressure taps simultaneously. The pressure transducers [2] measured the pressure difference between the local surface pressure and the static pressure of the freestream $(p - p_\infty)$ with an accuracy of ± 5 Pa and a sampling frequency of 4000Hz. The data was processed by a data-acquisition unit (DAQ) [3]. Furthermore, an embedded real-time control and monitoring system provided the time synchronisation between all 405 pressure ports and the real time Gurney flap position as given by the servo motor controller of the flap. The static measurements were averaged over a total time of 5min.

[2] Some results presented in this section were previously published by Bach et al. in [7] and [10]. For the first paper, co-author and Bachelor student R. Berg performed part of the pressure measurements and analysis for the first paper under the guidance of the author. All other tasks were carried out by the author.

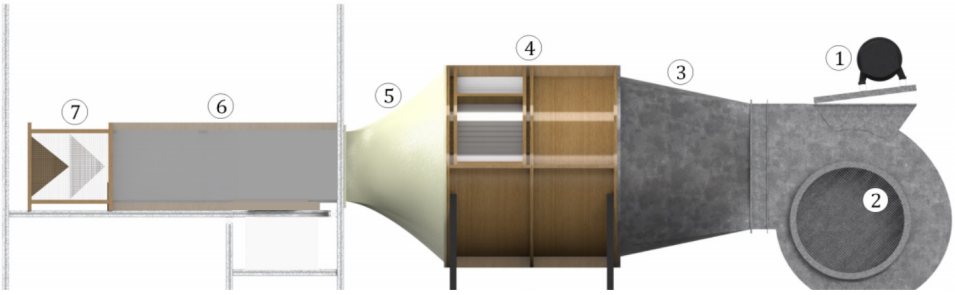

Figure 5.36: Eiffel wind tunnel at the *HFI* with motor (1), radial fan (2), diffuser (3), settling chamber (4), duct (5), measurement section (6) and a closure diffuser (7).

Additionally, high speed PIV (Particle Image Velocimetry) measurements were conducted in the flap's wake to understand the underlying structures and effect of the finite nature of the flap as well as the transient responses. The high speed camera was placed perpendicular to the airfoils chord to capture the vortex street and the wake response to the flap deflection behind the flap. The sampling frequency was 2000Hz. An additional trigger was used to assign each PIV shot to the temporal lift and flap position.

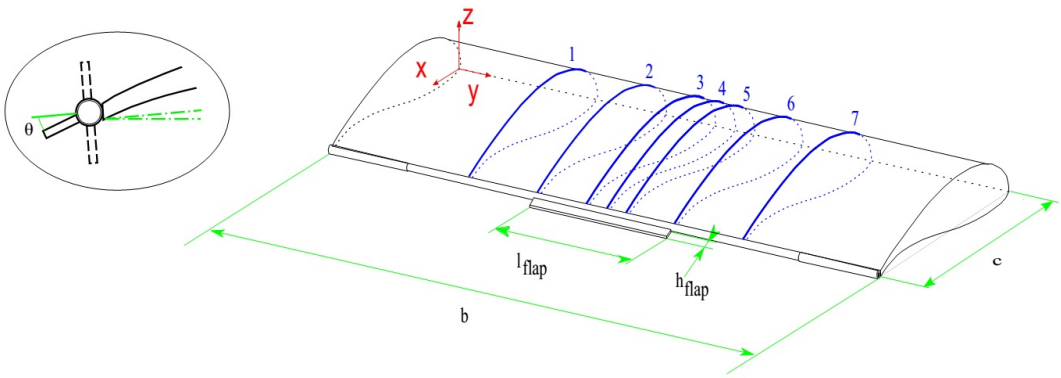

Figure 5.37: Pressure ports and flap position on the FX63-137 airfoil ($Re = 180000$)

5.3.2 Local Surface Pressure

Figure 5.38 shows the measured pressure distribution at half span for the airfoil without a flap. A good agreement was found with simulations performed with the in-house code QBlade based on XFoil [91] for the two dimensional airfoil calculations. The shown pressure distributions were performed with the two-dimensional part of the code with the same airfoil geometry. Since the pressure ports in the experiments ended at around $x/c = 0.8$ an interpolation of the values has been performed up to $x/c = 0.9$ to get a closer result to the theoretical lift value.

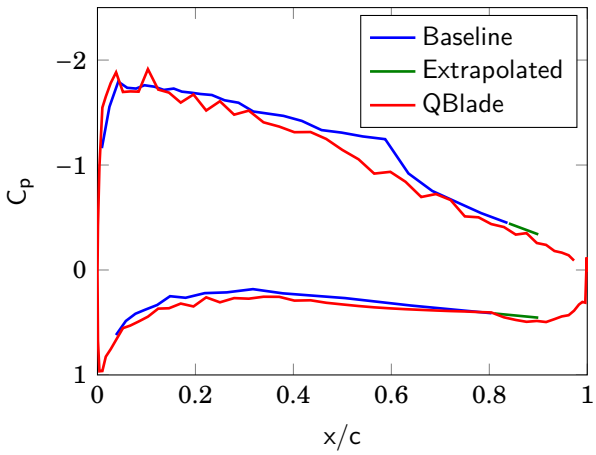

Figure 5.38: Comparison with simulation of the clean airfoil without flap (QBlade [91])

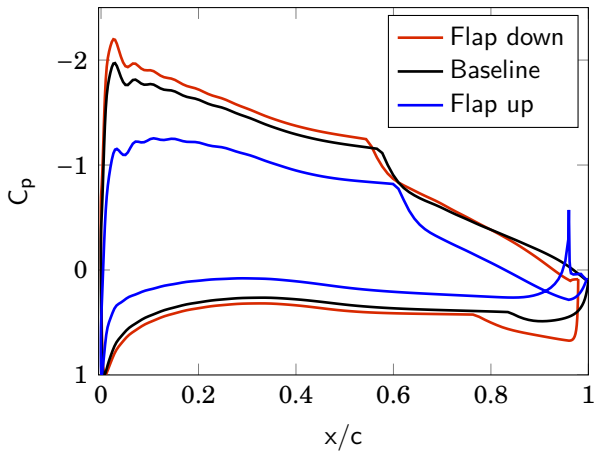

Figure 5.39: Simulation with Flaps (QBlade [91])

Figure 5.40 shows the measured pressure distribution at half span for the baseline (flap angle $\theta = 0°$), the two-dimensional full-span flap and the finite central span flap. The left plot shows the distributions for the flap deflected to the pressure side for a lift enhancing effect and the plot on the right hand side depicts the pressure coefficient for the flaps deflected to the suction side for lift reduction. After 90% chord length a pressure build-up in front of the flap is anticipated, whose individual shape is hard to predict. Therefore, the linear interpolation is only applied up to 90% chord length and hence the largest part of the anticipated pressure built-up in front of the flap is not incorporated in the later calculations of the lift.
For the flaps directed to the pressure side, the full-span flap shows a clear increase of the pressure difference C_p at all chordwise positions. The distribution in front of the finite flap shows hardly any change with respect to the original pressure distribution of the airfoil with a full-span flap with a flap angle of $\theta = 0°$.
For the positioning of the flap on the suction side the behaviour is found differently: The deflected full-span flap shows a reduction over all chordwise positions of the pressure differences. The finite flap shows a similar effect, however less pronounced. The pressure difference for the finite flap is larger than for the baseline case but smaller than for the full-span flap.

The boundary layer transition location of the baseline is found at $x/c = 0.6$. If the full-span flap deflects upwards it can be seen that the transition location moves slightly downstream (Figure 5.40, right). For the downwards deflected flap the opposite effect is the case and the transition location moves slightly upstream. This trend remains the same for a finite flap but the effect is less pronounced.
Generally, the transition location is set through the transit length and the velocity. If the angle of attack is increased, the stagnation point at the leading edge moves more in the direction of the pressure side and at the same the higher curvature of the streamlines induce a higher suction peak $|C_{p,min}|$ and a higher local velocity. Therefore, when the angle of attack is increased, the transit length and local velocity are increased, causing an earlier transition on the suction side.

For the airfoil with a flap, the mechanisms are similar: If the flap is deflected down, the stagnation point again moves further towards the pressure side and hence the transition location is moved to smaller x/c values. If the flap deflects to the suction side, the decamberisation of the flow yields that the stagnation point moves upward and hence the velocity on the suction side is decreased moving the transition location further backward to higher x/c values.
The same trend for the transition location could be reproduced by QBlade simulations illustrated in Figure 5.39. The simulations are based on the identical airfoil and Reynolds number. In Qblade the flap was included with the original XFOIL flap function at $x/c = 96\%$ with a flap angle of $\theta = +/-45°$. The transition locations of QBlade were found at $x/c = 0.54$ for the baseline case, $x/c = 0.56$ for the flap down and $x/c = 0.61$ for the flap up.

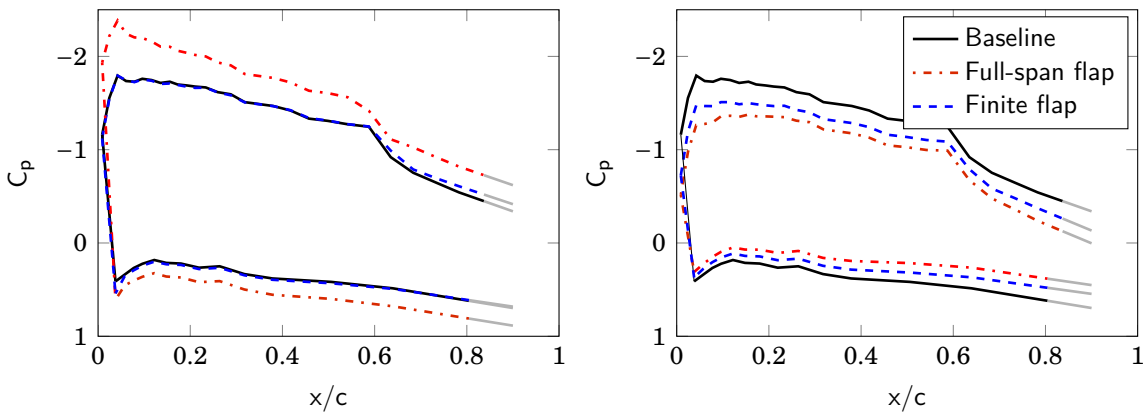

Figure 5.40: Comparison of the measured pressure distribution at $y/b = 0.5$ for the downwards deflected flap (left) and the upwards deflected flap (right)

5.3.3 Spanwise Lift Distribution

From each row of pressure measurements a spanwise lift coefficient C_l is calculated. Figure 5.41 shows the lift distribution for the full-span as well as the finite central-span configurations. The full-span flap deflected yielded a lift difference of around $\Delta C_l = +/-0.4$ for the flap deflected upward and downward.
The finite central span flap yielded a maximum lift difference of around $\Delta C_l = +0.12$ directly in front of the flap deflected to the pressure side (PS) and $\Delta C_l = -0.18$ for the flap deflected to the suction side (SS). However, the lift is significantly reduced as the edges of the finite flap are approached. This spanwise decay of the lift appears to be in the same range for the flap on the suction and pressure side.

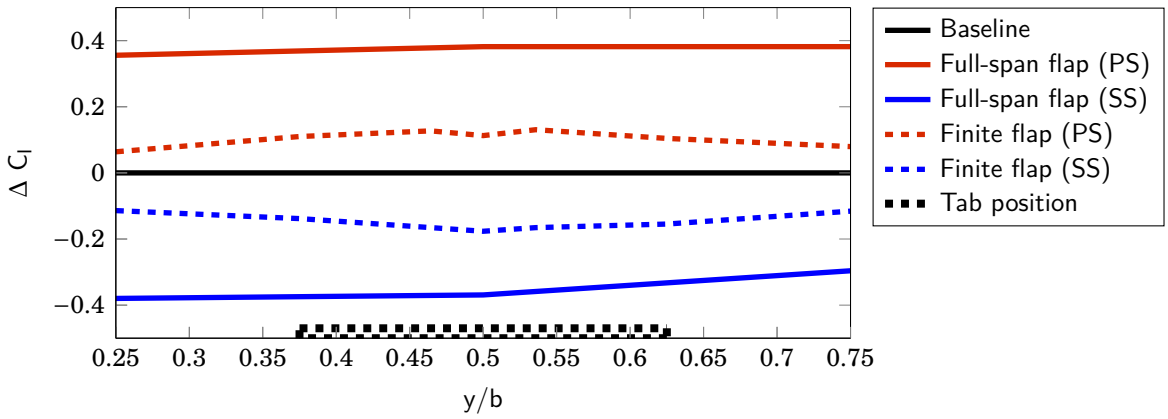

Figure 5.41: Spanwise lift distribution ($Re = 180000$)

5.3.4 The Wake Flow Field

In the following section the wake flow field behind the full-span and finite flap are evaluated and compared. Measurements with a high speed PIV systems were conducted and Proper Orthogonal Decompositions (POD) was employed to draw conclusions on the interaction of the wake flow field and the time-dependent airfoil loads.

The Average Flow Field

The average flow fields were computed from the PIV measurements behind the steady deployed flap configurations. Figure 5.42 represents the average vorticity for the case of the downward deflected flap. The coordinate origin is located at the position of the trailing edge. In the average wake no vortex structure of the vortex street can be seen. However, the shear layer and the wake position can be identified.

At the position of $x/h_{flap} \approx 4$, marked in Figure 5.42 with a dotted line, the average wake positions were determined. The differences of the wake positions can be associated with the effect on the apparent camber of the flap. If the flap is deflected downwards, the airfoil experiences a higher lift, resulting in a larger bound vortex of the airfoil. Consequently, the surrounding flow field experiences a higher circulation and the wake position is moved to lower z-values (Figure 5.43). The upwards deflected flap yields a wake position, which is moved to higher z-values with respect to the baseline case. It is interesting to note that the wake profiles of the finite flaps have an overall higher velocity deficit in the wake.

POD of Wake Flow-Field

For a further understanding of the wake behavior Proper Orthogonal Decompositions (POD) of the PIV snapshots were performed for all flap configurations. This technique is a powerful

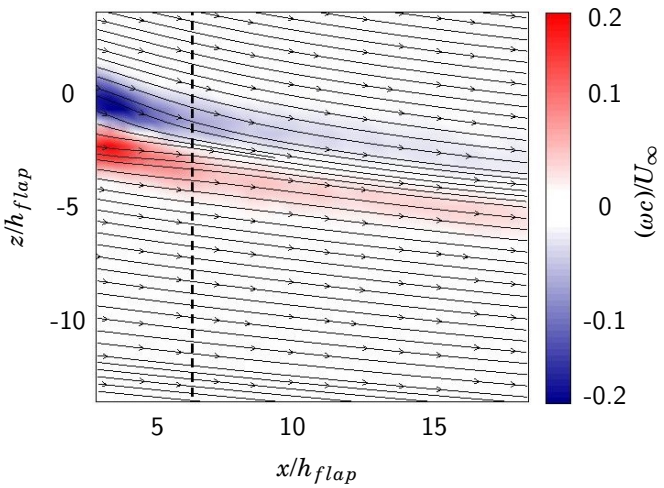

Figure 5.42: Vorticity of average flow field in the near wake (flap downwards, trailing edge at coordinate origin, $Re = 180000$)

and elegant tool of data analysis to extract a basis for a modal decomposition from a set of uncorrelated signals. With its application it is possible to obtain low dimensional approximation of an otherwise high-dimensional process. The POD was early introduced in 1967 for the study of spatial structures [86]. For a good introduction of the theoretical background and mathematics of this technique the reader is encouraged to read the summary of Chatterjee [29]. The POD applied to snapshots of flow fields is described further in the work of Sirovich [124]. A major advantage of POD is the linearity and robustness of the procedure.

In this context, the POD technique was applied on the series of PIV snapshots of the near wake behind the flap. Analysis of the following configurations were conducted: Full-span flap up (Figure 5.44), finite flap up (Figure 5.45), full-span flap down (Figure 5.46) and finite flap up (Figure 5.47). All four figures depict the vorticity at an phase angle of approx. $\phi \approx 0°$. The vorticity was calculated from the velocity components in x and in z direction subtracted by the mean flow field.
Each configuration clearly shows the underlying formation of the vortex street in the wake. The vortex street positions of the full-span and finite flaps are only slightly changed, as already suggested in Figure 5.43. Furthermore, for the flap deflected downwards (Figures 5.46 and 5.47) the strength of the single vortices of the vortex street Γ_{VS} is found to be larger for the case of the full-span flap. However, for the flap deflected upward, this does not seem to be the case.

POD of the Lift Component

According to Theodorsen's theory [132], the initial vortex of the vortex street leaving the trailing edge of the airfoil induces a change of the bound vortex of the airfoil and consequently a change of lift. Therefore, an additional POD analysis was performed to evaluate the effect of the spanwise vortex street on the lift. Pressure information in the wake measured with an additional

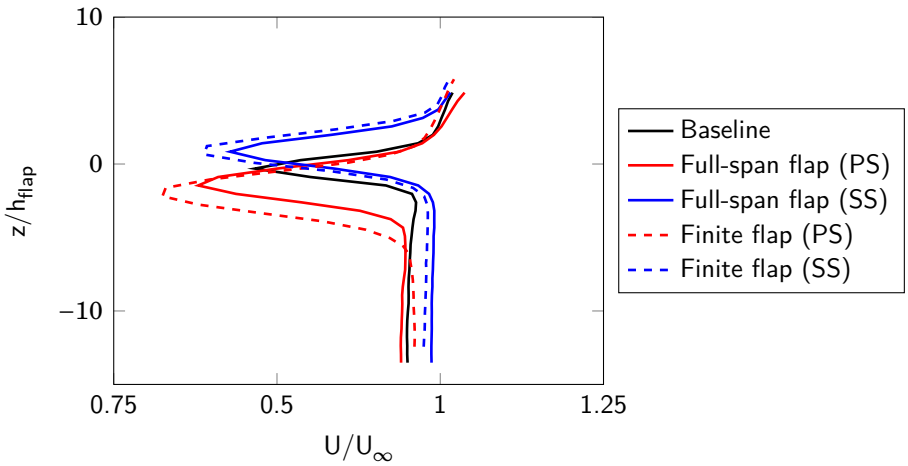

Figure 5.43: Wake position for various flap configurations ($Re = 180000$)

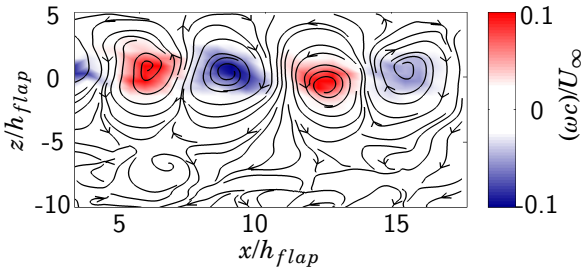

Figure 5.44: Phase averaged flow-field ($\phi \approx 0$) of full-span flap up ($Re = 180000$)

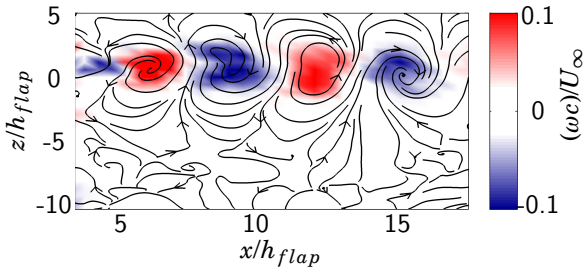

Figure 5.45: Phase averaged flow-field ($\phi \approx 0$) of finite flap up ($Re = 180000$)

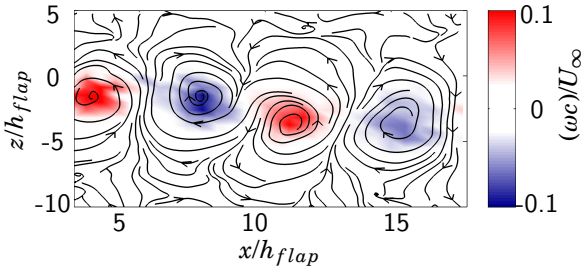

Figure 5.46: Phase averaged flow-field ($\phi \approx 0$) of full-span flap down ($Re = 180000$)

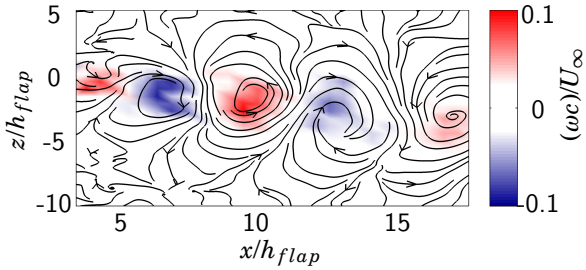

Figure 5.47: Phase averaged flow-field ($\phi \approx 0$) of finite flap down ($Re = 180000$)

wake rake were used for this POD. Phase angles of the cortex street were determined and the corresponding surface pressure measurements identified. Then, the associated lift was calculated from this surface pressure for each interval of the phase angle of the vortex street. Results showed that pressure and lift fluctuations according to the vortex street. Pressure fluctuations

on the surface were more pronounced closer to the trailing edge. However, the overall effect was still visible in the integrated lift value.
Figure 5.48 illustrates the variation of the lift coefficient over the phase angle of the full-span flap down. The lift was phase-averaged over a segment of $\phi = 5°$ and represented by the black markers. The lift more or less follows a sinusoidal oscillation around an average value. In the region of $-180° < \phi < 0°$, the lift is negative which corresponds to the event, when a spanwise vortex with the circulation $+\Gamma_{VS}$ leaves the trailing edge. When the phase angle is $0° < \phi < 180°$ the shedding vortex of the trailing edge has the opposite sign $-\Gamma_{VS}$. The underlying colours of the sinus are chosen according to the colours of the vorticity in the plots of the wake in Figures 5.46 to 5.47.

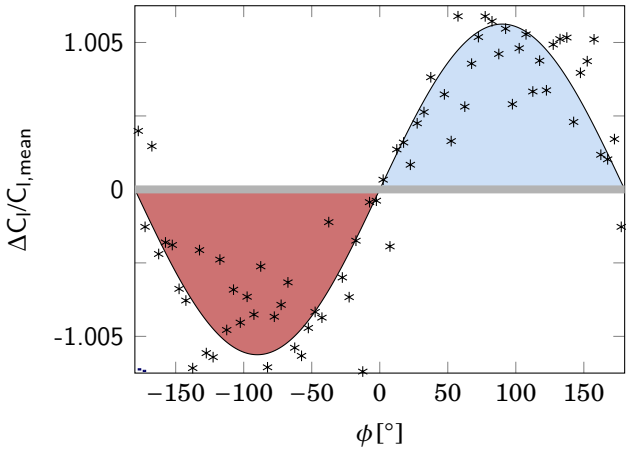

Figure 5.48: Lift variation of the full-span flap (POD, $Re = 180000$)

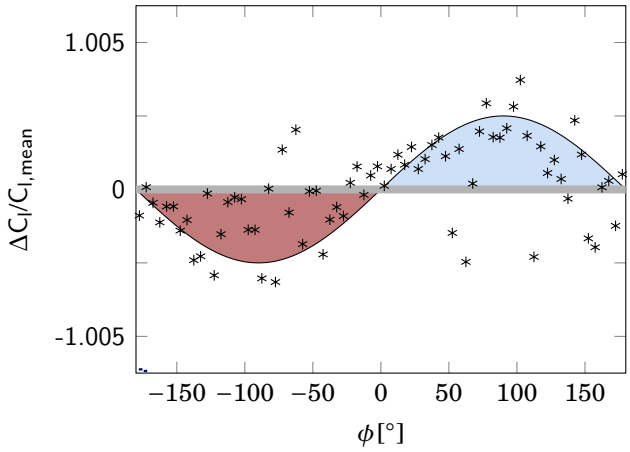

Figure 5.49: Lift variation of the finite flap (POD, $Re = 180000$)

It was shown earlier that the vortex strength of the street is reduced for the case of the downwards directed flap. Accordingly, the POD of the pressure field yields a lift variation of the finite flap down that is reduced in its magnitude (see Figure 5.49).

Frequency Analysis

For an accurate information of the wake frequencies a FFT (Fast Fourier Transformations) analysis were carried out from the PIV data, the airfoil's pressure measurements and additional wake rake measurements. The frequencies of all these measurements were found be consistent with each other.

Frequency Analysis at Centre-span

Figure 5.50 depicts the frequencies found in the centre-line of the airfoil (behind row 4 - compare Figure 5.37) for all four flap configurations. The frequency of the full-span flap deflected to the pressure side is $f = 402Hz$ and therefore lower than the flap deflected to the suction side ($f = 456Hz$). This trend is in line with the findings of the experiments of the Althaus

$AH93W174$ airfoil [9]. This difference may be explained by the local boundary layer height. If one assumes that the flap height is relatively larger than the local boundary layer height with its flap height of $h_{flap} = 3.5\%c$, then the flap penetrates more into the outer flow if the flap is deflected to the pressure side, where the boundary layer is thinner. Consequently, the frequency for the flap on the pressure side must be smaller.
If the flap configuration is changed into a finite flap, these frequencies shift for both cases (flap up and down) to lower values with $f = 383Hz$ for the finite flap to the pressure side and $f = 442Hz$ for the suction side. This may be due to a smaller local velocity at the finite flap, caused by the introduction of the gap. However, for an exact explanation of the phenomenon one would certainly need to carry out further experiments or simulations.
The concentration of energy at a frequency of around $f = 308Hz$ is apparent in all measurements including the baseline case and is therefore not associated with an aerodynamic effect of the flaps but moreover the frequency of the set-up.
These frequencies were transferred to Strouhal numbers based on the flap height with $St = f \cdot U/h_{flap}$. The Strouhal numbers for the full-span flap down corresponds to $St = 0.11$ and for the full-span flap up to $St = 0.12$ which is a slightly lower value than a comparison with the literature would suggest. In this context, the flap was attached to a round hinge located at the trailing edge, which made it difficult to determine the flap height accurately. Next to this, the round hinge at the flap root might influence the vortex shedding at this side and consequently further distort of the vortex street and the Strouhal number.
Finally, the Strouhal number itself is further dependent on multiple parameters: The angle of attack, the flap height, the deployment on either the suction or the pressure side, which all affect the state of the local the boundary layer [9]. Furthermore, McLachlan et al. have shown that the Strouhal number is a function of the Reynolds number [94], which influences the transition and hence the boundary layer.

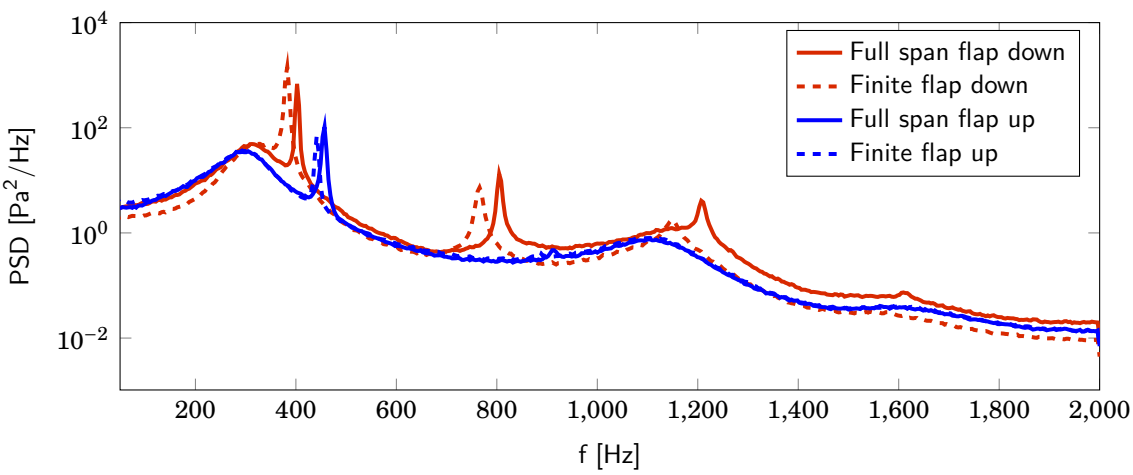

Figure 5.50: Dominant wake frequencies for various flap configurations (row 4, $Re = 180000$)

Flap configuration	Row 1	Row 3	Row 4	Row 5	Row 7
full-span flap down	408Hz		402Hz		408Hz
full-span flap up	444Hz		456Hz		444Hz
Finite flap down	/	381Hz	382Hz	381Hz	/
Finite flap up	/	433Hz	442Hz	423Hz	/

Table 5.3: Spanwise wake frequencies

Spanwise Frequency Distribution

The mono high speed PIV measurements were only performed in the airfoil's central line due to the symmetric flow. To extract information of the spanwise dependency on the frequencies, the wake rake equipped with the time-resolved pressure sensors were positioned at various spanwise positions behind the rows (row 1 - row 7) where the surface pressure measurements were located (compare Figure 5.37). For each spanwise position FFT analyses were generated and the dominant frequency extracted. The results are summarised in Table 5.3. For the full-span flap, measurements were only done at three positions (row 1, row 4 and row 7). For the finite flap it was measured at all 7 rows, however, the regions where no flap was located showed no dominant frequency in the wake.

Meanwhile the frequencies for the full-span flap remained mostly constant over the span, the frequencies of the vortex street behind the finite flap were found to change. In both cases, for the finite flap down and the finite flap up, the shedding frequencies in the centre-line were reduced in comparison with the full-span flap frequencies. Moving in the direction of the flap edges, the frequencies dropped further. At the same time the magnitude of the signal was reduced (not shown here).

Gurney Flap Noise

Broadband noise on airfoils can be associated with various sources, such as incoming turbulence [123] [31], pressure fluctuations in the boundary layer on the airfoil's surface [123] [98], tip clearance vortices [85] [46] and the vortex shedding from the trailing edge [78]. It was found by Sharland that the shear layer instability leading to the vortex street is the primary noise generating mechanism [123]. Sharland stated further that the noise from a vortex street can be directly calculated out of the fluctuating lift over time.

Hence, a smaller magnitude of the lift fluctuation for the finite flap in comparison with the full-span flap does result in less sound generation behind the flap. Even though the tip vortices represent an additional sound source, the overall sound generation over the span should be reduced. Furthermore, the stream-wise flap tip vortices entail a better mixing in the wake and hence contribute to a faster dissolution of the vortex system.

6 Static Airfoil with Active Micro-Tab and Gurney Flap

6.1 Active Micro-Tab

In this section the aerodynamics of the dynamically deploying or retracting active tab or flap are evaluated under different angles of attack and the dynamics of finite flaps are evaluated. and further PIV measurements were conducted to deepen the understanding of the physical effects.[1]

6.1.1 Experimental Set-up

Wind tunnel experiments were conducted on a two-dimensional NACA 0018 airfoil [38] with a full-span active micro-tab. The symmetric airfoil was chosen to eliminate effects from airfoil camber and hence produce generic aerodynamic responses of an active micro-tab employed on either the suction or the pressure side. A further advantage of using a symmetrical airfoil was the amount of data, which was available for further comparison of the results. The thickness of the NACA 0018 airfoil was reasonable high to integrate an active micro-tab mechanism in the airfoil section. The measurement were performed in the large wind tunnel of the *HFI*. Due to airfoil mounting in the wind tunnel, the micro-tab was located on the suction side for positive angles of attack, meanwhile for negative angles of attack the tab was placed on the pressure side (see Figure 6.2).
The airfoil had a chord length of $c = 0.7$m and an aspect ratio of $AR = 0.65$. The model was mounted perpendicular to the floor in the closed-loop wind tunnel. The turbulence intensity was $Tu < 0.5\%$. End-plates were employed to create a two-dimensional flow field. The airfoil's pitch could be changed through a shaft that was connected to a turntable located below the wind tunnel (Figure 6.1). The active micro-tab was placed at $x/c = 90\%$. Additional boundary layer trips were placed at the leading edge at $x/c = 15\%$ on both airfoil sides to secure a turbulent boundary layer. The symmetrical airfoil allowed the analysis of the transient effects of the micro-tab for load reduction as well as load enhancement at various angles of attack.
The active micro-tab was attached on both end-plates to two piston rods which were connected with a shaft located inside the airfoil. This shaft was driven by a servo motor (*AKM22E* from *National Instruments*), which was placed outside the wind tunnel. The tab could be deployed to a maximum height of $h_{tab}/c = 1.5\%$. The deployment and retraction time of the active

[1] Some results presented in this section were previously published by Bach et al. in [8]. Co-author D. Holst programmed the measurement programme in *LabView* and student S. Weiss helped with the analysis of the data under the guidance of the author. All other tasks were carried out by the author.

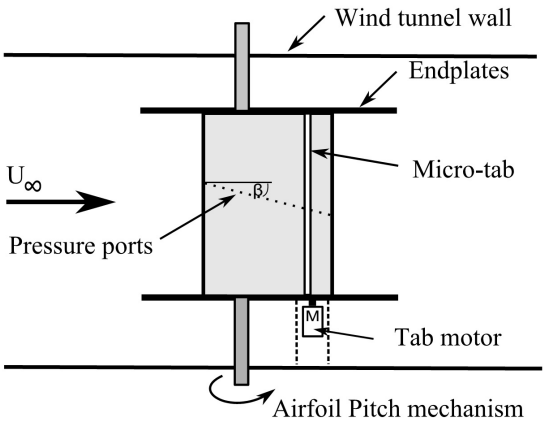

Figure 6.1: Experimental set-up for NACA0018 airfoil (view from the side)

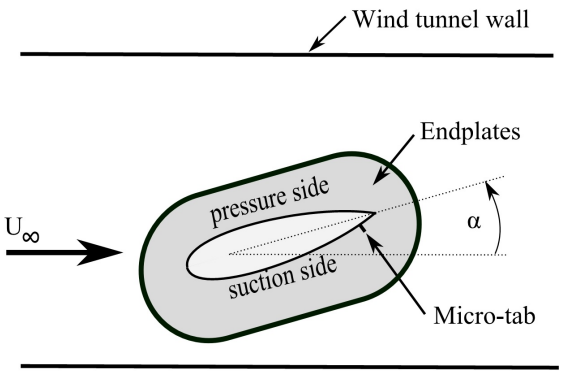

Figure 6.2: Declaration of angle of attack (view from above)

T_{act}	0.10s	0.20s	0.50s	0.75s	1.00s
Re $= 7 \cdot 10^5$	2.19	4.45	11.10	16.44	22.24
Re $= 1 \cdot 10^6$	3.15	6.21	15.65	23.27	30.89

Table 6.1: Dimensionless actuation times $T^*_{act} = T_{act} \cdot U_\infty / c$

micro-tab was varied between 0.1s $\leq T_{act} \leq$ 1.0s. Measurements were performed for Reynolds numbers of $7 \cdot 10^5$ and $1 \cdot 10^6$, yielding different dimensionless actuation times, summarized in Table 6.1. The angle of attack was investigated between $0° \leq \alpha \leq 15°$.

60 time-resolved pressure transducers along the mid-span region of the upper and lower surface measured the instantaneous pressure with a sampling rate of 6000 Hz. The ports were arranged along a line which was skewed by an angle of $\zeta = 10$ ° to the airfoil's centre-line, to ensure an undisturbed inflow of each single port. Furthermore, the airfoil shape and size enabled the setting of pressure ports close to the trailing edge. The pressure transducers [2] measured the pressure difference of the static pressure of the freestream and the local surface pressure $(p - p_\infty)$ with an accuracy of ± 5 Pa. The data was processed by a data-acquisition-unit *(DAQ)* [3]. Furthermore, an embedded real-time control and monitoring system ensured the alignment of the measurement data and the micro-tab position. The acquired data permitted the further computation of the time-dependent aerodynamic lift. The aerodynamic drag was not scope of this work and therefore not further evaluated.

Stereo PIV measurements were performed for an analysis of the steady state flow field around different tab heights ($h_{tab}/c = 0.4\%, 1.0\%, 1.4\%$ and 2.0%). The PIV pictures were allocated at central-span behind the tab to close behind the trailing edge in the wake. A quantel dual-Nd: Yag laser was employed with 170mJ per pulse, a frame rate of 5Hz and a wave length of 532 nm. Two *PCO 2000* cameras with a remote tiltmount/focus and 200 mm lenses completed

the system. The images featured a resolution of 2048 x 2048 pixels. The grid refinement produced images of 32 x 32 pixels with an overlap of 50%. The laser light sheet was located perpendicular to the airfoil's surface where the flow was assumed to be parallel to the inflow. The light sheet was approx. 2mm thick and the flow was seeded with silicon oil droplets with an diameter of $d = 10 \cdot 10^{-6} m$. *ScotchCal* foil by *3M* minimized the reflection on the tab and the surface. Remaining reflections were further reduced by a background subtraction calculated of the average image of each measurement. No velocity data is available on the pressure side underneath the airfoil due to the shading of the model. A linear mapping was used for the calibration of the images .

6.1.2 Steady State Measurements

Steady state measurements were performed for different inflow angles. Surface pressure data was collected and the steady lift coefficients were generated. The drag coefficient was not determined since it was not the scope of this study. Aerodynamic coefficients for a passive micro-tab of various heights were calculated and further compared to the baseline values. Time averaged PIV measurements were carried out to gain insight on the flow structure behind the passive micro-tab.

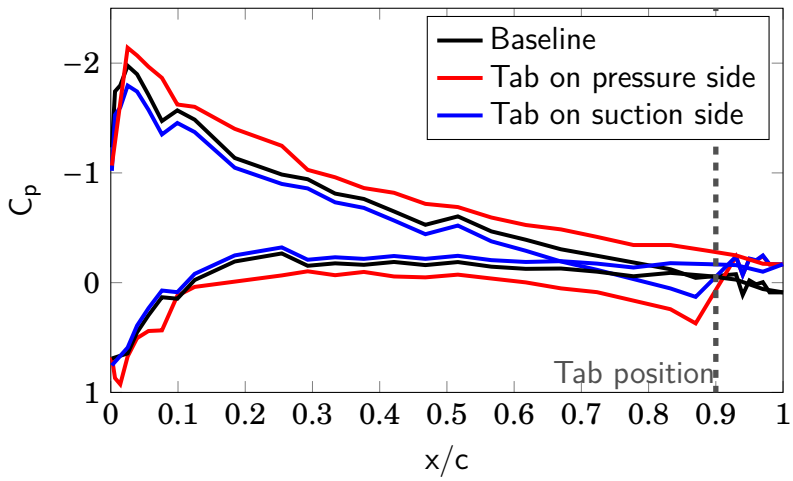

Figure 6.3: Steady pressure distribution ($|\alpha| = 7°$, $Re = 1 \cdot 10^6$)

Figure 6.3 depicts the pressure distribution C_p for the airfoil without tab and with a micro-tab of a height of $h_{tab}/c = 1.4\%$. Thereby, the tab was applied both on the suction and pressure side for an absolute angle of attack of $|\alpha| = 7°$.
An overall underestimation of the pressure is found for the airfoil without tab in comparison to distributions calculated by *XFOIL*. This is assumed to be due to the low aspect ratio of the airfoil model and the end-plates geometry, which have proven to have a strong effect on the pressure distributions [151, 115].
The pressure is altered along the entire chord by the presence of the micro-tab. If the tab is placed on the suction side, the overall pressure difference between the suction and the pressure

side is reduced. If the tab is placed on the pressure side, the effect on the pressure is opposite and the suction peak is more pronounced. Therefore, a reduction in lift is achieved for a tab placed on the suction side and lift enhancement for a tab placed on the pressure side. Furthermore, upstream of the micro-tab the surface pressure is building up at approx. $x/c = 85\%$. This build up is weaker if the tab is located on the suction side since the boundary layer is here thicker and the local flow around the tab has a smaller velocity. Consequently, the pressure build-up is less pronounced. Equivalent observations were made e.g. by Yen et al. [152].

Steady Loads

Steady lift and moment curves were generated from the pressure data for all micro-tab heights (see Figure 6.4). The red curve for the tab height of $h_{tab}/c = 1\%$ is emphasized because it is the final tab height for all the following transient results. It was found, that the higher the tab, the larger the produced differences in lift. For an angle of attack of $\alpha = 7\ ^\circ$ the tab on the suction side $(h_{tab}/c = 2.0\%)$ produced a maximal lift reduction of $|\Delta C_l| = 0.24$. Meanwhile, for an angle of attack $\alpha = -7\ ^\circ$ the equivalent tab placed on the pressure side gained a maximum lift enhancement of $|\Delta C_l| = +0.38$. If the angle of attack is increased, the boundary layer thickness on the suction side is increased until the onset of separation. This strongly affects the lift reduction and hence the tab's effectiveness. Therefore, if the angle of attack is increased, the lift reduction gained by a tab placement on the suction side is reduced.

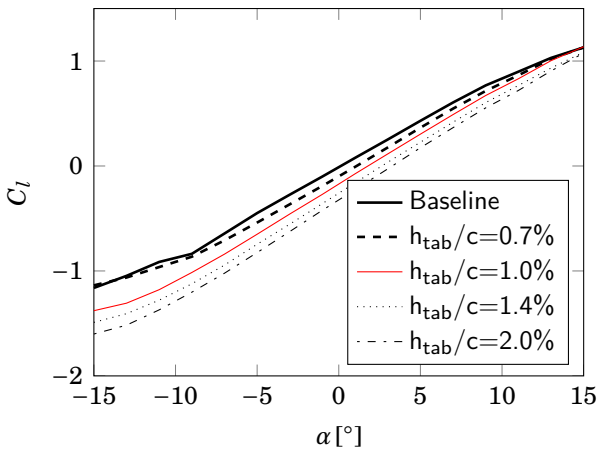

Figure 6.4: Lift curve for steady deployed tab $(Re = 1 \cdot 10^6)$

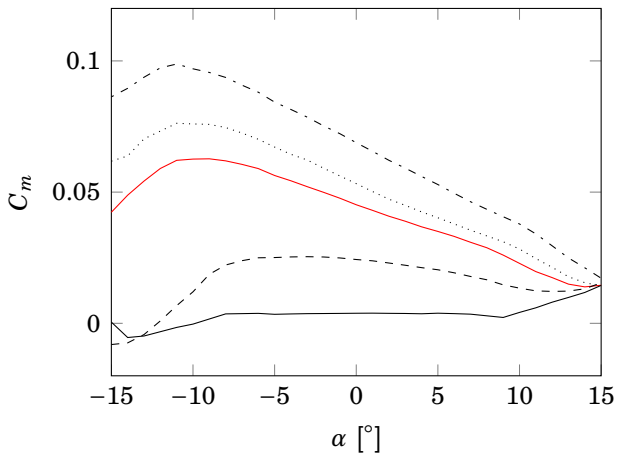

Figure 6.5: Moment curve for steady deployed tab $(Re = 1 \cdot 10^6)$

Along with the lift, the tab modifies the aerodynamic moment (see Figure 6.5). For a tab placement on the suction side $(\alpha > 0)$ the aerodynamic moment around the quarter chord is enlarged. However, in general a micro-tab or a Gurney flap causes the aerodynamic moment to decrease if placed on the pressure side of the airfoil, which is not the case in the shown plot. This is due to the sign notation, which was not changed for negative angles of attack. Therefore, it is more clearer and universal to say here that the tab on the pressure side causes an additional nose-down moment, meanwhile the suction side tab causes an additional nose-up

moment. This trend as well as the magnitude of the values for the suction and pressure side tabs are consistent with results found by Nakafuji et. al [100].
This simultaneous change lift and moment means that one can reduce fluctuating lift with such an active flow control device, however, at the same time an additional moment is created. In a three-dimensional geometry such as a wind turbine blade, the change of lift inflicts a flapwise root bending moment, which is more consequential for the blade structure than an additional torsion moment caused by the aerodynamic moment.

Time-Averaged Flow Field

PIV measurements were performed for the Reynolds number of $Re = 1 \cdot 10^6$ and for a tab located on the suction side ($\alpha = 7°$). The time-averaged flow field behind the tab was calculated for the tab heights $h_{tab}/c = 0.4\%$, 1.0% ,1.4% and 2.0%. In Figure 6.6 - 6.9 the average velocity field is shown. The region underneath the profile lay in the shadow, since the laser sheet originated form above; hence, no data could be gained within this region. It can be seen that the size of the recirculation zone behind the tab is enlarged with the tab height. Two characteristic points in the flow field are further highlighted: The point of the maximum upwash $(x := w/U_\infty)_{max}$ and the point of the minimum vorticity $o := \omega_{min}$ of the recirculation zone. The minimum vorticity (or maximum absolute vorticity) is the vorticity induced by the shear layer which collides with the tab. Hence, the minimum is positioned right behind the tab on the left side of the window of the PIV measurements. When the tab is deployed higher, the maximum induced upwash is found larger. As a result the free stream stagnation point is shifted further away and upward with respect to the trailing edge (not shown here). Therefore, the higher the tab on the suction side extends, the more upward the wake shifts. Simultaneously, the recirculation zone behind the tab increases in size and vorticity. As a result, the flow is decamberized more if the tab is larger and the lift is reduced.

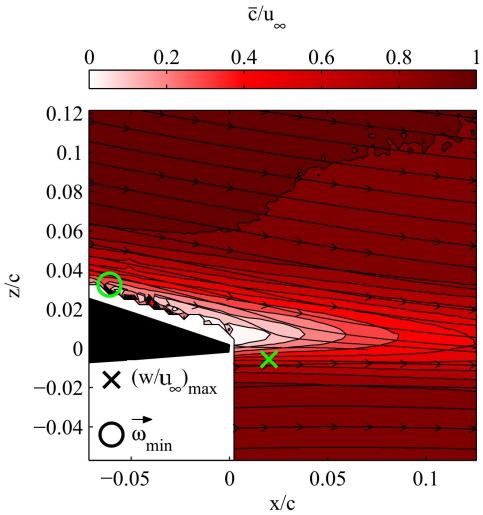

Figure 6.6: Averaged flowfield behind the tab ($h_{tab}/c = 0.4\%$, SS)

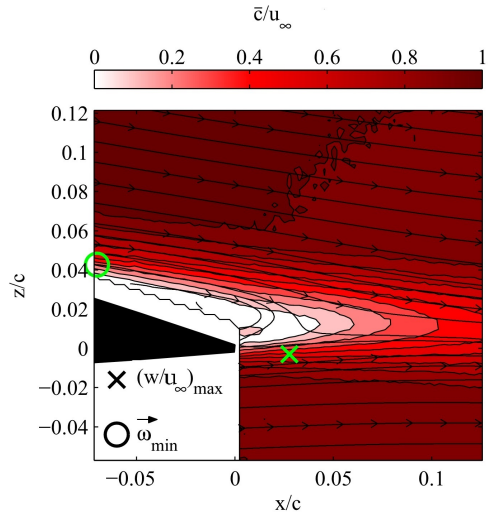

Figure 6.7: Averaged flowfield behind the tab ($h_{tab}/c = 1.0\%$, SS)

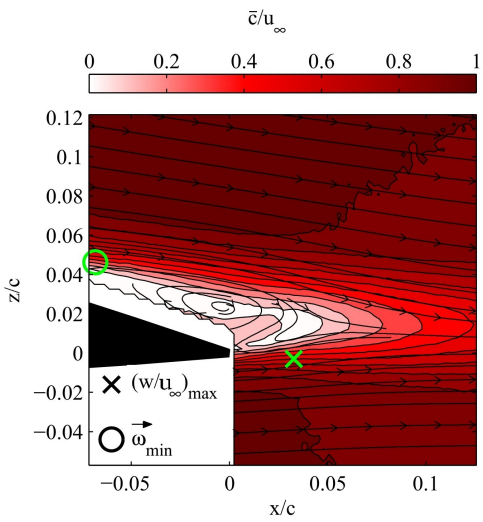

Figure 6.8: Averaged flowfield behind the tab ($h_{tab}/c = 1.4\%$, SS)

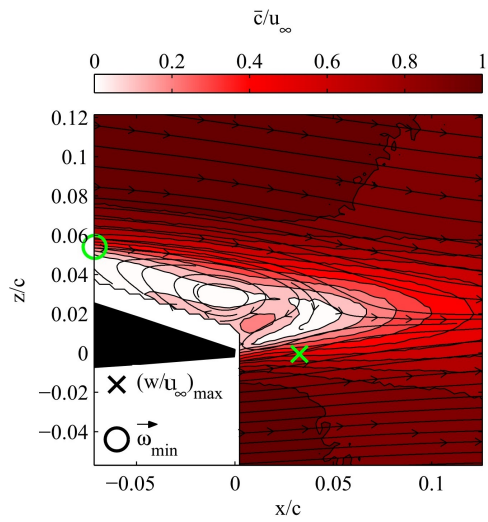

Figure 6.9: Averaged flowfield behind the tab ($h_{tab}/c = 2.0\%$, SS)

6.1.3 Unsteady Measurements

.5Transient responses of the surface pressure were measured for several configurations. Instantaneous pressure changes downstream of the tab were recorded for both the deployment and retraction process. Time-dependent negative pressure peaks indicated the presence of a convecting vortex downstream of the active micro-tab. During the investigations, the angle of attack as well as the actuation time T_{act} of the active micro-tab were varied. The data was acquired only for single deployment and retraction processes without investigating a continuous actuation. Results of the transient lift responses are displayed as functions of the non-dimensional characteristic time $t^* = t \cdot U_\infty / c$. Using this time-scale is advantageous because the change of lift can be related directly to one convective time unit of the surrounding flow which makes a comparison to other applications easier. The time-dependent drag coefficient was not determined since it was not the scope of this study.

Transient Pressure Response

The transient pressure distribution along the airfoil's chord was recorded during the tab deployment. Thereby, the time scale started together with the first tab movement. Figure 6.10 depicts the pressure evolution during a deployment process. The deployment time was $T^*_{dep} = 3.15$ and the angle of attack $\alpha = 7°$. The four sub-figures illustrate the distributions at the characteristic times $t^* = 1/3$, $2/3$, $3/3$ and $4/3 T^*_{act}$. The pressure changes along the whole chord along the tab deployment. After an initial pressure build-up in front

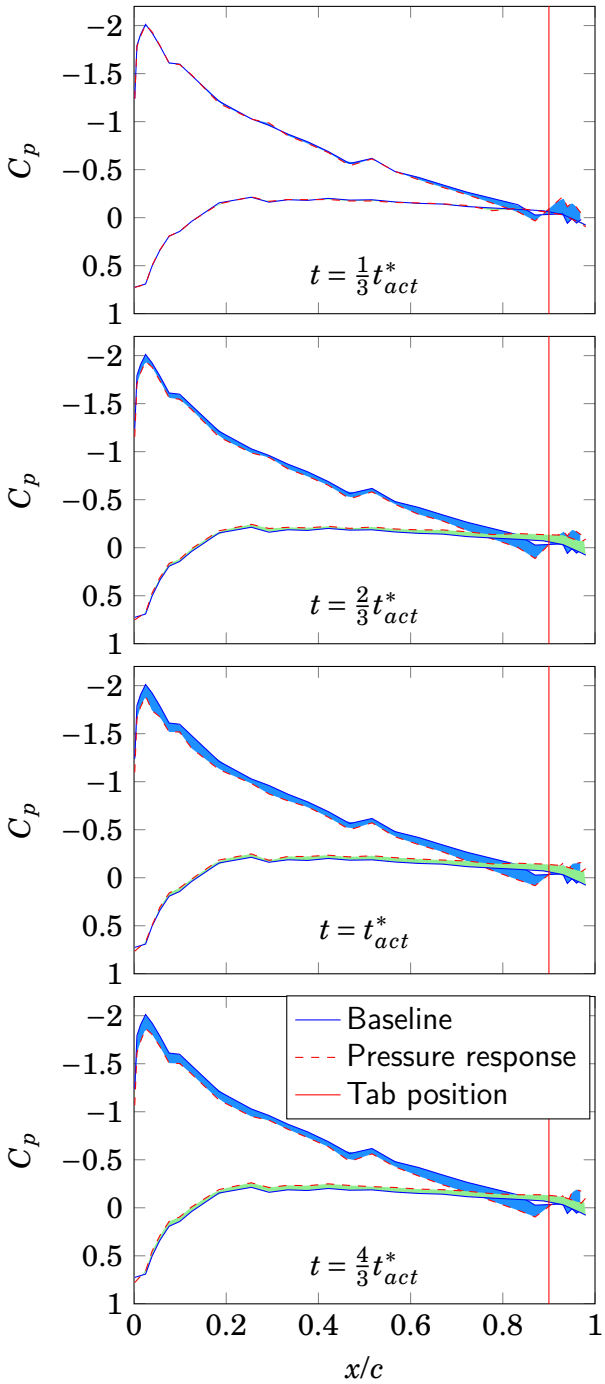

Figure 6.10: Pressure response during tab deployment ($T^*_{dep} = 3.15$, $Re = 1 \cdot 10^6$)

of the flap, the pressure level in this region is found constant after at least $t^* = 2/3T^*_{act}$.

Transients Dependent on Actuation Time

Various deployment times were tested to analyse the dynamics of the convecting vortex. The angle of attack was chosen to be $|\alpha| = 7°$ for a tab located on the pressure side. It was found that the shorter the deployment times, the faster the responses of the lift: At the same time the slope of the transient lift curve increased. It can be observed in Figures 6.11 and 6.12 that for slow actuation times the lift and the moment are more or less changing gradually along with the tab movement. However, if the tab deployed faster the airfoil's aerodynamics are not fully adapted when the tab comes to a stop and a change in lift and moment is evident even after the tab stopped moving. This post-deployment adaptation lasted at least over six characteristic time lengths for the shortest deployment time. This time is significantly longer than the vortex convection time and hence the transient lift is not dependent on the near tab behaviour but moreover dependent on the gradual global change in the circulation of the flow around the airfoil.

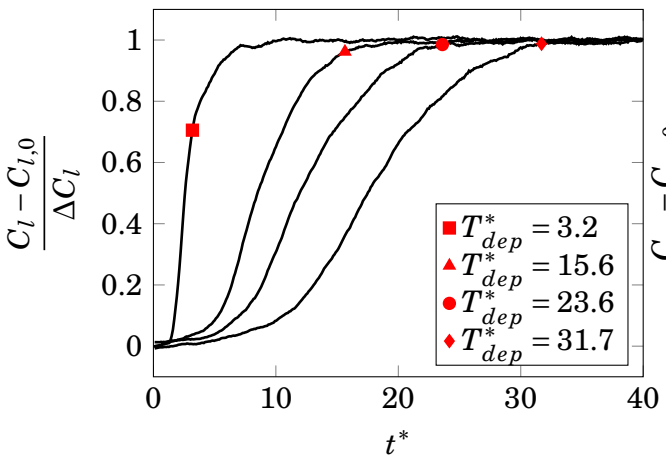

Figure 6.11: Standardised lift response to tab deployment for various actuation times ($\alpha = -7°$)

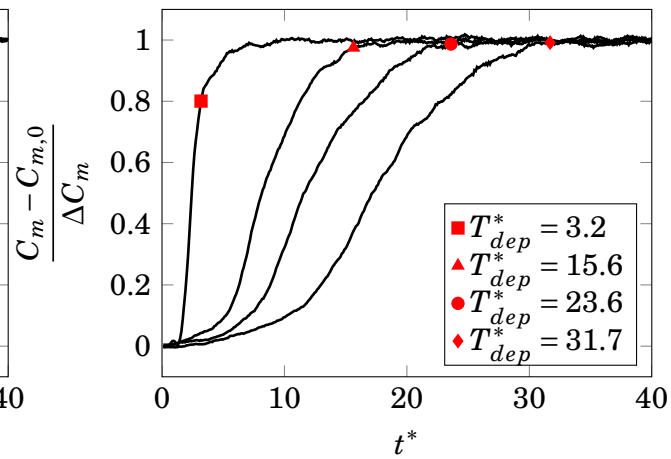

Figure 6.12: Standardised moment response to tab deployment for various actuation times ($\alpha = -7°$)

Additional tests were conducted to evaluate the tab retraction process and its aerodynamic transients. The transient performance of the retraction proved to have a behaviour similar to the tab deployment, however some differences remained. Figure 6.13 illustrates the absolute lift response of the deployment and retraction for the case of the actuation on the suction side with $T_{dep} = 0.2s$ and an angle of attack of $\alpha = 7°$. The two responses show a clear delay of the lift of the retraction process, even though the actual decay is quite similar. The different delay was also noted in some other experimental studies [7, 10, 102]. This difference can be explained by the convecting recirculation zone formed in front of the tab as well as the convection of the vortex street from the near to the far wake.

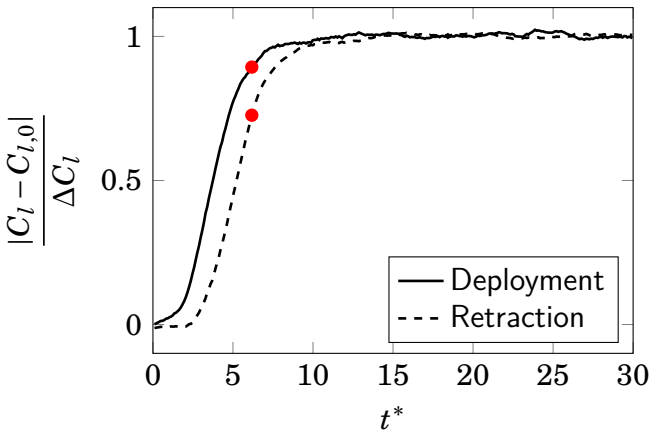

Figure 6.13: Standardised lift response of deployment and retraction ($\alpha = 7°$, $T^*_{dep} = 6.21$)

For an angle of attack of $\alpha = -7°$ different actuation times were evaluated and a time response delay T^*_{delay} and lift overshoot were calculated out of the lift response. This response delay time was defined as the time after which 10% of the overall lift difference ΔC_l is reached. The lift overshoot $C_{l,overshoot}$ was generated as the maximum adverse lift produced during the actuation. Figure 6.16 summarizes these values for all tested deployment times. It can be seen that the lift responses are slower (T^*_{delay} is larger) when the actuation time is longer. Furthermore, the lift response of a retracting tab clearly reacts slower than the equivalent deployment process. For nearly all deployment times there was not any adverse lift overshoot observed. Only for the fastest deployment process a very small overshoot is found while the retraction process did not show any overshoot.

Transients Dependent on Angle of Attack

The steady state result showed that the effect of micro-tabs placed on the pressure side is more pronounced than for a placement on the suction side. This was explained with the thicker boundary layer on the suction side. To understand if this has a further effect on the transient behaviour, the same deployment process was tested under various angles of attack. The deployment time was chosen to be $T^*_{dep} = 15.65$. The lift responses are shown in Figure 6.14 whereas Fig. 6.15 illustrates the moment responses due to the deployment process. At a time of $t^* = 0$ the tab movement started together with the measurements. The red marker found in the plots depict the end of the tab movement. The lift and moment values obtained before and after the tab actuation are consistent with the steady state values. As indicated by the steady state results, the total lift difference is more pronounced on the pressure side resulting in a steeper slope of the transient responses. Furthermore, the lift values for the undeployed tab at the start of the tab movement are slightly lower for the pressure side than for the suction side. However, this is caused by the manufacturing of the airfoil and the physical presence of

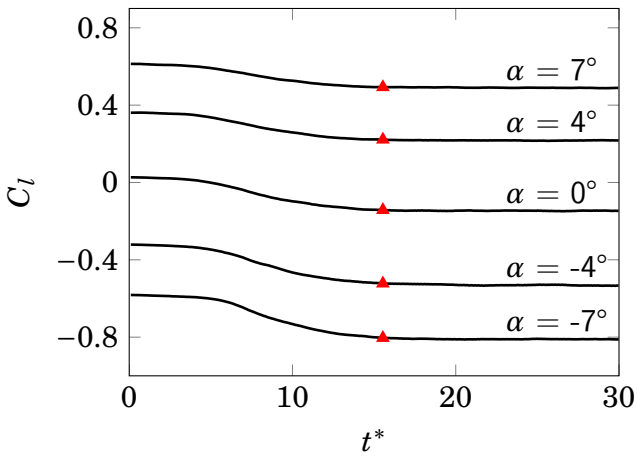

Figure 6.14: Lift response to tab deployment for various angles of attack ($T^*_{dep} = 15.65$)

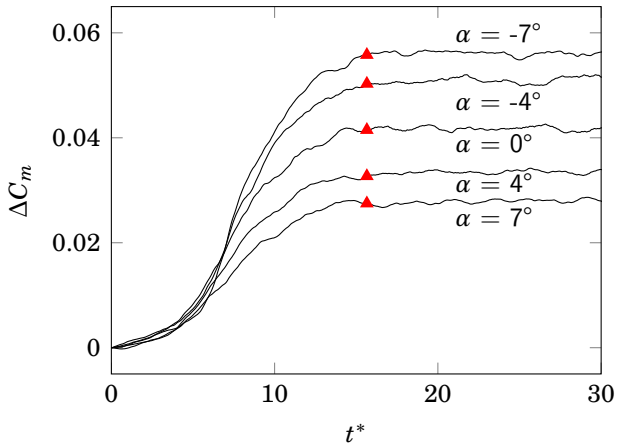

Figure 6.15: Moment response to tab deployment for various angles of attack ($T^*_{dep} = 15.65$)

the slot of the still retracted micro-tab.

For a deployment on the pressure side ($\alpha < 0$) the total change of lift ΔC_l increased and the slope of the transient is steeper. This can be explained by a thinner boundary layer of the pressure side than on the suction side. On the suction side the boundary layer thickness is increasing for higher angles of incidence. Therefore, the achieved lift reduction ΔC_l is smaller and the slope of the transient lift from one level to the other is less steep than for an application on the pressure side. For all angles of attack, the change of lift was found to occur only after a certain period of time. Before that time it mainly remained constant which can be explained by the convection of a vortex due to the tab deployment. Since the vortex induces an adverse effect on the lift one can see a delay in the lift response.
This delay can also be seen in the response of the aerodynamic moment in Figure 6.15. Furthermore, the effect of the angle of attack is clearly seen in the moment difference ΔC_m. These moment differences are consistent with the steady state results and are caused due to the different boundary layer thickness. It is noted that the time which is needed to reach the final moment value is again not affected by the angle of attack.

In earlier tests the overshoot has shown to be stronger for faster deployment times. For the fastest deployment time, the dependency of this overshoot on the angle of attack was analyzed. For a deployment and retraction time of $T^*_{act} = 2.1$ the overshoot as well as the response delay was generated.
Figure 6.17 illustrates that the time delay T^*_{delay} dependency on the angle of attack is in fact negligible. However, the lift overshoot formed in the deployment process of the tab was found to be less pronounced for higher angles of attack (see Figure 6.17). Hence, a tab placed on the suction side yields a lower overshoot at higher angles of attack, and a tab on the pressure side reacts with a stronger overshoot with rising absolute angles of attack. This effect may be explained again with the difference in the boundary layer thickness depending on the angle of

attack: On the suction side the boundary layer thickness is larger for higher angles of attack. Consequently, the tab is emerged in fluid with a smaller local velocity, and as a result the vortex is smaller in strength. Therefore, the convecting vortex induces a smaller overshoot on the lift. On the pressure side the opposite effect can be seen: The boundary layer is less thick with an increasing angle of attack and thus the tab experiences a higher local velocity and the vortex and the overshoot become stronger. However, this was only the case during the tab's deployment. For the retraction process no clear overshoot could be identified.

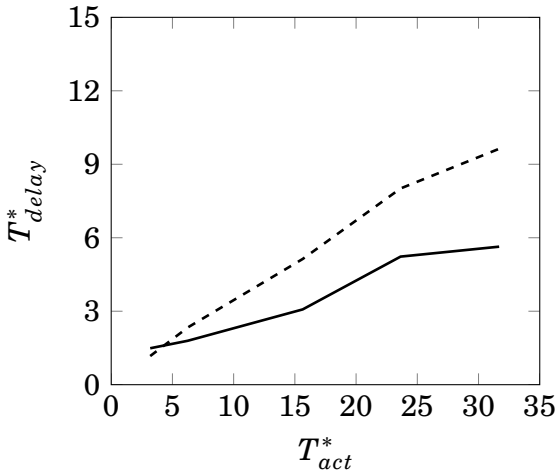

Figure 6.16: Lift response dependent on actuation time

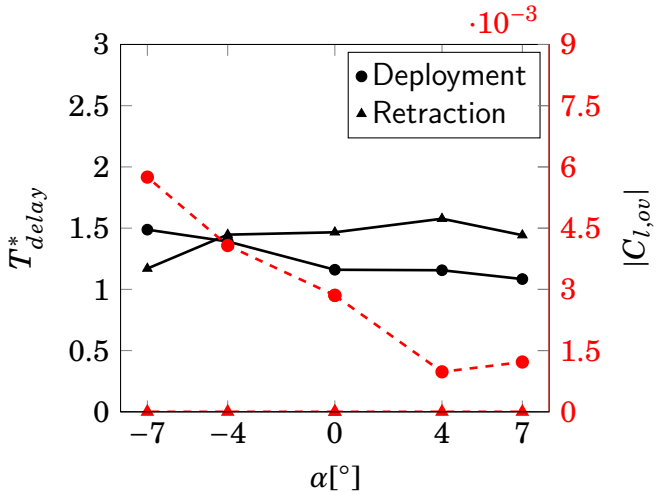

Figure 6.17: Lift response dependent on angle of attack

6.1.4 Comparison to Other Studies

In earlier numerical simulations Chow et al. [30] and van Dam et al. [135] conducted comparable test cases with an airfoil under fixed angle of attacks and a deploying tab. They were able to observe that the lift response for deployment times under $T^* < 2$ consisted of instantaneous adverse lift overshoots right at the beginning of the deployment. They showed in the CFD flow field, that this is due to build-up and convection of the vortex over the remaining surface behind the tab. The vortex then causes an instantaneous adverse lift response, when the deployment time of the tab is very fast.

For a comparison to this work, the time delay of the response and the lift overshoot were extracted from the published data of van Dam et al. [135] and Chow et al. [30]. The actuation time showed the same trends in all measurements (see Figure 6.18): The faster the deployment was, the faster the lift responded. Hereby, the gained data from all campaigns only differ slightly in the slope which might be caused by the influence of the airfoil geometry. Thereby, the data by van Dam is very close to the data gained in this study, which may be due to the similar airfoil shapes employed: Van Dam used a NACA 0012 for the simulations, which is very close in its

shape to the NACA 0018 employed in this study [135]. Furthermore, all splines of the different campaigns do not cross the axis at the point zero but slightly above. This implies, that even for a tab ramp deployment, a response delay will remain. In comparison, the overshoot was found to be more pronounced for the actuation time tested by van Dam et al. and Chow et al.. Therefore it can be concluded, that the overshoot starts to play a non-negligible role for deployment times under $T^*_{act} < 2$.
The dependency on the angle of attack was further compared to the data of Chow et al. in Figure 6.19. While van Dam only simulated for one angle of attack, Chow et al. tested three different angles with a tab deploying to the pressure side with $T^*_{dep} = 1$. The highest overshoot was found for the highest angle which confirms the general trend observed in this test.

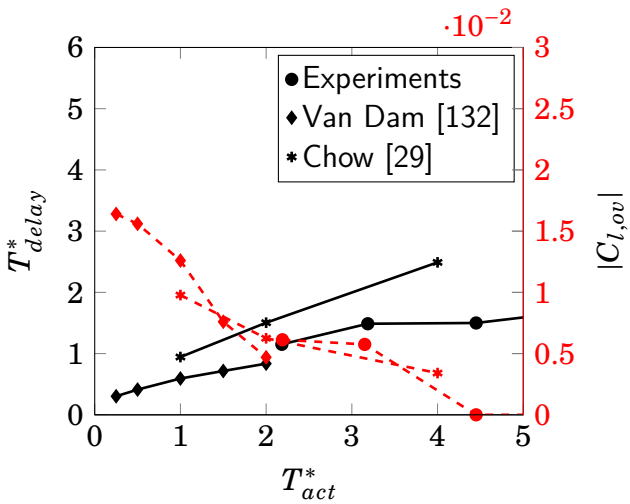

Figure 6.18: Lift response as a function of actuation time in the literature

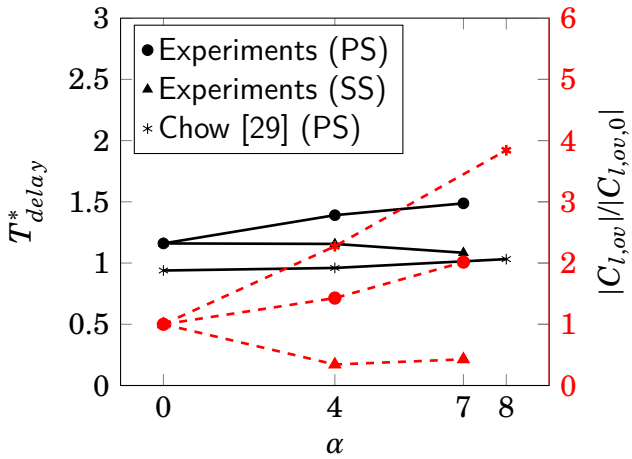

Figure 6.19: Lift response as a function of the angle of attack in the literature

6.1.5 Micro-Tabs Combined with Vortex Generators

Even though micro-tabs have proven to be a fast and effective means to alter fatigue loads, inflow changes inflicting high angles of attack cannot be counteracted. This is due to the tab on the suction side losing its effectiveness at high angles of attack which reduces the load reduction potential. Hence, loads e.g caused by gusts cannot be reduced. A gust is generally associated with higher velocities combined with higher inflow angles of attack. This shortcoming may be by remedied by combining the tabs or flaps with additional stall delay devices such as vortex generators (VGs). A stall delaying device which has the ability to reduce the boundary layer thickness will counteract the effect of the micro-tabs losing their effectiveness at high angles of attack. Additional fluid momentum is carried by the streamwise vortices of the VGs from the freestream close to the surface. This process energises the fluid and ensures the prolongation of an attached boundary layer at the trailing edge when high angles of incidence occur [97]. Stereo Particle Image Velocimetry (PIV) measurements were performed to study the effect of additional

VGs on the micro-tabs and the vortex system. For the measurements an angle of $\alpha = 15°$ was chosen. The laser sheet was placed at the centre of a vortex generator which generated counter-rotating vortices. The height of the VGs was set to $h_{VG} = 10mm$ and the spacing was chosen according to the findings of Vahl et al. [97] to $Z_{VG} = 3h_{VG}$ (compare Figure 3.2).
Figure 6.20 shows the vorticity field of the baseline airfoil, averaged over a minimum of 800 double PIV images. The vorticity of the shear layer on the suction side can be seen as well as the onset of separation at the trailing edge. When VGs were applied, the shear layer was closer to the surface with no trace of separation (see Figure 6.21).
To both flow fields the micro-tab was deployed to a height of $h_{tab}/c = 2\%$ and the average flow field behind the steady deployed tab was evaluated. Figure 6.22 depicts the vortex system for behind the tab without VGs, meanwhile Figure 6.23 illustrates the flow field for the case of combined VGs and micro-tabs. In both figures, the downstream vortex as well as the upstream vortex of the tab can be seen in the streamlines. Even though, the center of the vortex according to the streamlines implies, that the vortex centre is at the same location for both cases, the overall vortex strength is greater if VGs are applied. The maximum vorticity of the downstream vortex is found to be $|(\omega c)/U_\infty| = 1.008$ for the configuration without VGs. If VGs are employed, the vortex strength is higher: $|(\omega c)/U_\infty| = 1.875$. Meanwhile, the normalized maximum upwash for the airfoil with micro-tabs is $w/U_\infty = 0.027$, which is lower than for the case with additional VGs, where $w/U_\infty = 0.083$. At the same time, the position of the maximum upwash is shifted closer to the trailing edge when VGs are present.

For the configuration with vortex generators no time-dependent pressure measurements were performed, due to the three dimensional behaviour of the flow field with VGs. However, from the upwash data it can be said that the effect of the micro-tabs with VGs is stronger than without and more lift difference can be expected for this angle of attack. Furthermore, it is known that the time response of the tab strongly depends on the boundary layer of the airfoil. Since the VGs significantly reduce the shear layer thickness, one can suspect that the overshoot will now be more pronounced than it would be the case without VGs. At the same time, a greater overall lift difference ΔC_l will be obtained even for high angles of attack.

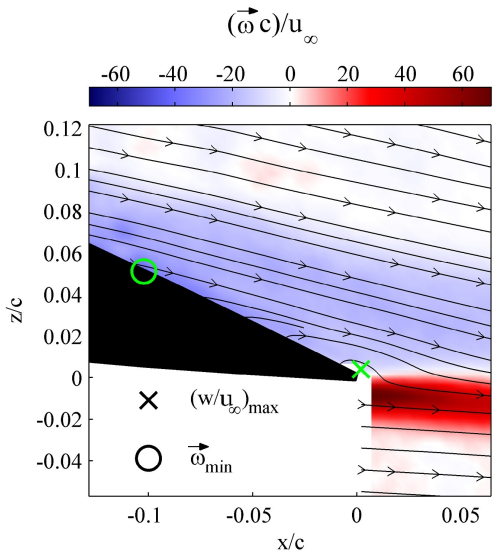

Figure 6.20: Vorticity field of the baseline airfoil

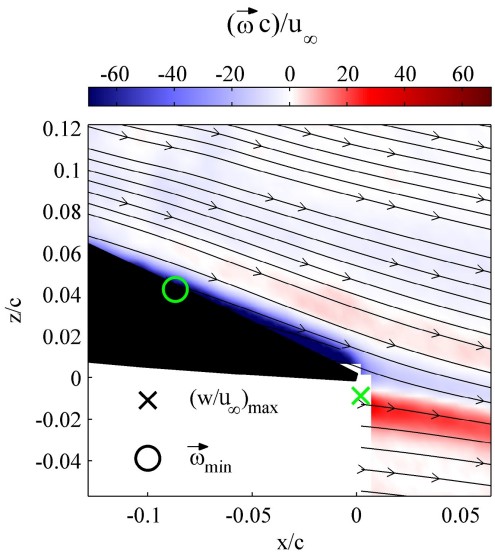

Figure 6.21: Vorticity field of the airfoil with VGs

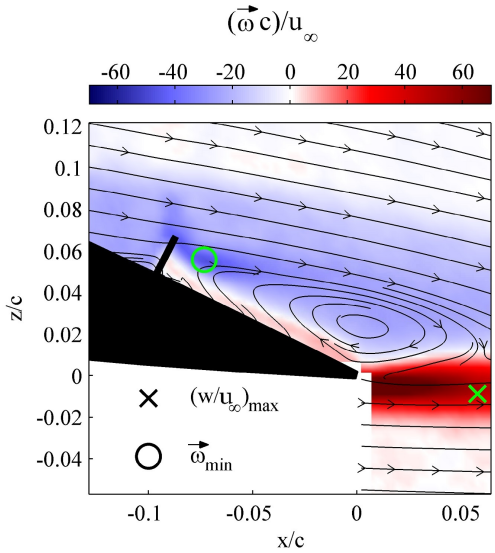

Figure 6.22: Vorticity field with a single micro-tab

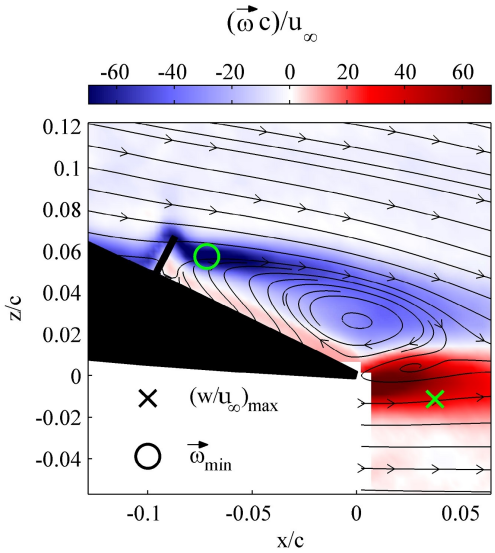

Figure 6.23: Vorticity field with VGs and micro-tab

6.1.6 Actuation Times on Wind Turbines

Fatigue loads along the turbine blade may be encountered with span-wise distributed active micro-tabs at the mid and outer blade regions. For the control of these loads various time scales need to be applied, depending on the wind turbine size, the inflow velocity and disturbance as well as the span-wise placement. Disturbances caused by the earth's boundary layer or by yaw misalignment occur once per revolution and gradually change the lift during one revolution [40] [37]. Hence, to alleviate these loads, the active micro-tabs only demand relatively slow actuation times and the time delay of the response in lift has a minor impact. However, when it comes to faster lift changes caused by passing the tower or gusts the micro-tab needs to actuate at faster time scales. Therefore, the delay of the active micro-tab as well as the response times have to be incorporated in the control sequence. Furthermore, a good sensor for the incoming flow disturbance is needed, so that the micro-tab control system can react beforehand while taking the initial time delay into account. Realistic time scales from wind turbines can be compared with experiments using the characteristic time t^*. For example, the investigated actuation times presented within this work correspond to actuation times between 0.014s $< T_{act} <$ 0.14s on an outer rotor section with a chord length of $c = 0.5m$ and a speed of the incoming flow of $U_\infty =$ 75m/s. However, the lift adjustment process took a minimum time of $t^* = 6$ which corresponds to $T = 0.04$s on the wind turbine.

6.2 Active Finite Flap

Measurements on an FX 63 -137 airfoil with an active Gurney flap were conducted in a wind tunnel to investigate the time-dependent behaviour of two-dimensional as well as finite flaps. The time-dependent pressure response of the deploying flaps was evaluated locally over the airfoils surface and the span-wise time-dependent lift was evaluated. Results have shown that the lift response behaves differently for a flap deployment than for a flap retraction where the convergence generally takes longer. Furthermore, the adjacent flap sections of the finite flap have shown to also experience a dynamic lift change. This response is different from the response in front of the flap which is due to the influence of the surface pressure expansion around the finite flap as well as the flap tip vortices. The measurements have shown that the time-dependent lift in the adjacent sections do play a relevant role in the overall lift response of the wing. In this section, the results for the time-dependent pressure distribution over the airfoil as well as the resulting lift are presented.[2]

6.2.1 Measurement Set-up

The measurement set-up used is identical to the one described in Section 5.3.1 for the passive finite flaps. In this investigation, the set-up was expanded to include moving active flaps.

[2]Some results presented in this section were previously published by Bach et al. in [7] and [10]. For the first paper, co-author and Bachelor student R. Berg performed part of the pressure measurements and analysis for the first paper under the guidance of the author. All other tasks were carried out by the author.

Experiments were conducted with a full-span Gurney flap as well as a finite Gurney flap which was centred at the wing's trailing edge with a span-wise length of $l_{flap} = c/2$. The flap could be deflected to a maximum of $\theta = +70°$ to the pressure side and a minimum of $\theta = -110°$ to the suction side. The actuation times of the flap as well as the lift response times are presented in a dimensionless time. Using this time-scale is advantageous because the change of lift can be related directly to one convective time unit of the surrounding flow which makes a comparison with other applications and inflow conditions easier. Within these experiments two actuation times were tested: A maximal deployment or retraction time of $T^*_{dep} = T_{dep} * U_\infty/c = 7$ as well as a slower time of $T^*_{dep} = 70$. The dynamic measurements were repeated and averaged over 10 separate measurements. The number of repeated dynamic measurements were determined by a sensitivity study. Furthermore, a Savitzky-Godoy filter [103] was used to smooth the time-dependent data.

6.2.2 Full-Span Flap

Pressure Distribution

The pressure distribution over the time was measured during a deployment of the full-span Gurney flap. Figure 6.24 depicts the development of the surface pressure along the chord at four different dimensionless times: $1/3T^*_{dep}$, $2/3T^*_{dep}$, $3/3T^*_{dep}$ and T^*_∞. The deployment time was $T^*_{dep} = 7$. Again, the pressure close to the trailing edge (marked in green) is extrapolated from closest the measured ports. It can be seen that even though the Gurney flap locally induces a geometrical change at the trailing edge, the pressure distribution along the whole span and chord is affected simultaneously over time. Furthermore, the slight forward movement of the boundary layer transition location is noted. It can be seen that when the tab is fully deployed ($t^* = T^*_{dep}$), the surface pressure distribution does not experience further changes but has already reached the final values.

Lift Response

From the time-dependent pressure values the lift over time was calculated. Figure 6.25 illustrates the corresponding dimensionless lift response $C^*_l = |\Delta C_l(t)| \ / \ |\Delta C_l|_{max}$ and the dimensionless flap position $\theta^* = |\theta(t)| \ / \ \theta_{max/min}$ over time. Three rows of chordwise pressure measurements are presented, thereby row 4 represents the symmetry line of the airfoil. It can be seen that the lift almost immediately reacts to the flap movement and starts to rise. Furthermore, at $t^* = T^*_{dep}$ the lift has nearly reached the final steady state value, which was seen accordingly in the pressure distribution before. The same behaviour was found for the dimensionless deployment time of $T^*_{dep} = 7$ calculated by a different Reynolds number of Re=140 000 (not shown here). This context was reproduced for the retraction process where the two curves for the two Reynolds numbers were still found to be nearly identical.

The lift response for the retraction process was found to differ from the deployment process

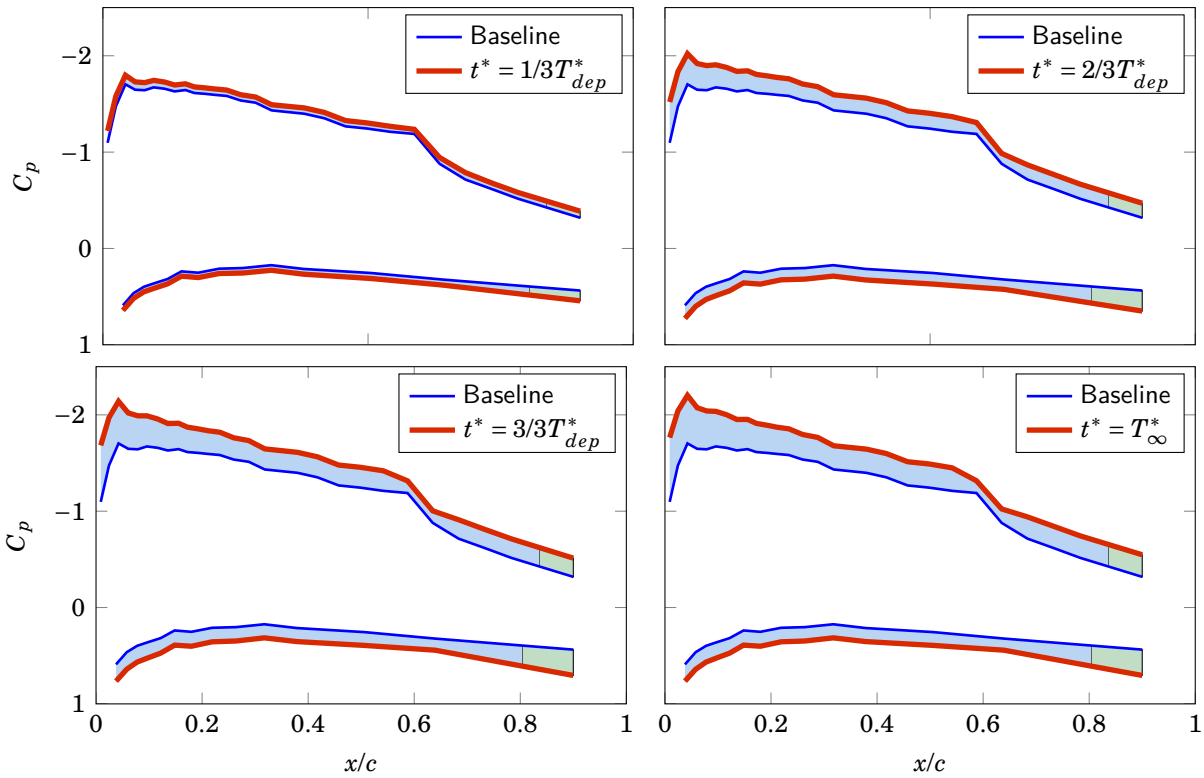

Figure 6.24: Development of the pressure distribution over time for the full-span flap deflected to the pressure side ($T^*_{dep} = 7$)

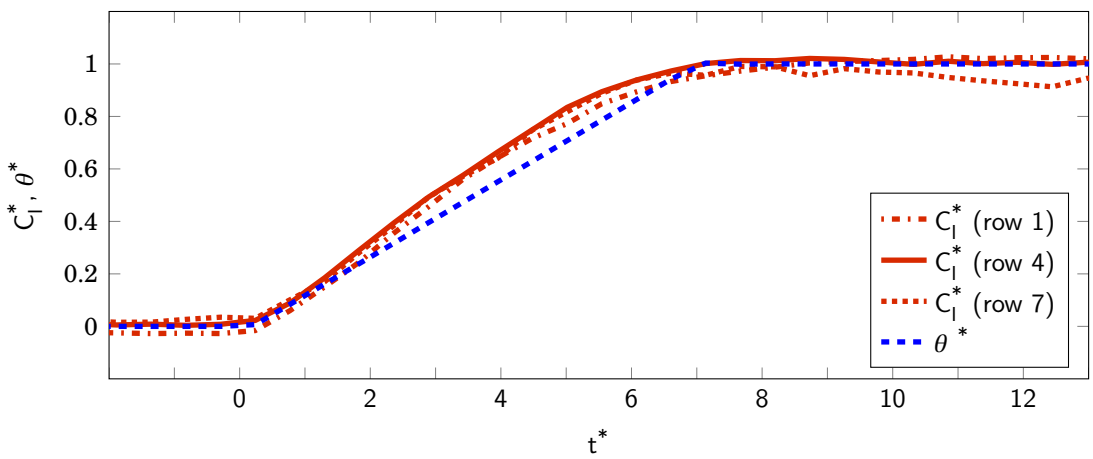

Figure 6.25: Lift response for flap deployment to pressure side ($T^*_{dep} = 7$)

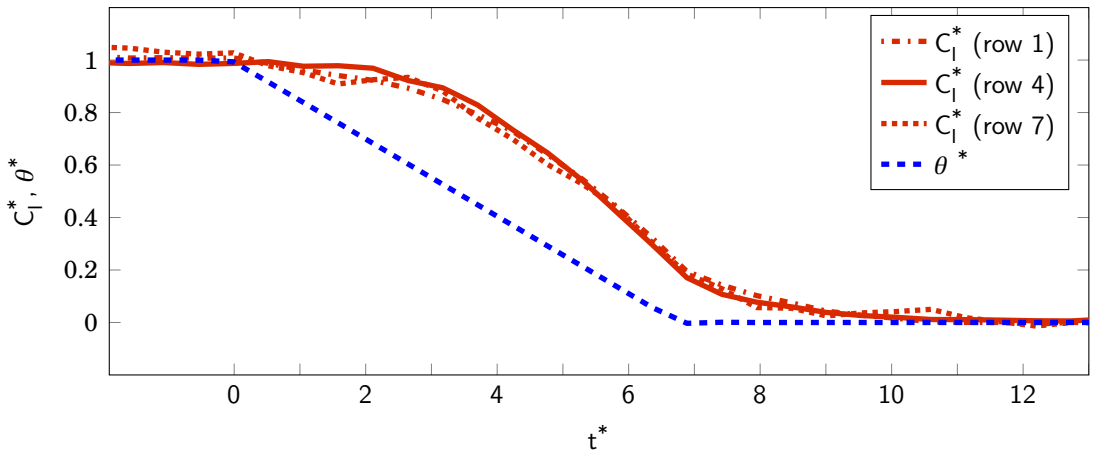

Figure 6.26: Lift response for flap retraction from pressure side $(T^*_{ret} = 7)$

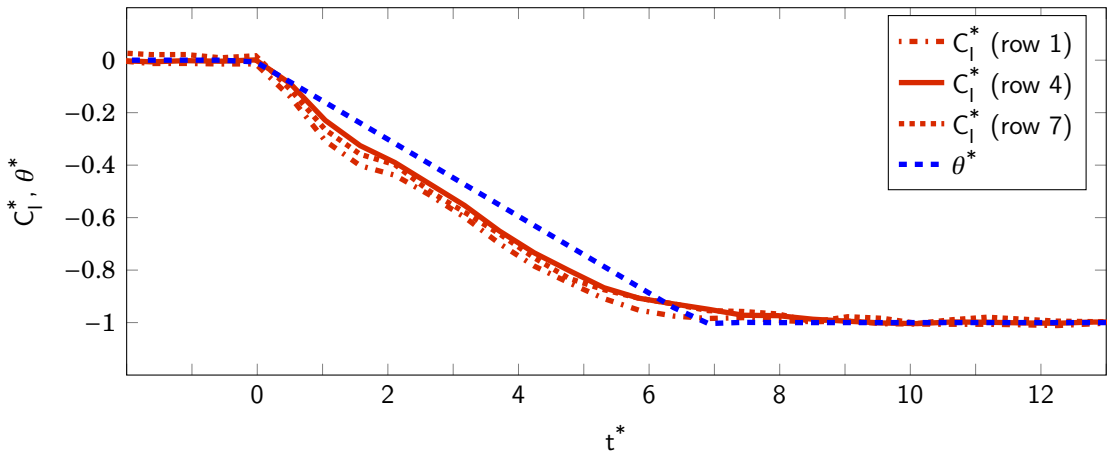

Figure 6.27: Lift response for flap deployment to suction side $(T^*_{dep} = 7)$

(see Figure 6.26). The lift responded more slowly during the retraction and reacted at least one dimensionless time unit $t^* = 1$ after the flap started to move. This goes along with the finding of the delayed response due to the retraction case of the micro-tab on the NACA 0018 presented in Section 6.1.3. Again, it is assumed that this difference is caused by the presence of the convecting vortex street from the near wake to the far wake.

Next to the fact of the delayed response, one can recognize in the lift curve the time $t^* = 7$ when the flap stops to move since it has reached its final position. This behaviour can be attributed to the flap motor, which slightly overshot its designated final position and readjusted its position afterward. Therefore, the lift delay of the lift adjustment between $7 < t^* < 10$ might be caused by the motor set-up and is not part of the plain aerodynamic response.
If the flap was actuated towards the suction side in an attempt to reduce lift, the lift responses were found to be different. In Figure 6.27 the lift response for the deployment is shown. Figure

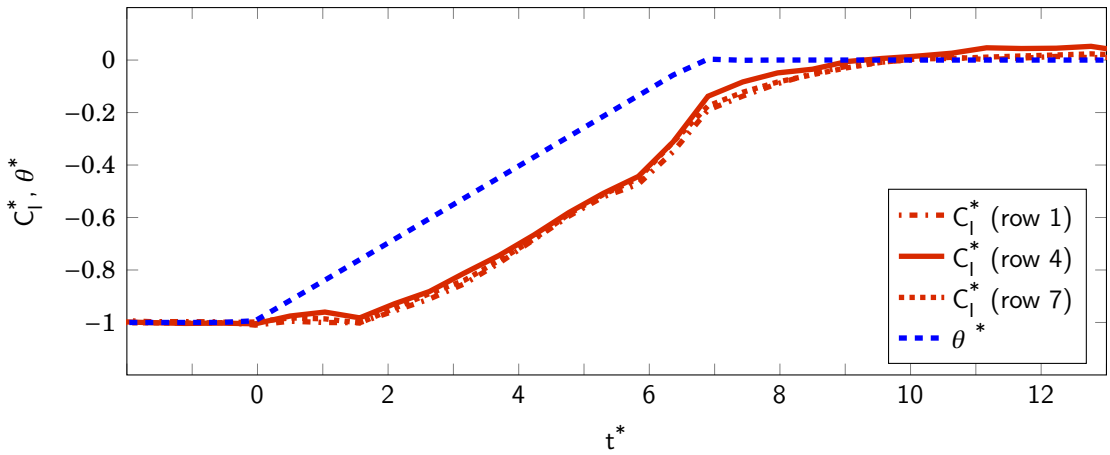

Figure 6.28: Lift response for flap retraction from suction side ($T^*_{ret} = 7$)

6.28 depicts the response for the retraction. Due to the flap deployment on the suction side, the lift is reduced. However, the function does look completely different than the lift reducing response of the flap retraction on the pressure side as seen in Figure 6.26. Here, for the deployment to the suction side, the lift reacts rapidly again after the flap started to move at $t^* = 0$. The reaction is more prompt than for the deployment on the pressure side but converges similar towards the end of the flap movement.

6.2.3 Finite Flap

The pressure and lift response of the finite central-span flap was analysed. The same deployment and retraction times as for the full-span flap were used and compared. Special attention was paid to the lift response in the adjacent sections on the airfoil next to the finite flap.

Pressure Distribution

For the flap deploying to the pressure side for lift enhancement, Figure 6.29 and Figure 6.30 depict the dimensionless surface pressure distribution $C_p^* = (|C_p(t)| - |C_{p,Base}|) \,/\, |C_{p,Base}|$ at a specific times during the deployment: $t^* = 1/3T^*_{dep}$, $t^* = 2/3T^*_{dep}$, $t^* = T^*_{dep}$ and $t^* = T^*_{\infty}$. Thereby, the four plots of Figure 6.29 show the pressure side and the four plots of Figure 6.29 show the suction side distributions for the same deployment process. The flap was placed between $0.3 < y/b < 0.7$ and is indicated as a rectangle at the top of each plot. The dotted line at $x/c = 0.8$ represents the line where the pressure values were interpolated.
On the pressure side, one can see that the pressure builds up gradually in front of the flap close to the trailing edge (Figure 6.30). This pressure build-up is even visible adjacent to the flap. However, the effect of the flap is visible next to the flap in the adjacent flap sections. On the suction side, the fluid experiences an acceleration close to the trailing edge. This effect is broader than on the pressure side and detectable over the whole span.
Hence, the finite flap influences the pressure in the adjacent section most likely due to the

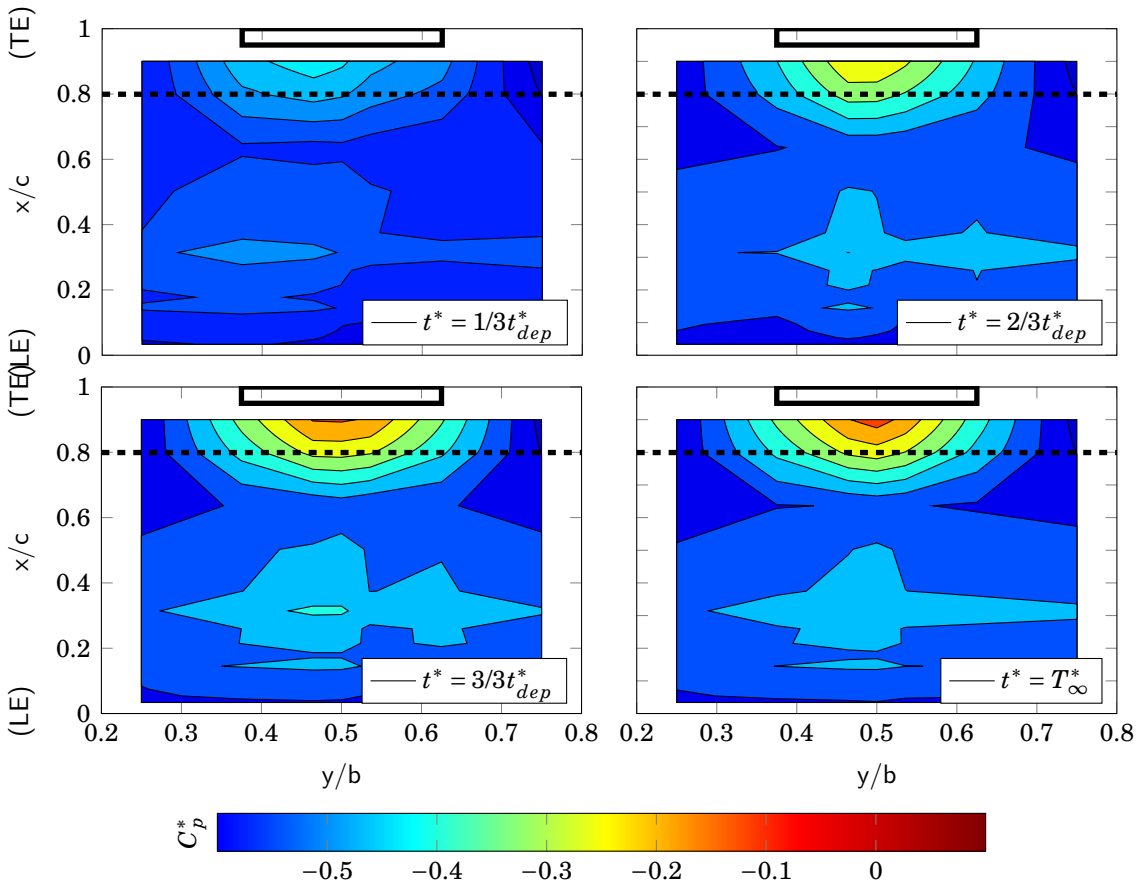

Figure 6.29: Surface pressure on the airfoils pressure side for the flap defecting to the pressure side ($T^*_{dep} = 7$)

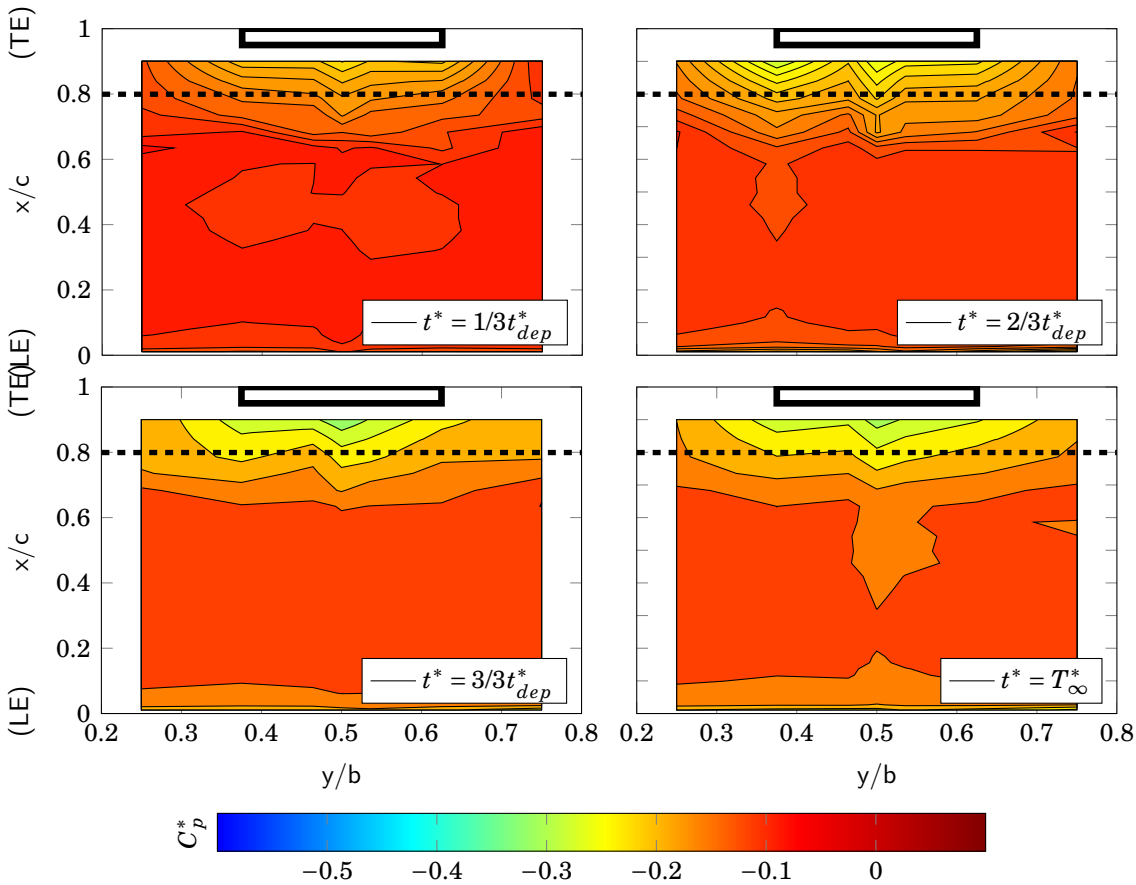

Figure 6.30: Surface pressure on the airfoil's suction side for the flap defecting to the pressure side $(T^*_{dep} = 7)$

pressure adjustment between the different pressure levels in front of the flap and the adjacent sections. Therefore, the time-dependent response in the adjacent sections should be in the same time range then the responses in front of the flap. An additional effect is certainly caused by the flap tip vortices which induce local velocities on the airfoil.

Lift Response

The span-wise lift response is gained from the surface pressure distributions. The left plot of Figure 6.31 shows the local normalized lift per row $C^*_l = |\Delta C_l(t)| \,/\, |\Delta C_l|_{max}$ calculated from the pressure distributions presented earlier. The calculated lift distributions per row were mirrored and averaged over time at the central-span. In the following, a response of the flap section $(y/b > 0.37)$ and of the adjacent section $(y/b < 0.37)$ will be distinguished. One can see that the lift gradually changes over time in the flap section. The adjacent section is affected as well,

even though the lift reacts in comparison more slowly here. However, it should be kept in mind that the each spanwise position has a different final value of the lift. Therefore, the lift in the adjacent section needs more time to reach this final value, but at the same time this final lift value is smaller than the final lift value in the section in front of the flap. On the right hand side, the lift response for the retraction process can be found. Generally, the lift needs longer to converge than for the deployment case shown before: For the deployment, the lift converges in both sections more or less at $t^* = 5.5$, for the retraction at $t^* = 6.5$.

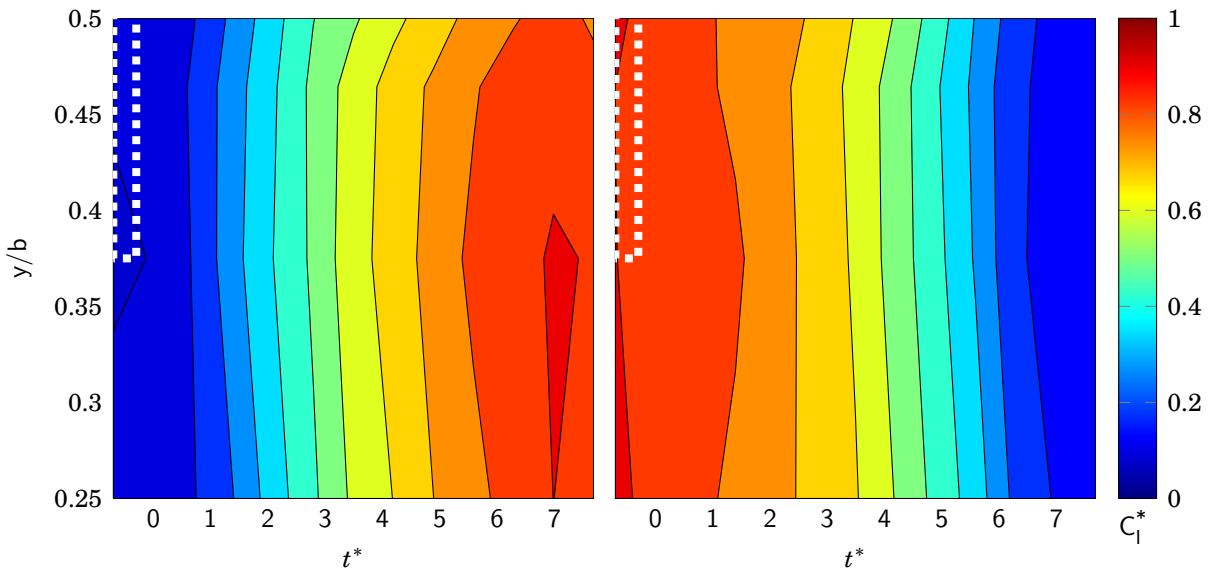

Figure 6.31: Lift response due to flap deployment (left) and retraction (right) for the flap defecting to the pressure side ($T^*_{dep} = 7$)

During the deployment and retraction process for the flap on the suction side, the lift response shows the opposite behavior (see Figure 6.32): During the deployment process the lift reacts slightly faster than in the flap section. During the retraction process, the adjacent section reacts more slowly.

Overall, the adjacent sections have shown to react similarly to the lift change in front of the flap. The lift response lagged behind for the flap deployment on the pressure side and the retraction of the flap on the suction side. For the two other cases, the lift reached its final value faster. However, for both cases at $y/b = 0.25$ (half of the flap span next to the flap), the maximum shift of the response was not larger than around $t^* = 0.5$. Since the span-wise resolution of the surface pressure measurements ended at $y/b = 0.25$, no statement can be made regarding the further span-wise decay of the lift.

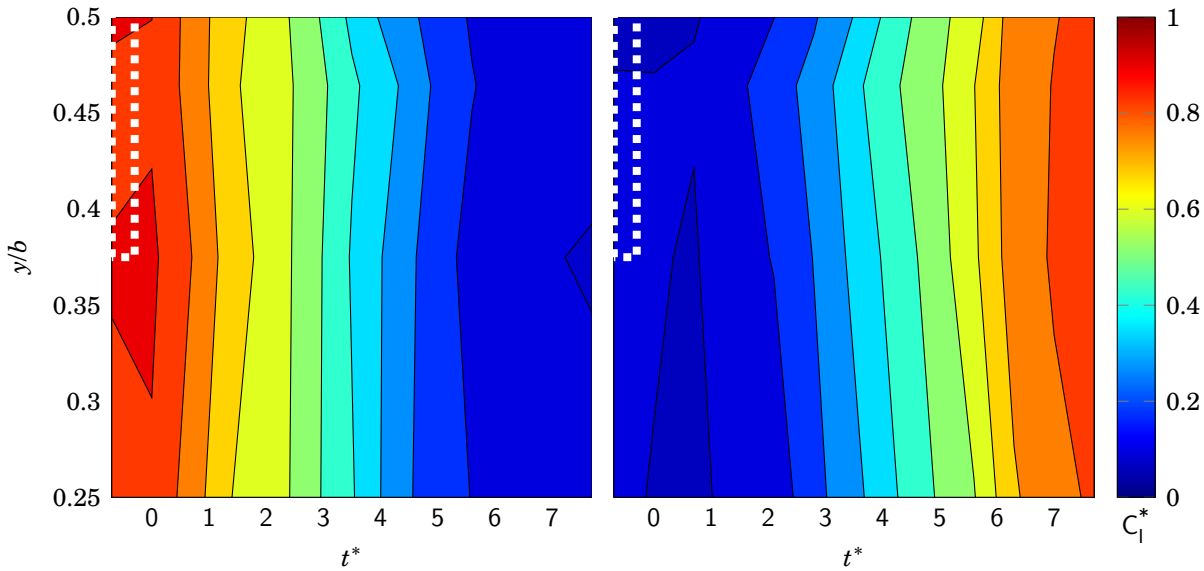

Figure 6.32: Lift response due to flap deployment (left) and retraction (right) for the flap defecting to the suction side ($T^*_{dep} = 7$)

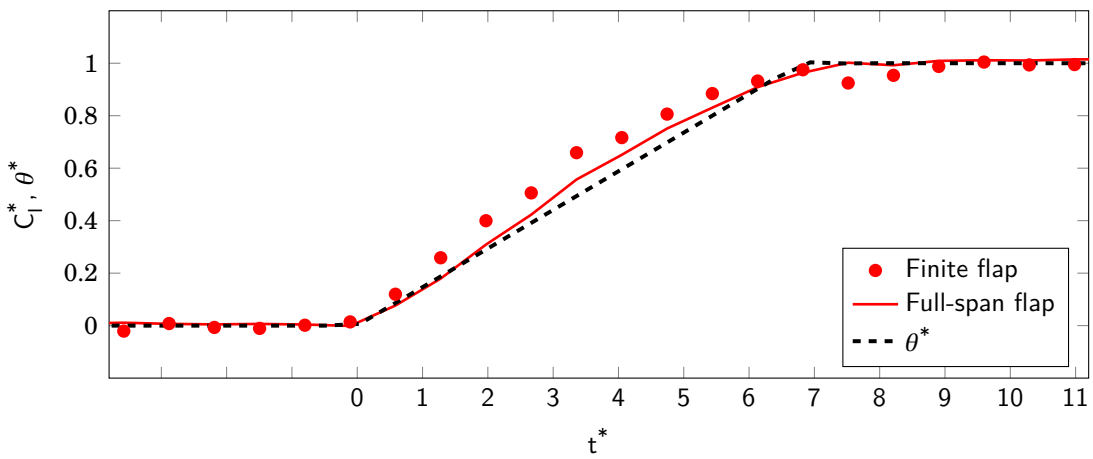

Figure 6.33: Lift response of finite flap during deployment ($T^*_{dep} = 7$)

6.2.4 Comparison of Full-Span and Finite Flap Responses

The lift responses in the centreline of the finite flap were calculated and compared with the response of the full-span flap. Figures 6.33 and 6.34 illustrates the difference of the response in front of the flap. It can be seen that the overall response function is very similar for the finite flap and the full-span flap.

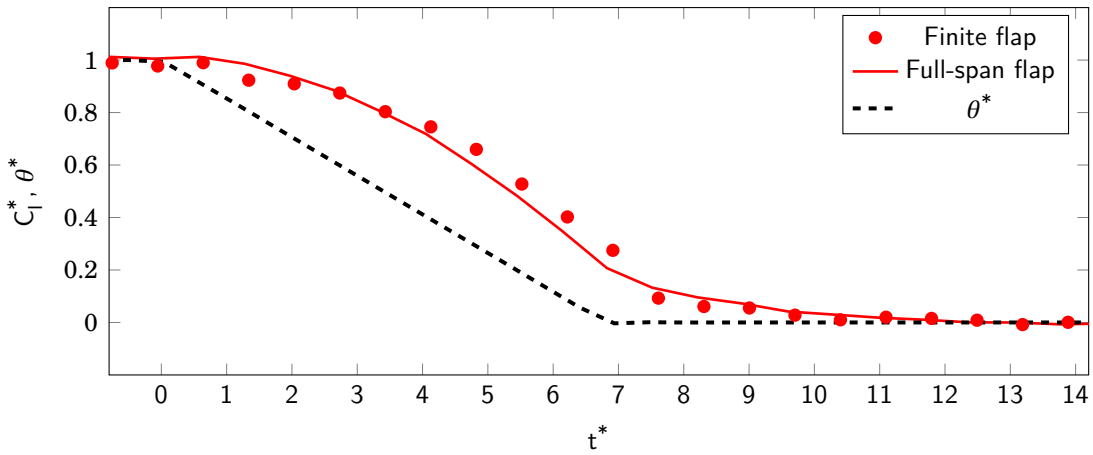

Figure 6.34: Lift response of finite flap during retraction ($T^*_{ret} = 7$)

6.2.5 Dynamic Wake

The wake development during the flap deployment was investigated with the high speed PIV system. The pressure measurements as well as the flap position were synchronized with a trigger to the PIV measurements, so that lift and wake development were made comparable over time. Within this section, just one actuation case was considered: The deployment and retraction process to the pressure side of the full-span flap. The dimensionless actuation time was chosen at $t^* = t \cdot U_\infty / c = 7$, which corresponded to $t = 0.05s$, the fastest actuation time possible within this experimental set-up.

Development of the Vortex Street

Figure 6.35 depicts the wake development during the deployment and retraction process of the flap according to the lift responses shown above in Figures 6.25 and 6.26. The wake shape was evaluated for four flap angles of $\theta = 0°$, $25°$, $50°$ and $70°$ corresponding to $\theta^* = 0$, 0.35, 0.7 and 1. It can be seen that during the flap deployment (Figure 6.35, left) and the rise of lift, the wake experiences a simultaneous change of the flow-field.
Several things can be noted: First of all, the wake position shifts from a more horizontal wake in $\theta^* = 0$ to a downwards directed wake in $\theta^* = 1$. This is due to the higher circulation which builds up when the lift is increased. Second, the vorticity is slowly increasing from a mere shear layer in $\theta^* = 0$ to a profound vortex street in $\theta^* = 1$. The vortex street can already be seen for the second plot where $\theta^* = 0.35$; however, it is noted that the vorticity of the single vortices is not as strong yet. Hence, the circulation of the single vortices increases together with the lift. Consequently, the lift oscillation, as found in the section before, increases over the deployment procedure. Third, the frequency of the vortex street is changing during the deployment process from high to low frequencies. Similar results have been observed by McLachlan [94] in the behaviour of vortex street formations behind spoilers. It is understood that as the flap further penetrates into the flow, the frequency of the vortex street will decrease accordingly. Hence,

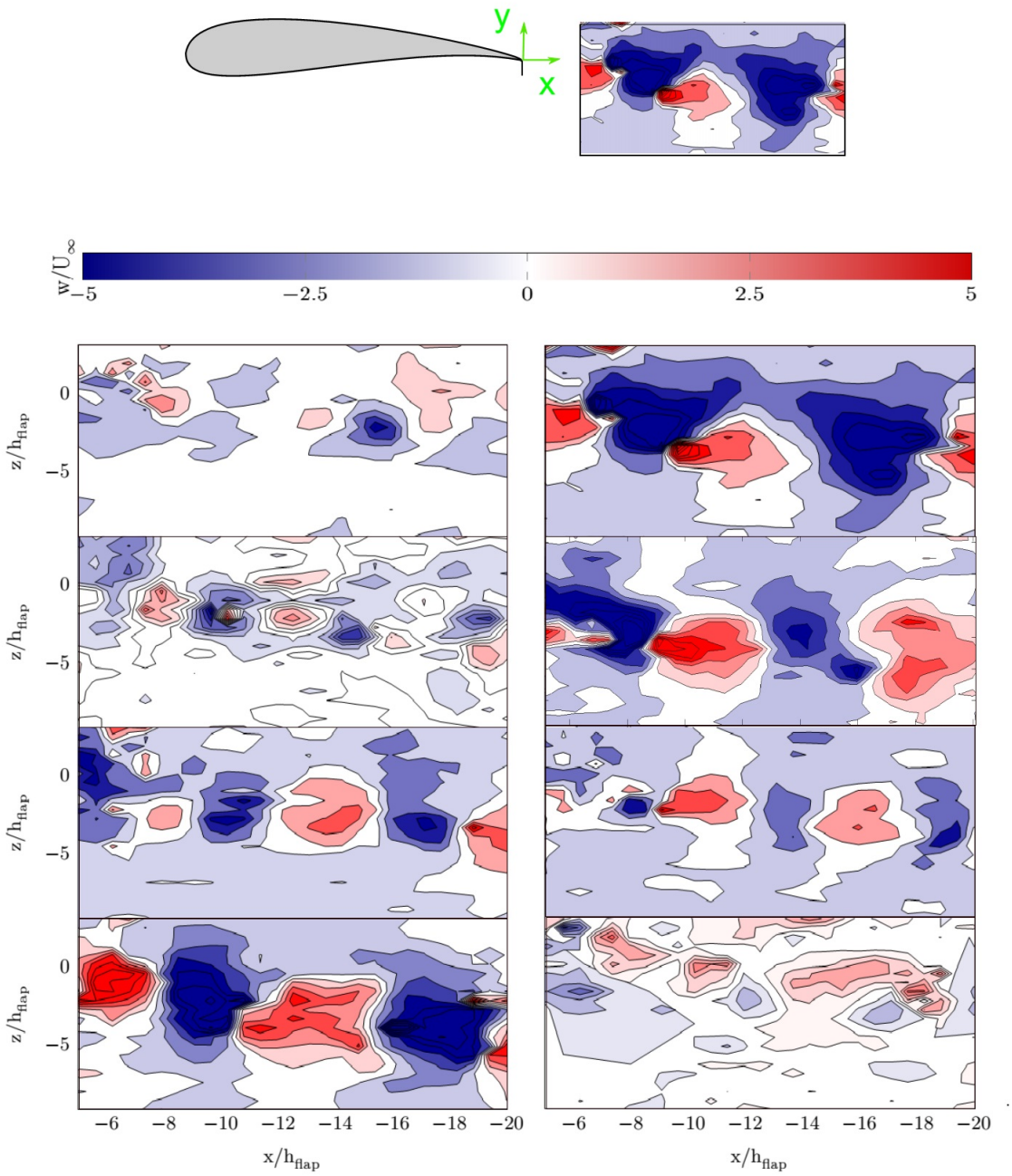

Figure 6.35: Flap vortex system during deployment (left - from top to bottom: $\theta^* = 0$, 0.35, 0.7 and 1) and retraction (right - from top to bottom: $\theta^* = 1$, 0.7, 0.35 and 0)

during the flap deployment the projected flap area emerges higher in the outer flow and the frequency is reduced.
The vortex street development of the retraction process is shown in the right side of Figure 6.35, which goes together with the lift response plotted in Figure 6.26. Carefully comparing the flow-fields of the same flap angle for the deployment and retraction case, one might say that all the points noted above take place slightly delayed for the retraction than for the deployment. This goes along with the lift response illustrated in Figure 6.26 which is also delayed in comparison to the lift response of the deployment.

Drag Development

For the wake rake measurements, an approximation of the overall drag was made. For the seven span-wise positions the velocity loss was measured with the wake rake and the total drag was approximated over time. The drag coefficient is normalized according to the lift with $C_D^* = \Delta C_D(t)/\Delta C_{D,total}$. In Figures 6.36 and 6.37 can be seen that the overall drag for the full-span-flap is much higher than for the finite flap, meanwhile the overall response over time is similar. Furthermore, the fluctuations of the drag are higher in magnitude.

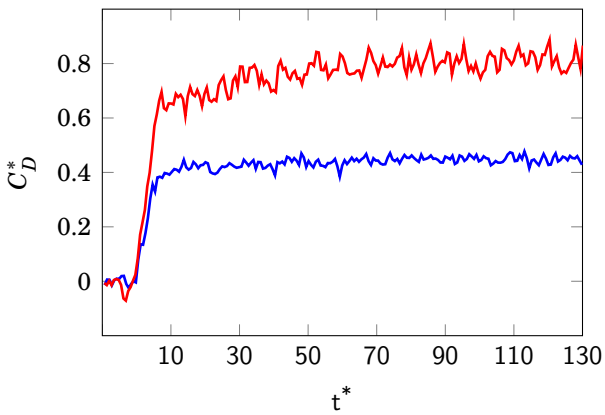

Figure 6.36: Drag development during deployment

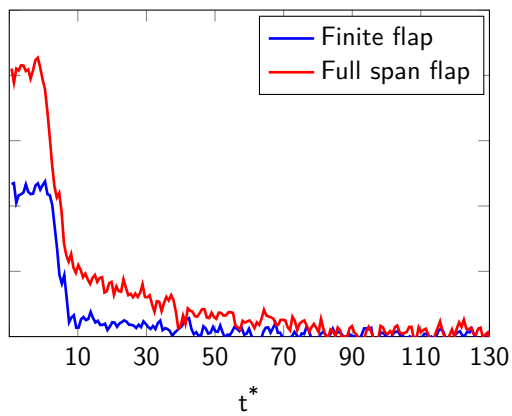

Figure 6.37: Drag development during retraction

6.2.6 Resulting Vortex System of Finite Flap

The lift at each span-wise position is directly coupled to the bound vortex strength at this position by the law of Kutta-Jakowsky: $L = -\Gamma \rho b U_\infty$. In the case of a flap applied for lift enhancement, the lift and therefore the bound vortex of the airfoil $\Gamma_{BV,airfoil}$ are increased in the flap section by the amount of the lift difference ΔL provided by the flap (see Figure 6.38). The law of Helmholtz states that a vortex cannot end in space and has to continue to infinity in potential flow theory. Therefore, at the span-wise position where the bound vortex of the airfoil experiences a change in circulation $\Delta\Gamma_{BV}$, a stream-wise vortex with the same strength has to

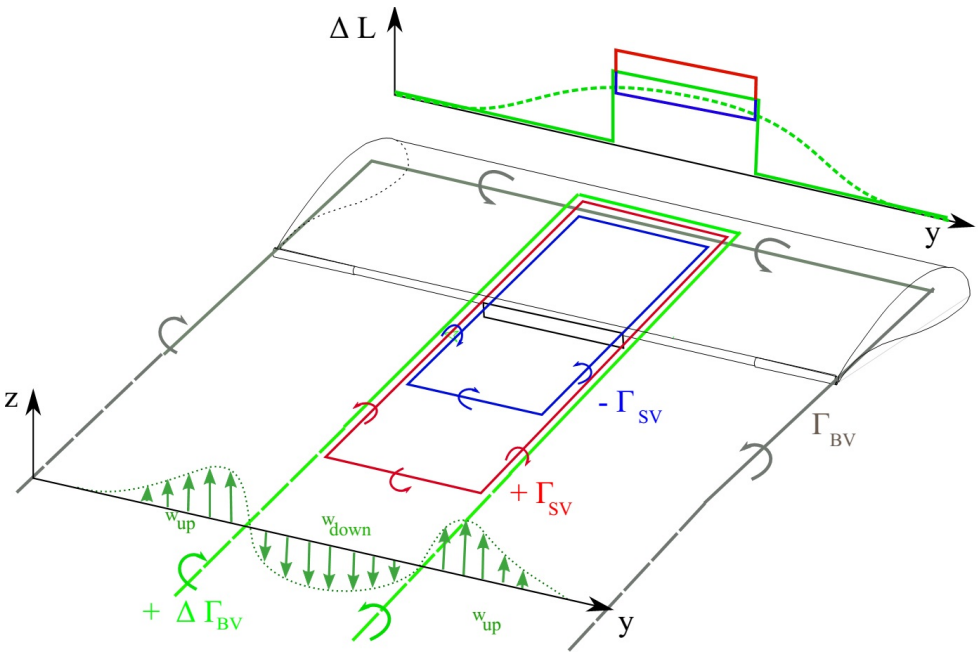

Figure 6.38: Flap vortex system

leave the trailing edge in the wake. This vortex has a strength which is proportional to the lift difference caused by the flap.
It was shown that the shape of the flap causes the flow to develop a vortex street in the flow behind the flap. These span-wise vortices of the strength of Γ_{SV} of opposite sign leave the trailing edge in an oscillating manner, causing the lift to vary over one phase around a mean value.
Bringing these two effects together, it is understood that the changing lift in the flap section must cause the stream-wise flap vortex to change in strength over time with the magnitude of $|\Gamma_{SV}|$. Furthermore, this stream-wise vortex strength oscillation must be in phase with the span-wise vortex street behind the flap. Therefore, the stream-wise vortex leaving the flap edge has a strength of $\Gamma = \Delta\Gamma_{BV} + \tilde{\Gamma}_{SV}(t)$. This behaviour was also found in the work of Holst et al. [60], which includes a POD analysis on stereo PIV measurements on the tip vortex system of the same experimental set-up. However, in this case a passive, attached Gurney flap with a slightly different geometry was used.

The stream-wise vortices emerging from the flap's edges are one reason why in reality the effect of the lift does not rapidly end at the flap edge, but extends in the span-wise direction (dotted green line in the lift diagram in Figure 6.38). According to the law of Biot-Savart, the span-wise vortex induces an up- or downwash over the airfoil. For the case of the downward directed flap, the two span-wise vortices at the flap edges introduce a downwash w_{down} in the flap region and an upwash w_{up} on the adjacent sections. This additional downwash causes the effective angle

of attack in these regions to change and hence the lift is also affected: The downwash in the flap section will cause the effective angle of attack to be smaller and therefore the lift in this region is decreased in comparison to the full-span flap 6.39. Furthermore, the downwash in the flap section does reduce the lift in comparison to the lift gained by the full-span flap.

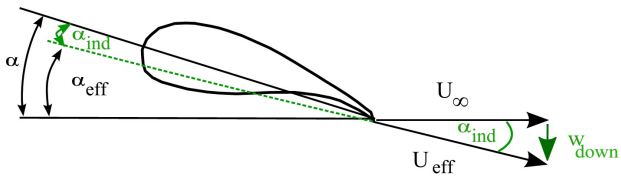

Figure 6.39: Effect of downwash

However, it should be noted that the downwash alone is not the only reason for the smooth transition of the lift from the flap section to the adjacent section. The surface pressure adjustment between the higher and lower lift regions certainly also play an important role. Furthermore, the smoother transition of the lift will cause a vortex sheet to leave the airfoil. This vortex sheet will later roll up to one span-wise tip vortex as illustrated in the more simplified sketch of Figure 6.38. Finally, if the stream-wise vortex is oscillating in strength over time, the range of the lift over span has to oscillate as a result. However, since the lift changes induced by the vortex street are relatively small, this effect certainly does not have any substantive effect on the span-wise lift distribution.

7 Dynamic Airfoil Motion with Passive Micro-Tab and Gurney Flaps

After the passive and active micro-tabs on steady state airfoils have been investigated the focus is now on dynamic pitching airfoils with passive micro-tabs, whereby the height and the position of the tabs were varied and studied under various angle of attack variations. For a better understanding of the results, a theoretical background on the unsteady aerodynamics of pitching airfoils is given in advance.[1]

7.1 Unsteady Aerodynamics of Pitching Airfoils

Unsteady aerodynamics of pitching airfoils can be divided into two major cases: The pitching with attached flow in the pre-stall region and pitching in the stall region where dynamic stall may occur. The pre-stall region is essential since all major operation for load control will be performed within this angle of attack range. However, dynamic stall investigations, which were studies in the past mostly on the inner rotor parts, where no load control is applied, is becoming more and more an issue on the outer rotor of large wind turbines. Dynamic on wind turbines is generally caused by wind shear and turbulence causing unsteady loads on the blades. Tower shadow, yaw misalignment as well as upwind turbine wakes further introduce unsteadiness into the system [24]. Usually due to the rotating system, the impact of dynamic stall is largest at the inner blade section close to the hub where the change of the incoming flow has the biggest impact on the relative angle of attack of the inflow. However, for large wind turbines, the phenomenon of dynamic stall can also be found on the outer blade section due to aeroelastic interactions causing massive blade bending. However, usually dynamic stall is controlled by leading edge devices. Trailing edge devices are often not sufficient to control the dynamic stall vortex. At the same time, trailing edge devices can change to aerodynamic damping which in turn effect the fatigue loads. Therefore, both angle of attack regions are from interest within this study in regard of lift and the aerodynamic moment which gives an idea about the damping characteristics. The theoretical background for both regions will be briefly described below.

7.1.1 The Reduced Frequency

A very important parameter for unsteady aerodynamics in the reduced frequency k. This parameter is a quantity for the degree of unsteadiness of the airfoil's aerodynamics. It is defined

[1] Results presented in the present chapter have not been published previously. D. Holst programmed the *LabView* measurement programme. All other tasks were carried out by the author.

as follows:

$$k = \frac{\omega c}{2U_\infty} \quad , \tag{7.1}$$

whereas ω is here the angular frequency of the pitching airfoil. For a reduced frequency of $k = 0$ the flow is generally regarded as steady. If $0 \leq k \leq 0.05$ the unsteady effects are small and the flow can be regarded as quasi steady. However, if the reduced frequency is above $k > 0.05$ the flow becomes unsteady.

7.1.2 Pitching in Attached Flow

The aerodynamic behaviour of a pitching or plunging airfoil in the attached flow region is well known and can be reproduced by analytical models. Theodorsen developed an analytical model based on thin airfoil theory and potential flow. For a reduced frequency of $k = 0$ the theory produces the steady state results. For higher reduced frequencies a hysteresis loop is is generally developed. On the one hand, the hysteresis loop of the lift rotates counter-clockwise in such a way that during the pitch-up motion of the airfoil the dynamic lift is lower than the steady state lift and the other way round. Furthermore, the amplitude of the lift response (half of the peak-to-peak value) decreases when the reduced frequency is increased. At the same time, the difference of the lift values in the pitch-up and pitch-down motion increases forming a larger hysteresis loop. On the other hand, the moment hysteresis loop is orientated in a counter-clockwise direction. The significance of this will be explained later in this chapter.

This behaviour of the aerodynamic coefficients can be found as long as trailing edge separation is not present and the assumption of potential-flow-like behaviour is not violated. A good overview of the restrictions of Theodorsen's theory due to separation is given in [22]. However, if trailing edge separation is observed, more sophisticated models may be used [56].

7.1.3 Introduction to Dynamic Stall

Dynamic stall is an effect that can occur when airfoils are undergoing a motion in the region of post-stall. Thereby, the motion can include pitching, plunging, heaving or a combination of these three. If dynamic stall occurs, a strong vortex is formed at the leading edge, which further convects over the airfoil's surface. This dynamic vortex causes the lift, drag and pitching moment to experience massive load changes well beyond the steady state values. Hence, dynamic stall is an occurrence of great importance, especially in the application of aerodynamics on helicopters, flapping wings or wind turbines.
Figure 7.1 depicts the basic principle of dynamic stall. At stage (a) the pitch movement starts with the pitch-up movement in the pre-stall region. Within this stage the boundary layer on the suction side is attached and the dynamic lift behaves in a similar way to the curve of the steady state values. When the dynamic pitching airfoil reaches the stall angle of the steady state (b),

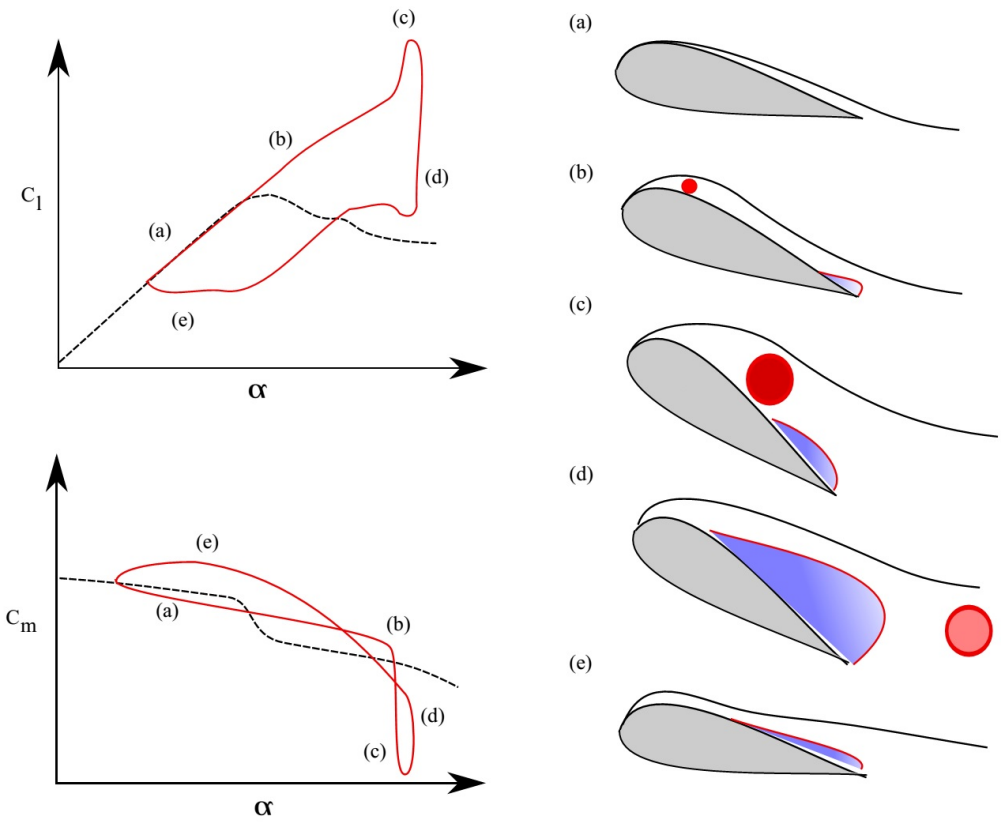

Figure 7.1: The formation of dynamic stall from a) attached flow to b) the formation of the dynamic stall, c) its convection over the airfoil d) into the far wake to e) the reattachment

the two curves behaves differently and the dynamic lift values further increase. This is due to two mechanisms: First of all, the boundary layer separation is delayed due to the dynamic motion and second, a closed separation bubble is formed at the leading edge of the airfoil [35].

Stage (b) in Figure 7.1 refers to the first appearance of the dynamic stall vortex close to the leading edge. The vortex is formed out of vorticity generated in the boundary layer which is further fed in the outer flow [136]. This affects the aerodynamic loading and consequently the curves of the dynamic and steady state aerodynamics differ. The convection of this vortex can be triggered by various mechanisms, such as the bursting of the separation bubble, an abrupt breakdown of the boundary layer reverse flow within the separation bubble, or boundary layer-shock interaction for high Mach numbers. However, it was observed that a laminar separation bubble at the leading edge had no further effect.
At point (c) the fully formed vortex convects over the airfoil's suction side in the wake. In doing so, the vortex induces a low pressure on the surface which in turn massively affects the airfoil's

loads. The lift is momentarily increased while the pitching moment experiences an instantaneous, strong nose-down moment. However, these two effects do not take place at the exact same time, rather the moment stall occurs slightly earlier than the so-called lift stall.

When the dynamic vortex finally reaches the trailing edge and convects in the wake, the flow on the airfoil is fully separated and consequently the lift drops sharply (d). This changes at some point during the pitch-down movement when the flow slowly reattaches from the leading edge to the trailing edge (e).

7.1.4 Aerodynamic Damping

The unsteady aerodynamic fatigue loads on a section can induce damping that is either positive or negative. Negative damping adds energy from the surrounding fluid to the structure while positive damping removes energy from the structure and hence dampens blade bending. Flutter is a phenomenon caused by negative damping and is defined as a single-degree-of-freedom aeroelastic motion.
Whether positive or negative damping is present can be quantified though the aerodynamic damping coefficient Ξ [26]. Generally the damping coefficient can be redivided from the experimental moment data around the quarter point $(C_{m,c/4})$ considering the following equation [35]:

$$\Xi_{cycle} = \frac{1}{\pi \alpha_{21}} \int_{\alpha_{min}}^{\alpha_{max}} (C^{D}_{m,c/4} - C^{U}_{m,c/4}) d\alpha \quad , \tag{7.2}$$

wherein D and U refer to the downward and upward motion of the airfoil.

Derived from Theodorsen's model for thin airfoils, the aerodynamic damping for a pitching airfoil in the pre-stall region can be simplified to

$$\Xi_{cycle} = \pi k/2. \tag{7.3}$$

Hence, in this region the aerodynamic damping is always positive and larger with increasing value of the reduced frequency [26].
If the airfoil pitches beyond the angle at which stall occurs, the moment response looks like depicted earlier in Figure 7.1. The intersections of the moment loop the integration of the damping according to Equation 7.2 yields a change in sign of the damping. Figure 7.2 illustrates the change of the aerodynamic damping throughout the cycle. The damping can be divided in three regions: Positive damping at low angles of attack, followed by a region of negative damping and when dynamic stall takes place, another region of negative damping.

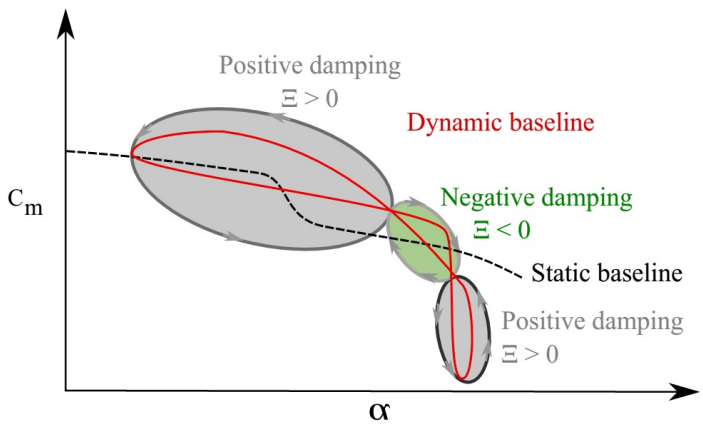

Figure 7.2: Aerodynamic damping during dynamic stall

7.2 Experimental Set-up

For this experiments a new test set-up was built specifically to meet the design constrains discussed beforehand. A dynamic test-rag for pitching airfoils with integrated time-resolved pressure measurements was constructed and manufactured. This set-up was placed in a new open-section wind tunnel whose collector and surrounding box was designed alongside for this propose. Furthermore, a complex *LabView* programme was built in order to measure and control all movements simultaneously. In this section the components of the set-up are explained.

7.2.1 Open Section Wind Tunnel

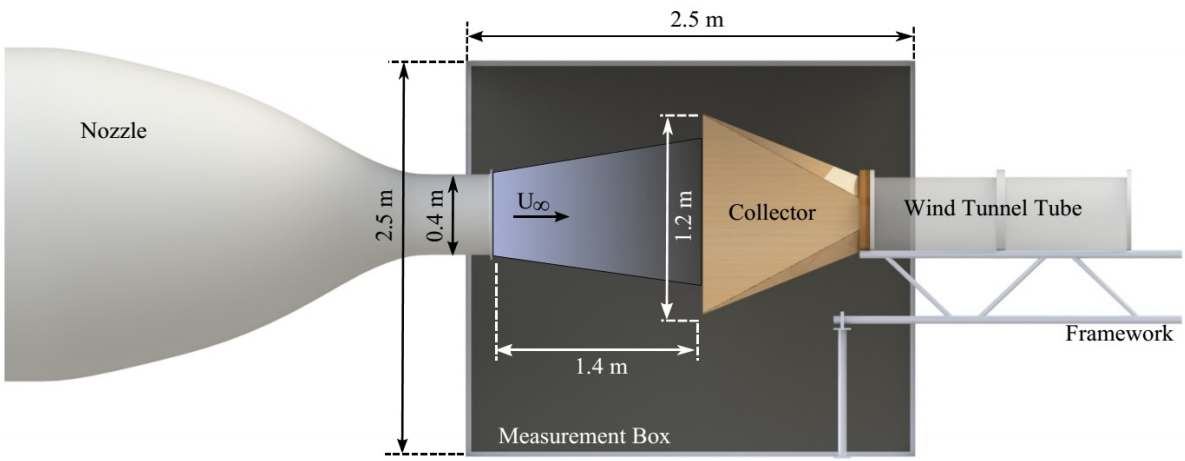

Figure 7.3: Dimensions of open-test-section

For an experimental set-up for dynamic pitching airfoils the wind tunnels which were used

beforehand proved insufficient. The test section was too small and the blocking too high to realistically represent the unsteady wake and its influence on the loads. Furthermore, it was planned to develop a set-up for measurements under very high angles of attack or measurements of $360°$ polar for further studies not connected to this work. Hence, either a wind tunnel with an increased test section height or an open test section was needed.
In this context it was decided to change the *Laminar Wind Tunnel* of the *HFI* to an open test section set-up. A literature review of open-test sections used for dynamic profile measurements was conducted to find the right dimensions for the collector and section design. Following the guidelines of the dynamic airfoil test set-up of *Risø* [45] the open section was planned as illustrated in Figure 7.3, with a contraction ratio of $1/3$ from nozzle to collector.

7.2.2 Dynamic System Design and Construction

A mounting construction for the airfoil and the measurement set-up was designed for the open test section. Therefore, the development of the potential core behind the nozzle was evaluated and a set-up developed which fitted in the potential core flow field. The design requirements were made as broad as possible to ensure a variable set-up and the possible use for future research on airfoils. For this study, two possible set-up frames for the airfoil model were planned (see Figures 7.4 and 7.5). Both versions use the same adapter for the connection with the wind tunnel nozzle (Pos. 1) and bearing (Pos. 2 and 3). Additional holdings in the adapter (Pos.1) are provided to dampen Eigen-frequencies of the system if needed. The first version illustrated in the left hand figure includes time-resolved force balances (Pos. 6.) at both sides of the airfoil. The airfoil is placed in the free space at the centre and integrated between two end-plates (Pos. 5) to support two-dimensional flow. The second version illustrated on the right side features pressure measurements on the airfoil without the additional balance (see Figure 7.5).

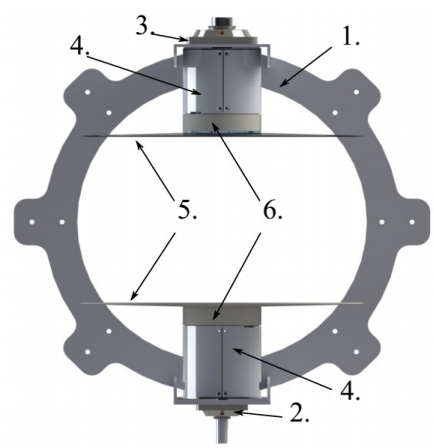

Figure 7.4: Set-up with force balance included

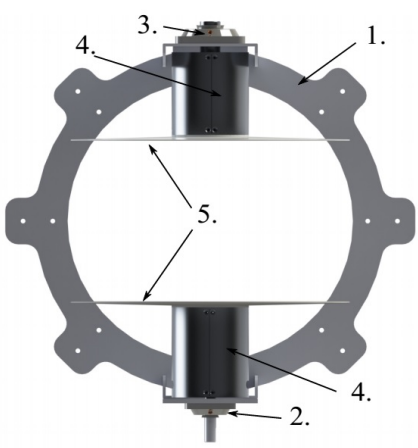

Figure 7.5: Set-up without force balance

1. Adapter nozzle
2. Fixed bearing
3. Loose bearing
4. Hollow shaft
5. End-plates
6. Force balance

The two shafts (Pos. 4) are made of a large diameter to include the pressure sensors close to the airfoil. In that way, the tubing length from pressure hole to pressure sensor is kept

Tab	h_{tab} [mm]	h_{tab}/c [%]
T1	1.0	0.714
T2	1.5	1.072
T3	2.0	1.429
T4	3.0	2.143
T5	3.5	2.500
T6	5.0	3.571

Table 7.1: Tab height configurations

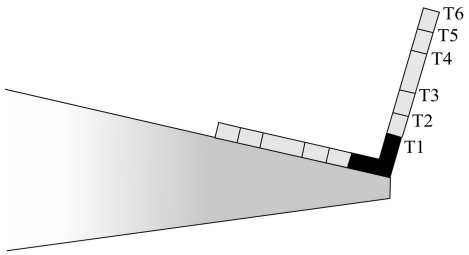

Table 7.2: Tab attachment on airfoil (illustrated at trailing edge)

minimal. The airfoil in driven via the shaft emerging out of the bearing from Pos. 1, which is further connected to a gearing mechanism (1:10) and a high-performance motor (*Mattke MSR0250/L3-045-0-B-SRM50*).

7.2.3 Airfoil Model

The airfoil was chosen to be a symmetrical NACA 0021 [38]. The choice for the thicker symmetrical airfoil was mainly due to the small inner space: More space at the trailing edge was needed to integrate pressure sensors close to it. The airfoil was built using a laser-sinter print of the *Center of Smart Interfaces* of the *Technische Universität Darmstadt*. The three dimensional model is divided into two parts which can be attached to each other with screws. The division plane was located at the lower surface at $x/c = 0.3$ and at trailing edge to not pre-trip the flow on the suction side close to the leading edge. The airfoil was further equipped with 36 surface pressure holes. The spanwise position of the holes was skewed at an angle of $\zeta = 10°$ in order to avoid the disturbance of downstream holes as well as for reasons of the inner space which was needed to connect the tubes.
The airfoil was further equipped with passive micro-tabs/flaps of various heights and positions. An overview of positioning on the airfoil and the height configurations are given in Figure 7.2 and Table 7.1.

7.2.4 Measurement Equipment

Pressure measurements were realised using time-resolved differential pressure sensors which measured each port simultaneously. The pressure transducers [2], measured the pressure difference between the local surface pressure and the static pressure of the freestream $(p - p_\infty)$ with an accuracy of ± 5Pa and a sampling frequency of 10000Hz. The pressure sensors were mounted in a way that the internal membrane was not exposed to acceleration forces due to the airfoil's pitching motion. The data was further processed by a data-acquisition unit [3]; and an embedded real-time control and monitoring system provided the time synchronisation between all pressure ports as well as the angle of attack information of the airfoil. Ambient conditions were monitored and measured during the whole data acquisition process.
The static measurements averaged over a total time of 4s per angle of attack. The dynamic

pitching motions were repeated between 30-50 times and the data was phase-averaged. This number of repeated measurements were determined through a sensitivity study. Throughout the measurements, the mean angle of attack, the pitching amplitude as well as the frequency was varied and the effect of the tabs was analysed.

7.2.5 Motion Profiles

The load variations on wind turbines are mostly periodical nature due to the rotational system of the blades. Hence, the change of angle of attack or inflow velocity can be approximated through a simple sinusoidal oscillation. These oscillating movements are generally characterised through the reduced frequency. Since the load changes during one revolution of a wind turbine blade are mostly periodical, an approximate reduced frequency can be calculated. Figure 7.6 shows the reduced frequency for the 5MW research wind turbine at the NREL [66] [69] at the rated wind speed. For the generation of the graph the wind turbine was modelled in QBlade [91] and the time-dependent data on each section was Fourier analysed and the gained frequency converted into a reduced frequency with the local parameters of the relative inflow speed and chord length.

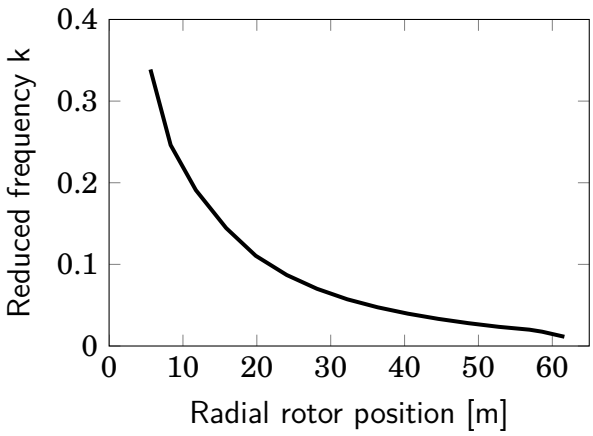

Figure 7.6: Reduced frequency over NREL rotor position

The results shown are typical for wind turbine blades: The unsteady effects are the highest at the inner blade sections and are less pronounced at the outer sections. Hence, at the outer sections, where the load control devices would be placed, the reduced frequency is low and well within the quasi-steady region. At the same time, the amplitude of the variations is the lowest at the outer blade regions and the highest close to the hub.
Based on this analysis, the experiments where conducted for three major airfoil motion profiles: $\alpha = 4° \pm 2°$ representing the outer blade region with low overall angle of attack and reduced frequencies of $k < 0.05$, $\alpha = 12° \pm 10°$ and $k = 0.05$ in the mid-stall region representing sections closer to the hub and $\alpha = 6° \pm 10°$ for larger angle of attack variations causing dynamic stall.

7.3 Pitching in the Pre-Stall Region

At the outer regions of wind turbine blades yaw as well as the presence of the earth boundary layer generally cause periodically changing inflow conditions. Generally, the mean angle of attack of the outer airfoils sections is low and the amplitudes caused by the changing inflow are generally not higher than a few degrees. A representative airfoil motion can be described by $\alpha = 4° \pm 2°$. In this test set-up the angle of attack starts at $\alpha = 2°$ rises to its maximum of $\alpha = 6°$ before it falls again to the initial value.

7.3.1 Clean Airfoil Behaviour

The load coefficients for the clean airfoil was measured in steady state as well as for the harmonically oscillating airfoil around the quarter point. The angle of attack motion of $\alpha = 4° \pm 2°$ was tested for several reduced frequencies ranging from $k = 0.01 - 0.16$. Figure 7.7 and Figure 7.8 show the steady state lift and moment coefficients. The drag coefficient was not determined since it was not the scope of this study. For reasons of symmetry, data was collected for angles of attack between $-26° < \alpha < +26°$. A clear hysteresis loop was found for the lift and moment in the region of high angles of attack on both airfoil sides. In the pressure distribution (not shown here), it can be seen that the laminar separation bubble is at a chordwise position of around $x/c \approx 0.15$. Hence, when the airfoil side, where the model division line is placed, acts as a suction side the transition happens upstream of the division line causing a hysteresis loop (for $\alpha < -10°$).

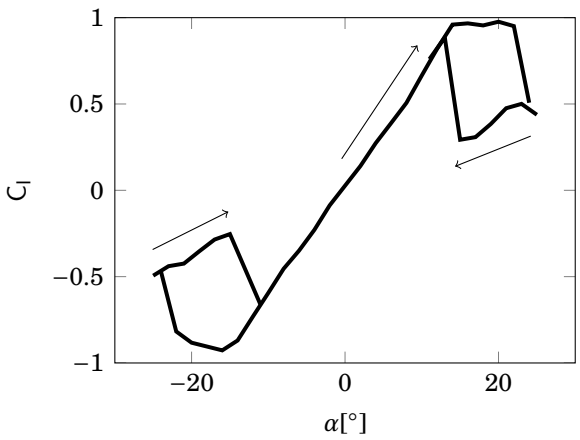

Figure 7.7: Steady lift of clean airfoil

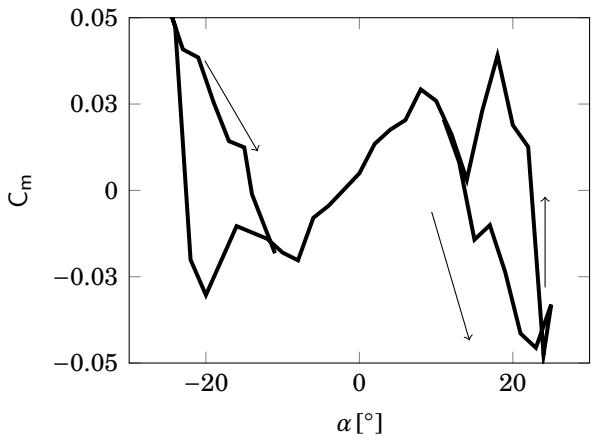

Figure 7.8: Steady moment of clean airfoil

Figure 7.9 shows the lift loops for the clean airfoil for reduced frequencies from $k = 0.01 - 0.1$ together with the steady state result. A typical loop of the lift coefficient as one would expect from Theodorsen's theory was not found. This is likely due to the relatively low reduced frequencies that result in only very small lift differences. Furthermore, if the airfoil motion is not a pure sinusoidal motion but is slightly off due to the motor control and airfoil torsion, even Theodorsen's theory can yield lift loops with multiple inter-crossings. In the case of the

measurements by Heerenbrink, these effects could be reduced by using a model material with a higher torsional stiffness [58].

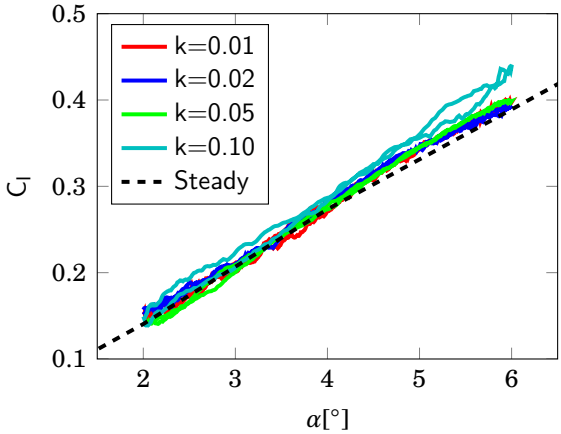

Figure 7.9: Dynamic lift of clean airfoil for various reduced frequencies (Re=200k)

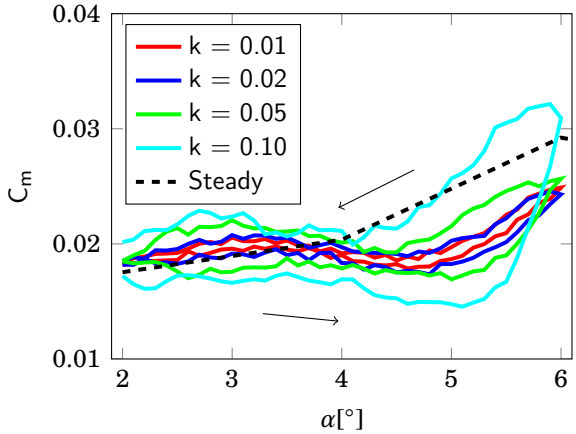

Figure 7.10: Dynamic moment of clean airfoil for various reduced frequencies (Re=200k)

The pressure distributions for various angles of attack during the motion are shown in Figure 7.11. It can be seen that during pitch-up, the laminar separation bubble present at around $x/c = 0.45$ is slightly compressed and moved forward. At an angle of $\alpha = 6°$ as well as during pitch-down the bubble is not present anymore. Furthermore, all distributions of the pitch-down movement have proven to be slightly wider than for the pitch-up movements (not shown here); hence, causing slightly higher lift.

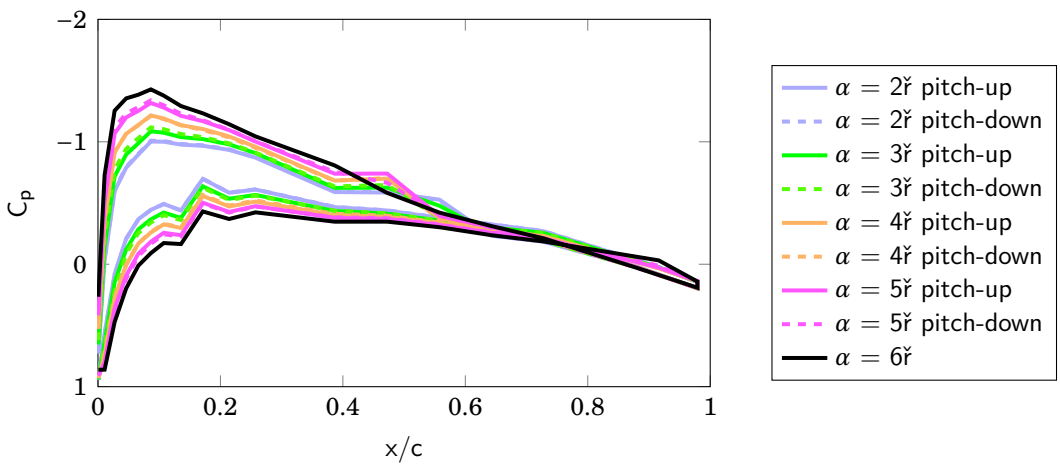

Figure 7.11: Pressure distribution during pitch cycle (k=0.05, Re=200k)

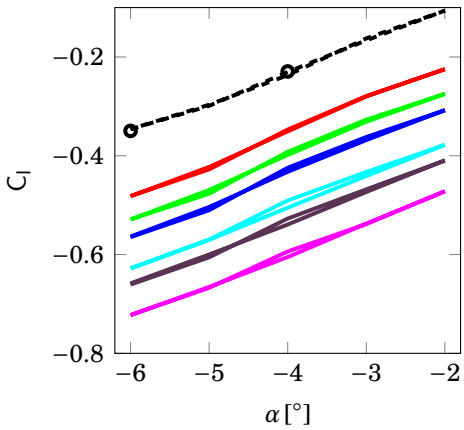

Figure 7.12: Dynamic lift for tab on pressure side of various heights ($k = 0.05$, $x/c = 1$, Re=200k)

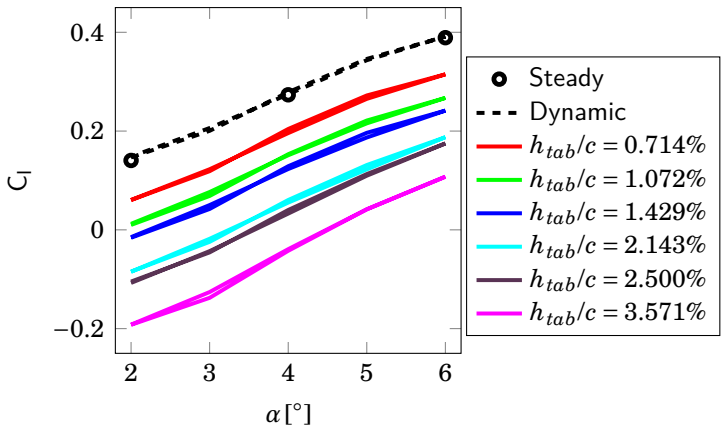

Figure 7.13: Dynamic lift for tab on suction side of various heights ($k = 0.05$, $x/c = 1$, Re=200k)

The moment curves can be seen in Figure 7.10. The moment hysteresis show a clear counter-clockwise rotating loop for all reduced frequencies without inter-crossings identifying a positive damping during the whole cycle. With rising reduced frequency the loop is clearly larger and hence the damping gets larger as the theory suggests (compare Equation 7.3).

7.3.2 Effect of the Tab Height

The effect of the tab height on the dynamic behaviour was studied for a fixed reduced frequency of $k = 0.05$ for a tab position of $x/c = 1$ at the trailing edge. The tab height was varied between 6 different tab heights as summarised in Table 7.1. All tabs were equal-sided L-shaped profiles made of brass with a thickness of 1mm. The tabs extended over the full span of the airfoil and were glued on the surface during the measurements. Instead of switching the tab from one side to the other to investigate load reduction or load enhancement, the airfoil motion was mirrored to negative angles of attack. Since transition through a laminar separation bubble took place on both airfoil sides, the differences of the aerodynamic behaviour of the two sides are minimal. Hence, for all positive angles of attack, the tabs were placed on the suction side for load reduction, meanwhile for all negative angles of attack, the tab side became the pressure side and hence the tab caused a load enhancement (regarding absolute lift values).

Figures 7.13 and 7.12 depict the dynamic lift loops for the tabs on the pressure side ($\alpha < 0$) and on the suction side ($\alpha > 0$). The dynamic lift loops are very close to the values of those of the steady state cases. Hence, the tabs undergoing a dynamic movement in the range of reduced frequencies up to at least $k = 0.05$ do not suffer from large unsteady effects, which would decimate their effectiveness as an active load control device.
Figure 7.14 shows the pressure distribution close to the end of the pitch-up motion at an angle of $\alpha = 5.5°$ for various tab heights. Here, the tab was placed at the trailing edge on the suction

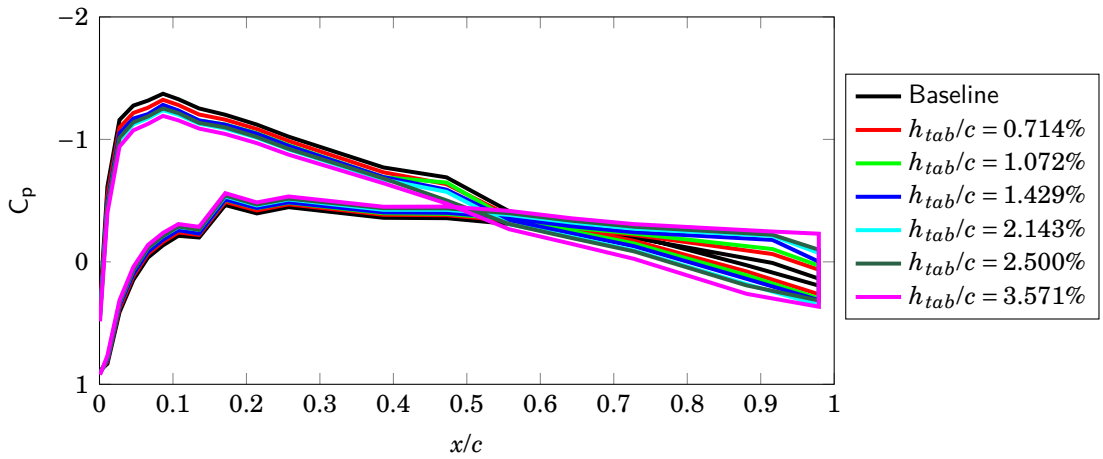

Figure 7.14: Effect on the pressure distribution of the tab height ($\alpha = 5.5°$, Re=200k)

side. The major differences for the various tab heights can be seen close to the trailing edge. The higher the tab, the higher the pressure build-up in front of the tab and the pressure differences between the suction and the pressure side. The pressure in front of the tab on the suction side is not influenced during the pitch-up motion but remains mostly the same for one tab configuration during the cycle (not shown here). The pressure on the pressure side, however, varies depending on pitch-up and pitch-down and the largest difference is found at the highest angles.
Figures 7.12 and 7.13 suggest that the tabs shifts the dynamic lift loop in their absolut vales. However, for a better understanding of the effect of the height, the lift coefficient is further shown over the phase angle in Figure 7.18. For a phase angle of $\phi = 0 - 180°$ the airfoil is pitching up, while from $\phi = 180 - 360°$ the airfoil is pitching down. For the baseline case the maximum lift is found very close to where the angle of attack is the highest at a phase angle of $\phi = 180°$. From Theodorsen's theory a slight phase lag of the lift maximum is expected, however, for these small reduced frequencies the results are very close to the steady state results and hence show nearly no unsteady effects and small phase lags. For curves with applied tabs placed at the trailing edge, it can be observed that the tab height does not affect the phase of the lift. The same could be found for the tabs of varying height on the pressure side (not shown here). Hence, the tabs affect the overall pressure distribution and lift values but do not change the response behaviour.
It can be observed further that with a higher tab height on the suction side, the lift difference during one cycle is more pronounced even though the overall lift values are smaller. However, this is not an effect which can be seen only in the dynamic curves, but also in the steady state distributions. Hence, this effect is connected to the steeper lift slope of the steady state lift curve when micro-tabs on the suction side are applied. This effect was explained earlier in this work with the thickening of the boundary layer. The thicker boundary layer at higher angles of attack makes the tab less effective and hence the lift slope is steeper.

As explained earlier, the moment is regarded more closely in the section due to its importance to

the aerodynamic damping properties of a pitching airfoil. Generally, the aerodynamic moment is declared as positive, when the airfoil experience a nose-up moment. This is the case for cambered airfoils under positive angle of attack. The static baseline of the moment has shown, that the moment for the NACA0021 is mostly positive for positive angles of attack and due to symmetry negative at negative angles of attack. If a tab is applied on the pressure side, it is known that the tab implies an additional negative (nose-down) moment to the airfoil. Meanwhile, a tab placed on the suction side adds an additional positive (nose-up) moment to the airfoil. Within this setup, the tab is attached to the same airfoil side. Therefore, the tab is on the suction side for positive angles of attack and for negative angles of attack on the pressure side. However, the same moment declaration is used. Hence, here the tab on the suction side will cause the moment to be more positive than the baseline and the tab on the pressure side also cause an even more positive moment difference due to the sign declaration.
Figures 7.15 and 7.16 show the moment curves for the various tab heights on the suction and pressure side: For the tabs placed on the suction side ($\alpha > 0$), all coefficients of the dynamic baseline are positive and the loop is counter-rotating inducing positive damping. The higher the tab height, the more are the loops changed to higher values of the moment coefficient. If the angles of attack are negative and the tab is now on the pressure side, the loop of the clean airfoil is negative and the tabs cause the loops to be shifted to higher and positive values of the moment coefficient. Again, all loops are counter-rotating and hence inducing positive damping.

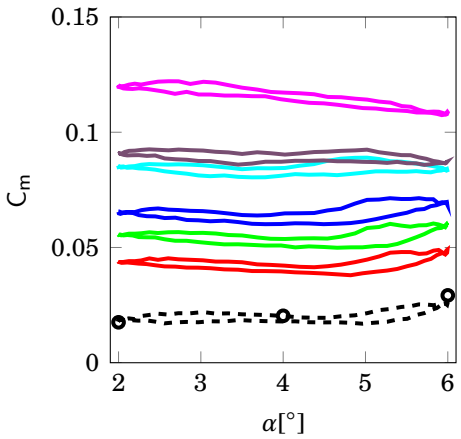

Figure 7.15: Effect on the dynamic moment for suction side tab of varying heights
($k = 0.05$, $x/c = 1$, Re=200k)

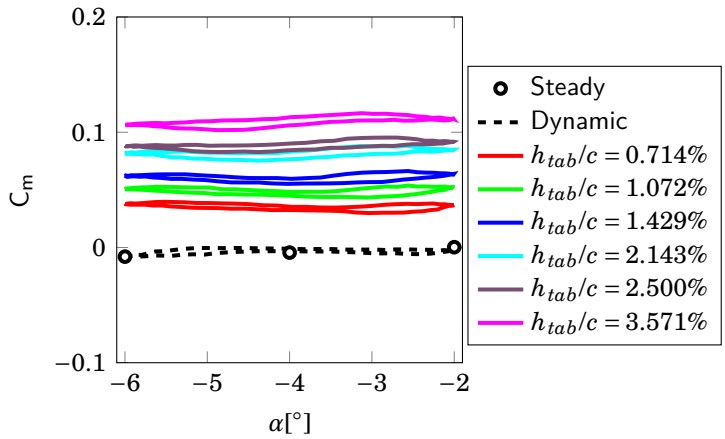

Figure 7.16: Effect on the dynamic moment for pressure side tab of varying heights
($k = 0.05$, $x/c = 1$, Re=200k)

7.3.3 Effect of Tab Position

The effect of the tab position was investigated based on the same motion profile of $\alpha = 4° \pm 2°$ and a reduced frequency of $k = 0.05$ as for the study of the effect of the tab heights. Figure 7.17 shows the lift over one pitch cycle for a fixed tab height of $h_{tab}/c = 3.571\%$ on the suction

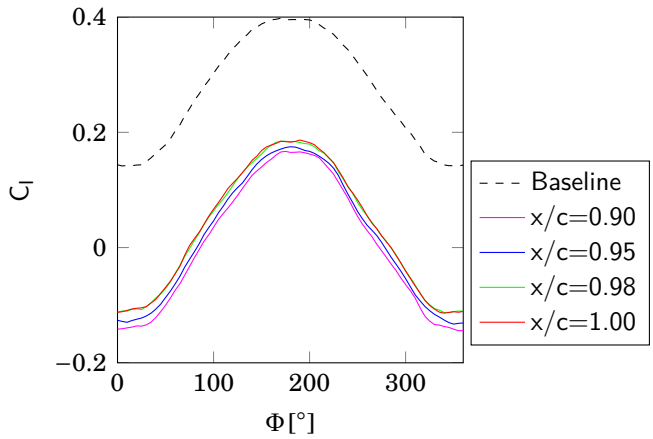

Figure 7.17: Effect on the lift over the phase from varying tab positions on the suction side ($k = 0.05$, $h_{tab}/c = 3.571\%$, Re=200k)

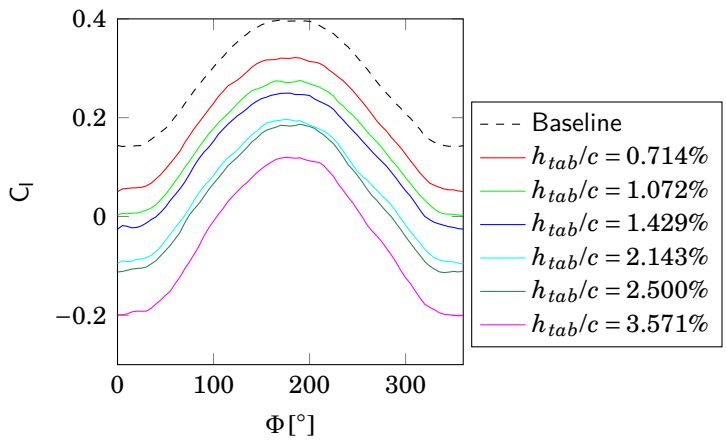

Figure 7.18: Effect on the lift over the phase from varying tab heights on suction side ($k = 0.05$, $h_{tab}/c = 3.571\%$, Re=200k)

side. It can be seen that the tab's lift reduction becomes larger over a whole cycle if the tab is placed further upstream. This finding is consistent with the steady state results for the tab on the suction side. In the dynamic measurements is can be seen further that the phase lag between the lift response and the angle of attack motion is negligible.

7.4 Pitching in the Light-Stall Region

In this section the angle of attack motion was moved in the region where trailing edge separation occurs. A motion profile of $\alpha = 12° \pm 10°$ and a reduced frequency of $k = 0.05$ were chosen.

7.4.1 Clean Airfoil Behaviour

Figure 7.19 illustrates the dynamic and steady lift curves for the clean airfoil pitching with a reduced frequency of $k = 0.05$. The dynamic lift hysteresis from the pitch-up and the pitch-down motion which starts at around an angle of attack of $\alpha = 12°$ is not due to the phenomenon of dynamic stall, since the dynamic stall angle is not reached yet. The phase-averaged pressure distributions show that the pressure difference for the pitch-down movement is reduced over all chordwise positions. Furthermore, the laminar separation bubble (at $x/c \approx 0.2$) is present during the whole cycle as illustrated in Figure 7.20.

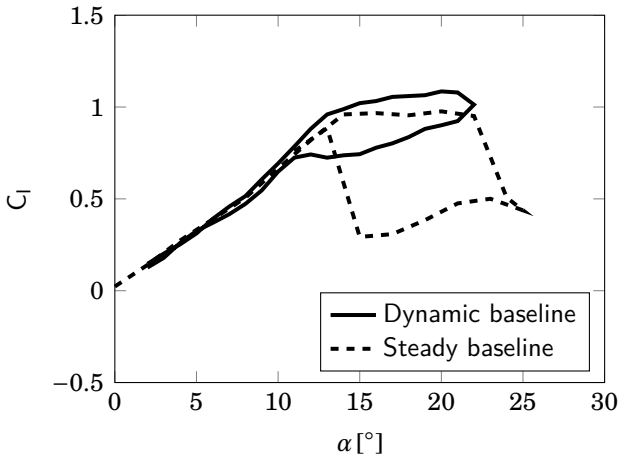

Figure 7.19: Dynamic and steady lift curve for movement in light stall region ($k = 0.05$, Re=200k)

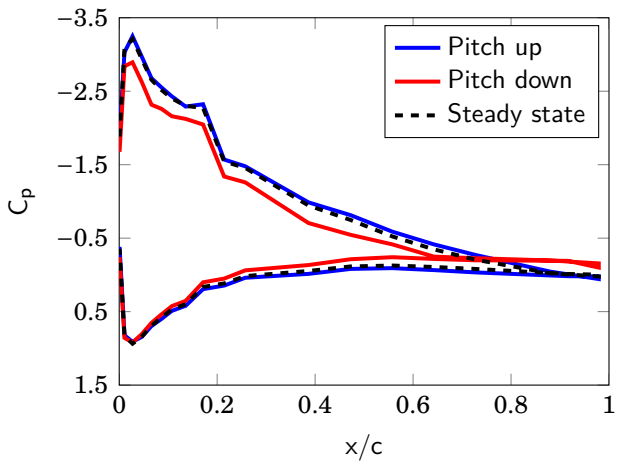

Figure 7.20: Comparison of pressure distribution from pitch-up and pitch-down ($k = 0.05$, Re=200k, $\alpha = 16°$)

7.4.2 Effect of the Tab Height

The placement of a tab at the trailing edge showed to have a significant impact on the lift in this motion profile. Figure 7.21 illustrates the curves for the baseline case as well as various tab heights for a tab placed on the suction side. It can be seen that the lift is massively reduced in the pre-stall region, as one would expect. However, the effect on the hysteresis loop was the most pronounced effect found. Meanwhile the lift in the pitch-up motion is reduced as one might expect from the steady state results, the downstroke lift was not shifted downwards in a similar manner. In the pitch-down movement the lift curves tend to be very close. This is due to the fact that during the pitch-down the tab is submerged in the recirculation zone and has no effect on the overall pressure distribution with the exception of the pressure in the separation region which is influenced by the presence of the tab within this zone.

Even though a load reduction is generally contemplated at these high angles of attack, the effect of a tab on the pressure side was studied additionally. Therefore, the tab was not removed

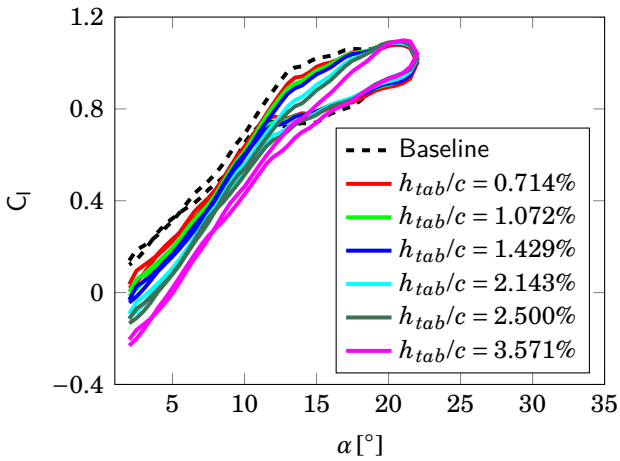

Figure 7.21: Effect of the suction side tab's height on the dynamic lift ($k = 0.05$, Re=200k)

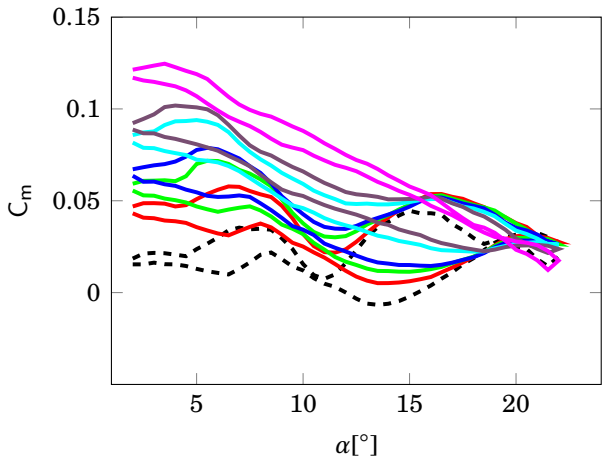

Figure 7.22: Effect of the pressure side tabs height on the dynamic moment ($k = 0.05$, Re=200k)

from the profile, but the motion profile was modified to $\alpha = -12° \pm 10°$ since the airfoil was symmetrical. It was found that the hysteresis loop could not be reduced in this case but the lift curve was shifted as a whole to higher angles of attack (not shown here).
The moment responses with tabs are shown in Figure 7.22. The baseline loop for the clean airfoil is for the most part counter-rotating inducing positive damping. However, at very high angles above $\alpha = 19°$ the loop changes direction causing a small area of negative damping. As found in the pre-stall region, the tab height itself shows only a very small effect on the loop width but generates higher overall moment values. The same effect can be seen for the pitching movement: In the pre-stall region, the loops clearly differ in the overall values; however, with higher angles of attack and hence more separation at the trailing edge, the moment curves merge. Furthermore, the area of negative damping remains but is reduced for all tab configurations at high angles of attack. The small tab heights seem to work better in this regard, causing the negative damping region to nearly disappear.

7.4.3 Effect of Tab Position

Figure 7.23 shows the dynamic lift curves for the airfoil with a tab placed on the suction side for lift reduction at various chordwise positions. It can be seen that a more upstream placement of the tab further improves the behavior and the suppression of the hysteresis loop. The more upstream the tab was placed, the more lift reduction was gained, due to the less thick boundary layer at upstream positions. As seen before for varying tab heights (Figure 7.21), the lift is further reduced in the pitch-up movement, meanwhile in the pitch-down movement the curves nearly coincide due to separation (e.g. $\alpha = 20°$).

Figure 7.24 depicts the moment curves for varying tab positions. Meanwhile a change in tab

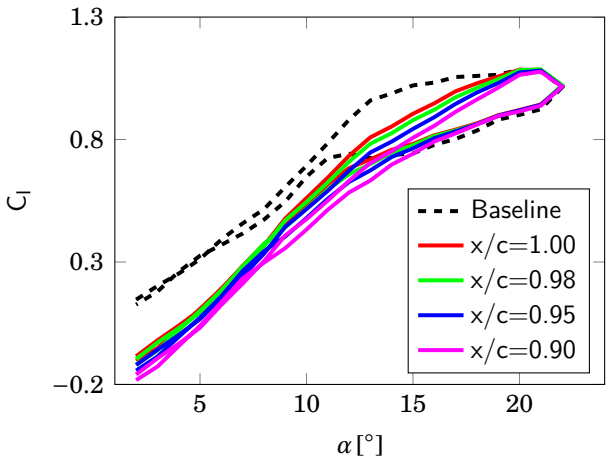

Figure 7.23: Effect of the suction side tab's position on the dynamic lift ($k = 0.05$, Re=200k)

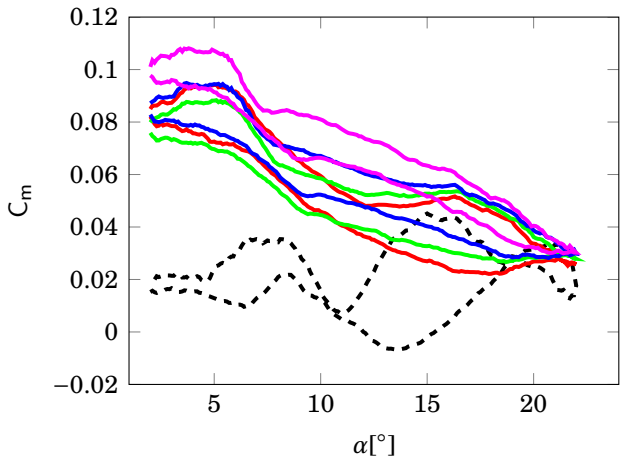

Figure 7.24: Effect of the suction side tab's position on the dynamic moment ($k = 0.05$, Re=200k)

height could only reduce the negative damping region at high angles of attack (compare again Figure 7.24), the change in the tab's position completely removed this effect.

7.5 Micro-tabs and Flaps under Dynamic Stall Conditions

Within this section the influence of a micro-tab on the phenomenon of dynamic stall is observed. Therefore, one motion profile was selected to study the interaction of dynamic stall and micro-tabs on the suction side. The tab height and position was varied and the lift and moment over time were observed. Furthermore, the dynamic stall strength and convection was analysed.

7.5.1 Clean Airfoil Behaviour

The motion profile which produced a visible dynamic stall in the measured data was the angle of attack profile of $\alpha = 16° \pm 10°$ with a reduced frequency of $k = 0.05$. Figure 7.25 shows the lift curve during the pitching motion over the angle of attack. A strong dynamic stall loop can be seen. Right before the airfoil reaches an angle of $\alpha = 26°$ a clear lift overshoot can be seen caused by the convection of the dynamic stall vortex. After this phenomenon the airfoil's lift goes into deep stall. Figure 7.26 gives an insight of the pressure distribution and hence the convection of the dynamic stall vortex in this brief moment. Between an angle of attack of $\alpha = 25.5 - 25.9°$ the local pressure distribution is shown. The presence of the vortex can be seen, as it convects over the surface. During this process the suction peak at the chordwise position of $x/c = 0.01$ drops from $C_p = -4.4$ to $C_p = -2$. The rest of the airfoil's suction side remains in full stall after the vortex has passed through.

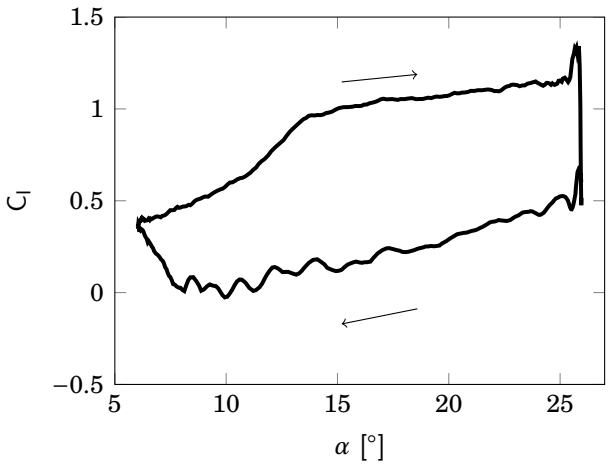

Figure 7.25: Lift curve during dynamic stall of the clean airfoil
($k = 0.05$, Re=200k)

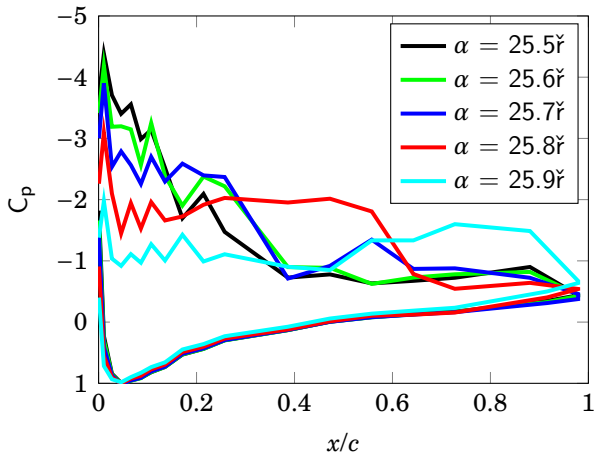

Figure 7.26: Convection of dynamic stall vortex on the clean airfoil
($k = 0.05$, Re=200k)

7.5.2 Effect of the Tab Height

A placement of tabs of various heights at the trailing edge on the suction side of the airfoil have shown an effect on the lift loop (see Figure 7.27). For the most part of the upstroke motion between an angle of $\alpha = 6° - 20°$ the lift is still reduced due to the presence of the tab. However, two remarkable effects can be seen:
First, the lift overshoot due to dynamic stall is clearly smaller, however not completely dismissed. This goes along with the observations by Lee and Su [79], who concluded that the formation and detachment of the dynamic stall vortex is generally not influenced by a flap; however, the low pressure signature of the vortex may be reduced. Within this study, the strength of the dynamic stall vortex was evaluated further by comparing the maximum induced negative pressure at mid-chord for different heights and placements. However, no clear dependency was found between the tab configuration and the dynamic stall strength. All pitching cycles were repeated up to 30 times and the pressure was phase-averaged, however, due to the high unsteadiness of the dynamic stall, larger numbers of cycle repetitions may be needed for a clear statement.
The second interesting effect is that the reattachment is promoted, when tabs are present ($\alpha \approx 8°$). Here, the tab's height does not seem to be an influential factor, just that the tab is generally present.

The moment responses are illustrated in Figure 7.28. All curves follow the typical loops as suggested by the literature. Two inter-crossings divide the loop into three damping regions: Negative damping at low angles of attack, positive damping during the onset of separation and negative damping caused by the dynamic stall vortex. The tab height does not have a clearly visible impact on the moment during angles above an angle of $\alpha > 17°$. This is most likely the case when the tab is already fully emerged in a separated region at the trailing edge.

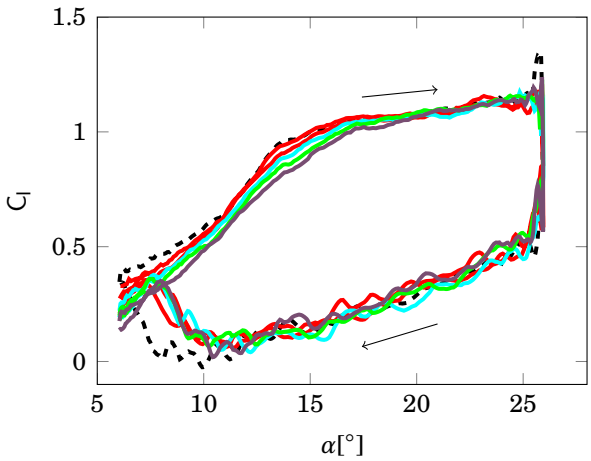

Figure 7.27: Effect of the suction side tab's height on the dynamic stall lift ($k = 0.05$, Re=200k)

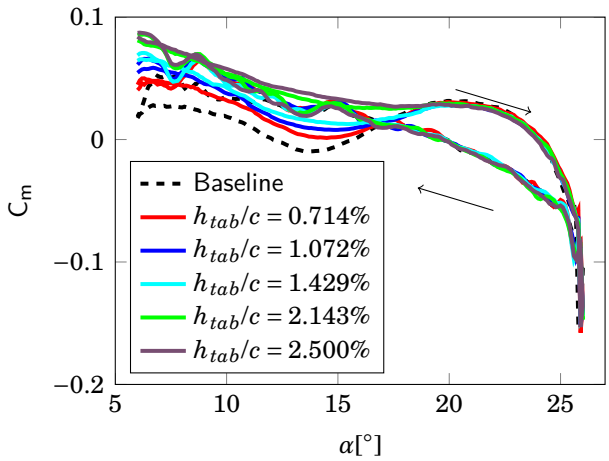

Figure 7.28: Effect of the suction side tab's height on the dynamic stall moment ($k = 0.05$, Re=200k)

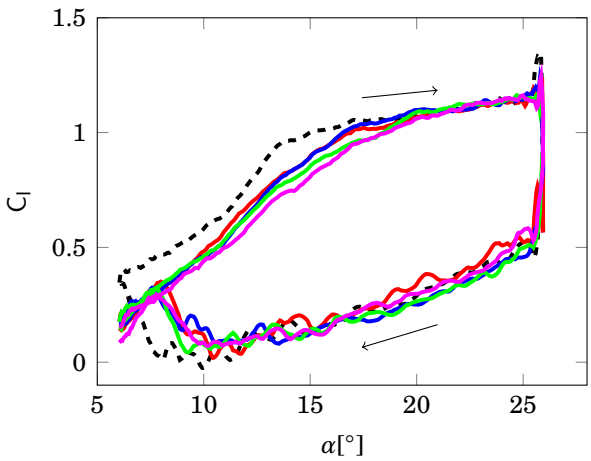

Figure 7.29: Effect of the tab position on the suction side on the dynamic stall lift ($k = 0.05$, Re=200k))

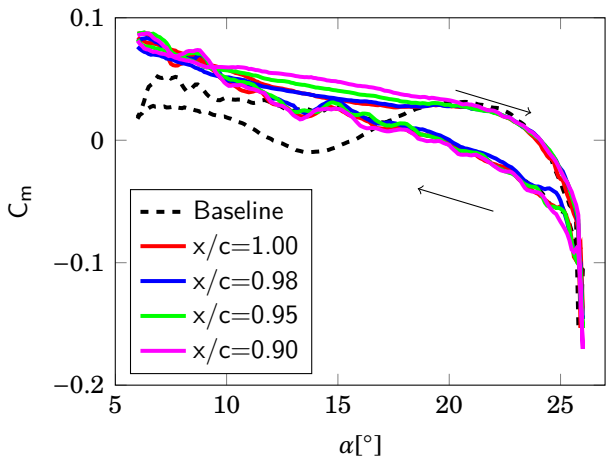

Figure 7.30: Effect of the tab position on the suction side ob the dynamic stall moment ($k = 0.05$, Re=200k)

7.5.3 Effect of Tab Position

The effect of the tab placement was examined for all tab heights for the same motion profile ($\alpha = 16° \pm 10°$). Figure 7.29 shows the lift loop for the tab ($h_{tab}/c = 2.5\%$) placed at four chordwise positions ($x/c = 1.00, 0.98, 0.95$ and 0.90). The upstream placement of the tab follows the same trend as found for an increase of the tab height: The lift is reduced during the upstroke, while being independent of the exact placement. Furthermore, the impact of the dynamic stall is reduced and the reattachment promoted. The moment curves illustrated in Figure 7.30 do only show a small impact at low angles of attack, where no stall is present.

8 Dynamic Airfoil with an Active Gurney Flap

A final experiment was performed to study the effects of an active system consisting of an oscillating airfoil with an active Gurney flap at the trailing edge. A Gurney flap was chosen for reasons of the lack of an adverse response caused by the convection of the vortex of the tab. The advantages of placing the tab further upstream of the trailing edge to gain a higher effectiveness of the tab at higher angles of attack is overcome by negative dynamic effects such as the overshoot. Furthermore, a tab/flap placement at the trailing edge offers an easier integration of the flap mechanism; it can even be placed there as a retro-fit system. The aim of this chapter was to study the dynamic effects of a combined system consisting of a pitching airfoil an actively oscillating flap.[1]

8.1 Active Gurney Flap Set-up

The measurements were performed with the same airfoil and set-up as described in the previous chapter. Furthermore, for reasons of comparison the reduced frequency as well as the driving angle of attack variations were the same as analysed in the earlier chapter of the oscillating airfoil with fixed tabs. The full-span flap was placed at the trailing edge and featured a hinge of the same diameter as the trailing edge thickness of 0.8mm. The flap itself had a thickness of 1mm and a flap height of $h_{flap} = 5mm$ which corresponds to $h_{flap}/c = 3.6\%$. The hinge of the flap reached through a hole in one end-plate and was driven by a servo-motor placed on the outer side of the end-plate with a maximum speed of $600°/s$. The maximum angular range possible was $\theta max = \pm 52°$. However, this value has proven to be even smaller if the flap is actuated very fast.
The tab's target and actual positions were included in the *LabView* programme and was saved alongside with the measurement data. The function for the movement of the flap was implemented in a way that the flap amplitude as well as the phase between the oscillating flap and the oscillating airfoil could be varied. Figure 8.1 illustrates possible scenarios of such a system for different phase angles.

[1] Results presented in the present chapter have not been published previously. D. Holst programmed the *LabView* programme used for the measuremente. All other tasks were carried out by the author.

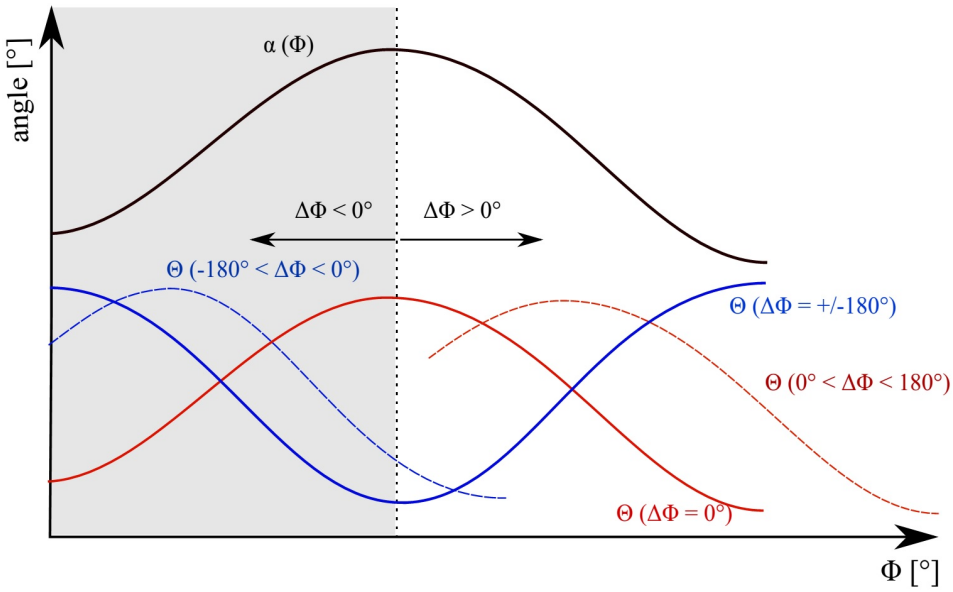

Figure 8.1: Definition of phase shift angle between airfoil and flap

8.2 Pitching in the Pre-Stall Region

For the airfoil in the pre-stall region, an angle of attack variation of $\alpha = 4° \pm 2°$ with a reduced frequency of $k = 0.02$ was chosen. Figure 8.2 shows the lift loops for various different cases: The curves for passive, non-moving flaps were compared to curves where the flap is actuated. Additionally the results from the steady state measurements are shown. As in the previous chapter, one can see that the dynamic curves with a passive flap attached are very close to the corresponding steady state results. It is however interesting to note that in the case of the passive flap with a flap angle of $\theta = 0°$, the lift loop looks much more like the theory of Theodorsen would suggest. The lift in the pitch-up motion is clearly lower than in the pitch-down movement. For the passive flaps directed up or down ($\theta = \pm 45°$), this behaviour cannot be seen. This may be due to the fact that the flap with zero incidence works in favour of Theodorsen's theory by not inducing a vortex street or recirculation zones in front of the flap.
Further shown are the results for the actively moving flap: The two extreme curves are illustrated, depicting the case where the phase shift between the airfoil and the flap movement is zero ($\Delta\phi = 0°$) or shifted by half a period ($\Delta\phi = 180°$). The loops created this way travel between the steady state curves. For the case of a phase shift of $\Delta\phi = 180°$ the effect of the flap is large enough the overcome the slope of the airfoil. The fact that both loops reach values beyond the steady state curves are due to the fact that the flap travels between $\theta = \pm 48°$ and not the $\theta = \pm 45°$ as used for the steady state measurements.
Even though the loops behave more or less as predicted, a few facts stand out: First of all, the hysteresis effects seem bigger in the case of the active flap and the loop appears 'thicker'. Secondly, the direction of the loop is massively influenced: While for the phase angle of $\Delta\phi = 180°$ the loop is counter-clockwise as Theodorsen would suggest, the loop for the phase angle of

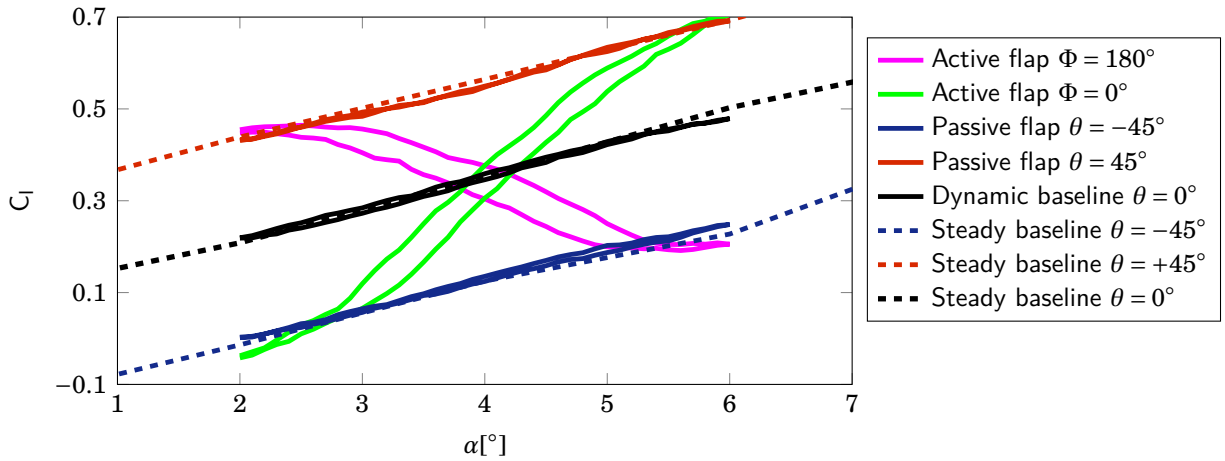

Figure 8.2: Lift loops for airfoil with active and passive flaps, ($k = 0.02$, Re=200k)

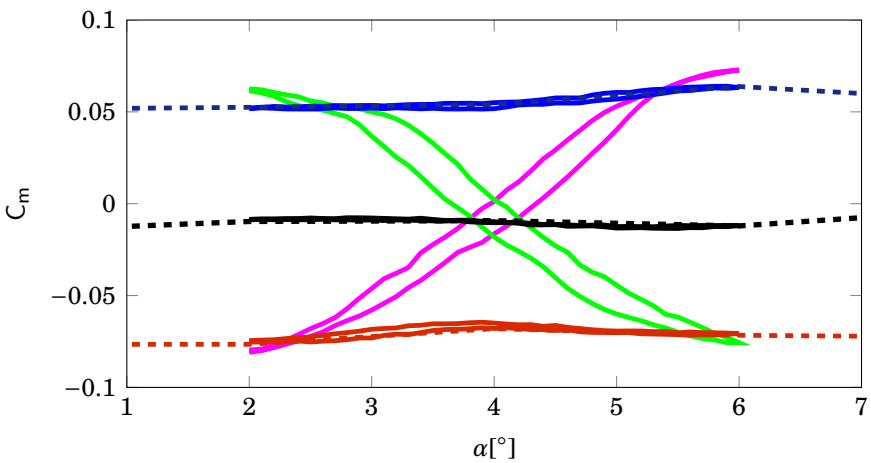

Figure 8.3: Moment loops for airfoil with active and passive flaps ($k = 0.02$, Re=200k)

$\Delta\phi = 0°$ is orientated in a clockwise direction.

The moment response which gives more insight into the aerodynamic damping behaviour is shown in Figure 8.3. All hysteresis loops of the passive flaps are found to be counter-rotating: Hence the aerodynamic damping is negative as it would be for this frequency range when no flap is present. Negative aerodynamic damping is also found for the case of the flap with no phase shift of ($\Delta\phi = 0°$). However, the active flap with a phase shift of $\Delta\phi = 180°$ has found to change the direction of the moment loop to a clock-wise hysteresis. Hence, in this case the aerodynamic damping is positive and energy is removed from the structure.

8.3 Effect of an Actuation Delay

While the load changes caused by yaw misalignment or the earth boundary layer are periodic and predictable, gusts and the wind's turbulence can cause single unpredictable load changes. To counteract these load changes a more sophisticated control cycle is necessary: Periodical loads can be altered with a simple open load control cycle as it is already done in the case of today's individual pitch mechanisms. To counter non-periodical events, however, a closed loop control unit is needed. A sensor is needed to measure the incoming flow, the signal needs to be processed and the counter action initiated. Hence, a significant delay between the inflow change and the counteraction needs to be anticipated. This delay depends massively on the control set-up and sensors. In this section a brief overview is given of control concepts followed by measurement results regarding the aerodynamic response of a delayed flap movement.

8.3.1 Control Concepts for Wind Turbines

Today's large turbines are generally controlled with either a collective or individual blade pitch system. Individual pitch generally allows the reduction of fatigue loads to a certain extent. However, even the more sophisticated individual pitch is not fast enough to react to sudden or local gusts or turbulence. Therefore, new control concepts such as local fast actuators are investigated [42, 141, 146]. In addition to the aerodynamic research focusing on the selection of the control actuator, research is needed on sensors and closed loop control cycles. This work in centered around the selection process of the actuators (in this case flaps and tabs), however the other two areas are equally important for a successful control set-up.

Innovative control concepts for wind turbines can be generally divided into passive or active control concepts. Passive control can improve the overall performance e.g. through the application of vortex generators or micro-tabs at the inner blade sections. Active methods however will always be driven by the question of energy efficiency: The energy that the control set-up requires must be less than the actual energy gained through the control. However, energy maximisation is not the only goal of wind turbine control. Minimisation of fatigue loads and hence a turbine life extension may result in a further reduction of costs. Fatigue loads can be minimised by a control which reduces the load fluctuation on the blade or which provides a better aerodynamic damping [125] [48].
Active mechanisms can be controlled further through either open-loop or closed-loop control cycles with an additional sensor as well as a controller. In both cases (open or closed-loop control) the sensor plays a major role when it comes to the system's reaction time. A suboptimal choice of sensors or controllers may have a negative impact on the loads and overall safety.

Flow sensors have to be robust and reliable without altering the flow that is measured by the same device. Well-known sensors which do not alter the flow are e.g. sensors that measure the skin friction or pressure on the surface, without changing the model geometry. However, these

sensors are generally more problematic when it comes to the application on wind turbine blades which are highly exposed to environmental substances such as ice, dirt or biological residues from insects. Up to date, the most promising sensors for wind turbines are the following:

Modern LiDAR (**Li**ght **D**etection **A**nd **R**anging) systems, which enable a characterisation of a large area of the incoming flow field in front of the turbine. The system transmits a laser beam in front of the turbine and monitors the back-scattered light from the present aerosol. Hence the signals have a Doppler shift proportional to the incoming wind speed. Generally the system transmits pulses by repetitively and simultaneously scanning the back-scattered light. Hence, the range and direction of particles can be gained from the data over a larger area [90].
SODAR (**SO**ound **D**etection **A**nd **R**anging) systems are closely related to the LIDAR systems and are also based on the monitoring of back-scattered signals in front of the wind turbine. In this case, acoustic pulses are sent in the air and are back-scattered on fluctuation of the refractive index of the air. The scattered signals are then measured with microphones on the ground. These acoustic signals have experienced a Doppler shift in frequency from which the velocity can be calculated [90].
Another method is the placement of local sensors in front of the blade during the operation. E.g. these sensors can be Pitot tubes or force sensors. Hence, for a complete sensor system, multiple sensors have to be placed on each blade for a sufficient data resolution needed for the localised control elements.
Another well-discussed method is the use of strain gauges on the blades. The gauges can either be placed along the blade or at the blade root, measuring the overall blade root bending moment. However, this is a sensor concept where the forces are measured when they are already inflicted on the structure. Hence, the time lag of this sensor set-up is the largest and generally depend on the distance between the actuator element and the blade root [107].

Various control strategies have been identified for flow control. Some of the better-known controls are e.g. Neural Networks, adaptive controls, physical model-based, dynamical systems based or controls based on the optimal control theory [71]. Research in the area is mostly done with the help of analytical models of wind turbine control systems. Some examples of control models concerning flap or micro-tab actuators can be found e.g. in [27, 75, 149, 18].

The actuator placement and speed, the sensor system as well as the controller determine how much time is needed from the detection of the disturbance to the reaction of the actuator. Whether the actuator can counter-act the anticipated load change further depends on the aerodynamic response time as well as the time the disturbance needs to reach the blade. Therefore, a general delay time of a system is hard to predict. In the following several delay times are assumed and the impact of the loads are analysed.

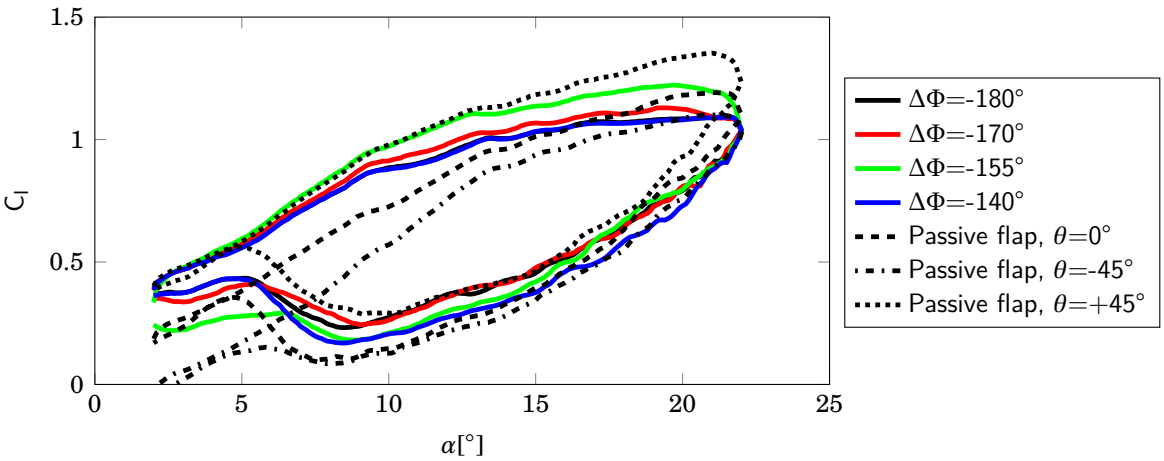

Figure 8.4: Lift loops for airfoil with active and passive flaps in light stall ($k = 0.05$, Re=200k)

8.3.2 Experimental Results for Actuation Delay

Within this set of experiments angle of attack variations up to high angles are investigated. For a basic evaluation the active flap as the counteracting device is used in phase ($\Delta\phi = 0°$) and with a phase shift of $\Delta\phi = 180°$. This is followed by the testing of the effects of a delayed counteraction for several further phase shifts.
Figure 8.4 shows the lift curves for several different phase shifts between the airfoil motion and the flap motion. It can be seen that an optimal phase shift of $\Delta\phi = -180°$ yields the smallest lift for high angles of attack. With increasing delay of the flap actuation ($\Delta\phi > 180°$) the lift reaches higher overall values.

The moment response is illustrated in Figure 8.5. The aerodynamic damping of the dynamic baseline for the passive non-deployed flap ($\theta = 0°$) displays two different aerodynamic damping regions: The lower angles of attack show a region of positive damping while the pitching in the higher angles of attack causes a region of negative damping. If passive flaps are deployed the sizes of the damping regions shift. If the flap is deployed, to the pressure side ($\theta = -45°$) the regions of the positive damping grows at the expense of the negative damping region. This behaviour is the opposite if the flap is deployed to the suction side of the airfoil. If the flap is actively actuated with a phase shift of $\Delta\phi = -180°$ the balance between the two damping regions is influenced as well and the positive damping region is more pronounced. If a delay of the flap is anticipated ($\Delta\phi > -180°$) this effect gets stronger and the size of the negative damping region is further reduced.

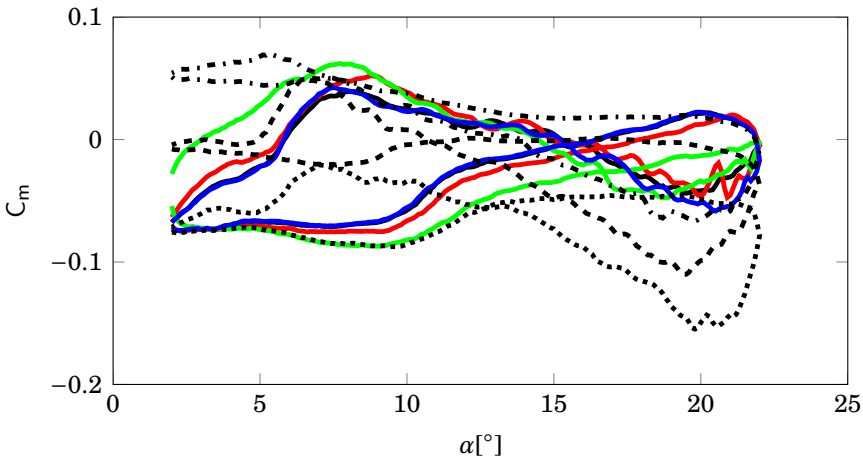

Figure 8.5: Moment loops for airfoil with active and passive flaps in light stall ($k = 0.05$, Re=200k)

8.4 Effect of the Flap Amplitude

In the pre-stall region the maximum achievable flap amplitude of $\theta_{max} = \pm 52°$ has shown to be more than sufficient since the slope of the overall lift could be completely revered (see again Figure 8.2). However, if the airfoil is pitched on occasion to high angles of attack caused by turbulence or gusts, the small flap may not be high enough to counteract these loads completely. To investigate the effect of the flap height further, the maximal flap height was reduced and the impact on the dynamic lift, moment and the damping was observed.
Figures 8.6 and 8.7 show the lift and moment response for varying maximal flap heights. The angle of attack variation is $\alpha = 12° \pm 10°$ and the phase shift between the airfoil and the flap is chosen to be $\Delta\phi = -150°$.

It can be seen that with reduced flap amplitude the effectiveness at high angles of attack is clearly reduced as the passive results in the previous section already suggested. For the smallest flap height of $\theta_{max} = 5°$ the lift loop is nearly identical to the dynamic baseline of the non-deployed flap. Even though slight differences in the stalled pitch-down cycle can be seen, the general behaviour and moment of reattachment remains more or less the same.
The moment loops prove a strong impact of the flap amplitude on the aerodynamic damping: With increasing maximal amplitude the positive damping region at low angles of attack grows in terms of the angle of attack region as well as in width which is equivalent to the strength of the damping.
Most of the studies concerning active flaps only feature flaps with low maximum deflection angles. This is mostly due to the fact, that for bigger flaps, the drag penalty is very high, when the flap is deflected to higher angles. Hence, most of the flaps with a larger flap length only deflect up to around $\theta = 10°$ [133] For most airfoils, larger flap angles are associated with the development of a vortex street and hence a higher drag. The smaller Gurney flap, however, does not suffer from these high drag values and can deflect up to $\theta = 90°$.

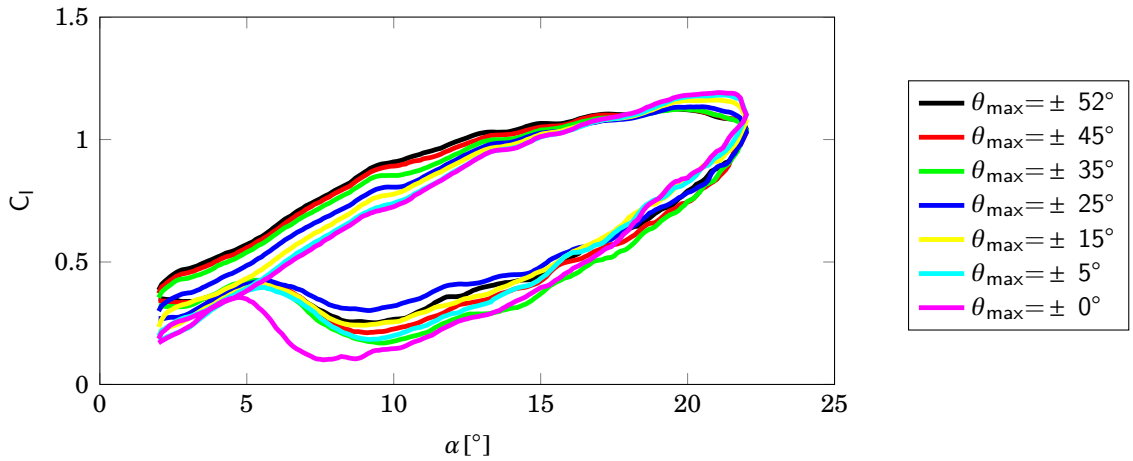

Figure 8.6: Lift loops for airfoil with active flap of varying amplitude, ($k = 0.05$, Re=200k)

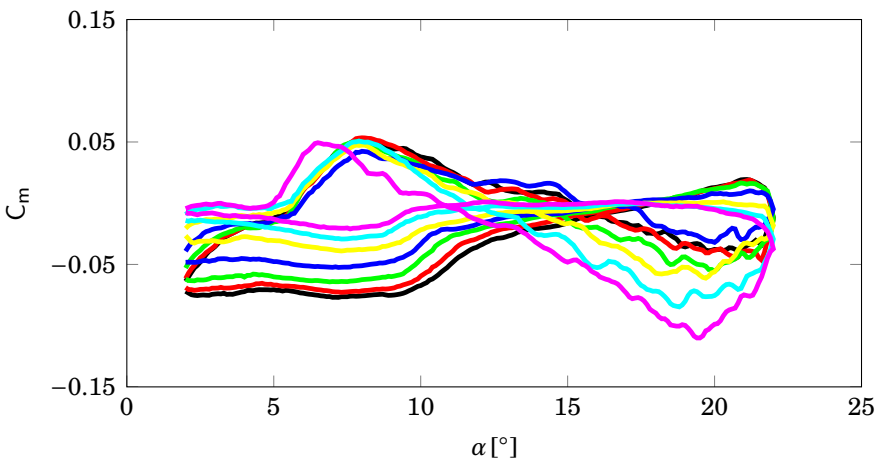

Figure 8.7: Moment loops for airfoil with active flap of varying amplitude, ($k = 0.05$, Re=200k)

8.5 Counteracting Dynamic Stall

The airfoil movement in the stall region was evaluated with passive and active flaps. The angle of attack motion was chosen to be $\alpha = 16° \pm 10°$ corresponding to the previous section. Figure 8.8 illustrates the lift curves for the passive and active flaps. As for the plain airfoil or the airfoil with micro-tabs studied in earlier experiments, the measurements with flaps also display the manifestation of a dynamic stall vortex at the end of the pitch-up cycle. However, it can be seen that the vortex starts shifting slightly with the angle of the passive flap: For both cases, the passive flap deflected upward as well as the passive flap deflected downward, the shedding of the vortex is shifted to lower angles of attack. Thereby, for the upwards deflected flap, the angle of attack where the shedding takes place is the lowest with $\alpha = 25°$. Furthermore, a clear difference in effectiveness can be seen between the passive flaps. The downwards directed flap for load enhancement clearly maintains the lift difference over nearly all angles of attack in the

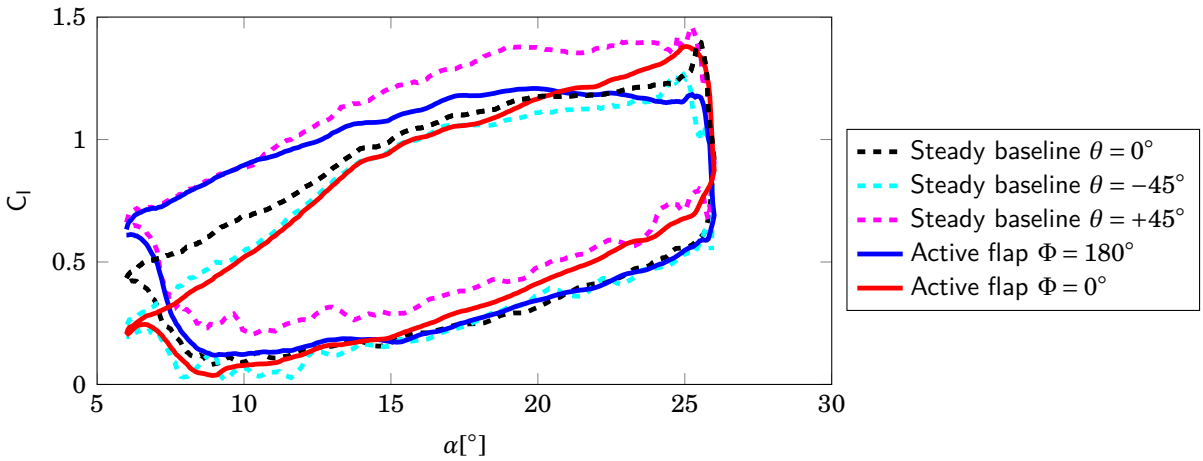

Figure 8.8: Dynamic lift for active and passive flap with dynamic stall, ($k = 0.05$, Re=200k)

pitch up cycle. The upwards directed flap, however, loses lift difference as higher angles are approached. After an angle of attack of $\alpha = 15°$ the lift difference remains more or less constant until the dynamic stall is shed.

The active flap was tested for a phase angle of $\Delta\phi = 0°$ and $\Delta\phi = 180°$. The maximal angular flap deflection possible was $\theta_{max} = 48°$. At the mean angle of attack of $\alpha = 16°$ the flap is in a neutral position, however, the angle of attack where the lift curves of the active flap crosses the baseline curve is much higher around $\alpha = 21°$. This can be explained by the delay of the lift response as found earlier. Additionally it can be seen that the dynamic stall vortex is influenced as well. On the one hand, for the active counteracting flap ($\Delta\phi = 180°$) the lift is massively reduced right before the airfoil pitches down again. The lift peak caused by the vortex is smaller than for the passive flap deflected downwards. On the other hand, the lift peak of the flap which is acting in phase with the airfoil ($\Delta\phi = 0°$) is larger and wider and a single peak which can be associated with the shedding of the dynamic stall vortex cannot be identified.

The aerodynamic damping of the flap system was analysed using the moment curves. Figure 8.9 shows the dynamic moment curves of the pitching airfoil with active and passive flaps. The airfoil with a passive non-deflected flap depicts a typical shape as the literature would suggest. The usual two inter-crossings of the curves can be found, dividing the motion in three sections of aerodynamic damping: Between $6° < \alpha < 14°$ the aerodynamic damping is positive, followed by a negative damping from an angle around $15° < \alpha < 25°$. In the last part of the pitching cycle the dynamic stall vortex influences the moment and the damping changes back to positive damping. The deflection of the passive flaps influences the aerodynamic damping. The downwards deflected flap inflicts a larger first region of positive damping, while the upwards orientated flap early dissolves this first damping region. However, at the same time, the third (positive) damping region caused by the dynamic stall is enlarged for both cases with a deflected passive flap.

Comparing the two extreme cases for the active flap with $\Delta\phi = 0°$ and $\Delta\phi = 180°$ it can be

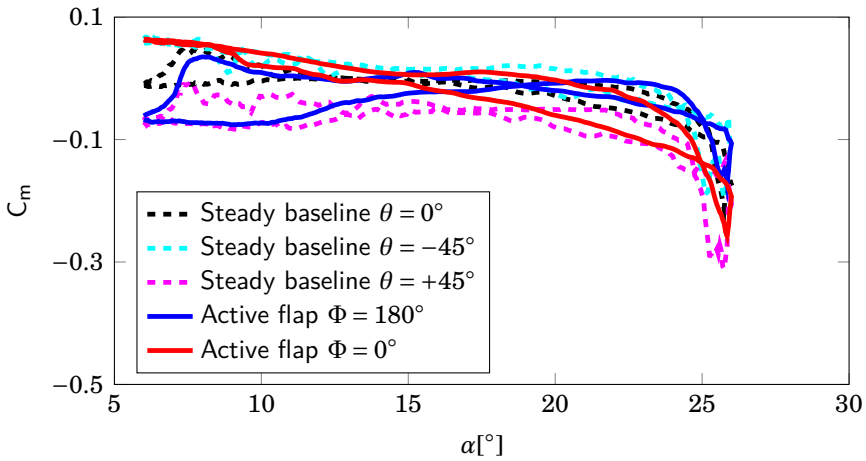

Figure 8.9: Dynamic moment for active and passive flap with dynamic stall ($k = 0.05$, Re=200k)

seen that the aerodynamic damping is significantly changed. Meanwhile the flap working under a phase shift of $\Delta\phi = 180°$ massively increases the first positive damping region, the moment curve for $\Delta\phi = 0°$ features only two damping regions: A large negative damping region and a smaller positive one associated with the dynamic stall.

Therefore, an active flap working with a phase shift of $\Delta\phi = 180°$ does reduce maximum lift and may work favourable to reduce cyclic load changes. However, at the same time, the overall damping properties are degraded. For the opposite flap movement with a phase-shift of $\Delta\phi = 0°$ the lift is increased and fatigue loads are enhanced but the positive damping is larger. It was shown in the past that most dynamic stall methods cannot improve lift and pitching/damping characteristics at the same time [77]. This contradicting problem was also found in studies concerning conventional flaps [79].

9 Analytical Model

This final chapter focuses on the analytical models which can be used to simulate dynamic actuation of flaps and micro-tabs on pitching airfoils. A theoretical background on basic unsteady aerodynamic modelling is given, followed by a comprehensive model for the load response of a micro-tab actuation. The different models have been coupled and provide a good simulation tool to compare several actuation and configuration cases. [1]

9.1 Unsteady Aerodynamic Modelling

9.1.1 Theodorsen's Theory

Models on unsteady aerodynamics were developed first in the 1930's. These models are elegant and powerful tools to predict unsteady phenomena such as flutter, buffeting, transient flows or gusts. Theodorsen's theory developed in 1935 [132] is a well-known solution of the aerodynamic response of an unsteady moving airfoil in viscid, incompressible flow with only small disturbances. The model is based on thin airfoil theory and potential flow where the wake is represented by a continuously shed vortex sheet (see Figure 9.1).

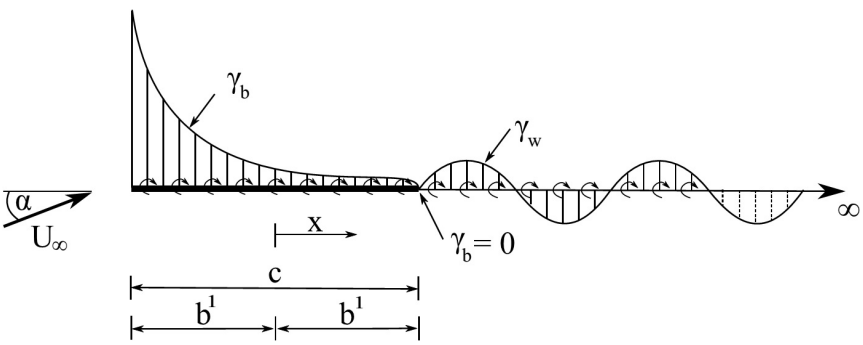

Figure 9.1: Mathematical model used by Theodorsen [80]

If the circulation on the airfoil is changed over time, the vortex sheet experiences a change of vortex strength. Hence the vortex sheet can be understood as a time history of the airfoil's

[1] Results presented in the present chapter have not been published previously. The micro-tab model is the work of B. Vieira of the PSU - Department of Aerospace Engineering and was kindly provided prior to publishing. The implementation and application of the model as well as the coupling with further aerodynamic models leading to the results presented in this chapter were done by the author.

loads. The governing equation here is the calculation of the downwash w on the surface caused by all vortices of the system:

$$w(x,t) = \frac{1}{2\pi}\int_0^c \frac{\gamma_b(x,t)}{(x-x_0)}dx + \frac{1}{2\pi}\int_c^\infty \frac{\gamma_w(x,t)}{(x-x_0)}dx \quad . \tag{9.1}$$

Hence, if the airfoil loads and therefore the airfoil's circulation is changed due to an external forcing, the shed vortices will change over time and induce a time-dependent downwash. This in turn again affects the loads. The solution of this problem is given in a state-space formulation which connects the forcing function (e.g. a pitching $[\alpha, \dot{\alpha}]$ or plunging motion $[h, \dot{h}]$) to the aerodynamic response of the loads. Equations (9.2) and (9.3) show the result of Theodorsen's theory in coefficient form:

$$C_l = \pi b^1 \left(\frac{\ddot{\alpha}}{U_\infty} + \frac{\ddot{h}}{U_\infty^2} - \frac{b^1 a \ddot{\alpha}}{U_\infty^2} \right) + 2\pi C(k) \left[\frac{\dot{h}}{U_\infty} + \alpha + b^1 \left(\frac{1}{2} - a \right) \frac{\dot{\alpha}}{U_\infty} \right] \tag{9.2}$$

$$\begin{aligned} C_{m_{1/2}} &= \frac{\pi}{2} \left[\frac{b^1 a \ddot{h}}{U_\infty} - \frac{(b^1)^2}{U_\infty^2} \left(\frac{1}{8} + a^2 \right) \ddot{\alpha} \right] + \pi \left(a + \frac{1}{2} \right) \\ &\times \left[\frac{\dot{h}}{U_\infty} + \alpha + b^1 \left(\frac{1}{2} - a \right) \frac{\dot{\alpha}}{U_\infty} \right] C(k) - \frac{\pi}{2} \left[\left(\frac{1}{2} - a \right) \frac{b^1 \dot{\alpha}}{U_\infty} \right] \quad . \end{aligned} \tag{9.3}$$

The second parts in Equations (9.2) and (9.3) include the so-called *Theodorsen's function* $C(k)$ and are known as the *circulatory lift* part. The circulatory lift is the part of the lift which originates from the effect of the shed wake on the unsteady loads. In it, the parameter k represents the dimensionless frequency of the harmonic forcing as defined earlier in Section 7.1.1. The remaining terms result from the *apparent mass* or *non-circulatory* effect. These additional forces are caused by the acceleration of the fluid in the vicinity of the airfoil due to its motion. Theodorsen's function $C(k)$ within the circulatory part can further be expressed as:

$$C(k) = F(k) + i\,G(k) = \frac{H_1^{(2)}(k)}{H_1^{(2)}(k) + i\,H_0^{(2)}(k)} \quad , \tag{9.4}$$

wherein the Hankel function is defined as $H_v^{(2)} = J_v - i\,Y_v$ with the Bessel functions J_v and Y_v.

9.1.2 Indicial Formulation

The presented formulation of Theodorsen is written in a state-space formulation. This approach is advantageous when it comes to computational costs and is suitable e.g. if control cycles need to be implemented. Alternatively, a transfer function between the forcing and the aerodynamic response can be formulated instead of the state-space formulation. Using this form is advantageous for analyses in the frequency domain. However, for arbitrary motions and further inclusion of aeroelastic effects the use of a third formulation, the indicial functions, have

proven to be useful. Indicial functions are written in the time domain and are therefore detached from the reduced frequency k.

Wagner and Küssner Function

The first exact solution of the indicial formulation for the circulatory lift was found in 1925 by Wagner [143] for a thin airfoil experiencing a step change in angle of attack:

$$C_l(t) = \frac{\pi c}{2U_\infty}\delta(t) + 2\pi\alpha\Phi(s) \quad . \tag{9.5}$$

In it, $2\pi\alpha$ represents the steady state lift coefficient of the thin airfoil theory, $\delta(t)$ is the Dirac-delta function, and $\Phi(s)$ is the so called *Wagner function*. The latter is dependent on the variable s which describes the distance travelled by the airfoil in half chords. A first approximation of the Wagner function was given by Jones in 1945 [65] with

$$\Phi(s) \approx 1 - 0.165e^{-0.041s} - 0.335e^{-0.32s} \quad . \tag{9.6}$$

In a rotating system of wind turbines, unsteady inflow conditions are an important issue. The blades experience a changing inflow condition over one resolution, e.g. due to yaw or the earth boundary layer. Hence the induced downwash as defined in Equation (9.1) varies over the rotor plane. The solution to this problem differs from the problem tackled by Wagner since the change of inflow does not simultaneously affect the whole blade element as it is e.g. the case for a pitching or plunging motion of the airfoil. Rather, a gust hits the leading edge and then travels over the airfoil's surface with time. As a result, the indicial response to such a gust must look different than the Wagner function. A first attempt to solving this problem was made by Küssner in 1935 [72] leading to the following expression:

$$C_l(t) = 2\pi\left(\frac{w_0}{U_\infty}\right)\Psi(s) \quad . \tag{9.7}$$

Thereby, $\Psi(s)$ represents the so called *Küssner function* [72]. The Küssner function, similar to the Wagner function, can be approximated as

$$\Psi(s) \approx 1 - 0.5e^{-0.13s} - 0.5e^{-1.0s} \quad . \tag{9.8}$$

Figure 9.2 compares the development of the Wagner and the Küssner function. The Wagner function initially starts at a value of 0.5 and asymptotically builds up to a value of 1 for s approaching infinity. Meanwhile, the Küssner function starts at a value of 0 but approaches the value of 1 faster.

9.1.3 Indicial Function for a Plain Airfoil

A main advantage of indicial function is that they can be used for arbitrary motions of the airfoil or unsteady inflow conditions. So far, only the exact solutions for incompressible flow for a step

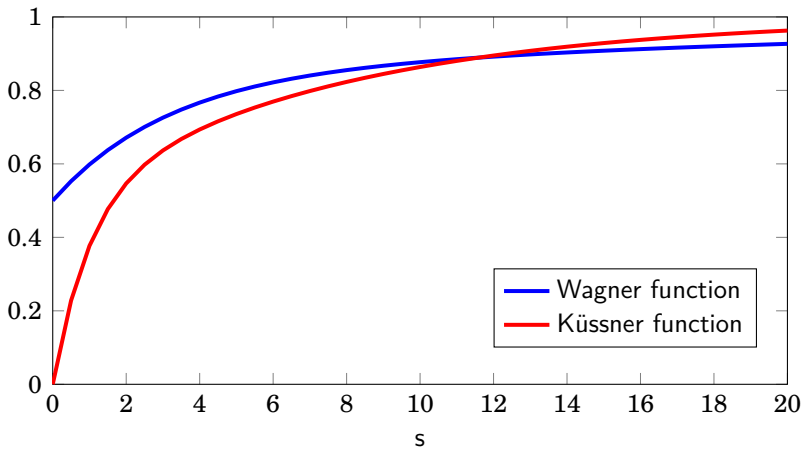

Figure 9.2: Wagner and Küssner function

change in angle of attack (Wagner) or inflow (Küssner) are known. Hence, to model arbitrary motions numerical methods must be found for the superposition of the response functions. Furthermore, experimental measurements can be used to gain the transfer functions of the forcing and the aerodynamic response to obtain good approximations of the indicial response functions.

Circulatory Lift of an Airfoil

Generally, the time-dependent circulatory lift can be expressed through the lift slope $C_{l,\alpha}$ and an effective angle of attack α_{eff} (for derivation see [80]):

$$C_l = C_{l_\alpha} \cdot \alpha_{eff} \quad . \tag{9.9}$$

The effective angle of attack α_{eff} at the time step n contains the information of all precious actions and can be derived further as

$$\alpha_{eff,n} = \alpha_n - X_n - Y_n, \tag{9.10}$$

$$X_n = X_{n-1} e^{-b_1 \beta \Delta s} + A_1 \Delta \alpha_n e^{-b_1 \beta \Delta s/2} \quad , \tag{9.11}$$

$$Y_n = Y_{n-1} e^{-b_2 \beta \Delta s} + A_2 \Delta \alpha_n e^{-b_1 \beta \Delta s/2} \quad , \tag{9.12}$$

where the functions X_n and Y_n incorporate the time-history information. The compressibility of the fluid is taken into account through the factor $\beta = \sqrt{(}1 - Ma^2)$. Usually the system constants b_1, b_2, A_1 and A_2 are determined through experiments by fitting the data to the modelled results.

Non-Circulatory Lift of an Airfoil

The non-circulatory lift part or apparent mass term can also be expressed in an indicial formulation at the time step n [19]:

$$C_{l,nc} = \frac{4K_\alpha c}{U_\infty}\left(\frac{\Delta\alpha_n}{\Delta t} - D_n\right) \quad . \tag{9.13}$$

wherein the deficiency function is calculated as

$$D_n \quad = \quad D_{(n-1)}e^{\frac{-\Delta t}{K_\alpha T_l}} + \left(\frac{\Delta\alpha_n - \Delta\alpha_{n-1}}{\Delta t}\right)e^{\frac{-\Delta t}{2K_\alpha T_l}} \quad . \tag{9.14}$$

The function K_α is a function of the Mach number and given by

$$K_\alpha = \frac{0.75}{(1-Ma)+\pi\beta^2 Ma^2(A_1 b_1 + A_2 b_2)} \quad . \tag{9.15}$$

9.2 Indicial-Based Micro-Tab Model

In the case of a micro-tab, the response model is more complicated. The part of the response which originates from the building vortex if the micro-tab is applied can not be represented by the circulatory or apparent mass terms. Vieira et al. [142] have proposed an aerodynamic response model based on indicial concepts for the response of micro-tabs. For an aerodynamic model on the response of micro-tabs, the lift overshoot caused by the vortex build-up and convection over the airfoil surface is essential. A normal flap response could be modelled by simply using a indicial concept based on the circulatory lift and apparent mass terms as defined before. Vieira et al. developed two versions of indicial models for micro-tabs: The first version gives a basic idea of the indicial method applied to micro-tabs [142]; the second and improved version was provided prior to publishing and after having consultated with B. Vieira, will be explained below. This improved version includes the moment response and is more accurate and universally applicable.

9.2.1 Circulatory Lift

The lift response is calculated from a circulatory as well as vortex lift increment. The apparent mass term is negligible for reduced frequencies of $0 \leq k \leq 1$. If the reduced frequency is higher than that, the apparent mass term can be added as described in [142]. Hence the total lift response can be expressed as:

$$\Delta C_l^n \quad = \quad \Delta C_{l,circ}^n + \Delta C_{l,vtx}^n \quad . \tag{9.16}$$

The circulatory lift increment is based on the micro-tab height over time as the driving forcing function. Hence, according to Equations 9.9 and 9.10 the circulatory lift is determined with

$$\Delta C^n_{l,circ} = \frac{h^n_{l,eff}}{h_{MT}} \cdot \Delta C_{l,MT} \quad \text{and} \tag{9.17}$$

$$h^n_{l,eff} = h^n_{l,qs} - D^n_{1,circ} - D^n_{2,circ} - D^n_{3,circ} \quad . \tag{9.18}$$

Hereby, the effective micro-tab height consists of three circulatory deficiency functions D^n_{circ} and not of two as for the effective angle of attack of Equation 9.10. This is due to the underlying indicial function, which is characterised by a three-term exponential function for the case of the response of a micro-tab:

$$\Phi(s) = 1 - A_{1,circ} e^{-b_{1,circ}\beta^{\gamma} s} - A_{2,circ} e^{-b_{2,circ}\beta^{\gamma} s} - A_{3,circ} e^{-b_{3,circ}\beta^{\gamma} s} \quad . \tag{9.19}$$

The deficiency functions D^n_{circ} are calculated as follows:

$$D_{1,circ} = D^{n-1}_{1,circ} \cdot e^{-b_{1,circ}\beta^{\gamma}\Delta s} + A_{1,circ} \cdot \Delta h^n_{l,qs} \cdot e^{\frac{-b_{1,circ}\beta^{\gamma}\Delta s}{2}} \quad , \tag{9.20}$$

$$D_{2,circ} = D^{n-1}_{2,circ} \cdot e^{-b_{2,circ}\beta^{\gamma}\Delta s} + A_{2,circ} \cdot \Delta h^n_{l,qs} \cdot e^{\frac{-b_{2,circ}\beta^{\gamma}\Delta s}{2}} \quad , \tag{9.21}$$

$$D_{3,circ} = D^{n-1}_{3,circ} \cdot e^{-b_{3,circ}\beta^{\gamma}\Delta s} + A_{3,circ} \cdot \Delta h^n_{l,qs} \cdot e^{\frac{-b_{3,circ}\beta^{\gamma}\Delta s}{2}} \quad , \tag{9.22}$$

wherein $\Delta h^n_{l,qs}$ is the effective quasi-steady micro-tab height $\Delta h^n_{l,qs} = h^n_{l,qs} - \Delta h^{n-1}_{l,qs}$. As explained in Section 5.1.2, the micro-tab has a minimal height at which the tab works effectively. For tab heights smaller than this effective height, the recirculation bubble behind the tab does not extend to the trailing edge. Hence, the effect on the lift is opposite to that intended. To account for this non-linear effect of the micro-tab height, the forcing function is represented through the effective quasi-steady micro-tab height. This height is defined as follows:

$$h^n_{l,qs} = \left(\frac{C^n_{l,qs} - C_{l,base}}{\Delta C_{l,MT}} \right) \cdot h_{MT} \quad . \tag{9.23}$$

In it, the quasi-steady lift coefficient $C^n_{l,qs}$ is an empirical value and gained by interpolating measured data. The values for the baseline $C_{l,base}$ and $\Delta C_{l,MT}$ are the maximum possible values, even if the tab is not extend to its full capacity. Finally, h_{MT} represents the actual micro-tab height in chord lengths.

9.2.2 Circulatory Moment

The calculation of the circulatory moment increment corresponds with the calculation of the circulatory lift increment:

$$\Delta C_m^n = \Delta C_{m,circ}^n + \Delta C_{m,vtx}^n \quad . \tag{9.24}$$

Hence, Equations 9.17-9.23 can be applied analogously. However, another effective quasi-steady micro-tab height needs to be introduced for the moment calculation.

9.2.3 Vortex Lift

The vortex lift increment in Equation 9.16 plays an important role in the initial part of the response. In the first moments after the deployment, the vortex formed at the micro-tab convects over the surface and causes an instantaneous pressure region on the surface which in turn affects the lift and the moment. The strength of the vortex as well as the convection speed determine the maximal lift overshoot and the exact time of the occurrence. When the vortex finally convects in the wake, the effect of the vortex on the lift vanishes and the circulatory lift is dominating the aerodynamic response. The vortex lift increment is determined by Vieira et al. by

$$\Delta C_{l,vtx}^n = V_f \cdot \Delta C_{l,MT} \qquad \text{with} \tag{9.25}$$

$$V_f = \Gamma_{vtx,l} \left[sin\left(\frac{\pi(s - s_{ini})}{2T_{v,eff}} \right) \right]^{\frac{3}{2}} \quad . \tag{9.26}$$

Hereby, $\Gamma_{vtx,l}$ represents the vortex strength, s_{ini} is the dimensionless time delay (in half-chords of travel) that the vortex needs to detach from the tab, and $T_{v,eff}$ is the dimensionless time that the vortex needs to reach the trailing edge. For a better understanding, these parameters are illustrated in Figure 9.3.

<u>Vortex Detachment</u>

The first unknown in this equation is the initial delay s_{ini} which is determined through the height of the micro-tab where the onset of the vortex convection occurs: $s = s_{ini}$ if $h = h_{ini,0}$. It was found that the height at which the vortex detaches is not constant but further dependent on the non-dimensional rate of motion of the tab h^+ and the Mach number Ma:

$$h_{ini} = h_{ini,0} + h^+ \cdot \left(\frac{T_{ini}}{\beta_{data}} \right) \quad . \tag{9.27}$$

Since Equation 9.27 is a linear function, it was assumed that the aerodynamic lags which govern the start of the vortex detachment are of a first order. Hence, the underlying indicial function can be written as:

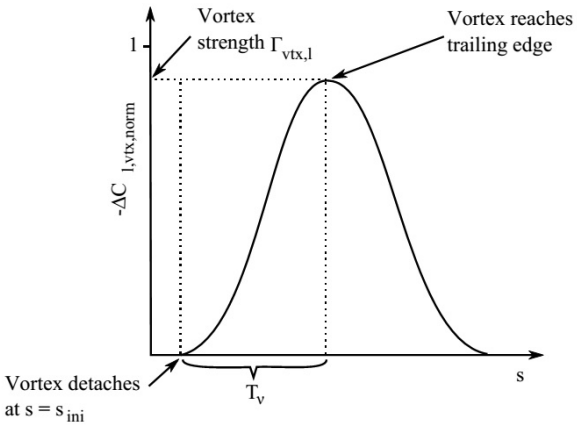

Figure 9.3: Parameters of the vortex lift

$$\Phi_{vtx,ini} = 1 - e^{\left(-\frac{\beta \cdot s}{\beta_{data}}\right)} \quad . \tag{9.28}$$

The solution of this indicial function is gained as described above through the Duhamel integral by introducing an effective initial height.

$$h^n_{ini,eff} = h^n - D^n_{1,ini} \qquad \text{with} \tag{9.29}$$

$$D^n_{1,ini} = D^n_{1,ini} \cdot e^{\left(-\frac{\beta \Delta s}{T_{ini}}\right)} + \Delta h^n \cdot e^{\left(-\frac{\beta \Delta s}{2T_{ini}}\right)} \quad . \tag{9.30}$$

Vortex Convection

The second unknown parameter of Equation 9.26 is the effective reduced time the vortex needs to travel to the trailing edge $T_{v,eff}$. During the convection, the vortex gains in strength and speed until it finally reaches the trailing edge. How fast it reaches the trailing edge and how strong the vortex becomes is further dependent on the rate of the micro-tab deployment h^+ and compressibility factor β. The average reduced time T_v can be calculated by

$$T_v = A_{tv}\, \beta_{data}\, (h^+)^{n_{Tv}} \quad . \tag{9.31}$$

Here, $\beta_{data} = 0.3$ is the compressibility factor of the CFD data used for the derivation of Equation 9.31. A_{tv} and n_{Tv} are constants summarised in Table 9.2. The time T_v can again be associated with a corresponding tab height h_{TE}, which is the tab height where the vortex reaches the trailing edge. From the CFD data available, Vieira et al. extrapolated the dependency of the tab height h_{TE} on the dimensionless deployment rate h^+:

$$h_{TE} = h_{TE,0} + h^{+} \cdot \left(\frac{T_{TE}}{\beta_{data}} \right) \quad , \tag{9.32}$$

wherein $h_{TE,0}$ and T_{TE} again are constants listed in Table 9.2. Furthermore, $h_{TE,0}$ represents the minimum Gurney flap height which is needed to achieve the desired lift change as mentioned above. Below that height, the separation bubble behind the tab does not reach the trailing edge and changes the lift in the opposite direction to that intended.
The vortex convection process is further associated with an aerodynamic lag. The separation region does not react instantaneously but with a lag. Hence, the first-order indicial response can be formulated with a corresponding effective height

$$h^{n}_{TE,eff} = h^{n} - D^{n}_{1,TE} \qquad \text{with} \tag{9.33}$$

$$D^{n}_{1,TE} = D^{n}_{1,TE} \cdot e^{\left(-\frac{\beta \Delta s}{T_{TE}}\right)} + \Delta h^{n} \cdot e^{\left(-\frac{\beta \Delta s}{2 T_{TE}}\right)} \quad . \tag{9.34}$$

Here, the effective tab height represents the cumulative effect on the vortex convection of the time history of the underlying arbitrary tab motion. From this equation the effective non-dimensional motion rate can be derived as

$$h^{+^{n}}_{TE,eff} = \frac{h^{n}_{TE,eff} - h^{n-1}_{TE,eff}}{\Delta s} \quad . \tag{9.35}$$

Finally, the corresponding effective vortex convention time can be calculated, which is needed for the lift associated with the vortex convention (Equation 9.26):

$$T_{v,eff} = A_{tv}\, \beta (h^{+}_{TE,eff})^{n_{Tv}} \quad . \tag{9.36}$$

Vortex Strength

The last unknown parameter of Equation 9.26 is the vortex strength $\Gamma^{n}_{vtx,l}$. Generally, the vortex strength build-up during the convention process until it reaches its final value when the vortex arrives at the trailing edge. Vieira et al. showed in CFD investigations, that the additional lift associated with the vortex is proportional to the magnitude of the corresponding aerodynamic lag. Hence, the vortex strength is formulated as follows:

$$\Gamma^{n}_{vtx,l} = C_{vtx,l} \cdot \beta^{\gamma} \left(h^{n}_{TE,eff} - h^{n} \right) \quad , \tag{9.37}$$

wherein $C_{vtx,l}$ is a constant listed in table 9.1 .

	A_1	A_2	A_3	b_1	b_2	b_3
Lift - deployment	0.3589	0.1764	0.4647	0.1496	0.00214	2.9835
Lift - retraction	0.3589	0.1764	0.4647	0.2169	0.05738	0.9814
Moment - deployment	0.7949	0.2051	-	2.9503	0.00857	-
Moment - retraction	0.7949	0.2051	-	1.5113	0.053169	-

Table 9.1: Semi-empiric constants of the indicial micro-tab model by Vieira

T_{ini}	$h_{ini,0}$	T_{TE}	$h_{TE,0}$	A_{Tv}	n_{Tv}	$C_{vtx,l}$	$C_{vtx,m}$	γ
0.2972	0.003629	0.9536	0.006614	0.0435	-0.64876	1.715	1.159	4

Table 9.2: Further parameters of the micro-tab model by Vieira

9.2.4 Vortex Moment

For the calculation of the aerodynamic moment caused by the presence of the vortex $C_{m,vtx}$, an elegant and simple solution was found by multiplying the lift force of the vortex with the moment arm. The moment arm is the distance from the quarter-chord point of the airfoil to the Gurney flap position on the airfoil $(x/c)_{MT}$.

$$\Delta C^n_{m,vtx} = \left(\frac{C_{vtx,m}}{C_{vtx,l}}\right) \cdot \Delta C^n_{l,vtx} L_{arm} \quad \text{and} \tag{9.38}$$

$$L_{arm} = \left(\frac{x}{c}\right)_{MT} - 0.25 \tag{9.39}$$

wherein $C_{vtx,m}$ is a constant determined through CFD.

For the retraction case, Vieira et al. did not find any delay as it was found in the conducted measurements in this thesis. However, the response functions were found to differ slightly and the indicial constants for the retraction process vary. All constants found by Vieira et al. are summarised in Tables 9.1 and 9.2 .

9.3 Comparison of Model and Conducted Measurements

Within this section, the model explained above will be applied to simulate the experiments conducted within this work. The aim is to get a better idea of how universally applicable the model is as well as building a foundation for future integrations in more complex aerodynamic wind turbine models. For the simulation and reproduction of the experiments on the NACA0018 the steady state data presented in Section 6.1 is used.

	$h_{tab}/s = 0$	$h_{tab}/c = 0.0005$	$h_{tab,crit}/c = 0.001$
$C_{l,estimated}$	$C_{l,base}$	$C_{l,base} + 0.002$	$C_{l,base}$
$C_{m,estimated}$	$C_{m,base}$	$C_{m,base} + 0.0001$	$C_{m,base}$

Table 9.3: Additional data created to model behavior underneath critical tab height

From the set of experiments performed, the tab deployment to the suction side at an angle of $\alpha = 7°$ was chosen to be remodelled. However, for a physically correct behaviour, a critical tab height was estimated and added to the available steady state data. Hence, first an estimation was needed to be conducted for the critical tab height as well as for the lift and moment values when the tab is below this tab height. Since the adverse response in this experiment was very small, only small adverse coefficient values were considered. Furthermore, since the tab deployment was on the suction side at a rather high angle of attack, it was assumed, that the critical tab height under this circumstances would also be very small. The additional data chosen for the model is listed in Table 9.3.

Lift and moment values for tab height stages in between the known measured and estimated steady state values were calculated through a spline function since abrupt changes of the quasi-steady lift response produce unphysical behaviour in the calculation process of the circulatory lift term.

After the input from the experiments was done, the model parameters needed to be optimised in order to match the experimental response functions. First of all, since no obvious lift overshoot was found in these results, the vortex response needed to be modified. As explained in earlier sections, the slot between the micro-tab and the airfoil is suspected to be the major reason for this behaviour. From research in the area of spoilers, this slot is suspected to massively reduce the lift overshoot. Consequently, the lift does not produce any adverse values at the beginning of the motion but the vortex effect influences the way the lift rises, since the vortex lift is not strong enough in comparison to the circulatory lift. Therefore, the vortex strength was reduced while the time dependent parameters of the vortex shedding were not changed. The latter was not possible since high-speed PIV data was not available to estimate these parameters. Secondly, the parameters driving the shape of the response functions needed to be modified. E.g. the parameters of the original lift function of Vieira et al for the VR-8 airfoil were set in a way that the lift needed a very long time to reach the steady state values. In the experiments performed in this work, however, the steady state lift values were reached rather fast in comparison. All parameters used to simulate this experiment ($\alpha = 7°$) are summarised in Tables 9.4 and 9.5.

Figures 9.4 and 9.5 show the comparison of the modeled and experimental responses for the lift and moment for four different deployment times. For a better comparison with the experiments, these were illustrated over the dimensionless time t^* which is related to the dimensionless time s in the following way: $t^* = s/2$. All model parameters remained the same for the various times. Hence, even though slight differences remain the overall prediction is reasonable under

	A_1	A_2	A_3	b_1	b_2	b_3
Lift - deployment	0.5689	0.1764	0.4647	0.2169	0.05738	0.9814
Lift - retraction	0.3589	0.1764	0.4647	0.2169	0.05738	0.9814
Moment - deployment	0.7949	0.2051	-	2.9503	0.00857	-
Moment - retraction	0.7949	0.2051	-	1.5113	0.053169	-

Table 9.4: Indicial constants of the micro-tab model to remodel the experiments

T_{ini}	$h_{ini,0}$	T_{TE}	$h_{TE,0}$	A_{Tv}	n_{Tv}	$C_{vtx,l}$	$C_{vtx,m}$	γ
0.2972	0.003629	0.9536	0.006614	0.0435	-0.64876	1.715	1.159	4

Table 9.5: Further parameters of the micro-tab model to remodel the experiments

the circumstances that no detailed input data on the vortex size and strength was available and, moreover, the steady state data only consisted of the data of four tab heights. An overall improvement can certainly be achieved by gathering more steady state data including data for the critical tab height and below it.

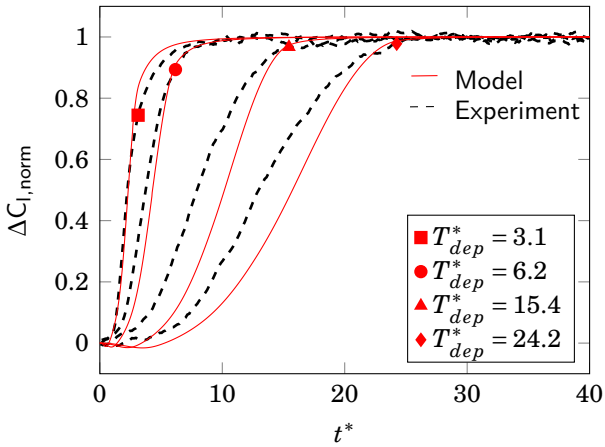

Figure 9.4: Comparison of modeled and experimental lift response for tab with varying deployment times

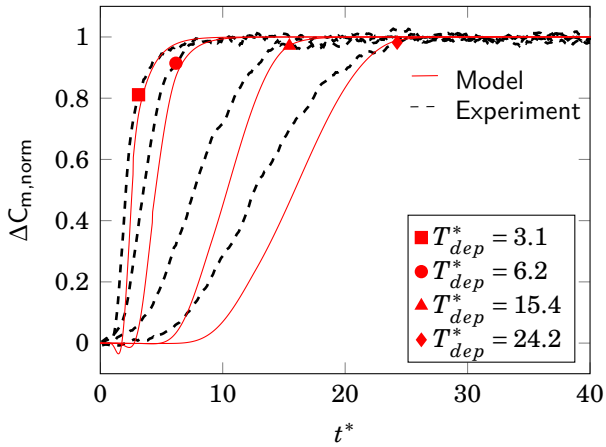

Figure 9.5: Comparison of modeled and experimental moment response for tab with varying deployment times

9.4 Parameter Study with Indicial Micro-Tab Model

The model constants used above were derived from CFD results by Vieira [142] for a Boeing-Vertol VR-7 airfoil with a tab placed at 90% chord. CFD was conducted for various tab heights and deployment procedures and the model parameters gained (listed in Tables 9.1 and 9.2).

The indicial approach of the model allows to simulate various tab movements such as a ramp deployment, a quarter-sine deployment as well as continuous actuation. In the following the model results are discussed for the three motions mentioned. In doing so, all original model parameters for the VR-7 were used.

9.4.1 Influence of the Deployment Function

In the following, the model was applied to different tab deployment functions to investigate if one function is more advantageous than the other. The lift response of a tab deploying following the first $\pi/4$ of a sinusoidal curve can be seen in Figure 9.6. The dimensionless deployment time is $s_{deploy} = 1$ and the final tab height $h_{tab}/c = 0.02$. First, the circulatory lift (as defined in Equation 9.17) drops before it asymptotically rises to its steady state value. This phenomenon is caused by the ambivalent effect that as long as the tab has not yet reached the critical height, the tab produces a lift increment of opposite sign to that intended. This critical height is integrated in the model through the input of the quasi-steady lift data. In this case the data comes from the simulations of Vieira et al. [32] on the VR-7 airfoil, where the critical tab height was $h_{tab} = 0.005c$. After this initial phenomenon, the effect of the vortex can be seen. At a dimensionless time of $s = 0.45$ the effect of the vortex on the lifts starts and rises in its influence up to $s = 1.0$, causing the total lift to drop to a minimal value of $\Delta C_{l,norm} = -0.45$.
The sinusoidal deployment function is now compared to a ramp function where the tab height rises linearly to its final value (see Figure 9.7). Here, the deployment time was the same as for the case of the sinusoidal deployment. The two curves are very similar in their general behaviour and in the overall reached values. However, comparing the two lift curves carefully, one can see that the vortex effect on the lift for the ramp function behaves more abruptly at the end of the tab motion, causing the total lift to change its direction abrupt. But the overall duration of the effect of the vortex lift is not changed. Hence, one can summarise that the deployment function in this case is of no further importance from the point of aerodynamics. However, the sinusoidal deployment might have some advantages when it comes to the constructional integration and design of the tab actuation.

9.4.2 Influence of the Deployment Time

If the deployment time is changed, the model is designed in a way that no other parameters needs to be adjusted. Figures 9.8 - 9.10 show how the lift is changing with increasing deployment time from $s_{dep} = 1 - 40$ using the same final tab height of $h_{tab}/c = 0.02$. The change in the circulatory lift (Figure 9.8) illustrates that with increasing deployment time, the adverse lift gets more pronounced. This is due to the fact that for longer deployment times, the tab stays below the critical tab height for a longer period of time and, as a result, produce an adverse circulatory lift. Hence, if longer deployment times are considered for an application, this effect needs to be taken into account: For short deployment times the adverse effect can often be neglected since the structural response e.g. of a wind turbine blade is too slow to react to such a fast load change. However, for larger actuation times this might change.

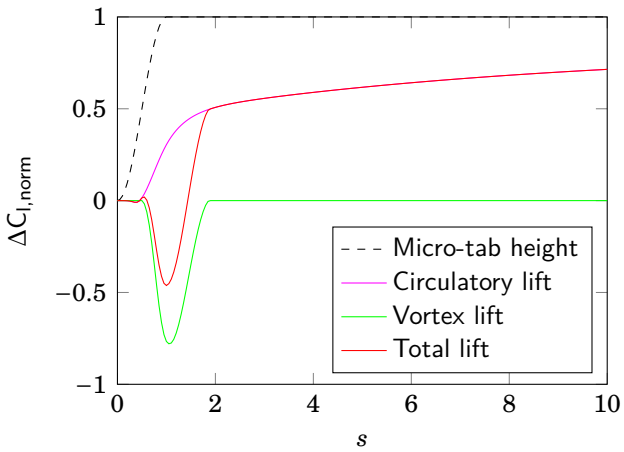

Figure 9.6: Simulated lift response after sinusoidal tab deployment (VR-7 airfoil)

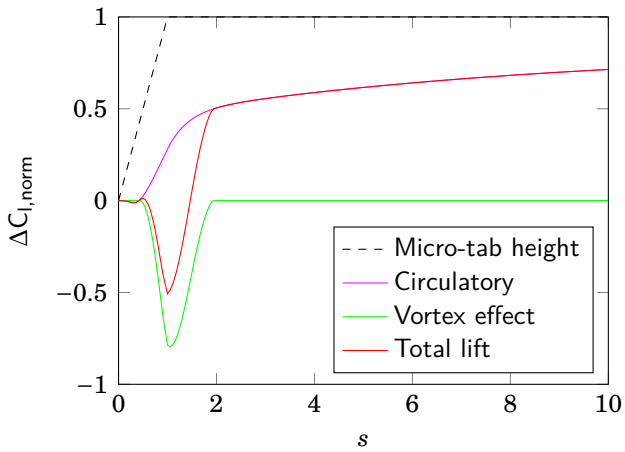

Figure 9.7: Simulated lift response after ramp tab deployment (VR-7 airfoil)

The vortex lift effect is reduced considerably when the deployment time is extended (Figure 9.9). However, at the same time the vortex effect lasts for a longer period of time, contributing together with the circulatory lift to an adverse lift over a longer period of time, as it can be seen in Figure 9.10 of the total lift.

9.4.3 Influence of the Deployment Height

A variation of the deployment height was not possible in the experimental work performed earlier in this work. However, the model is able to reproduce the expected effects. Figures 9.11 - 9.13 illustrate the variation in the lift components due to a change in the final height of the micro-tab. In them, the tab height varied between $h_{tab}/c = 0.01 - 0.02$ but the deployment time was held constant at $s_{dep} = 1$ and the deployment function was sinusoidal. Since the plotted values are all normalised, the values are made more comparable. However, it is understood, that the absolute final lift values reached are much higher when the tab height is increased.

An increasing tab height while maintaining the same actuation time of the tab has a clear impact on the circulatory lift (Figure 9.11). The adverse negative lift is reduced due to the fact that the tab spends less time below the critical tab height. It is interesting to note that a significant difference in the response is only seen in the first two dimensionless time units: After that, the response functions more or less coincide.
The minimal vortex lift gets more pronounced the higher the final tab height is (Figure 9.12). Furthermore, the maximum shifts in time and occurs preliminary. It should be noted that for very small deployment heights the model seems to have difficulies to produce a smooth vortex response.
In the resulting total lift response, the sum of the circulatory lift part and the vortex lift produce an intricate response function: The higher the tab deploys, the higher and sharper the adverse response is (Figure 9.13). Furthermore, a secondary lift variation develops at around $s = 0.6$,

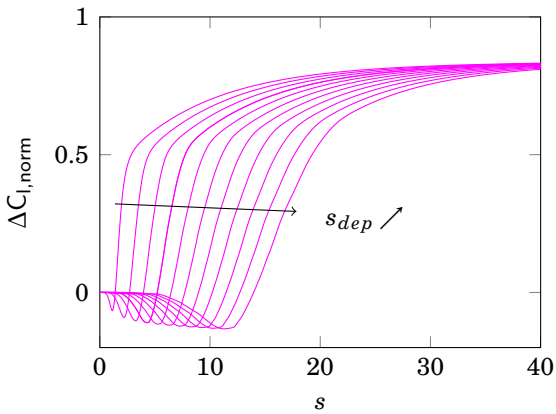

Figure 9.8: Circulatory lift for varying deployment time
(tab deployment range: $s_{dep} = 1 - 40$)

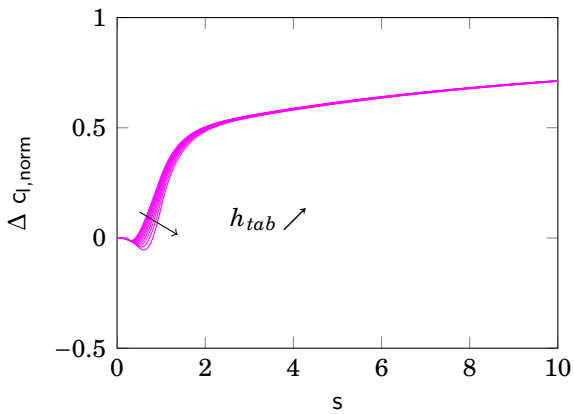

Figure 9.11: Circulatory lift for varying tab height
(tab height range: $h_{tab}/c = 1 - 2\%$)

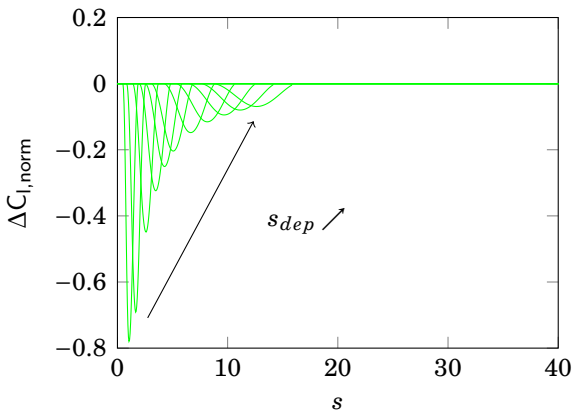

Figure 9.9: Vortex lift for varying deployment time
(tab deployment range: $s_{dep} = 1 - 40$)

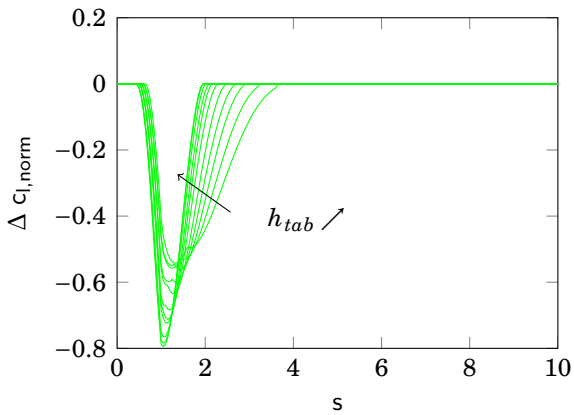

Figure 9.12: Vortex lift for varying tab height
(tab height range: $h_{tab}/c = 1 - 2\%$)

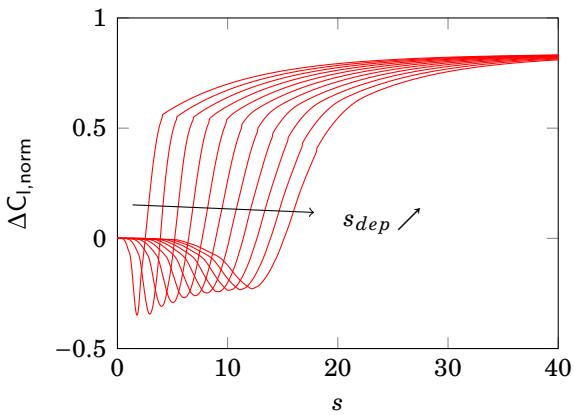

Figure 9.10: Total lift for varying deployment time
(tab deployment range: $s_{dep} = 1 - 40$)

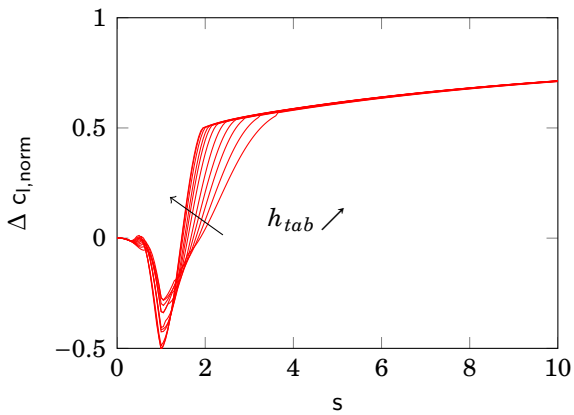

Figure 9.13: Total lift for varying tab height
(tab height range: $h_{tab}/c = 1 - 2\%$)

due to the fact that the produced adverse lift of the circulatory and the vortex parts do not take place at the same dimensionless time.

9.4.4 Continuous Actuation

Figure 9.14 shows the lift over the dimensionless time s, as it is used in this model. The micro-tab is being continuously deployed and retracted following a sinusoidal movement with a maximum height of $h_{tab} = 2\%c$ and a reduced frequency of $k = 1$. It can be seen, how the circulatory lift part first briefly drops and then rises along with the micro-tab height. The first drop is due to the adverse effect of the tab before it has reached the critical tab height of h_{min}. Furthermore, a clear delay of the lift in comparison to the tab movement can be seen. This was to be expected, since the actuation rate was chosen to be very high; hence, the unsteady aerodynamic response is more pronounced. At the same time as the tab rises, the vortex is formed and shed and the negative vortex lift has to be taken into account. As a result, the total lift drops before it rises to its maximum. During the retraction, no vortex is formed and hence no vortex lift is added. However, another impact on the circulatory part can be seen e.g. at $s = 6.3$ which is caused by the tab being below the critical limit of h_{min}.
The lift as a function of the tab height is illustrated in Figure 9.15. From this perspective, one can easily see the massive impact of the vortex lift which drags the whole lift loop to lower lift values during the pitch-up motion. The effect of the vortex on the moment distribution (not shown here) is even more pronounced: The vortex induces a massive nose-down moment during the pitch-up motion and as a result, the whole loop structure of the moment response is changed.

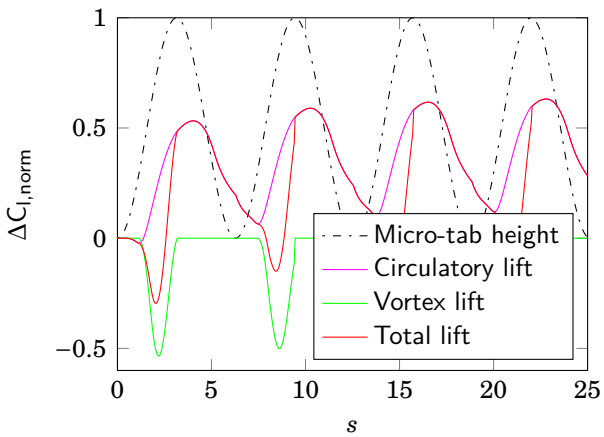

Figure 9.14: Normalized lift difference during fast continuous tab actuation (k=1)

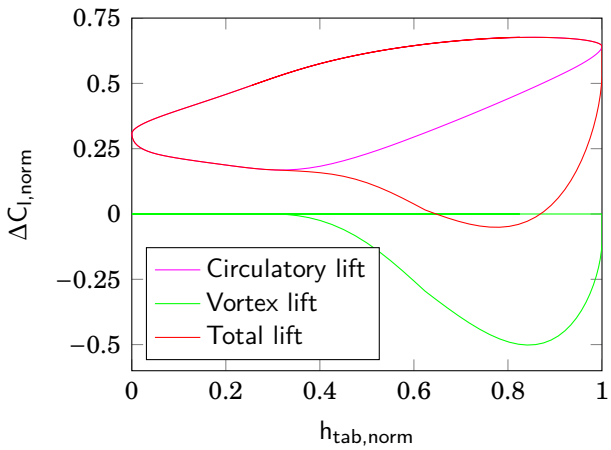

Figure 9.15: Lift loop formed by fast continuous actuation (k=1)

The reduced frequency used for this simulation was very high with k=1. For a typical application on wind turbines, the reduced frequency is a lot smaller. If the same model is used with a much smaller reduced frequency of k=0.02 the resulting responses do look differently. Figure 9.16

shows the lift over the dimensionless time s. The slower actuation shows a massive impact on the lift response. If the reduced frequency is smaller, the tab generally spends more time below the critical tab height. Consequently, the adverse circulatory lift response from this occurrence is stronger and creates in one actuation cycle two incidences with adverse lift (e.g. at $s \approx 100$ and $s \approx 220$). However, the degree of the adverse effect strongly depends on the airfoil shape. This strong adverse lift effect is particular to the tested VR-airfoil and not representative for all airfoils with micro-tabs.
For this slow actuation a further disturbance can be seen in the circulatory lift of the micro-tab (e.g.$s \approx 160$). This is the point where the tab reaches its maximum which differs from the maximum of the lift response but still causes a visible impact.

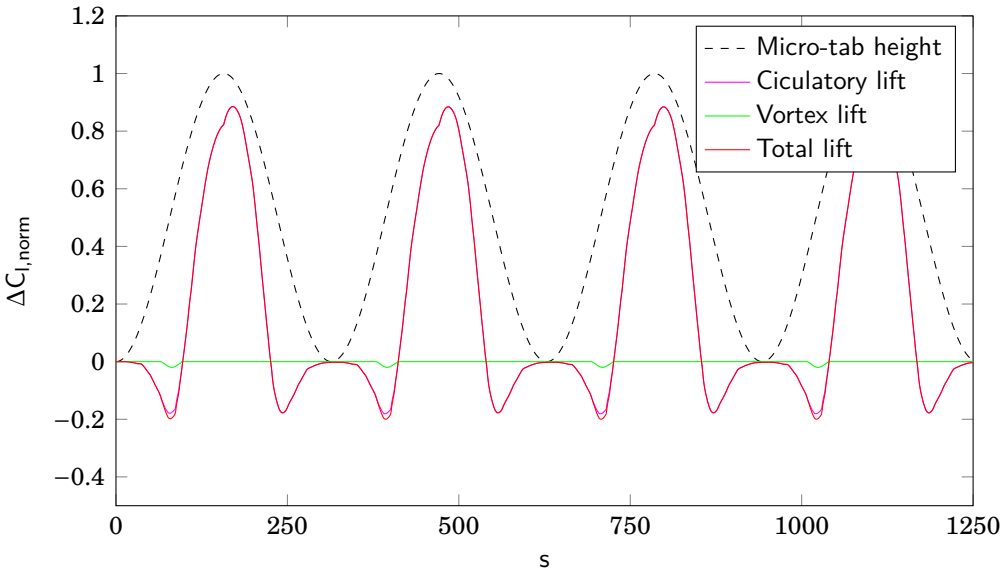

Figure 9.16: Normalised lift difference during slow continuous tab actuation (k=0.02)

9.5 Combination of Aerodynamic Models

In this section the continuous actuation of flaps and micro-tabs shall be compared using the models explained above in indicial formulations for the pitching airfoil together with the micro-tab model. For the model, the well validated parameters for the VR-7 airfoil with a micro-tab placed at 90% chord are used [142]. For the application as a load control device on wind turbines, the mean angle of attack as well as the amplitude of the airfoil are assumed to be small. Hence, it is acceptable to neglect the dependency of the lift difference gained by the micro-tabs on the angle of attack. Therefore, for all angles of attack during the pitch motion the same lift difference is used. In that way, the total lift of the system is a sum of the lift of the airfoil and the lift differences caused by the micro-tabs.

9.5.1 Pitching Airfoil with Micro-Tab on Pressure Side

The unsteady aerodynamic models for a harmonically pitching airfoil with a micro-tab on the pressure side are combined. The airfoil is given a pitching movement of $\alpha = 4° \pm 2°$ with a reduced frequency of $k = 0.02$. The micro-tab motion is phase-shifted by $\Delta\phi = 180°$ to counteract the aerodynamic lift (see Figure 9.17 a) with a maximal tab height of $h_{tab} = 0.01$. The modelled lift over time caused by the airfoil is illustrated in Figure 9.17 b. The total lift is a sum of the circulatory and non-circulatory lift, however for this angle of attack region and small amplitudes of the airfoil, the lift differences are still small. Furthermore, the non-circulatory or apparent mass term is small. The lift differences caused by the micro-tab on the pressure side, which can be seen in subplot c, are similar to the one seen before in Figure 9.16, since the driving parameters for these two cases were the same. The last subplot (Figure 9.17 d) shows the total lift response with and without an active micro-tab. Since the micro-tab is one-sided and can only contribute positive lift only the lift and low angles of attack can be enhanced.

9.5.2 Pitching Airfoil with Micro-Tab System

For a further load reduction as it can be achieved with a one sided micro-tab, a simulation with two micro-tabs was conducted. Here, the assumption was made, that the micro-tab on the suction side has the same impact in terms of maximum achievable lift as well as a similar response behaviour (which means the same indicial constants). The second micro-tab had a motion which was in phase with airfoil motion, however, causing negative lift since it is placed on the suction side. The airfoil motion was kept the same as in the case shown before with $\alpha = 4° \pm 2°$ and a reduced frequency of $k = 0.02$. The maximal tab height was altered to keep the lift variation minimal to $h_{tab,max} = 0.014$.
Figure 9.18 shows the same time traces as shown before in Figure 9.17. On the one hand, the resulting lift is found to be more constant than when only one micro-tab is used. On the other hand, the extreme adverse lift parts caused by the minimal effective tab height, induce an overall more disrupted lift response. This might be improved further by not using sinusoidal variations of the tab height but a more sophisticated control e.g. through look up-tables or more complex functions.

9.5.3 Pitching Airfoil with Flap

A last model is set-up to simulate the performance of an airfoil equipped with a Gurney flap at the trailing edge. For the direct comparison of a Gurney flap and micro-tab, it is assumed that both configurations gain the same lift difference and have the same indicial response parameters. Therefore, one major difference in the model approach is that the vortex lift component of the indicial micro-tab model is not used in the Gurney flap model. Furthermore, the flap can continuously move between deploying to the suction and pressure side without interfering responses as it is the case for the two-sided micro-tab system. The major advantage, however, is that the flap does not have an adverse lift for small tab heights but is effective for all deflection angles. To achieve a physical representation of a flap's behaviour with the same lift performance

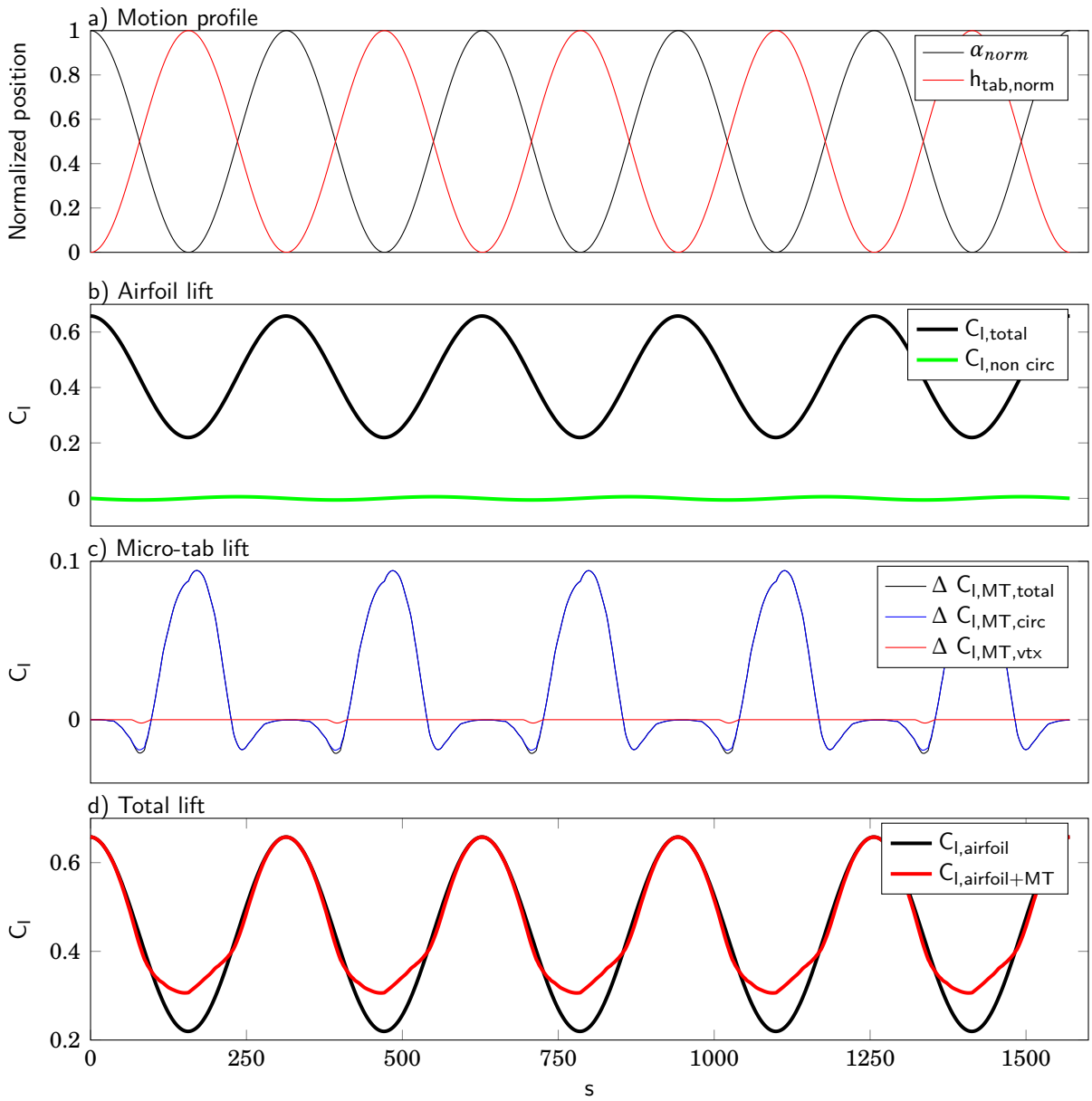

Figure 9.17: Lift contribution of pitching airfoil with micro-tab on pressure side (k=0.02)

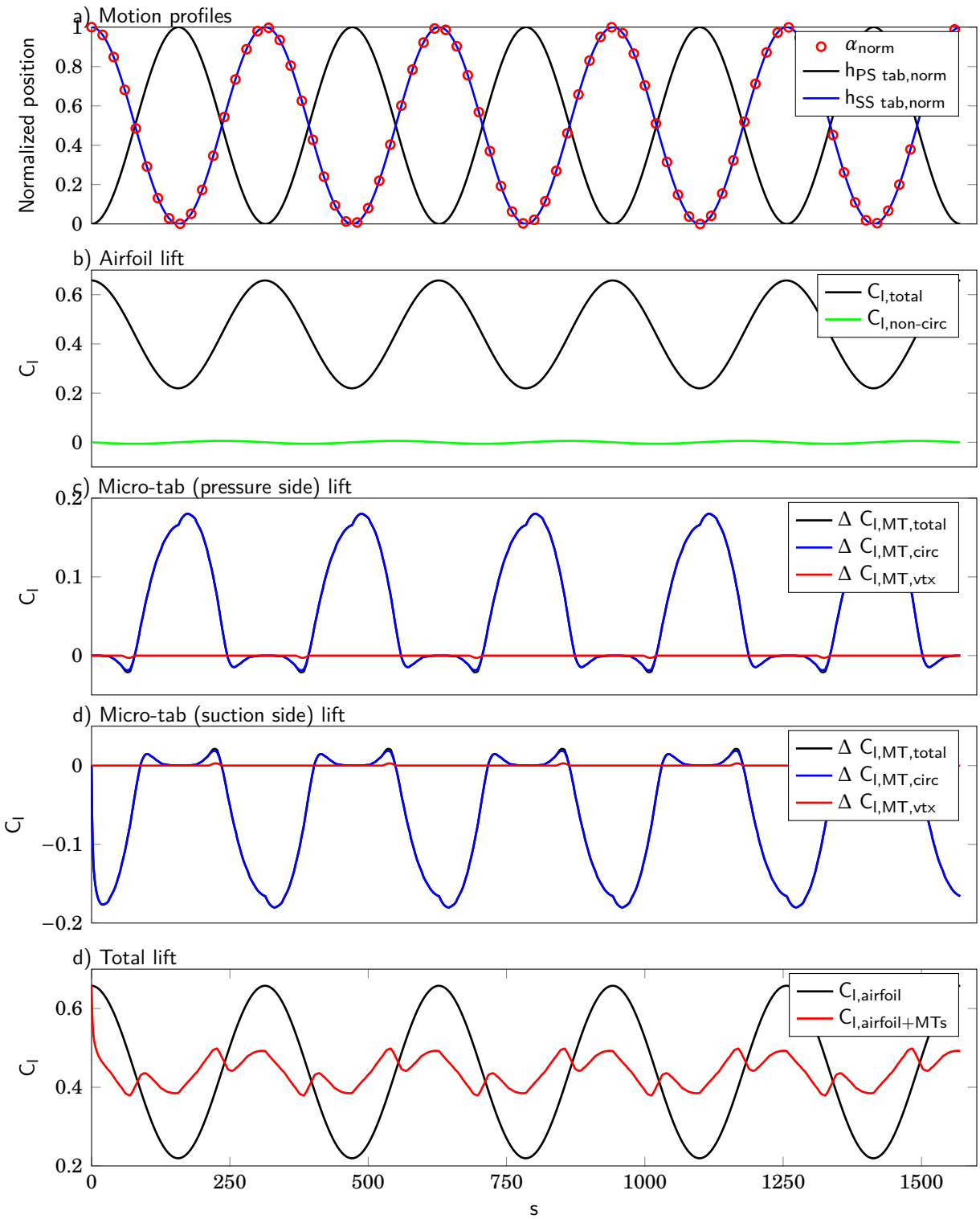

Figure 9.18: Lift contribution of pitching airfoil with two micro-tabs (pressure and suction side, k=0.02)

as the experiments on the VR-airfoil, the data from Vieira et al. was modified and the adverse lift removed.
Figure 9.19 shows the lift response of an airfoil with a Gurney flap placed at the trailing edge, deflecting between $\theta_{max} = \pm 90°$. For reasons of comparison, the maximum tab height as used for Figure 9.18 was used again ($h_{tab,max} = 0.014$). The normalised flap and airfoil movement can be seen in the first plot. The flap is phase shifted by exactly $\Delta\phi = 180°$. Furthermore, in the second plot b, the flap's lift response can be observed. This response is much more homogeneous than the response of the micro-tab and can compensate the lift response of the airfoil better. The small kink in the lift response close to the maximum is where the flap reaches its maximum position. Such an impact was also previously seen in the experiments in Section 6.2.2. The overall lift amplitude of the airfoil is found to be $\Delta C_l = 0.2191$ while the flap produces a lift amplitude of $\Delta C_l = 0.185$. The resulting overall lift response of the system can be seen in the last plot c. The lift varies with a total lift amplitude of $\Delta C_l = 0.0827$. However, the total lift response of the system does not have a sinusoidal shape. This is due to the fact that even though the flap and the airfoil movement are shifted by $\Delta\phi = 180°$ the lift response of each element are not.
Therefore, a phase shift of the flap was introduced in order to match a phase difference of $\Delta\phi = 180°$ for the lift responses. It was found that a phase shift of $\Delta\phi = +162°$ between the moving elements resulted in the best complementary lift responses. The results for this configuration are highlighted in blue in each plot. It can be seen that the overall lift response has a slightly smaller peak-to-peak difference than before; however, the shape did not become more sinusoidal.

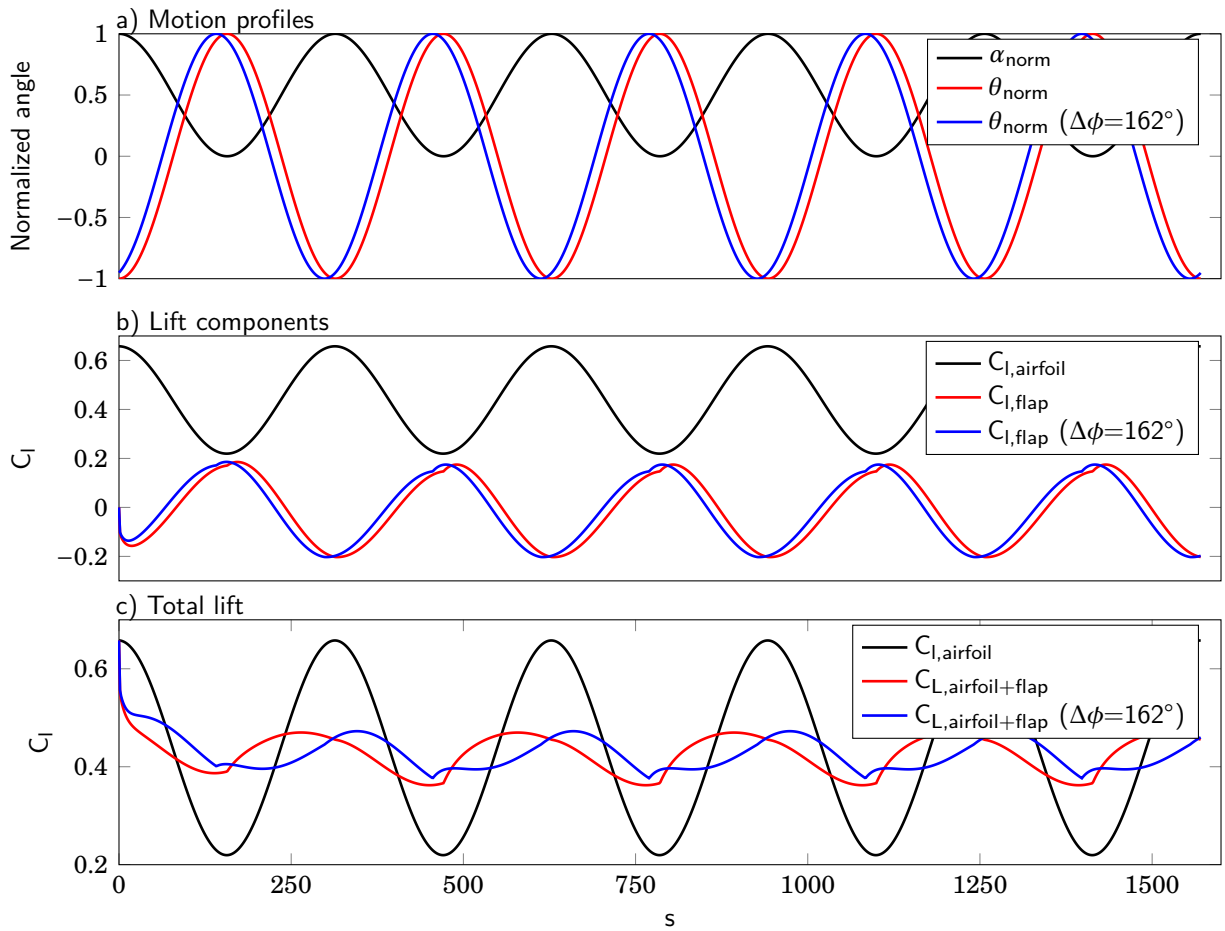

Figure 9.19: Lift contribution of pitching airfoil with Gurney flap (k=0.02)

10 Conclusion

An extensive study on micro-tabs and Gurney flaps has been conducted to evaluate their effectiveness as load control devices on wind turbines. From earlier studies, Gurney flaps and micro-tabs are known to effectively change the airfoil's camber and therefore altering the steady aerodynamic characteristics. The underlying principle of a steady Gurney flap is the formation of two counter-rotating vortices which form behind the flap and change the overall airfoil circulation and thus the lift. The closely related micro-tabs work in a similar fashion: The tabs are usually placed up to 10% upstream of the trailing edge and form a recirculation zone behind the tab extending to the trailing edge. If the tab is placed on the pressure side, this recirculation zone captures the streamline leaving the airfoil from the suction side and leads it through the bubble to the end-point of the micro-tab where the streamlines from the suction- and pressure side meet and leave in the wake. This process changes the airfoil circulation and hence the lift.

Even though the basic principle of both devices for steady inflow conditions are known, research is still needed on the further effects of the tab height, position or airfoil geometry. Therefore, an extensive study on various experimental set-ups and airfoil models was conducted covering steady and unsteady tab/flap motions. These were further evaluated under unsteady airfoil motions. In the following an overview about the experiments and the key findings are given:

At the beginning of this work the effects of passive micro-tabs and Gurney flaps under steady inflow conditions were evaluated. The effect on lift and drag depending on the tab height as well as the chordwise position was investigated in more detail. It was shown that a higher tab/flap produced a greater lift difference as well as higher drag. However, the lift-to-drag ratio could be influenced to produce higher values, when the tab height was below a certain tab height. The optimal tab height with the best lift-to-drag ratio depends on the airfoil geometry but is often found to be around $h_{tab}/c = 2\%$.
In addition, the tab position has proven to influence the aerodynamic performance further. Generally, a more upstream position ($x/c < 1$) of the suction side tab was found to be advantageous. Pressure side tabs yielded higher lift differences if placed closer to the trailing edge. However, if the tab was placed upstream of the trailing edge, it must generally be considered that there is a critical tab height h_{crit}. The critical tab height represents the height which is needed for the formation of a sufficiently large recirculation bubble that reaches the trailing edge and hence alters the Kutta condition. If the tab has a height less than the critical tab height, the presence of the tab causes a local deflection of the surface streamlines, but does not have the desired effect on the lift. Instead, an opposite lift difference to that intended is created.

In the second part of this work, the transient effects of micro-tabs and Gurney flaps were studied. In the past, Gurney flaps have proven to have little unsteady effects during the deployment. The aerodynamic response due to a flap deflection generally follows the same theoretical approach as the circulatory lift change due to a change in angle of attack (Wagner function). However, the aerodynamic response of a micro-tab is more complex: During the deployment the tab forms an unsteady vortex which, after the formation, convects in the wake inflicting a negative pressure on the airfoil's surface. This negative pressure leads to an instantaneous lift in the opposite direction of that intended. Furthermore, during the deployment the tab passes though the region where the tab height is smaller than the critical tab height; hence, an additional temporal opposite lift is generated. Comparing the two different adverse lift parts, the one generated by the unsteady vortex plays bigger role. Therefore, if the tab is deployed more slowly, the vortex strength and hence the adverse lift becomes smaller as well. It was also shown that the angle of attack of the airfoil still had an effect on the lift difference but did not influence the overall characteristics of the aerodynamic response of the tab.

In addition to single full-span elements, finite tabs and flaps were investigated. It was shown that the steady state lift-to-drag ratio could be further improved in comparison to the full-span configurations by using multiple passive tabs or flaps. The finite elements (flaps and tabs) generally had a lower lift difference in the section where the element was placed, however they caused an additional lift difference in the adjacent sections next to the device. Furthermore, the lift of an active finite flap showed a very similar response in all regions when compared to the results of the full-span flap.

In the third part of these studies, passive tabs and flaps were analysed on pitching airfoils. In the pre-stall region, the effect of the tab height and tab position caused overall shifted lift values as the steady state results implied earlier. Hence, the hysteresis loops were shifted, but the overall dynamic behaviour such as the phase lag of the response was not further changed. When pitching in the stall region, the effect of tabs on the suctions side for load reduction was explored. During the beginning of the trailing edge separation the presence of the tab on the suction side reduced the hysteresis loop width. If dynamic stall occurred, the tab height as well as an upstream placement of the tab on the suction side again reduced the hysteresis loop width and the peak lift induced by the convecting vortex.

The last experimental work was focused on a complete active system, consisting of a harmonic pitching airfoil equipped with an active full-span flap. The active flap has proven to work effectively to migrate dynamic loads. The most important parameter was the phase-shift between the flap actuation and the airfoil pitching. For optimal load reduction the flap needs to act well before the anticipated disturbance (in this case the pitching) and have the correct flap height to

balance the lift difference caused by the disturbance. However, this optimal load reduction case was directly connected to a degradation of the aerodynamic damping properties.
Due to the complex experimental setup, an active micro-tab integrated in a pitching airfoil could not be realised. Instead, a verified aerodynamic model for micro-tabs on helicopters was coupled with Theodorsen's theory for pitching airfoils to model various flap/tab scenarios.

The results have shown a deeper insight in the steady and unsteady aerodynamics of tabs and flaps. Both have been proven to be beneficial tools for load control applications. When it comes to load control designated only for predictable loads per one revolution (caused e.g. by wind shear) the flaps have more advantages than micro-tabs since they have a more smooth load response without adverse effects. However, for load control including the altering of gusts and turbulence that might cause high angles of attack, the flap is not as beneficial, since the beginning separation at the trailing edge causes the flap to be less effective. Hence, one can either use micro-tabs instead or apply additional vortex generators with the flap and accept the associated higher drag penalties.

However, which solution to choose depends on further aspects: A micro-tab which is included in the blade structure will need slots and inner space for the tab mechanisms and electronics. This affects the blade stiffness and hence may further effect the bending of the blade and thus the fatigue loads. The flap has an advantage there, as it can be easily mounted as a retro-fit mechanism using small motors that can be applied on the pressure side under small aerodynamically shaped covers. Thus, the manufacturing procedure of the blades in not influenced. If the actuation mechanism is placed on the outer blade, maintenance is further simplified.

Thus, more research is needed on the structural integration and reliable design for the long-term application under environmental influences. Compatible sensors and control algorithms need to be found and tested as an interdisciplinary system. This work is designated as a guideline of the physical explanations of the flow and aerodynamic effects of flaps and tabs for future systems, proving that from this point of view the application of both devices are effective means to alter and reduce fatigue loading on wind turbines.

Bibliography

[1] German Patent, DE10 2012 000 431 A1, 2013.

[2] HPO series - Differential pressure sensors, Sensortechnics (www.sensortechnics.com).

[3] NI 9188 cDAQ mainframe, NI National Instruments, (www.ni.com).

[4] S.A. Ahmadi and S. Sharif andR. Jamshidi. A numerical investigation on the dynamic stall of a wind turbine section using different turbulent models. *Engineering and Technology*, 58:290 – 296, 2009.

[5] D. Althaus. *Niedriggeschwindigkeitsprofile*. Vieweg, 1996.

[6] D. Althaus and F.X. Wortmann. Stuttgarter Profilkatalog. Technical report, Friedr. Vieweg & Sohn (Braunschweig), 1981.

[7] A. B. Bach, R. Berg, G. Pechlivanoglou, C.N. Nayeri, and C.O. Paschereit. Experimental investigation of the aerodynamic lift response of an active finite Gurney flap. In *AIAA , Aerosp. Sci. Tech.*, 2015.

[8] A.B. Bach, D. Holst, C.N. Nayeri, and C.O. Paschereit. Transition effects of active micro-tabs for wind turbine load control. In *Proceedings of the ASME Turbo Expo, June 3-7, San Antonio, Texas, USA*, 2013.

[9] A.B. Bach, M. Lennie, G. Pechlivanoglou, C.N. Nayeri, and C.O. Paschereit. Finite micro-tab system for load control on a wind turbine. In *Journal of Physics: Conference Series*, 2014.

[10] A.B. Bach, G. Pechlivanoglou, C.N. Nayeri, and C.O. Paschereit. Wake vortex field of an airfoil equipped with an active finite Gurney flap. In *AIAA, Aerosp. Sci. Tech.*, 2015.

[11] M. Bachmann, C. O. Paschereit, S. Utehs, S. Vey, and D. Greenblatt. Plasma-based active control on low reynolds number airfoils. In *Proc. 49th Israel Annual Conference on Aerospace Sciences, Tel Aviv, Israel*, pages 1–20, 2009.

[12] P. Baek and M. Gaunaa. Modeling the temporal response of a microtab in an aeroelastic model of a wind turbine. In *49th AIAA Aerospace Sciences Meeting including the New Horizons Forum and Aerospace Exposition*, 2011.

[13] J.P. Baker, K.J. Standish, and C.P. van Dam. Two-dimensional wind tunnel and computational investigation of a microtab modified airfoil. *Journal of Aircraft*, 44:563–572, 2007.

[14] T.K. Barlas and G.A.M. van Kuik. Review of state of the art in smart rotor control research for wind turbines. *Progress in Aerospace Sciences*, 46:1–27, 2010.

[15] D. W. Bechert, R. Meyer, and W. Hage. Aeroflexible oberflächenklappen als rückstrombremsen nach dem vorbild der deckfedern des vogelflügels. Technical report, DLR Zwischenbericht, BMBF-Vorhaben 13N6537-8; DLR IB 92517-96/B2, Berlin, 1995.

[16] D.W. Bechert, M. Bruse, W. Hage, and R.Meyer. Biological surfaces andcontrol technological application- laboratory and flight experiments on drag reduction and separation control. In *AIAA 97-1960, June*, 1997.

[17] D.W. Bechert, R. Meyer, and W. Hage. Drag reduction of airfoils with miniflaps - can we learn from dragonflies? In *Fluids 2000, Denver, CO*, 2002.

[18] L. Bergami. *Smart Rotor Modeling: Aero-Servo-Elastic Modeling of a Smart Rotor with Adaptive Trailing Edge Flaps*. Spinger International, 2014.

[19] A. Björck. Dynstall: Subroutine package with a dynamic stall model. Technical report, FFA - The Aeronautical Research Institute of Sweden, 2000.

[20] P. Bæk, M. Gaunaa, N.N. Sørensen, and P. Fuglsang. A comparison of two devices for distributed active load control of wind turbine blades. In *The Science of Making Torque from Wind*, 2010.

[21] M. Blaylock, R. Chow, and C.P. van Dam. Comparison of microjets with microtabs for active aerodynamic load control. In *5th Flow Control Conference*, 2010.

[22] S.L. Brunton and C.W. Rowley. Modeling the unsteady aerodynamic forces on small-scale wings. In *47th AIAA Aerospace Sience Meeting*, 2009.

[23] T. Burton. *Wind Energy Handbook*. John Wiley and Sons, LTD, 2001.

[24] C.P. Butterfield, A.C. Hansen, and D. Simmsand G. Scott. Dynamic stall on wind turbine blades. Technical report, National Renewable Energy Laboratory (NREL), Golden, CO, USA, 1991.

[25] L.W. Carr and K.W. McAlister. The effect of a leading-edge slat on the dynamic stall of an oscillating airfoil. In *AIAA Design, Systems and Technology Meeting, AIAA*, 1983.

[26] F.O. Carta and C.F. Niebanck. Prediction of rotor instability at high forward speed. Technical report, US Army Aviation Mater. Lab., Fort Eustis, VA, 1969.

[27] D. Castaignet. *Model predictive control of trailing edge flaps on a wind turbine blade*. PhD thesis, Technical University of Denmark, 2011.

[28] D. Castaignet, J.J. Wedel-Heinen, T. Kim, T. Buhl, and N.K. Poulsen. Results from the first full scale wind turbine equipped with trailing edge flaps. In *28th AIAA Applied Aerodynamics Conference, Chicago, Illinois*, 2010.

[29] A. Chatterjee. An introduction to the proper orthogonal decomposition. *Current Science*, 78, 2000.

[30] R. Chow and C.P. van Dam. On the temporal response of active load control devices. *Wind Energy*, 13:135 – 149, 2010.

[31] P.J.F. Clark and H.S. Ribner. Direkt correlation of fluctuating lift with radiated sound for an airfoil in turbulent flow. *Journal of Acoustical Society of America*, 46:802–805, 1969.

[32] J.G. Coder, M.D. Maughmer, and P.B. Martin. CFD investigation of unsteady rotorcraft airfoil aerodynamics: Mites and dynamic stall. In *49th AIAA Aerospace Sciences Meeting including the New Horizons Forum and Aerospace Exposition, Orlando, Florida*, 2011.

[33] J.A. Cole, B.A.O. Vieira, J.G. Coder, A. Premi, and M.D Maughmer. Experimental investigation into the effect of Gurney flaps on various airfoils. *Journal of Aircraft*, pages 1–8, 2013.

[34] H. Consigney, A. Gravelle, and R. Molinaro. Aerodynamic characteristics of a two-dimensional moving spoiler in subsonic and transonic flow. *Journal of Aircraft*, 21(9):687–693, 1984.

[35] T.C. Corke and F.O. Thomas. Dynamic stall in pitching airfoils: Aerodynamic damping and compressibility effects. *Annual Review of Fluid Mechanics*, 47:479–505, 2015.

[36] R.D. Corrigan and J.M. Savino. Vortex generators as a means for increasing rotor performance. In *Proceedings of the 20th Intersociety Energy Conversion Engineering Conference, Vol. 3, Miami, Florida*, 1984.

[37] J.C. Dai, D. Liu, Y. Hu, and X. Shen. Research on joint power and loads control for large scale directly driven wind turbines. *Journal of Solar Energy Engeneering*, 136(2):1–10, 2013.

[38] N. Eastman, K. Jacobs, E. Ward, and R.M. Pinkerton. The characteristics of 78 related airfoil sections from tests in the variable-density windtunnel. Technical report, NACA, Technical Report No.460, 1933.

[39] O. Edenhofer, R. Pichs-Madruga, Y. Sokona, K. Seyboth, P. Matschoss, S. Kadner, T. Zwickel, P. Eickemeier, G. Hansenand S. Schlömer, and C. von Stechow. Ipcc special report on renewable energy sources and climate change mitigation. Technical report, Cambridge University Press, Cambridge, United Kingdom and New York, NY, USA, 2011.

[40] A.J. Eggers, R. Digumarthi, and K. Chaney. Wind shear and turbulence effects on rotor fatigue and loads control. *Journal of Solar Energy Engineering*, 125(4):402–409, 2003.

[41] O. Eisele, G. Pechlivanoglou, C.N. Nayeri, and C.O. Paschereit. Experimental investigation of dynamic load control strategies using active microflaps on wind turbine blades. In *EWEA, March 14.-17., Brussels, Belgium*, 2011.

[42] N. Fichaux, J. Beurskens, P.H. Jensen, and J. Wilkes. UPWIND - Design limits and solutions for very large wind turbines. Technical report, European UPWIND Project, 2011.

[43] J. Fischer, O. Eisele, G. Pechlivanoglou, S. Vey, C.N. Nayeri, and Paschereit C. O. Development of a medium scale research hawt for inflow and aerodynamics research in the large wind tunnel of tu berlin. In *12th German Wind Energy Conference*. DEWEK 2015, 2015.

[44] J. Fischer, G. Weinzierl, J. Wagner, and g. Pechlivanoglou. Development of a flexible trailing edge flap and system integration concept for wind turbine blades. In *11th German Wind Energy Conference DEWEK, 7-8 November 2012, Bremen, Germany*, 2012.

[45] P. Fuglsang, I. Antoniou, C. Bak, and H.A. Madsen. Wind tunnel test of the Risø -1 airfoil -Risø -R-999. Technical report, Risø National Laboratory, Roskilde, Denmark, 1998.

[46] T. Fukana, Y. Kodama, and T. Takamatsu. The effects of tip clearance on the noise of low pressure axial and mixed flow fans. *Journal of Sound and Vibration*, 105:291–308, 1986.

[47] R.A. McD. Galbraith. The aerodynamic characteristics of a GU25-5(11)8 aerofoil for low Reynolds numbers. *Experiments in Fluids*, 3:253–256, 1985.

[48] M Geyler. Advanced pitch control for wind turbines. Technical report, Delft University of Technology - DUWIND, 2011.

[49] G. Godard and M. Stanislas. Control of a decelerating boundary layer. Part 1: Optimization of passive vortex generators. *Aerospace Science and Technology*, 10:181–191, 2006.

[50] J. Gottschall and J. Peinke. How to improve the estimation of power curves for turbines. Technical report, Environmental Research Letters 3, 015005, 2008.

[51] D. Greenblatt. Application of large Gurney flaps on low Reynolds number fan blades. *Journal of Fluids Engineering*, 133(2), 2011.

[52] D. Greenblatt, S. Vey, C.O. Paschereit, and R. Meyer. Flap vortex management using active Gurney flaps. *AIAA Journal*, 47(12):2845 – 2856, 2009.

[53] D. Greenblatt and R. Visbal. Plasma control for a maneuvering low-aspect-ratio wing at low Reynolds number. *Journal of Fluids Engineering*, 134, 2012.

[54] D.A. Griffin. Evaluation of design concepts for adaptive wind turbine blades. Technical report, Sandia National Laboraties, 2002.

[55] D.A. Griffin. Windpact turbine design scaling studies technical area 1 Ű Composite blades for 80 - to 120 - meter rotor. Technical report, National Renewable Energy Laboratory, Golden, CO, USA, 2011.

[56] M.H. Hansen, M. Gaunaa, and H.A. Madsen. A Beddoes-Leishman type dynamic stall model in state-space and indicial formulation. Technical report, Risø National Laboratory, Roskilde, Denmark, 2004.

[57] M.O. L. Hansen. *Aerodynamics of Wind Turbines*. Earthscan, 2008.

[58] M.K. Heerenbrink. Simultaneous PIV and balance measurements on a pitching aerofoil. Master's thesis, Aerospace Egineering, Delft University of Technology, 2011.

[59] D. Holst. Untersuchung von endlichen Gurney Flaps zur Lastregulierung an Windenergieanlagen. Master's thesis, TU Berlin, Istitut für Strömungsmechanik und Technische Akustik, 2012.

[60] D. Holst, A.B. Bach, G. Pechlivanoglou, C.N. Nayeri, and C.O. Paschereit. Wake analysis of a finite width Gurney flap. In *Proceedings of ASME Turbo Expo*, 2015.

[61] R. I. Issa. Solution of the implicitly discretized fluid flow equations by operator-splitting. *Journal of Computational Physics*, 62:40–65, 1986.

[62] D. Jeffrey, X. Zhang, and D.W. Hurst. Aerodynamics of Gurney flaps on a single-element high-lift wing. *Journal of Aircraft*, 37(2):295–301, 2000.

[63] J. Johansen, N. Sørensen, M.R. Martin, O.L. Hansen, A. Stuermer, J. Ramboer, C. Hirsch, J. Ekaterinaris, S. Voutsinas, and Y Perivolaris. Rotor blade computations with 3D vortex generators. Technical report, Risø National Laboratories, Roskilde, Danmark, 2005.

[64] S.J. Johnson, J.P. Baker, C.P. van Dam, and D. Berg. An overview of active load control techniques for wind turbines with an emphasis on microtabs. *Wind Energy*, 13(2-3):239–253, 2010.

[65] W.P. Jones. Aerodynamic forces on wings in nonuniform motion. Technical report, R & M 2117, ARC, 1945.

[66] J. Jonkman, S. Butterfield, W. Musial, and G. Scott. Definition of a 5-MW reference wind turbine for offshore system development. Technical report, National Renewable Energy Laboratory (NREL), Golden, CO, USA, 2009.

[67] TEMBRA GmbH & Co. KG. Strukturelle und aerodynamische Auslegung eines Rotorblattes mit Active Flow Control (AFC)-Elemente in modularer Hybridbauweise. Technical report, Förderprogramm des BMU zu Forschung und Entwicklung im Bereich Windenergie, 2011.

[68] J.H. Kim and O.H. Rho. Numerical simulation of the flowfield around an airfoil with stationary and oscillating spoiler. In *AIAA*, 1996.

[69] H.J.T. Kooijman, C. Lindenburg, D. Winkelaar, and E.L. van der Hooft. DOWEC 6 MW pre-design: Aero-elastic modeling of the DOWEC 6 MW pre-design in PHATAS. Technical report, Energy Research Center of the Netherlands, 2003.

[70] S. Kota, J. Hetrick, R. Osborn, E. Pendleton, P. Flick, and C. Tilmann. Design and application of compliant mechanisms for morphing aircraft structures. In *Smart Structures and Materials 2003: Industrial and Commercial Applications of Smart Structures Technologies, Proceedings of SPIE Vol. 5054*, 2003.

[71] L.D. Kral. Active flow control technology. Technical report, ASME Fluids Engineering Division Technical Brief.

[72] H.G. Küssner. Augenblicklicher Entwicklungsstand der Frage des Flügelflatterns. *Luftfahrtforschung*, 6:193–209, 1935.

[73] C. Lachmann. Experiments with slotted wings. Technical report, National Advisory Commitee for Aeronautics, 1921.

[74] M.A. Lackner and G. van Kuik. A comparison of smart rotor control approaches using trailing edge flaps and individual pitch control. In *47th AIAA Aerospace Sciences Meeting, Florida*, 2009.

[75] J. Laks, L. Pao, and A. Wright. Combined feed-forward/feedback control of wind turbines to reduce blade flap bending moments. In *AIAA*, 2009.

[76] B. Lambie. *Aeroelastic investigation of a wind turbine airfoil with self-adaptive camber*. PhD thesis, TU Darmstadt, 2011.

[77] B. Lee, K. Yee, W. Joo, and D.F. Lee. Passive control of dynamic stall via nose droop with Gurney flap. In *43rd AIAA Aerospace Science Meeting and Exibit*, 2005.

[78] C. Lee, M.K. Chung, and Y.-H. Kim. A prediction model for the vortex shedding noise from the wake of an airfoil or axial flow fan blades. *Journal of Sound and Vibration*, 164(2):327–336, 1993.

[79] T. Lee and Y. Su. Unsteady airfoil with a harmonically deflected trailing-edge flap. *Journal of Fluids and Structures*, 27:1411–1424, 2011.

[80] J.G. Leishmann. *Principles of Helicopter Aerodynamics*. Cambridge University Press, 2006.

[81] R.H. Liebeck. Design of subsonic airfoils for high lift. *Journal of Aircraft*, 15(9):547 – 561, 1978.

[82] J.C. Lin. Review of research on low-profile vortex generators to control boundary-layer separation. *Progress in Aerospace Sciences*, 38:389–420, 2002.

[83] J.C. Lin, S.K. Robinson, R.J. McGhee, and W.O. Valarezo. Separation control on high-lift airfoils via micro-vortex generators. *Journal of Aircraft*, 31(6):1317–1323, 1994.

[84] T. Liu and J. Montefort. Thin-airfoil theoretical interpretation for gurney flap lift enhancement. *AIAA Journal of Aircraft*, 44(2):667–671, 2007.

[85] R.E. Longhouse. Control of tip-vortex noise of axial flow fans by rotating shroud. *Journal of Sound and Vibration*, 58:201–214, 1978.

[86] J.L. Lumley. The structure of inhomogeneous turbulent flows. *Atmospheric Turbulence and Radio Wave Propagation*, 1967.

[87] T. Macquart and A. Maheri. Integrated aeroelastic and control analysis of wind turbine blades equipped with microtabs. *Renewable Energy*, 75:102–114, 2015.

[88] T. Macquart, A. Maheri, and K. Busawon. Microtab dynamic modelling for wind turbine blade load rejection. *Renewable Energy*, 64:144–152, 2014.

[89] H.H. Mai, G. Dietz, W. Geissler, K. Richter, J. Bosbach, H. Richard, and K. de Groot. Dynamic stall control by leading edge vortex generatos. In *American Helicopter Society, 62nd Anual Forum, Phoenix, AZ*, 2008.

[90] J.F. Manwell, J.G. McGowan, and A.L. Rogers. *Wind Energy Explained: Theory, Design and Application*. John Wiley & Sons Ltd., 2009.

[91] D. Marten, G. Pechlivanoglou, C.N. Nayeri, and C.O. Paschereit. Integration of a WT blade design tool in XFOIL/XFLR5. In *Proceedings of DEWEK 2010,17-18 November 2010, Bremen, Germany*, 2010.

[92] E.A. Mayda, C.P. van Dam, and D.Y. Nakafuji. Computational investigation of finite width microtabs for aerodynamic load control. In *43rd AIAA Aerospace Sciences Meeting and Exhibit, Reno, Nevada*, 2005.

[93] T. Mücke, D. Kleinhans, and J. Peinke. Influence of small scale wind velocity fluctuations and the aerodynamic alternating loads. In *EWEC Conference Proceedings*, 2009.

[94] B.G. McLachlan and K. Karamcheti. An experimental study of the airfoil-spoiler aerodynamics. Technical report, NASA Ames Research Center, 1984.

[95] R. Meyer. *Experimentelle Untersuchungen von Rückstromklappen auf Tragflügeln zur Beeinflussung von Strömungsablösungen*. PhD thesis, Technische Universität Berlin, Fachbereich 10, Verkehrswesen und Angewandte Mechanik, Hermann-Föttinger-Institut für Strömungsmechanik, 2000.

[96] G.E. Miller. Comparative performance tests on the MOD-2 2.5MW wind turbine with and without vortex generators. Technical report, Proc. Workshop on Horizontal Axis Wind Turbine Technology, 1984.

[97] H. Müller-Vahl, G. Pechlivanoglou, C.N. Nayeri, and C.O. Paschereit. Vortex generators for wind turbine blades: A combined wind tunnel and wind turbine parametric study. In *Proceedings of the ASME Turbine Technical Conference & Exposition, Copenhagen, Denmark*, 2012.

[98] B.D. Mugridge. Turbulent boundary layers and surface pressure fluctuations on two-dimensional airfoils. *Journal of Sound and Vibration*, 18:475–486, 1971.

[99] X. Munduate and F.N. Coton. Identification of dynamic stall regions on horizontal axis wind turbines. In *ASME Wind Energy Symposium, 19th, Aerospace Sciences Meeting and Exhibit, 38th, Reno, NV, Jan. 10-13*, 2000.

[100] D.T.Y. Nakafuji, C.P. van Dam, J. Michel, and P. Morrison. Load control for turbine blades - A non traditional approach. In *AIAA Aerospace Science Meeting and Exihibit, 40th, Collection of Technical Papers, Reno, NY*, 2002.

[101] S. Niether, B. Bobusch, D. Marten, G. Pechlivanoglou, C.N. Nayeri, and C.O. Paschereit. Development of a fluidic actuator for adaptive flow control on a thick wind turbine airfoil. *Journal of Turbomachinery*, 137(6), 2015.

[102] P. Nikoueeyan, J.A. Strike, A.S. Magstadt, M.D. Hind, and J.W. Naughton. Characterization of the aerodynamic coefficients of a wind turbine airfoil with a Gurney flap for flow control applications. In *32nd AIAA Applied Aerodynamics Conference, Kissimmee, Florida*, 2015.

[103] S.J. Orfanidis. *Introduction to Signal Processing*. Technology & Engineering, 1996.

[104] F. Ostermann, R. Woszidlo, C.N. Nayeri, and C.O. Paschereit. Phase-averaging methods for the natural flowfield of a fluidic oscillator. *AIAA Journal*, 53:8:2359–2368, 2015.

[105] C. Ostowari, W.H. Wentz, and H.C. Seetharam. Effects of design variable on spoiler control effectiveness hinge moments and wake turbulance. In *AIAA 19th Aerospace Science Meeting*, 1981.

[106] S. Oye. The effect of vortex generators on the performance of the ELKRAFT 1000 kW turbine. In *9th IEA Symposium on Aerodynamics of Wind Turbines Stockholm, Sweden*, 1995.

[107] G. Pechlivanoglou. *Passive and Active Control Solutions for Wind Turbines*. PhD thesis, TU Berlin, 2012.

[108] G. Pechlivanoglou, S. Fuehr, C.N. Nayeri, and C.O. Paschereit. The effect of distributed roughness on the power performance of wind turbines. In *Proceedings of ASME IGTI Turbo Expo, Glasgow, Scotland, UK*, 2010.

[109] G. Pechlivanoglou, C.N. Nayeri, and C.O. Paschereit. Fixed leading edge auxiliary wing as a performance increasing device for HAWT blades. In *Proceedings of DEWEK, 17-18 November 2010, Bremen, Germany*, 2010.

[110] G. Pechlivanoglou, C.N. Nayeri, and C.O. Paschereit. Performance optimization of wind turbine rotors with active flow control. In *Proceedings of ASME IGTI Turbo Expo, Vancouver, Canada*, 2011.

[111] G. Pechlivanoglou, C.N. Nayeri, and C.O. Paschereit. Active stall control solutions for power regulation and load alleviation of large wind turbines. In *Conference of Modelling Fluid Flow (CMFF), Budapest, Hungary*, 2012.

[112] G. Pechlivanoglou, J. Wagner, C. N. Nayeri, and C. O. Paschereit. Active aerodynamic control of wind turbine blades with high deflection fexible flaps. In *48th AIAA Aerospace Sciences Meeting Including the New Horizons Forum and Aerospace Exposition, Orlando, Florida*, 2010.

[113] C. Plumley, W. Leithead, P. Jamieson, E. Bossanyi, and M. Graham. Comparison of individual pitch and smart rotor control strategies for load reduction. *The Science of Making Torque from Wind, Journal of Physics: Conference Series*, 524, 2014.

[114] S. Raghu. Fluidic oscillators for flow control. *Experiments in Fluids*, 54, 2013.

[115] K.S.V. Reddy, D.M. Sharma, and K. Poddar. Effect of end plates on the surface pressure distribution of a given cambered airfoil: Experimental study. In *New Trends in Fluid Mechanics Research*, page 286, 2009.

[116] J. Schneemann, P. Knebel, P. Milan, and J. Peinke. Lift measurements in unsteady flow conditions. In *European Wind Energy Conference and Exhibition (EWEC), Warsaw, Poland, April 20.-23.*, 2010.

[117] S. Schreck and M. Robinson. Wind turbine blade flow fields and prospects for active aerodynamic control. In *ASME Fluids Engineering Division*, 2007.

[118] H.C. Seetharam, W.G. Kuhn, M.D. Mack, and J.T. Bright. Aerodynamics of spoiler control devices. In *AIAA Aircraft Systems and Technology Meeting*, 1979.

[119] RH.C. Seetharam, M. Janiszewska, and G.M. Gregorek. Wind tunnel testing of a S809 spoiler flap model (for wind turbines). In *AIAA Meeting papers, pp.11*, 1997.

[120] A. Seifert, A. Darabi, and I. Wygnanski. Delay of airfoil stall by periodic excitation. *Journal of Aircraft*, 33(4), 1996.

[121] A.R. Serakawi and K.A. Ahmad. Experimental study of half-delta wing vortex generator for flow separation control. *Journal of Aircraft*, 49:76–81, 2012.

[122] A. Seshagiri, E. Cooper, and L.W. Traub. Effects of vortex generators on an airfoil at low Reynolds numbers. *Journal of Airc*, 46:116–122, 2009.

[123] I.J. Sharland. Sources of noise in axial flow fans. *Journal of Sound*, 1:302–322, 1964.

[124] L. Sirovich. Turbulence and the dynamics of coherent structures, parts i, ii and iii. *Quarterly of Applied Mathematics*, XLV:561–590, 1987.

[125] C.P. van Dam S.J. Johnson and D.E. Berg. Active load control techniques for wind turbines. Technical report, Sandia National Laboratories, 2008.

[126] A.M.O. Smith. High-lift aerodynamics. In *AIAA 6th Aircraft Design, Flight Test and Operations Meeting, Los AngelesCalifornia, August 12-14*, 1974.

[127] D.M. Somers. Design and experimental results for the S809 airfoil. Technical report, NREL National Renewable Energy Laboratory, Golden, Colorado, USA, 1997.

[128] D.M. Somers and M.D. Maughmer. Theoretical aerodynamic analyses of six airfoils for use on small wind turbines. Technical report, NREL, National Renewable Enery Laboratory, Golden, Colerado, USA, 2002.

[129] K.J. Standish and C.P. van Dam. Computational analysis of a microtab-based aerodynamic load control system for rotor blades. In *AHS 4th Decennial Specialists' Conference on Aeromechanics, San Francisco, CA*, 2004.

[130] K.J. Standish and C.P. van Dam. Computational analysis of a microtab-based aerodynamic load control system for rotor blades. *Journal of the American Helicopter Society*, 50:249–258, 2005.

[131] T.L. Sullivan. Effect of vortex generators on the power conversion performance and structural dynamic loads of the MOD-2 wind turbine. Technical report, NASA TM-83680, 1984.

[132] T. Theodorsen. General theory of aerodynamic instability and the mechanism of flutter. *NACA Rep. No. 496*, pages 413–433, 1935.

[133] P. Thiede. *Aerodynamic Drag Reduction Technologies: Proceedings of the CEAS/DragNet European Drag Reduction Conference*. Spinger International, 2000.

[134] D. R. Troolin, E.K. Longmire, and W.T. Lai. The effect of Gurney flap height on vortex shedding modes behind symmetric airfoils. In *13th Int. Symp. on Applications of Laser Techniques to Fluid Mechanics, Lisbon, Portugal*, 2006.

[135] C.P. van Dam, R. Chow, J.R. Zayas, and D.E. Berg. Computational investigations of small deploying tabs and flaps for aerodynamic load control. *Journal of Physics: Conference Series*, 75, 2007.

[136] L.L. van Dommelen and S.F. Shen. The spontaneous generation of the singularity in a separating laminar boundary layer. *Journal of Computational Physics*, 38:125–40, 1980.

[137] C.M. Velte, M.O.L. Hansen, and D. Cavar. Flow analysis of vortex generators on wing sections by stereoscopic particle image velocimetry measurements. Technical report, Environmental Research Letters, 2008.

[138] C.M. Velte, M.O.L. Hansen, and K.E. Meyer. Evaluation of the performance of vortex generators on the DU91-W2-250 profile using stereoscopic PIV. In *International Symposium on Energy, Orlando, Florida*, 2008.

[139] S. Vey, H.M. Lang, C. N. Nayeri, C.O. Paschereit, and G. Pechlivanoglou. Extracting quantitative data from tuft flow visualizations on utility scale wind turbines. In *Science of Making Torque of Wind*, 2014.

[140] S. Vey, H.M. Lang, G. Pechlivanoglou, C.N. Nayeri, and C.O. Paschereit. Quantitative surface flow visualization on wind turbines. In *Journal of Physics: Conference Series*, 2014.

[141] S. Vey, D. Marten, G. Pechlivanoglou, C.N. Nayeri, and C.O. Paschereit. Experimental and numerical investigations of a small research wind turbine. In *AIAA Aviation, 33rd AIAA Applied Aerodynamics Conference, June 22-26, Dallas, Texas, USA*, 2015.

[142] B.A.O. Vieira, M.P. Kinzel, and M.D. Maughmer. Unsteady aerodynamics of miniature trailing-edge effectors based on indicial methods. In *49th AIAA Aerospace Sciences Meeting including the New Horizons Forum and Aerospace Exposition, Orlando, Florida*, 2011.

[143] H. Wagner. Über die Entstehung des dynamischen Auftriebes von Tragflügeln. *ZAMM*, 5:17–35, 1925.

[144] D. Keith Walters and Davor Cokljat. A three-equation eddy-viscosity model for Reynolds-averaged NavierŰStokes simulations of transitional flow. *Journal of Fluids Engineering*, 130(December):121401, 2008.

[145] J.J. Wang, Y.C. Li, and K.-S. Choi. Gurney flap - Lift enhancement, mechanisms and applications. *Progress in Aerospace Sciences*, 44:22–47, 2008.

[146] G. Weinzierl. A BEM based simulation-tool for wind turbine blades with active flow control elements. Master's thesis, Technische Universität Berlin, ISTA, 2011.

[147] G. Weinzierl, G. Pechlivanoglou, C.N. Nayeri, and C.O. Paschereit. Performance optimization of wind turbine rotors with active flow control, Part 2: Active aeroelastic simulations. In *Proceedings of ASME IGTI Turbo Expo 2012, ASME/IGTI, June 11 - 15, Copenhagen, Denmark*, 2012.

[148] H. G. Weller, G. Tabora, and H. Jasak. A tensorial approach to computational continuum mechanics using object-oriented techniques. *Computers in Physics*, 12(6):620–631, 1998.

[149] D.G. Wilson, D.E. Berg, D.W. Lobitz, and J. R. Zayas. Optimized active aerodynamic blade control for load alleviation on large wind turbines. In *AWEA Windpower*, 2008.

[150] R. Woszidlo, F. Ostermann, C.N. Nayeri, and C.O. Paschereit. The time-resolved natural flow field of a fluidic oscillator. *Experiments in Fluids*, 56, 2015.

[151] S. Yarusevych and M. Boutilier. Effects of end plates and blockage on a low Reynolds number airfoil experiment. In *41th AIAA Fluid Dynamic Conference and Exhibit, Honululu, Hawai*, 2011.

[152] D.T. Yen, C.P. van Dam, R.L. Smith, and S.D. Collins. Active load control for wind turbine blades using MEM translational tabs. In *ASME Wind Energy Symposium, 20th, Aerospace Sciences Meeting and Exhibit, 39th, Reno, NV*, 2001.

[153] D.T. Yen-Nakafuji, C.P. van Dam, R.L. Smith, and S.D. Collins. Active load control for airfoils using microtabs. *Journal of Solar Energy Engineering*, 123:282–289, 2001.

[154] W.W.H. Yeung, C. Xu, and W. Gu. Reduction of transient adverse effects of spoilers. *Journal of Aircraft*, 34(4):479 – 484, 1997.